



The University of
Nottingham

UNITED KINGDOM • CHINA • MALAYSIA

Simulations of Dynamic Nuclear Polarization pathways in large spin ensembles

BY: DANIEL WIŚNIEWSKI, MSCI

THESIS SUBMITTED TO THE UNIVERSITY OF
NOTTINGHAM FOR THE DEGREE OF DOCTOR OF
PHILOSOPHY

01 OCTOBER 2016

Abstract

Dynamic Nuclear Polarization (DNP) is a method for signal enhancement in NMR, with numerous applications ranging from medicine to spectroscopy. Despite the success of applications of DNP, the understanding of the underlying theory is still limited. Much of the work on the theory of DNP has been carried out on small spin systems; this is a restriction due to the exponential growth of the Liouville space in quantum simulations. In the work described in this thesis, a methodology is presented by which this exponential scaling can be circumvented. This is done by mathematically projecting the DNP dynamics at resonance onto the Zeeman subspace of the density operator. This has successfully been carried out for the solid effect, cross effect and recently for the Overhauser effect in the solid state (see appendix A.4). The results are incoherent state-dependent dynamics, resembling classical behaviour.

Such form of effective dynamics allows the use of kinetic Monte Carlo algorithms to simulate polarization dynamics of very large spin systems; orders of magnitude larger than has previously been possible.

We verify the accuracy of the mathematical treatment of SE-DNP and CE-DNP, and illustrate the insight large spin-system simulations provide into the mechanism of DNP. For SE-DNP the mechanism of polarization to the bulk of spin systems is determined to be spin diffusion, and we carried out studies into the efficiency and performance of radicals, with an outlook on radical design. We also show that the Zeeman projection can be applied to heteronuclear spin systems if the nuclear species are close in frequency, and we present a formalism for simulating ^{13}C nuclear spin systems based on a linear rate approach, enabling simulations of thousands of spins in a matter of minutes. A study into the scaling of the kinetic Monte Carlo algorithm error, and the simulation run time, with respect to an increasing number of spins is also presented.

For CE-DNP the error analysis led to establishing a parameter regime in which the effective dynamics are accurate. We show that spin diffusion is the mechanism of transfer of polarization to bulk nuclei. We also show how the effective rates for CE-DNP can be used to understand the efficiency of bi-radicals, point to optimisation possibilities, and hold a potential to aid in bi-radical design.

We finally show large scale simulations for CE-DNP bi-radical systems with improved parameters; leading to very rapid build-up of nuclear polarization.

Acknowledgements

I would like to express my gratitude to everyone who has helped and supported me during my PhD. In particular I would like to thank my supervisors: Walter Köckenberger and Igor Lesanovsky for giving me the opportunity to work with them on a challenging and exciting project, and giving their support throughout. Alexander Karabanov for his help, support, and patience when working together. Thank you also to: Josef Granwehr, Jim Leggett, Sankeerth Hebbar, Grzegorz Kwiatkowski, and the whole "K-team", in particular: Edward Breeds, Ben McGeorge-Henderson, and Adam Gaunt.

Thank you to the many friends I have made during my time at the Sir Peter Mansfield Imaging Centre.

And finally, I would also like to thank my family, especially my mother for the many sacrifices she has made to help me get to where I am now.

Contents

1	Introduction	1
1.1	Quantum mechanical description of polarization	5
1.2	Dynamic Nuclear Polarization	6
1.3	DNP mechanisms	7
1.4	Current work	9
1.5	Thesis structure	10
2	Theory	13
2.1	Open quantum systems - relaxation theory	13
2.1.1	The density operator formalism	13
2.1.2	Quantum operation	16
2.1.3	Markovian evolution – Lindblad master equation	18
2.1.4	Lindblad propagator	20
2.1.5	Use of Lindblad master equation in NMR and DNP	22
2.1.6	Link between quantum and classical dynamics	24
2.2	Theory of solid effect DNP	25
2.2.1	Solid effect	26
2.2.2	Hamiltonian	27
2.2.3	Rotating frame of reference	28
2.2.4	SE-DNP master equation	30
2.3	Theory of cross effect DNP	32
2.3.1	Cross effect	32
2.3.2	Hamiltonian	34
2.3.3	CE-DNP master equation	35
2.4	Adiabatic elimination	36
2.4.1	Mathematical procedure	37
2.4.2	Effective dynamics	40
2.5	Kinetic Monte Carlo algorithm	42
2.5.1	Quantum Jump Monte Carlo	43
2.5.2	Classical kinetic Monte Carlo	44

3	Solid Effect	48
3.1	Adiabatic elimination of Solid Effect dynamics	48
3.1.1	Elimination of non-zero quantum coherences	48
3.1.2	Superoperator \mathbf{M}	51
3.1.3	Elimination of non-Zeeman spin orders	54
3.1.4	The Lindblad form	57
3.1.5	Analysis of SE-DNP effective dynamics	58
3.2	Error testing of Zeeman projection in SE-DNP	60
3.3	Spin diffusion studies	66
3.3.1	Mathematical treatment of spin diffusion	68
3.4	Large spin ensemble calculations	74
3.4.1	Hydrogen nuclei	74
3.4.2	Carbon-13 nuclei	76
3.4.3	Carbon-13 – large spin system simulations	78
3.4.4	Fitting of polarization curves	81
3.5	Monte Carlo scaling and error analysis	85
3.5.1	Scaling of error with number of spins	85
3.5.2	Scaling of simulation duration	90
3.6	Adiabatic elimination of Solid Effect dynamics for hetero-nuclear spins	91
3.6.1	Analysis of hetero-nuclear SE-DNP effective dynamics	93
3.6.2	Error testing	94
3.6.3	Large heteronuclear spin system simulations	96
3.7	Linear rate equation approach for simulating SE-DNP	97
3.7.1	Projection onto the polarization subspace	98
3.7.2	Error testing against Zeeman projection	101
3.7.3	Very large spin-system simulations	103
4	Radical design	105
4.1	Introduction	105
4.2	Model spin system	106
4.3	Influence of nuclei close to the electron	110
4.4	Radical design	115
5	Cross Effect	117
5.1	Effective Cross Effect dynamics	117
5.1.1	Elimination of non-zero quantum coherences	117
5.1.2	Superoperator \mathbf{M}	120
5.1.3	Elimination of non-Zeeman spin orders	121

5.1.4	The Lindblad form	124
5.1.5	Analysis of CE–DNP effective dynamics	125
5.2	Validity of assumptions	130
5.2.1	Testing the zero–quantum subspace master equation	130
5.2.2	Testing the Zeeman subspace projection	132
5.2.3	Summary	140
5.3	Predicting regions of excessive error	140
5.3.1	Error under shorter decoherence times	144
5.3.2	Error testing with shorter $T_1^{(S)}$ times	147
5.3.3	Error testing for nuclei with lower $\gamma - {}^{13}\text{C}$	149
5.3.4	Error testing summary	150
5.4	Spin diffusion studies	150
5.5	Optimisation studies	154
5.5.1	Optimising bi–radical coupling	156
5.5.2	Simulations for bi–radicals with optimised parameters	162
5.5.3	CE–DNP at low temperature	165
6	Conclusion & Outlook	170
	Appendix	173
A.1	Commutative form of Hamiltonian superoperators	173
A.2	Explicit derivation of rate Γ^{IS} for a two-spin system	173
A.3	Computational form of operator-valued rates	175
A.4	Overhauser Effect dynamics projected onto Zeeman subspace	177
	Bibliography	180

List of commonly used symbols

Symbol	Meaning	Page
γ	gyromagnetic ratio	p.2
ω	Larmor frequency	p.5
$\omega_{\mu w}$	microwave frequency	p.28
ω_1	microwave field amplitude	p.24
$\delta t, \delta$	small time step, error	p.18, p.86
ϵ	enhancement	p.7
Δ	frequency offset from electron Larmor frequency	p.30
$\Delta\omega_S$	difference between electron Larmor frequencies (CE-DNP)	p.33
B_Z	static magnetic field strength	p.5
m_s	quantum spin number	p.2
E_z	energy eigenstates	p.6
A_k	secular hyperfine coupling	p.30
$B_{k\pm}$	pseudo-secular hyperfine coupling	p.30
D	electron dipolar coupling	p.34
$d_{kk'}$	nuclear dipolar coupling	p.27
$r_{kk'}$	spin-spin separation	p.28
T_1, T_2	relaxation time constants; longitudinal and transverse respectively	p.23
R_1, R_2	relaxation rates; longitudinal and transverse respectively	p.23
$\lambda, \lambda_1, \lambda_2$	frequency offsets from SE-DNP and CE-DNP resonance conditions, respectively	p.49, p.118
Ψ	wavefunction	p.2
$\hat{}$	hat notation used for operators	p.6
$\langle \rangle$	expectation value of operator	p.24
$\hat{\rho}$	density operator	p.14
$\text{col}\hat{\rho}$	column-stacked density operator	p.21
p_{th}	thermal polarization	p.23
\hat{H}	Hamiltonian	p.13
$\hat{1}$	identity operator	p.17
$\hat{\leftrightarrow}$	interaction tensor	p.27
\hat{R}_z	rotation operator/matrix	p.29

Symbol	Meaning	Page
\hat{H}	commutation operation with Hamiltonian	p.49
\hat{M}_μ	Kraus operator	p.16
\mathbf{L}	Lindbladian	p.20
$\mathbf{D}[\cdot]$	Lindblad dissipator	p.20
\hat{L}_k	Lindblad jump operator	p.19
Γ	rate of process	p.22
$*$	operator/matrix conjugate	p.21
\dagger	Hermitian transpose	p.14
\otimes	direct (Kronecker) product	p.15
Tr	trace operation	p.14
\mathcal{L}	Liouville space/subspace	p.49
\mathcal{H}	Hilbert space/subspace	p.16
\mathbf{K}	Kernel function	p.38
\mathcal{P}	Nakajima-Zwanzig projection operator	p.37
\mathcal{Q}	Nakajima-Zwanzig complimentary projection operator	p.37

Chapter 1

Introduction

Nuclear magnetic resonance (NMR) relies on exciting nuclear spins with radio-frequency radiation. In the presence of a static magnetic field the spins precess around the field vector, with a characteristic Larmor frequency. Radio frequency pulses are then used to rotate the macroscopic magnetization into the transverse plane, where detection takes place – a free induction decay signal is detected. As a technique, it has quickly found uses in spectroscopy as well as imaging. As a tool for spectroscopy, NMR is a non-destructive method as it does not require the use of ionising radiation. The sample tested is not in any way affected by the magnetic field, and the energy deposited due to heating from the radio waves tends to be negligible. NMR is therefore suitable for studies of large biomolecules [1], such as proteins [2] and organic molecules [3], and has proven to be an invaluable tool for solving their molecular structures. Such studies are usually conducted on samples in the liquid state, however there exist studies in the solid state on samples where liquid state NMR is not feasible; one example is studies of amyloid fibrils [4]. In the solid state, NMR can be combined with magic angle spinning (MAS) [5] to solve structures of powdered materials [6]. Magic angle spinning averages out the dipolar interactions of the nuclei and therefore reduces, or removes altogether the broadening of the spectrum. MAS NMR holds a true advantage over X-ray crystallography, since X-ray crystallography is only suitable for regular crystalline structures or single crystals. In cases of powder materials, the spectrum becomes very difficult to analyse [7], and the structures become impossible to solve. Magnetic resonance imaging (MRI) of human subjects very quickly found regular use [8], [9], [10] following its discovery for similar reasons. With use of non-ionising radiation, NMR is less harmful than X-ray imaging or CAT scans [11], as it does not damage human tissue. In addition, MRI enables imaging of soft tissue, which is much harder to achieve with X-ray imaging.

The one disadvantage of NMR is the low signal sensitivity [12]. NMR is generally an insensitive technique, and often averaging over many scans would be required

to obtain a reasonable signal-to-noise ratio. The signal strength is proportional to the magnetization of the sample, which tends to be low for atomic nuclei at room temperature, even at high magnetic fields. Magnetization is a macroscopic property which relies on the ordering of spin states of nuclei in the sample. It thus relies on the polarization of individual spins, which is a statistical entity describing the probability of finding a nucleus in one spin eigenstate over the probability of the spin being in any of the other accessible states. Protons, next to tritium, have the highest gyromagnetic ratio (γ_I) amongst atomic nuclei, however even with proton NMR, the degree of polarization at room temperatures tends to be on the order of 10^{-5} . At low temperatures approaching 1 K, the polarization is approximately 0.3 %. This is directly the reason for the insensitivity of NMR. Atomic nuclei of ^{13}C have an even lower gyromagnetic ratio – their gyromagnetic ratio is approximately 4 times lower than that of hydrogen. Electronic spins, on the other hand have a gyromagnetic ratio, that is almost three orders of magnitude larger. As a comparison, the polarization of electron spins, and that of hydrogen and ^{13}C nuclear spins is shown as a function of temperature in fig. (1.1).

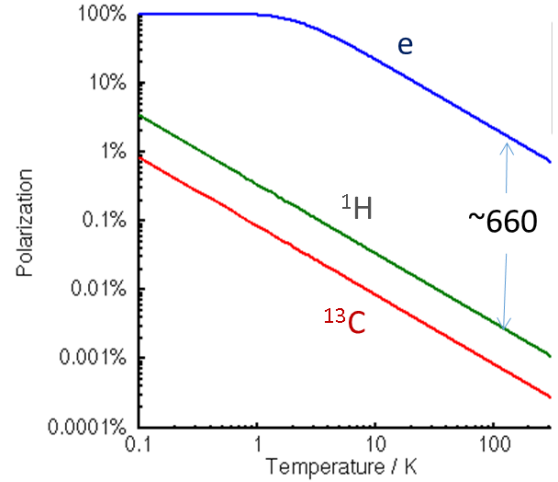


Figure 1.1: Polarization shown as a function of temperature for an electron spin, ^1H , and ^{13}C nuclei.

Several methods have been developed to attempt to increase the polarization of nuclear spins, such as dynamic nuclear polarization (DNP), use of parahydrogen [13], nitrogen vacancy centres [14], [15], spin-exchange optical pumping (SEOP) of noble-gas nuclei [16], and chemically induced DNP [17].

Parahydrogen

Hydrogen gas (H_2) obeys Fermi-Dirac statistics, thus the molecular wavefunction must be anti-symmetric with respect to a permutation between the atoms. By the Born-Oppenheimer approximation the wavefunction may be factored into individual components of: electronic, vibrational, rotational, and nuclear. The product of the electronic and vibrational energy levels is symmetric for lower-lying energy states. Thus the product of the nuclear (ψ_{nuc}) and rotational (ψ_r) wavefunctions

must be anti-symmetric. In the presence of a magnetic field the nuclear spin states are separated into a triplet (odd values of rotational quantum number $-J$; anti-symmetric rotational wavefunction), and a singlet (even J values; symmetric rotational wavefunction), with a population ratio of 3:1. The singlet state is referred to as parahydrogen, and transitions between the singlet and triplet states are forbidden. At low temperatures, and in the presence of a catalyst (iron filings or activated charcoal), it is however possible to convert the triplet state hydrogen nuclei to singlet states. This way the hydrogen gas becomes enriched. The parahydrogen gas can be stored for very long periods of time, and eventually used in a hydrogenation reaction targeting unsaturated bonds. Placing the parahydrogen in this kind of symmetry-breaking environment causes the protons to become distinguishable, and thus their wavefunction changes instantaneously. This results in the two distinct hydrogen nuclei having high polarization, which can then be transferred to other protons in the target molecule.

The methods of sensitivity enhancement using parahydrogen in use are PASADENA [13], where the hydrogenation reaction is carried out within a magnetic field, ALTADENA [13], where the hydrogenation reaction is carried out in Earth's magnetic field, and more recently developed SABRE [18], where signal amplification by reversible exchange is achieved without modification of the target molecule.

Parahydrogen induced polarization gives large signal enhancements, however the list of molecules which these techniques can be applied to is limited, particularly in the case of the PASADENA and ALTADENA methods – these rely on hydrogenation of unsaturated bonds. In addition, the polarization is divided up between protons in the target nuclei lowering their individual polarization enhancement.

Nitrogen–Vacancy centres

Nitrogen vacancy (NV) centres are defects in diamond lattice structures with a C_{3v} symmetry. They consist of a nitrogen–lattice vacancy electron pair oriented along the $[1,1,1]$ crystalline direction. These can exist in either negative (NV^-) or neutral (NV^0) charge states. The two can be distinguished by their optical zero phonon lines [19]. The NV centre exists in a triplet state ($S = 1$).

Laser radiation is used to excite the NV centre from its ground state (3A) to its first excited state (3E). There processes of internal conversion and fluorescence relaxation lead to generation of a non-Boltzmann eigenstate population, in the triplet ground state. This is due to spin angular momentum not being conserved in these transitions, and the degeneracy of the spin sublevels of 3A being lifted due to the presence of a zero field splitting term. The high polarization of the NV centre spin state can be utilised via level anti-crossing to increase the nuclear

polarization. Level anti-crossings occur at specific magnetic field strengths, and lead to a significant population difference of the nuclear eigenstates.

The advantage of this approach is that the procedure of nuclear polarization enhancement can be carried out at room temperature, whereas DNP is often carried out at liquid helium temperatures, or lower. Polarization levels close to 100 % have been reported [20]. The disadvantage is that the mechanism is restricted to specific systems, mostly diamonds, and cross-polarization or diffusion of polarization into other surfaces is difficult to achieve.

Spin-Exchange Optical Pumping

In spin-exchange optical pumping glass cells containing alkali-metal atoms, a noble gas, as well as a buffer gas are used. Often the experiments are carried out at pressures below 1 atm. Nitrogen gas is frequently chosen as a buffer to reduce radiation trapping, as it does not lead to very significant depolarization of the hyperpolarized noble gas. The glass cell is irradiated with circularly polarized laser light, a significant percentage of which is absorbed by the alkali atoms. Circularly polarized light causes atomic transitions with a change in angular momentum of ± 1 , and in effect the valence electrons of the alkali-metal atoms, as well as their nuclei become highly spin-polarized. Subsequent collisions between the alkali metal atoms and the noble gas atoms cause a transfer of the electron-spin polarization from the alkali atoms to the nuclei of the noble gas. The transfer of angular momentum between the two is also possible while the atoms are bound in van der Waals molecules, this particularly applies to noble gasses with heavier atoms. For ^3He binary collisions dominate the spin exchange.

The result is a large polarization of the noble gas nuclei, often exceeding 50 %. The hyperpolarized noble gas can then be used in a mixture with oxygen or atmospheric air, for lung imaging and diagnostics. The disadvantage is the limitation to gaseous samples, the relatively large cost of noble gases (for example Krypton), or the fact that ^3He is a non-renewable resource.

Chemically induced Dynamic Nuclear Polarization

In CiDNP radicals are formed as a consequence of photochemical reactions. The mechanism underlying the enhancement of NMR signal due to CiDNP has been associated with radicals reacting in the presence of a magnetic field, as well as the effect nuclear magnetic moments have on their reaction rates [21]. If the exchange interaction between electrons is comparable in magnitude to the difference between the energy eigenstates of nuclear spins, the nuclei can effectively induce singlet-triplet mixing of the electronic pair spin states. Nearly all radical-radical

chemical reactions produce observable singlet–state products, the reaction rate is thus proportional to the percentage of singlet–state radicals pairs in the system. It has also been found to be dependent on the state of nearby nuclear spins. A triplet pairing cannot lead to a reaction, however one of the radicals can undergo a spin inversion – depending on the state of a nearby nuclear spin state. The nuclear spin state has thus been compared to a catalyst [22] for the triplet to singlet state conversion of the radical spin pair. If the nearby nuclear spin is in a unfavourable spin state, the radicals could physically separate and react instead with other radicals in the presence of a nucleus found in the more favourable spin state. This leads to ordering of nuclear spin states in the product, and thus an increased nuclear polarization.

CiDNP has use in signal enhancement of NMR, but in addition can serve as a method for study of the reaction mechanisms of transient electron radicals in chemistry. It is limited to use in molecules which form radicals in photochemical reactions.

1.1 Quantum mechanical description of polarization

In the presence of a static magnetic field B_Z , and for $m_s \neq 0$ the Zeeman energy eigenstates of a spin lose their degeneracy and split according to the value of the spin quantum number m_s . The quantum number m_s can take half–integer or integer values, and for a given m_s , the number of accessible Zeeman energy eigenstates is $2 \times m_s + 1$, i.e. all possible integer–step permutations between $-m_s$ to m_s .

For $m_s = \frac{1}{2}$, there are two eigenstates, often denoted as $|\alpha\rangle$, $|\beta\rangle$ or $|\uparrow\rangle$, $|\downarrow\rangle$ with eigenvalues $+\frac{1}{2}$, $-\frac{1}{2}$, respectively. Throughout my work, I have focused on spin $\frac{1}{2}$ species, hence unless otherwise stated, all relations and properties will be portrayed for spins with $m_s = \frac{1}{2}$. The Zeeman energy difference, i.e. the difference in energies between the two states for a spin- $\frac{1}{2}$ particle relies directly on the Larmor frequency of a spin. The Larmor frequency of a spin is the frequency at which a spin will precess around the magnetic field vector B_Z , given as

$$\omega = -\gamma \cdot B_Z.$$

The constant γ is the gyromagnetic ratio of a particular nuclear spin, related to its mass via $|\gamma| = \frac{|e|\hbar}{2m}g$, B_Z , the magnetic field strength, and g the g–factor [23]. Electrons which have a much lower mass than atomic nuclei, leading to a much

higher value of the gyromagnetic ratio.

The Zeeman energy eigenstates of a nuclear spin are obtained from

$$E_Z = \omega_0 \hbar \hat{I}_z,$$

where \hat{I}_z for $m_s = \frac{1}{2}$ is a 2×2 Pauli σ_z matrix, with eigenstates $+\frac{1}{2}$, $-\frac{1}{2}$. According to Boltzmann statistics, the difference between the populations of the two eigenstates is

$$\Delta P = \frac{e^{-P_\alpha} - e^{-P_\beta}}{e^{-P_\alpha} + e^{-P_\beta}} = \frac{e^{\frac{\gamma \hbar B_Z}{2k_b T}} - e^{-\frac{\gamma \hbar B_Z}{2k_b T}}}{e^{\frac{\gamma \hbar B_Z}{2k_b T}} + e^{-\frac{\gamma \hbar B_Z}{2k_b T}}} \equiv \tanh\left(\frac{\gamma \hbar B_Z}{2k_b T}\right), \quad (1.1)$$

where k_b is the Boltzmann constant, and T the temperature of the surrounding environment. The final product in eq. (1.1), is referred to in magnetic resonance as the thermal polarization of that spin. Due to the relatively small gyromagnetic ratio of nuclear spins, their Zeeman energy E_Z is much smaller than the thermal energy ($k_b T$). This in turn means that nuclei have low polarization. At room temperature experiments ($T = 298$ K) and a field of $B_Z = 3.4$ T, we have a proton polarization of 1.16×10^{-5} , and an electronic polarization of 7.7×10^{-3} . This is why NMR suffers from low sensitivity. Changing T to 1 K, however the polarization values then become 3.5×10^{-3} and 0.98 respectively. It is clear from the above relation that the electron polarization rapidly approaches 100% as $T \rightarrow 0$ K.

1.2 Dynamic Nuclear Polarization

As mentioned, electron spins have a much higher gyromagnetic ratio (γ_S) than nuclear spins. As a comparison to protons, the ratio of electronic γ_S to the nuclear one γ_I is $\gamma_S/\gamma_I \approx 658$, meaning electrons will have a much higher degree of polarization at any non-negligible magnetic field strength, and at temperatures of $T \gtrsim 1$. DNP is concerned with transferring the polarization from the electron to the surrounding nuclei to create a highly polarized non-thermal state, resulting in a large signal enhancement. The most efficient of the DNP mechanisms in the solid state is the cross effect (CE DNP) mechanism. To date enhancements as high as ~ 400 have been achieved [24] with the use of MAS DNP, and biradical molecules that exhibit a strong inter-electronic coupling.

In addition to a DNP-driven enhancement, rapid changes of sample temperature may also lead to an enhancement of the signal. Using equation (1.1), it is straightforward to see that the ratio of polarization values for a nucleus at 1 K, to that at room temperature results in a theoretical enhancement of 300. The total enhance-

ment in such case is a product of the DNP enhancement, and the enhancement due to the temperature change

$$\epsilon = \epsilon_{DNP} \times \epsilon_T,$$

For protons this leads to a total theoretical maximal enhancement close to 200,000. The advantage and importance of DNP is therefore very clear.

Several applications of DNP have recently highlighted the huge potential that this method offers for increasing the low sensitivity of MRI and spectroscopy experiments [25, 26]. In particular, use of highly polarized ^{13}C labelled molecules in conjunction with spectroscopic MRI have led to the development of novel experimental protocols for human cancer diagnostics [27, 28].

There are two types of experiments where a rapid temperature change in the sample is induced: dissolution DNP [29] and rapid temperature jump DNP [30].

In the case of dissolution DNP, a sample is cooled down to temperatures close to 1K, and irradiated with microwave radiation to build-up polarization in nuclei. Following the build-up, the sample is dissolved and brought up to room temperature with the use of hot solvents. Typically the dissolved sample would then be either shuttled, or transferred through a magnetic tunnel to a conventional NMR magnet. In either case a liquid-state spectrum of the sample would then be obtained.

In the case of temperature jump DNP, instead of using a hot solvent, rapid heating is applied, typically with the use of microwave radiation or optical lasers, to melt the sample and bring it up to room temperature. A liquid state spectrum would then be obtained. Experimental studies have been published, where with the use of dissolution DNP enhancements of over 10,000 have been observed [29]. In the case of temperature jump DNP, the enhancements seen have not been as large, as previously experiments have been carried out at 90 K, with a temperature jump to room temperature. Greater enhancements are expected in the case of a temperature jump from a few Kelvin to room temperature.

1.3 DNP mechanisms

Several possible mechanisms of DNP exist. In liquid state samples, the only DNP mechanism that is known to exist is the Overhauser effect. Predicted in theory by Albert Overhauser in 1953 [31] to occur in metallic conductors with delocalised electron carriers, and later in the same year verified experimentally by Carver and Slichter [32], this is the first DNP mechanism to have been discovered. The Over-

hauser effect can also exist in non-metallic solid state samples which have highly delocalised electrons; e.g. graphene samples [33]. Recent studies also suggest the Overhauser effect can exist in solid dielectric samples undergoing periodic rotation of MAS DNP [24]. The process of nuclear polarization build-up in static samples is driven by cross-relaxation of an electron radical spin state, and the spin state of a coupled nucleus, where one path of cross-relaxation has a higher rate than the other, i.e. either the zero-quantum (ZQ) or double-quantum (DQ) transition dominates. The cross-relaxation flips are believed to be caused by a rotational and translational modulation of the electron-nuclear hyperfine coupling terms.

In the solid state there are additionally: the solid effect, cross effect, and thermal mixing mechanisms. The solid effect mechanism is predominant in samples at very low temperatures (few K) which have a low concentration of radical molecules. They have narrow EPR linewidths, with very little broadening. Each radical electron is typically surrounded by several thousand nuclear spins.

The cross effect mechanism relies on electron spin pairs, thus is predominant in samples where the radical concentration is higher and the separation between electron radicals is smaller or alternatively where bi-radical or tri-radical molecules are used. This mechanism tends to be predominant at temperatures of a few tens of Kelvin. In conjunction with MAS, experiments where CE-DNP is the dominant mechanism are often carried out at liquid nitrogen temperatures. EPR spectra of samples where CE-DNP is active are typically broad and inhomogeneous, and the electron radicals exist in a large variety of magnetic environments.

Thermal mixing (TM) is a many-body process of a strongly coupled electronic network interacting with atomic nuclei. This mechanism is the dominant DNP pathway when the homogeneous (and typically the inhomogeneous too) broadening is significantly greater than the nuclear Larmor frequency $\omega_I < \eta, \zeta$. Due to the exponential growth of the Liouville space with respect to an increasing number of simulated spins, it is difficult to describe thermal mixing systems using quantum-mechanical approaches. Such attempts are limited – one example of such work is by Hovav et al. [34]. Thermodynamic approaches are usually used for a description of TM. In these approaches the system is usually described as consisting of three spin reservoirs [35], and the principle of spin temperature is used in describing nuclear polarization enhancement. Often more than one DNP mechanism would be active in a sample, and in certain circumstances DNP mechanisms are incorrectly categorised as thermal mixing, when in fact a mixture of SE and CE-DNP takes place [36].

1.4 Current work

My PhD project was focused on the theory and spin dynamics of DNP. Although DNP has already been successfully used in a variety of applications, outlined above, the theory underlying the mechanisms is not yet entirely understood. A lot of insight has already been provided by small spin system simulations in previous work by ourselves and others [37, 38, 36, 39], but what is missing is insight into large spin system simulations. This in particular applies to understanding the transport of polarization into the bulk of the sample or when conducting studies into the optimisation of the DNP mechanisms to improve steady-state polarization and reduce the build-up times. More insight and a better understanding of the physics underlying DNP will lead to improvement of signal enhancement in applications, where DNP is already proven as a useful tool.

In addition, we believe that the systems exhibiting DNP are of interest to a much wider community conducting research into dissipative quantum systems. SE-DNP can be described as a central spin model, with the electron spin in the centre, driving nuclear spins out of thermal equilibrium. In CE-DNP, we have a case where a three-spin mechanism dominates over a two-spin mechanism, and the two electrons act as one entity, which is much more efficient than two individual electron sources exhibiting SE-DNP would be.

The aim of my project was therefore to develop new methodology for modelling and simulating the DNP mechanisms in order to gain an improved understanding of the underlying physics, and to seek ways to potentially improve the detected signal enhancements. We sought an approach which would allow simulations of spin systems much larger than was at the time possible, to gain more understanding of DNP. In the case of SE-DNP, one electron is typically surrounded by thousands of nuclear spins – our goal was to make such simulations possible, and in effect attempt to make the simulations more realistic.

Using mathematical techniques of adiabatic elimination, novel tools were developed for SE-DNP and CE-DNP allowing simulations with numbers of spins three orders of magnitude greater than was previously possible. This was carried out by projecting the dynamics of each mechanism onto the population subspace of the density operator. With this procedure, effective rate equations are extracted from the full dynamics. These rates resemble classical state-dependent dynamics and in such form provide new, clearer insight into these mechanisms of DNP.

Simulations were then implemented for 1-D spin chain systems in order to test an existing hypothesis [38] regarding transport of polarization in SE-DNP. It was shown that contrary to the previous model, transport of polarization into the bulk

is governed by spin–diffusion. Polarization transport pathways were fitted to a solution to the diffusion equation, more importantly however, it was discovered that a reflective boundary solution fits the simulated data much more closely. This highlighted the importance of large spin system simulations: small spin systems suffer severely from finite, reflective boundaries.

A large spin simulation involving 1331 spins was implemented to show the capability of our approach. The result was compared to a simulation where nuclear dipolar interactions were set to 0, to show spin diffusion effects in a 3–D lattice. A study into radical efficiency was then carried out, where a total of 26 nuclei out of 124 were subsequently removed from the system – a study as such is only possible with our formalism, as full master equation approaches are limited to a few spins. The study shows that removal of core nuclei can increase the polarization of the bulk, and thus an optimal separation between the electron and nearest surrounding nuclei exists, and the formalism has radical study and optimisation capability. A similar formalism for heteronuclear simulations was derived, and in addition simulations using a linear rate approach were implemented for a system, of 9260 ^{13}C nuclei.

For CE–DNP, the effective rate treatment showed that the SE–DNP mechanism is still present in cases of electron radical pairs. The mechanism of polarization transport was confirmed to again be spin–diffusion. A comprehensive error analysis showed the suitability of the formalism for studies of bi–radicals or mono–radicals in close proximity. It was discovered that the rate corresponding to the three–spin process of CE–DNP corresponded well to a region of shortest polarization build–up, and greatest steady–state nuclear polarization. The form of the effective rates shows a dependence of rate magnitude on relaxation parameters, microwave field amplitude, and electronic dipolar coupling strength. Varying those terms leads to the possibility of optimisation and design of bi–radicals, which our formalism holds. Large spin system simulations were then carried out with more optimal parameters.

1.5 Thesis structure

The thesis is divided into four main chapters, not including the introduction. Chapter 2 is a theory chapter. The theory of open quantum systems is first described, including the Kraus operator formalism and the Lindblad master equation. The theory of SE–DNP as well as CE–DNP are discussed in depth. Following this, the general principle of adiabatic elimination and separation of subspaces is described. In the last section the kinetic Monte Carlo algorithms, and their use are described.

Chapter three is focused entirely on SE-DNP. Firstly, the explicit derivation of the effective dynamics using adiabatic elimination is shown and discussed, including a qualitative description of the effective dynamics. In the next section a comprehensive error analysis is shown. This is followed by an analysis of the polarization transport in spin ensembles, and simulations of large spin systems. The scaling of Monte Carlo error and the simulation duration, with respect to an increasing number of spins are quantified and discussed. In section 6, we show how the effective dynamics can be extended to hetero-nuclear systems that are close in frequency. The final part of this chapter shows our linear-rate approach to SE-DNP, suitable for simulating systems of nuclei with lower gyromagnetic ratios (^{13}C is a perfect 'candidate'). This approach avoids the use of Monte Carlo algorithms, and allows simulations of spin systems consisting of 10s of thousands of spins in a manner of minutes.

In chapter four the effective formalism from chapter three is used to study the effect of removing core nuclei from a spin system. A tightly bound lattice of 124 ^{13}C nuclei and one central electron is used. Core nuclei are subsequently removed from the system, and the effect this has on the polarization of the ensemble is studied. We show that these spin systems intricately depend on the parameter choice, and an optimal separation between the central electron and nearest nuclei can be found, leading to an improved polarization transfer to the ensemble. We illustrate how this works using simulated DNP frequency spectra, and discuss the potential this holds for radical study and design.

Our work on cross effect DNP is described in chapter five. First the derivation of the effective dynamics is shown. The conditions for which the projection is valid are shown, and the effective rates leading to polarization build-up are individually described. The effective rates alone already provide a lot of insight into the mechanism of CE-DNP. A comprehensive error analysis follows, and we show the parameter region for which our formalism is valid, as well as showing how regions of excessive error can be predicted. The formalism is suitable for simulating systems of bi-radicals or mono-radicals in a relatively close proximity, up to approximately 40 Å. We then show that polarization transport in CE-DNP is also governed by spin diffusion. In the last section of chapter five, we show the dependence of nuclear polarization on the system parameters, especially on the electronic dipolar coupling strength, and their decoherence rate. We show the potential our formalism holds in bi-radical study, design and optimisation, as the effective rate for the three-spin process is seen to correspond to areas of

shortest polarization build-up and largest steady-state polarization levels in the ensemble. We show one example simulation as a comparison to SE-DNP where a good parameter choice leads to polarization build-up in CE-DNP being orders of magnitude faster.

In chapter six we present a summary and conclusion of our work to date, as well as an outlook into future research our group intends to conduct.

Chapter 2

Theory

This chapter summarises the theory behind dynamic nuclear polarization, starting from a quantum-mechanical description of the problem. Relaxation plays a very important role in DNP, and coherent evolution alone does not explain the phenomenon of polarization transfer. A closed system quantum-mechanical description of the problem is not suitable and one has to turn to the open quantum system approach, where relaxation of the system is described by a semi-classical phenomenological interaction with an effective environment. The theory of open quantum systems including the Kraus operator formalism and the Lindbladian approach are described in this chapter.

2.1 Open quantum systems - relaxation theory

An important starting point of the description of quantum mechanics of a many-body spin system is the density operator formalism.

2.1.1 The density operator formalism

For small spin systems (e.g. particle in an infinite energy well, or free electron approaching potential barrier) a suitable wavefunction is chosen, the squared amplitude of which corresponds to a probability of locating that particle at a particular point in space (and possibly time). The system Hamiltonian describes the interactions of the particle. For states stationary in time the time-independent Schrödinger is solved

$$\hat{H} |\Psi\rangle = E |\Psi\rangle. \quad (2.1)$$

Otherwise, if the wavefunction evolves under the action of a closed-system Hamiltonian, then the time-dependent variant of eq. (2.1) is used

$$i\hbar \frac{\partial}{\partial t} |\Psi\rangle = \hat{H} |\Psi\rangle. \quad (2.2)$$

However, for systems of 2 or more interacting particles, equation (2.2) becomes increasingly difficult to solve. The particles are often coupled with coherences existing between their states, and the dynamics of each particle become difficult to separate. The usual method of separating variables cannot be applied. One should instead use the density operator formalism. If the system can be described by a set of ortho-normal (orthogonal and normalised) quantum states $|\Psi\rangle = c_1\psi_1 + c_2\psi_2 + \dots + c_k\psi_k$, with associated normalisation coefficients c_1, c_2, \dots, c_k , the density operator is defined as

$$\hat{\rho} = |\Psi\rangle \langle\Psi| \equiv \sum_k p_k |\psi_k\rangle \langle\psi_k|, \quad (2.3)$$

where $p_k = |c_k|^2$ are probabilities of the system existing in a particular state.

The density operator has the following properties:

1. it is a Hermitian operator $\hat{\rho}^\dagger = \hat{\rho}$. For a complete set of basis states, it can be represented as a matrix – the dagger denotes a Hermitian conjugate
2. due to the Hermitian property $\hat{\rho}$ has real eigenvalues, and if Ψ is ortho-normal these eigenvalues are p_k , where $0 \leq p_k \leq 1$
3. the trace $Tr(\hat{\rho})$ of the density operator equals 1, if the underlying quantum states are properly normalised
4. the expectation value of any operator can be calculated if $\hat{\rho}$ is known: $\langle \hat{X} \rangle = Tr(\hat{X}\hat{\rho})$.

In the case that one of the $p_k = 1$, and the others are 0, the density operator represents a pure state. This implies there is 100% probability of finding the system in the corresponding state $|\psi_k\rangle \langle\psi_k|$. Otherwise the system is in a mixed state. The measure of how mixed the states of a density operator are is $Tr(\hat{\rho}^2)$. A trace value of 1 implies a pure state, while a trace value of <1 denotes a mixed state. Due to a small degree of polarization in NMR, as shown in eq. (1.1), nuclear states are always mixed. At very low temperatures and moderate-high magnetic fields, electronic spin states are approximately pure states.

To find the time evolution of the density operator, eq. (2.2) is used.

$$\frac{\partial}{\partial t} |\Psi\rangle = -\frac{i}{\hbar} \hat{H} |\Psi\rangle \quad \text{conjugating both sides gives} \quad \frac{\partial}{\partial t} \langle\Psi| = \frac{i}{\hbar} \langle\Psi| \hat{H}$$

hence

$$\frac{\partial}{\partial t} \hat{\rho} \equiv \frac{\partial}{\partial t} (|\Psi\rangle \langle\Psi|) = \frac{\partial |\Psi\rangle}{\partial t} \langle\Psi| + |\Psi\rangle \frac{\partial \langle\Psi|}{\partial t} = -\frac{i}{\hbar} \hat{H} |\Psi\rangle \langle\Psi| + \frac{i}{\hbar} |\Psi\rangle \langle\Psi| \hat{H}$$

$$\frac{\partial}{\partial t} \hat{\rho} = -\frac{i}{\hbar} [\hat{H}, \hat{\rho}]. \quad (2.4)$$

Equation (2.4) is called the Liouville von Neumann (LvN) equation, and it describes the time-evolution of a closed quantum system with density operator $\hat{\rho}$.

As a final point, it is worth mentioning that the thermal equilibrium density operator is well approximated by

$$\hat{\rho}_{\text{th}} = \frac{z}{\text{Tr}(z)}, \quad \text{where } z = \exp\left(-\frac{\hbar\hat{H}}{k_b T}\right), \quad (2.5)$$

for a thermal equilibrium Hamiltonian containing no time-dependent interactions, i.e. the system is not driven.

This form of the LvN equation describes unitary evolution, of a closed quantum system. A dissipative part can be added to accommodate for relaxation in an open quantum system.

For a two-spin system, for any given state of spin 1, spin 2 can exist in any of its accessible states. The states of each spin are independent of each other, hence when computing the total density operator for the two spins, a direct product \otimes is used

$$\hat{\rho}_A = \hat{\rho}_1 \otimes \hat{\rho}_2.$$

For an ensemble of spins, each having independent states, the ensemble density operator consists of a product of the individual spin density operators

$$\hat{\rho}_A = \hat{\rho}_1 \otimes \hat{\rho}_2 \otimes \hat{\rho}_3 \otimes \cdots \otimes \hat{\rho}_n.$$

For spin $\frac{1}{2}$ particles the dimension of the density operator of a single spin is 2^1 , for a two-spin system, this dimension becomes 2^2 . In general the system density operator scales as 2^n for n spins, and has $(2^n)^2 = 4^n$ elements.

2.1.2 Quantum operation

The theory in this section is described in detail by Preskill [40] and Fisher [41].

As mentioned previously, the systems we deal with in DNP are not isolated systems. These are subject to dissipation due to their coupling to the environment (often referred to as the lattice in NMR), and as such an open quantum system approach is necessary.

The system of interest (A) and coupled environment (E) behave together as an entangled bipartite system. The entire system density operator is of the form of $\hat{\rho} = \hat{\rho}_A \otimes \hat{\rho}_E$, where \otimes is again a direct product signifying that for a given state of the system - A, the environment may exist in any one of its possible states and vice versa. A pure state of the bipartite system may behave like a mixed state when A is observed alone [40], and an orthogonal measurement of the bipartite system may be a non-orthogonal positive operator-valued measure on A alone. If a state of the bipartite system undergoes unitary evolution, the problem is attempting to describe the evolution of A alone.

Supposing the initial density matrix of the bipartite system is a tensor product state of the form

$$\hat{\rho}_A \otimes |0\rangle_E \langle 0|,$$

the system has density operator $\hat{\rho}_A$, and the environment is in a pure state $|0\rangle_E$. The whole system evolves under the action of a unitary time evolution operator \hat{U}_{AE} :

$$\hat{U}_{AE} (\hat{\rho}_A \otimes |0\rangle_E \langle 0|) \hat{U}_{AE}^\dagger,$$

a partial trace is performed over the Hilbert space of the environment \mathcal{H}_E to find the density matrix of the system A

$$\hat{\rho}'_A = \text{Tr}_E \left(\hat{U}_{AE} (\hat{\rho}_A \otimes |0\rangle_E \langle 0|) \hat{U}_{AE}^\dagger \right) = \sum_{\mu} {}_E \langle \mu | \hat{U}_{AE} | 0 \rangle_E \hat{\rho}_A {}_E \langle 0 | \hat{U}_{AE}^\dagger | \mu \rangle_E,$$

where $\langle \mu |_E$ is an orthonormal basis for \mathcal{H}_E and in such case ${}_E \langle \mu | \hat{U}_{AE} | 0 \rangle_E$ is an operator acting on \mathcal{H}_A .

If the unitary operator acting in the subspace \mathcal{H} of density operator $\hat{\rho}_A$ is denoted as

$$\hat{M}_\mu = {}_E \langle \mu | \hat{U}_{AE} | 0 \rangle_E,$$

the evolution in this subspace is expressed as

$$\hat{\rho}'_A \equiv \mathbf{X}(\hat{\rho}_A) = \sum_{\mu} \hat{M}_\mu \hat{\rho}_A \hat{M}_\mu^\dagger. \quad (2.6)$$

Because the evolution of $\hat{\rho}_A \otimes |0\rangle_E \langle 0|$ is unitary under \hat{U}_{AE} , the operators \hat{M} in eq. (2.6) satisfy the property

$$\begin{aligned} \sum_{\mu} \hat{M}_{\mu}^{\dagger} \hat{M}_{\mu} &= \sum_{\mu} {}_E \langle 0 | \hat{U}_{AE}^{\dagger} |\mu\rangle_E {}_E \langle \mu | \hat{U}_{AE} |0\rangle_E \\ &= {}_E \langle 0 | \hat{U}_{AE}^{\dagger} \hat{U}_{AE} |0\rangle_E = \hat{1}_A. \end{aligned} \quad (2.7)$$

Throughout the thesis **bold notation** is used for superoperators. In equation (2.6) \mathbf{X} is a linear map, taking linear operators to linear operators. This map is called a superoperator or a quantum operation. The representation of \mathbf{X} is called an operator sum representation or Kraus representation of a superoperator, where \hat{M}_{μ} are the Kraus operators. Unitary evolution is invertible; there exists an inverse that can reverse the evolution of the system, forming an analogy to time-reversal. Unitary evolution forms a group. Superoperators describing non-unitary evolution define a dynamical semigroup. Decoherence, a dissipative process due to the interaction with the environment is an irreversible process that defines an arrow of time in quantum dynamics. As such, decoherence leads to an irreversible loss of information any real system is subject to – truly closed quantum systems do not exist in reality.

Map \mathbf{X} takes an initial density operator to a final density operator

$$\mathbf{X} : \hat{\rho} \rightarrow \hat{\rho}'.$$

There are a set of properties this map has to satisfy to make it physical:

1. \mathbf{X} must preserve hermiticity; $\hat{\rho}'$ will be hermitian if $\hat{\rho}$ is
2. \mathbf{X} should be linear
3. \mathbf{X} must be trace preserving, and therefore preserve the normalisation of the density operator; if $Tr(\hat{\rho}) = 1$, $Tr(\hat{\rho}') = 1$
4. \mathbf{X} is completely positive.

The complete positivity is a requirement that if any possible environment is chosen, coupled to the system, resulting in a joint density matrix $\hat{\rho} = \hat{\rho}_A \otimes \hat{\rho}_E$, the result of a composite operation (map ξ)

$$\xi\rho = (\mathbf{X} \otimes \hat{1}) (\hat{\rho}_A \otimes \hat{\rho}_E)$$

is another positive operator; \mathbf{X} is completely positive acting on the subspace of $\hat{\rho}_A$ if $\mathbf{X} \otimes \hat{1}$ is positive for any coupled environment. This is a consequence of

the fact that a quantum system is not completely isolated, and one can never be certain that when studying the evolution of the system A, it isn't coupled to some environment. If the system evolved but the environment does not, complete positivity ensures the density operator will evolve to another density operator.

2.1.3 Markovian evolution – Lindblad master equation

The superoperator formalism provides a description of the evolution of density operators in a way analogous to unitary evolution in closed quantum systems. There the dynamics can be described by a differential equation – eq. (2.2), enabling the computation of the evolution of the state vector $|\Psi\rangle$ over a finite time. To a good approximation, it is possible to describe the evolution of a density operator under the action of a superoperator, with the use of a differential equation analogous to eq. (2.2).

A description as such is only possible if the evolution of the system is Markovian [41], i.e. it is local in time, and the system is memoryless; if the density operator evolves from $\hat{\rho}(t)$ to $\hat{\rho}(t + \delta t)$ – that state only depends on $\hat{\rho}(t)$, and earlier states do not have any influence.

Generally an open system has a two-way information flow, hence the system is dissipative. Information can flow from the system to the environment, but the opposite is true as well. The environment is not memory-less and affects the system, resulting in non-Markovian fluctuations in the system. A Markovian description is however, an accurate description provided there is a clear separation between time-scales of the system and environment. Three different time-scales can be distinguished; τ_S – the time-scale during which the system evolves, τ_E – the time-scale during which the environment evolves and 'forgets' the information acquired from the system, and τ_D – the time scale at which dissipation in the system occurs due to the interaction with the environment. The general requirement is that

$$\tau_D \gg \tau_S \gg \tau_E.$$

Given the above assumption, after time τ the information in the environment can be disregarded as it is 'forgotten' and the probability of it feeding back to the system is negligible, and in effect this is comparable to a coarse-graining of the dynamics. Studying the system at time-scales of δt , where $\tau_D \gg \delta t \gg \tau_E$ results in a Markovian approximation of the master equation.

Under these assumptions, $\hat{\rho}_A$ in the master equation can be written to the or-

der of δ_t , ensuring linearity

$$\hat{\rho}_A(\delta t) = \mathbf{X}\hat{\rho}_A(0) \equiv \sum_{\mu} \hat{M}_{\mu}\hat{\rho}_A(0)\hat{M}_{\mu}^{\dagger} = \hat{\rho}_A(0) + O(\delta t).$$

Dictated by the order with respect to time, and the form of \mathbf{X} , the Kraus operators must be of the form

$$\hat{M}_0 = \hat{1}_S + \left(\hat{K} - \frac{i}{\hbar} \hat{H} \right) \delta t \quad (2.8)$$

$$\hat{M}_k = \sqrt{\delta t} \hat{L}_k \quad (\text{for } k \geq 1), \quad (2.9)$$

where \hat{H} is the system Hamiltonian, operators \hat{L}_k are later defined as Lindblad jump operators, and \hat{K} is an arbitrary hermitian operator, the need for which is shown later. The condition in eq. (2.7) requires

$$\sum_{\mu} \hat{M}_{\mu}^{\dagger} \hat{M}_{\mu} = \hat{1}_A$$

which implies

$$\hat{1}_A = \hat{1}_A + \left(2\hat{K} + \sum_k \hat{L}_k^{\dagger} \hat{L}_k \right) \delta t + O(\delta t)^2,$$

thus

$$\hat{K} = -\frac{1}{2} \sum_k \hat{L}_k^{\dagger} \hat{L}_k$$

is a normalisation term, required in evolution time-steps where no quantum jumps occur. Hence

$$\begin{aligned} \hat{\rho}_A(\delta t) &= \left[\hat{1}_S + \left(\hat{K} - \frac{i}{\hbar} \hat{H} \right) \delta t \right] \hat{\rho}_A(0) \left[\hat{1}_S + \left(\hat{K} + \frac{i}{\hbar} \hat{H} \right) \delta t \right] + \sum_k \hat{L}_k \hat{\rho}_A(0) \hat{L}_k^{\dagger} \\ &= \hat{\rho}_A(0) + \hat{\rho}_A(0) \left[\hat{K} + \frac{i}{\hbar} \hat{H} \right] \delta t + \left[\hat{K} - \frac{i}{\hbar} \hat{H} \right] \hat{\rho}_A(0) \delta t + \sum_k \hat{L}_k \hat{\rho}_A(0) \hat{L}_k^{\dagger} \delta t \\ &= \hat{\rho}_A(0) - \frac{i}{\hbar} \left[\hat{H}, \hat{\rho}_A(0) \right] \delta t + \sum_k \left[\hat{L}_k \hat{\rho}_A(0) \hat{L}_k^{\dagger} - \frac{1}{2} \left\{ \hat{\rho}_A(0), \hat{L}_k^{\dagger} \hat{L}_k \right\} \right] \delta t. \end{aligned}$$

Following the standard definition of derivatives, where

$$\dot{\hat{\rho}}_A(0) = \lim_{\delta t \rightarrow 0} \frac{\hat{\rho}_A(0 + \delta t) - \hat{\rho}_A(0)}{\delta t}$$

we have the form of the master equation

$$\begin{aligned} & \lim_{\delta t \rightarrow 0} \frac{\hat{\rho}_A(0 + \delta t) - \hat{\rho}_A(0)}{\delta t} \equiv \dot{\hat{\rho}}_A(0) \\ & = -\frac{i}{\hbar} [\hat{H}, \hat{\rho}_A(0)] + \sum_k \left[\hat{L}_k \hat{\rho}_A(0) \hat{L}_k^\dagger - \frac{1}{2} \left\{ \hat{\rho}_A(0), \hat{L}_k^\dagger \hat{L}_k \right\} \right] \end{aligned}$$

and have thus derived the **Lindblad** master equation for the density operator of system (A) coupled to the environment (E)

$$\frac{d\hat{\rho}}{dt} = \mathbf{L}\hat{\rho} \equiv -i [\hat{H}, \hat{\rho}] + \sum_k \mathbf{D} [\hat{L}_k] \hat{\rho}. \quad (2.10)$$

The Hamiltonian is in the frequency domain (divided by \hbar). The Lindblad dissipator superoperator is of the form

$$\mathbf{D} [\hat{L}_k] \hat{\rho} = \hat{L}_k \hat{\rho} \hat{L}_k^\dagger - \frac{1}{2} \left\{ \hat{\rho}, \hat{L}_k^\dagger \hat{L}_k \right\}. \quad (2.11)$$

The dissipative part – eq. (2.11) – is responsible for relaxation in the system. Different relaxation pathways are modelled with so-called **Lindblad jump operators**, \hat{L}_k . These operators cause instantaneous jumps between eigenstates of the system. The form of these operators is described further in this chapter in section 2.1.5. The square bracket represents a commutator relation, and corresponds to the coherent part of the master equation. The curly bracket represents an anti-commutator relation. The master equation as a whole describes a non-unitary evolution of the density operator in the Markovian Limit. In the case of no dissipative pathways, the standard LvN equation (2.4) is recovered, and unitary evolution would be seen. The Hamiltonian \hat{H} , however, is not necessarily identical to the Hamiltonian of the closed system – in some cases important corrections will be seen [41] in the system Hamiltonian due to the interaction with the environment (E). The environment our system is coupled to evolves on a time-scale that is much shorter than the system-evolution time-scale; the information flow from the system to the environment is by assumption non-reversible on the time-scale over which the system evolves.

2.1.4 Lindblad propagator

The form of eq. (2.10) makes analytical integration difficult, particularly for systems consisting of more than 1 spin. An ordinary differential equation solver may be employed to find numerical solutions.

It is however possible to re-write the form of eq. (2.10) to act in Liouville space, i.e. operator space, in which case the result is a Lindblad superoperator acting on

the density operator from the left. A simple method for conversion of the form of the master equation has been presented by Tim Havel [42]. A superoperator form of eq. (2.10) is obtained by again starting from the Kraus formalism. It is proven in the text that eq. (2.6) is equivalent to

$$\mathbf{X}(\hat{\rho}) = \sum_{\mu} \left(\hat{M}_{\mu}^* \otimes \hat{M}_{\mu} \right) \hat{\rho}_A,$$

where the asterisk denotes a complex conjugate $(\hat{M}^{\dagger})^T \equiv \hat{M}^*$, where T denotes a transpose.

Plugging in the Kraus operators of the form shown in eqs. (2.8, 2.9);

$$\sum_{\mu} \left(\hat{M}_{\mu}^* \otimes \hat{M}_{\mu} \right) = \delta t \left(\hat{1} + \left(\hat{K} - i\hat{H} \right) \right)^* \otimes \left(\hat{1} + \hat{K} - i\hat{H} \right) \delta t + \delta t \sum_k \hat{L}_k^* \otimes \hat{L}_k.$$

Since $(A + B)^* \equiv A^* + B^*$, and $(-iA)^* \equiv iA^*$, this becomes

$$\sum_{\mu} \left(\hat{M}_{\mu}^* \otimes \hat{M}_{\mu} \right) = \delta t \left(\hat{1} \otimes \hat{K} - i\hat{1} \otimes \hat{H} + i\hat{H}^* \otimes \hat{1} + \hat{K}^* \otimes \hat{1} + \sum_k \hat{L}_k^* \otimes \hat{L}_k \right),$$

which in a manner similar to deriving eq. (2.10) results in

$$\mathcal{L} = i \left(\hat{H}^* \otimes \hat{1} - \hat{1} \otimes \hat{H} \right) + \sum_k \left(\hat{L}_k^* \otimes \hat{L}_k - \frac{1}{2} \hat{1} \otimes \hat{L}_k^{\dagger} \hat{L}_k - \frac{1}{2} \left(\hat{L}_k^{\dagger} \hat{L}_k \right)^* \otimes \hat{1} \right). \quad (2.12)$$

Here, the identity operators $\hat{1}$ have the same dimension as the Hamiltonian and Lindblad jump operators. The superoperator \mathcal{L} acts on the density operator from the left, it is therefore straightforward to solve the differential equation for the evolution of $\hat{\rho}$ in time to give the form of the time-propagator

$$\frac{d\hat{\rho}}{dt} = \mathcal{L}\hat{\rho} \implies \hat{\rho}(t) = e^{\mathcal{L}t}\hat{\rho}(0). \quad (2.13)$$

Previously, the dimension of the Lindbladian eq. (2.10) would be equivalent to the density operator dimension i.e. 2^n , for n spins. Rewriting the Lindbladian in the form of eq. (2.12) makes the Liouville space dimension it acts on scale as 4^n . The density operator this form of master equation acts on is column-stacked, resulting in a size of $4^n \times 1$, in which case eq. (2.13) is strictly written as

$$\text{col} \hat{\rho}(t) = e^{\mathcal{L}t} \text{col} \hat{\rho}(0).$$

Despite the increased space dimension, this form of the master equation provides an advantage computationally.

The Lindbladian is commonly used in quantum optics and in the description of dissipation in open quantum systems [43], [44], [45]. The action of the Lindbladian dissipator is identical to the use of double-commutator relaxation superoperators, which can be illustrated by the following simple rearrangement. If we take a generic operator \hat{X} (which could for example be a lowering or raising operator) along with its hermitian conjugate, we can write a double-commutator form of a relaxation superoperator:

$$\begin{aligned}\Gamma &= -\frac{R_1}{2} \left([\hat{X}, [\hat{X}^\dagger, \hat{\rho}]] + [\hat{X}^\dagger, [\hat{X}, \hat{\rho}]] \right) \\ &\equiv -\frac{R_1}{2} \left(-2\hat{X}\hat{\rho}\hat{X}^\dagger - 2\hat{X}^\dagger\hat{\rho}\hat{X} + \hat{X}\hat{X}^\dagger\hat{\rho} + \hat{\rho}\hat{X}\hat{X}^\dagger + \hat{X}^\dagger\hat{X}\hat{\rho} + \hat{\rho}\hat{X}^\dagger\hat{X} \right) \\ &\equiv R_1 \left(\hat{X}\hat{\rho}\hat{X}^\dagger - \left\{ \hat{\rho}, \hat{X}^\dagger\hat{X} \right\} / 2 + \hat{X}^\dagger\hat{\rho}\hat{X} - \left\{ \hat{\rho}, \hat{X}\hat{X}^\dagger \right\} / 2 \right) \\ &\equiv R_1 \left(\mathbf{D} [\hat{X}] + \mathbf{D} [\hat{X}^\dagger] \right) \hat{\rho}.\end{aligned}$$

The subtle difference is that no normalisation term is required with the Lindbladian for the system to relax to thermal equilibrium, as a normalisation term may be included in the effective rate using the principle of detailed balance. The Lindbladian is also analogous to the Redfield relaxation superoperator form where a secular approximation is applied [46].

2.1.5 Use of Lindblad master equation in NMR and DNP

The dissipator shown in eq. (2.11) is responsible for relaxation in the system. Longitudinal relaxation is crucial for the DNP mechanisms, decoherence is the unwanted loss of information. Both are unavoidable and are a consequence of the system being coupled to some fluctuating environment [39], causing relaxation of spins in the system. Each process is modelled using a different Lindblad jump operator \hat{L}_k . Generally these operators are of the form

$$\hat{L}_k = \sqrt{\Gamma_k} \hat{X},$$

where \hat{X} would be one of the operators $\hat{X} \in \left\{ \hat{1}, \hat{S}_+, \hat{S}_-, \hat{S}_z, \hat{I}_{k+}, \hat{I}_{k-}, \hat{I}_{kz}, \right\}$. In DNP operators acting on electrons are often designated as \hat{S} , and operators acting on nuclei as \hat{I} . These operators are formed from spin-1/2 Pauli matrices and their direct products with $\hat{1}$. The rate corresponding to a particular jump process is Γ_k . Since Γ_k are scalars, they can be taken out before the dissipator in eq. (2.11). The lowering/raising operators (also called annihilation and creation

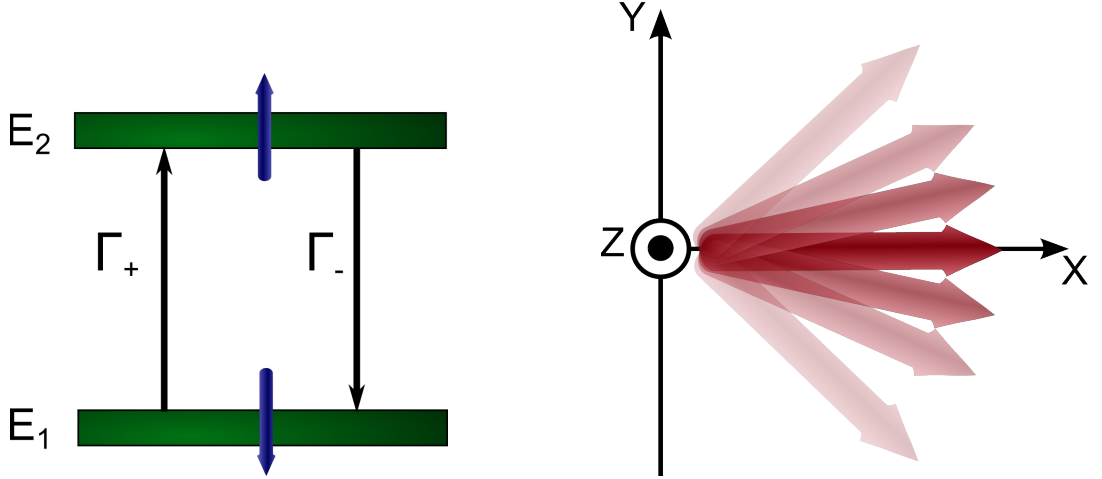


Figure 2.1: Illustration of the processes of longitudinal (T_1) relaxation – left part of figure, and transverse (T_2) relaxation – right part of figure, modelled using Lindblad jump operators. Operators consisting of σ_{\pm} cause jumps between the eigenstates (energy levels) of the system, and are weighted by the thermal polarization coefficient, eq. (1.1), so that in the absence of coherent evolution the system will relax back to its thermal equilibrium state (LHS figure). Operators consisting of σ_z , cause decoherence (RHS figure) of the spin state, i.e. causing spins to go out of phase with respect to one another.

operators) are of the form $\hat{S}_{\pm} = \hat{S}_x \pm i\hat{S}_y$ and $\hat{I}_{k\pm} = \hat{I}_{kx} \pm i\hat{I}_{ky}$ for electrons and nuclei respectively.

The operators S_{\pm} , $I_{k\pm}$ are responsible for transitions between eigenstates of the system and introduce longitudinal relaxation in the system. The operators \hat{S}_z , \hat{I}_{kz} are mainly responsible for decay of coherences in the system. In fig. 2.1, left, a schematic representation of transitions leading to dissipation due to T_1 processes is shown. Operators containing σ_+ will cause transitions from the eigenstate E_1 to the state E_2 , with a rate $\Gamma_+ = \frac{R_1}{2}(1 + p_{\text{th}})$. The opposite is true for operator σ_- , where the transition rate is $\Gamma_- = \frac{R_1}{2}(1 - p_{\text{th}})$. The two rates are weighted by the thermal equilibrium polarization of a spin, to ensure that spin relaxes back to thermal equilibrium without any driving of the system. In fig. 2.1, right, dissipation due to T_2 processes is shown in a similar manner. Dissipation due to T_2 processes leads to the spins coming out of phase with respect to one another. The rate associated with this process is $\Gamma_z = 2R_2$. The dissipative processes due to T_1 and T_2 are both incoherent and irreversible.

Using this dissipator form it is straight-forward to introduce more complicated relaxation pathways for the system (e.g. spin cross-relaxation). In [39] we discussed the differences in simulations seen between using a Lindblad form dissipator defined in the Zeeman basis, and the relaxation superoperator form used by Hovav et al. [37] in the eigenbasis of the stationary Hamiltonian. Furthermore, we describe in [39] the possibility of addition of other dissipation parts to the relaxation

superoperator.

2.1.6 Link between quantum and classical dynamics

The expectation value for an arbitrary operator \hat{X} is given as

$$\langle \hat{X} \rangle = Tr(\hat{\rho} \hat{X}) \equiv Tr(\hat{X} \hat{\rho}).$$

Using the Lindblad master equation – eq. (2.10), and multiplying it from the left by a spin operator \hat{X} , if the trace of both sides is taken; the time-evolution of the expectation value of the operator \hat{X} can be found:

$$\left\langle \frac{d\hat{X}}{dt} \right\rangle = -i Tr \left[\hat{X} [\hat{H}, \hat{\rho}] + \hat{X} \sum_k \left(L_k \hat{\rho} L_k^\dagger - \frac{1}{2} \{ \hat{\rho}, L_k^\dagger L_k \} \right) \right].$$

The cyclic properties of the trace operation can then be used to give a slightly altered form of eq. (2.10), used for the expectation value of an operator \hat{X}

$$\langle \dot{\hat{X}} \rangle = \left\langle i [\hat{H}, \hat{X}] + \sum_k \left(L_k^\dagger \hat{X} L_k - \frac{1}{2} \{ \hat{X}, L_k^\dagger L_k \} \right) \right\rangle. \quad (2.14)$$

Using eq. (2.14) for a single isolated electronic spin, the expectation values were obtained for each operator in the basis

$$\hat{X} \in \{ \hat{1}, \hat{S}_+, \hat{S}_-, \hat{S}_z \},$$

with Hamiltonian $H = \Delta \hat{S}_z + \frac{\omega_1}{2} (\hat{S}_+ + \hat{S}_-)$, and Lindblad jump operators $\hat{L}_+ = R_1(1 - p_{\text{th}})/2$, $\hat{L}_- = R_1(1 + p_{\text{th}})/2$, $\hat{L}_z = 2R_2$. The result is given as:

$$\begin{aligned} \langle \dot{\hat{S}}_+ \rangle &= -i\omega_1 \langle \hat{S}_z \rangle + \{i\Delta - R_2\} \langle \hat{S}_+ \rangle \\ \langle \dot{\hat{S}}_- \rangle &= i\omega_1 \langle \hat{S}_z \rangle + \{-i\Delta - R_2\} \langle \hat{S}_- \rangle \\ \langle \dot{\hat{S}}_z \rangle &= \frac{i}{2}\omega_1 \langle \hat{S}_- \rangle - \frac{i}{2}\omega_1 \langle \hat{S}_+ \rangle - R_1 \langle \hat{S}_z \rangle + \frac{1}{2}p_{\text{th}}R_1 \langle \hat{1} \rangle, \end{aligned}$$

and the time-evolution of the expectation value of identity is 0. The operator expectation value time evolution equations can be represented in matrix form

$$\begin{pmatrix} \langle \dot{\hat{S}}_+ \rangle \\ \langle \dot{\hat{S}}_- \rangle \\ \langle \dot{\hat{S}}_z \rangle \end{pmatrix} = \begin{pmatrix} i\Delta - R_2 & 0 & -i\omega_A \\ 0 & -i\Delta - R_2 & i\omega_A \\ \frac{-i\omega_A}{2} & \frac{i\omega_A}{2} & -R_1 \end{pmatrix} \begin{pmatrix} \langle \hat{S}_+ \rangle \\ \langle \hat{S}_- \rangle \\ \langle \hat{S}_z \rangle \end{pmatrix} + \begin{pmatrix} 0 \\ 0 \\ \frac{1}{2}p_{\text{th}}R_1 \end{pmatrix}$$

which has the equation form of

$$\langle \dot{\mathbf{s}} \rangle = M \langle \mathbf{s} \rangle + b. \quad (2.15)$$

Setting the left hand side of eq. (2.15) to 0, the steady-state solutions for the operator values are obtained:

$$\langle \mathbf{s} \rangle_{ss} = -M^{-1} (b)$$

$$\begin{pmatrix} \langle \hat{S}_+ \rangle_{ss} \\ \langle \hat{S}_- \rangle_{ss} \\ \langle \hat{S}_z \rangle_{ss} \end{pmatrix} = \frac{\frac{1}{2} p_{\text{th}} R_1}{R_1 (\Delta^2 + R_2^2) + R_2 \omega_1^2} \begin{pmatrix} -i\omega_1 (i\Delta + R_2) \\ -i\omega_1 (i\Delta - R_2) \\ (\Delta^2 + R_2^2) \end{pmatrix},$$

from which the classical steady-state Bloch equations are recovered

$$\begin{aligned} \langle \hat{S}_x \rangle_{ss} &= \frac{\omega_1 \Delta (T_2)^2}{1 + (\Delta T_2)^2 + \omega_1^2 T_1 T_2} \cdot \frac{p_{\text{th}}}{2} \\ \langle \hat{S}_y \rangle_{ss} &= \frac{-\omega_1 T_2}{1 + (\Delta T_2)^2 + \omega_1^2 T_1 T_2} \cdot \frac{p_{\text{th}}}{2} \\ \langle \hat{S}_z \rangle_{ss} &= \frac{1 + (\Delta T_2)^2}{1 + (\Delta T_2)^2 + \omega_1^2 T_1 T_2} \cdot \frac{p_{\text{th}}}{2}. \end{aligned}$$

In some circumstances, coupling to the environment causes an object to behave 'classically' even though the intrinsic dynamics of the system are quantum. This has led some to speculate [41] that the open quantum system approach provides a link between quantum mechanics and the macroscopical classical limit.

2.2 Theory of solid effect DNP

In this section, the theory of SE-DNP is described on a microscopic scale. This mechanism is most pronounced at low temperatures, when low radical concentrations are used. In such case, the dipolar coupling between electron radicals is negligible and a central electron spin model [47] is suitable for modelling SE-DNP dynamics. A basic description entails an electron spin surrounded by atomic nuclei. Polarization is transferred to nuclei surrounding the electron, these nuclei in turn transfer their polarization to the bulk via nuclear dipole-dipole interaction.

2.2.1 Solid effect

This is the simplest case of DNP in solid state systems, driven by a two-spin process. The mechanism is most pronounced in cases where the electron-electron dipolar coupling is very weak or negligible in the sample. Radicals that lead to SE-DNP are characterised by their narrow EPR linewidth, such that the inhomogeneous (η) and homogeneous (ζ) broadening is much smaller than the nuclear Larmor frequency; $\omega_I \gg \eta, \zeta$. The mechanism of polarization transfer relies on the secular and pseudo-secular hyperfine coupling between an electron and surrounding nuclei. The resonance frequency for the electron in SE-DNP is $\Delta = \pm\omega_I$, where $\Delta = \omega_S - \omega_{\mu w}$. Thus the microwave frequency is set to $\omega_{\mu w} = \omega_S \pm \omega_I$, in effect irradiating on either the zero-quantum or double quantum frequency, and driving one of the forbidden transitions – indicated in fig. (2.2), leading to flip-flops (ZQ) if $\Delta = \omega_I$ or flip-flips (DQ) if $\Delta = -\omega_I$, of the electron-nuclear spin states. Fast electronic T_1 relaxation causes the electron spin state to return to its thermal equilibrium state, following which the electron can undergo further ZQ or DQ transitions, leading to a polarized ensemble.

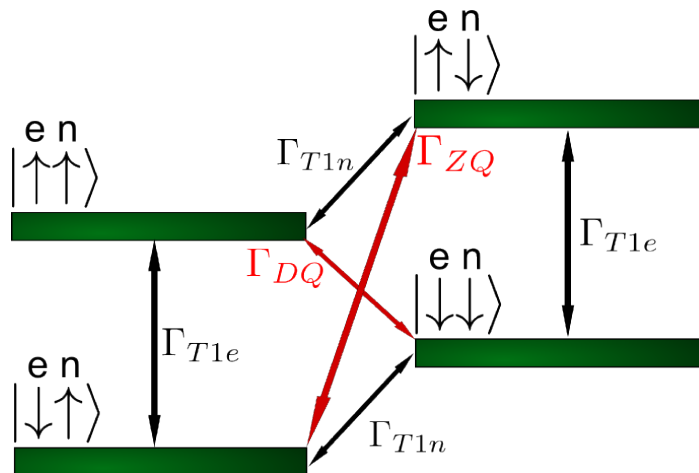


Figure 2.2: Energy levels of a coupled two-spin system; 1 electron and 1 nucleus. Irradiating at one of the resonance conditions (red arrows) drives either the ZQ or DQ transitions. Fast electron T_1 relaxation then causes the electron to flip back to its ground state. A DQ or ZQ transition with a different nucleus is then possible. That process leads to a difference in populations of the two nuclear eigenstates, and therefore leads to a polarization increase for the nuclei. The nuclear polarization is gradually lost due to T_1 relaxation of nuclear spins.

Perturbation theory suggests that the enhancement is proportional to the inverse of the square of the magnetic field $\propto B_Z^{-2}$ [26], hence SE-DNP is more efficient at lower magnetic fields strengths.

2.2.2 Hamiltonian

The Hamiltonian for the central spin model is of the form

$$\hat{H} = \hat{H}_Z + \hat{H}_{IS} + \hat{H}_{II} + \hat{H}_{mw}. \quad (2.16)$$

Due to the presence of a magnetic field, each spin has its Larmor frequency with which it precesses around the vector of the magnetic field \vec{B}_Z , and each spin therefore has a Zeeman energy. The Zeeman Hamiltonian has the form

$$\hat{H}_Z = \omega_S \hat{S}_z + \omega_I \sum_k \hat{I}_{kz}.$$

The Larmor frequency of electron spins (ω_S) is orders of magnitude greater than that of atomic nuclei (ω_I). In addition to the Zeeman terms, there exists a hyperfine coupling between the nuclei and the electron. It consists of two parts; the Fermi contact interaction and the dipolar coupling interaction. The Fermi contact interaction is scaled by the squared absolute value of the electronic wavefunction, calculated at the position of the nucleus. This term tends to only be relevant for nuclei that are very close to the electron, but is generally not important for the DNP mechanisms; the contribution of the Fermi contact interaction is a shift in frequency of nuclei close to the electron. The dipolar part of the hyperfine interaction is in the form of a tensor interaction, and has the general form

$$\hat{H}_{IS} = \sum_k \hat{S} \cdot \overset{\leftrightarrow}{\mathbf{A}} \cdot \hat{I}_k, \quad (2.17)$$

where the full form of $\hat{S} \cdot \overset{\leftrightarrow}{\mathbf{A}} \cdot \hat{I}_k$ is

$$\begin{aligned} \hat{S} \cdot \overset{\leftrightarrow}{\mathbf{A}} \cdot \hat{I} &= a_1 \hat{S}_z \hat{I}_z + a_2 \hat{S}_z \hat{I}_+ + a_3 \hat{S}_z \hat{I}_- + a_4 \hat{S}_+ \hat{I}_z + a_5 \hat{S}_+ \hat{I}_+ \\ &+ a_6 \hat{S}_+ \hat{I}_- + a_7 \hat{S}_- \hat{I}_z + a_8 \hat{S}_- \hat{I}_+ + a_9 \hat{S}_- \hat{I}_-. \end{aligned}$$

The coupling strength coefficients a_i depend on the separations and relative positions of the electron and surrounding nuclei. Generally the coupling strength scales proportionally to the cubic inverse of the separation between the spins.

The Hamiltonian part \hat{H}_{II} describes interactions between the nuclei. In moderate to high magnetic fields only the secular part of the dipolar Hamiltonian needs to be considered, so the Hamiltonian takes the form

$$\hat{H}_{II} = \sum_{kk'} d_{kk'} \left(2\hat{I}_{kz} \hat{I}_{k'z} - \frac{1}{2} \hat{I}_{k+} \hat{I}_{k'-} - \frac{1}{2} \hat{I}_{k-} \hat{I}_{k'+} \right),$$

where the coupling parameter $d_{kk'}$ has the form

$$d_{kk'} = -\frac{\mu_0}{4\pi} \frac{\gamma_k^{(I)} \gamma_{k'}^{(I)} \hbar}{2r_{kk'}^3} (3 \cos(\Theta_{kk'}) - 1), \quad (2.18)$$

and $\gamma_k^{(I)}, \gamma_{k'}^{(I)}$ are the gyromagnetic ratios of the two coupled spins, μ_0 is the magnetic permeability, $r_{kk'}$ is the separation between the two spins, and $\Theta_{kk'}$ is the angle between the vector joining the two spins, and the magnetic field vector \bar{B}_Z . The parameter $d_{kk'}$ is maximised for a given separation $r_{kk'}$, when $\Theta_{kk'} = 0^\circ$ or 180° , i.e. the vector joining the two spins is parallel or anti-parallel to \bar{B}_Z . This is the interaction responsible for the distribution of polarization among nuclei, and leads to enhancements in the bulk.

DNP is a dynamic process, and as such it relies on a driving force pushing the system out of equilibrium. In the case of DNP, the driving force is microwave radiation – electro-magnetic radiation in a wavelength regime of 1mm – 1m, usually applied orthogonally to the static magnetic field B_Z . By convention, the applied field is taken to be along the x-axis, however a field applied along the y-axis would not fundamentally change the physics of the process. In some cases of optimal control [48], there may be two fields present; each applied along a different, orthogonal axis. The microwave Hamiltonian is given as

$$\hat{H}_{mw}(t) = \frac{\omega_1}{2} e^{-i\omega_\mu t \hat{S}_z} (\hat{S}_+ + \hat{S}_-) e^{+i\omega_\mu t \hat{S}_z},$$

where ω_μ is the frequency of the microwave radiation, and ω_1 is the amplitude of the microwave field (Hz). The presence of this Hamiltonian takes the dynamics of the full Hamiltonian, eq.(2.16) to the interaction frame. The factor of 1/2 appears if linearly polarized microwave radiation is used. Linearly polarized waves can be represented as two counter-propagating circularly polarized waves, which are in phase. One component will be in resonance with the system, while the other will be out of resonance and have a magnetic field vector rotating in a direction opposite to the precession of the spins, when proceeding to the rotating frame of reference (also referred to as RWA [49]).

2.2.3 Rotating frame of reference

The rotating frame of reference is in resonance with the microwave radiation Hamiltonian, and typically in DNP, it is close to the resonance of the electron spin. The transformation of the frame of reference in this case is a rotation about

the z-axis of the system. The transformation operator has the form

$$\hat{R}_z(t) = e^{-i\omega_\mu t \hat{S}_z}.$$

The entire dynamics of the system are then transformed to this rotating frame of reference. The state vector $|\Psi\rangle$ in the rotating frame of reference has the form [12]

$$|\Psi\rangle' = \hat{R}_z(t) |\Psi\rangle \quad \text{and} \quad \langle\Psi|' = \langle\Psi| \hat{R}_z(t)^\dagger$$

hence

$$\hat{\rho}' = \hat{R}_z(t) \hat{\rho} \hat{R}_z(t)^\dagger. \quad (2.19)$$

Using the Schrödinger equation, eq. (2.2) and its Hermitian conjugate form:

$$\frac{\partial \langle\Psi|}{\partial t} = i \langle\Psi| \hat{H} \quad ; \quad \hat{H}^\dagger \equiv \hat{H},$$

the RWA density operator dynamics are found

$$\begin{aligned} \frac{\partial}{\partial t} (|\Psi\rangle' \langle\Psi|') &= \frac{\partial |\Psi\rangle'}{\partial t} \langle\Psi|' + |\Psi\rangle' \frac{\partial \langle\Psi|'}{\partial t} \\ &= \frac{\partial}{\partial t} \left(\hat{R}_z(t) |\Psi\rangle \right) \langle\Psi|' + |\Psi\rangle' \frac{\partial}{\partial t} \left(\langle\Psi| \hat{R}_z^\dagger(t) \right) \\ &= \left(\frac{\partial \hat{R}_z(t)}{\partial t} |\Psi\rangle + \hat{R}_z(t) \frac{\partial |\Psi\rangle}{\partial t} \right) \langle\Psi|' + |\Psi\rangle' \left(\frac{\partial \langle\Psi|}{\partial t} \hat{R}_z^\dagger(t) + \langle\Psi| \frac{\partial \hat{R}_z^\dagger(t)}{\partial t} \right). \end{aligned}$$

Here the following relations, as well as those concerning their complex conjugates are used

$$\begin{aligned} \frac{\partial \hat{R}_z(t)}{\partial t} &= i\omega_\mu \hat{S}_z \hat{R}_z(t) & \hat{R}_z(t) \frac{\partial |\Psi\rangle}{\partial t} &\equiv -i\hat{R}_z(t) \hat{H} |\Psi\rangle = -i\hat{R}_z(t) \hat{H} \hat{R}_z^\dagger |\Psi\rangle' \\ \frac{\partial \hat{R}_z(t)^\dagger}{\partial t} &= -i\omega_\mu \hat{S}_z \hat{R}_z(t)^\dagger & \frac{\partial \langle\Psi|}{\partial t} \hat{R}_z(t) &\equiv i \langle\Psi| \hat{H} \hat{R}_z^\dagger(t) = i \langle\Psi|' \hat{R}_z(t) \hat{H} \hat{R}_z^\dagger(t) \end{aligned}$$

to give

$$-i \left(\hat{R}_z(t) \hat{H} \hat{R}_z^\dagger(t) - \omega_\mu \hat{S}_z \right) |\Psi\rangle' \langle\Psi|' + i |\Psi\rangle' \langle\Psi|' \left(\hat{R}_z(t) \hat{H} \hat{R}_z^\dagger(t) - \omega_\mu \hat{S}_z \right),$$

from which the LvN, eq. (2.4), RWA dynamics are recovered

$$\dot{\hat{\rho}}' = -i \left[\hat{H}', \hat{\rho}' \right],$$

where $\hat{\rho}'$ is defined in eq. (2.19), and $\hat{H}' = \hat{R}_z(t) \hat{H} \hat{R}_z^\dagger(t) - \omega_\mu \hat{S}_z$. The Lindbladian dissipator responsible for relaxation, eq. (2.11), is invariant under rotations [50]. The terms contained in \hat{H}_Z, \hat{H}_{II} , commute with \hat{S}_z , and are unaffected by the

rotation. Terms in equation (2.17) that do not commute with \hat{S}_z will acquire time-dependent coefficients, oscillating with frequency ω_μ , hence these terms average out.

2.2.4 SE-DNP master equation

$$\begin{aligned} \hat{H} = & \Delta \hat{S}_z + \sum_k \omega_I \hat{I}_{kz} + \sum_k \left(A_k \hat{I}_{kz} + B_{k+} \hat{I}_{k+} + B_{k-} \hat{I}_{k-} \right) \hat{S}_z \\ & + \sum_{kk'} d_{kk'} \left(2 \hat{I}_{kz} \hat{I}_{k'z} - \frac{1}{2} \hat{I}_{k+} \hat{I}_{k'-} - \frac{1}{2} \hat{I}_{k-} \hat{I}_{k'+} \right) + \frac{\omega_1}{2} \left(\hat{S}_+ + \hat{S}_- \right). \end{aligned} \quad (2.20)$$

The parameter Δ is the offset from the electronic resonance, and as discussed previously, the SE-DNP resonance condition is $\Delta = \pm\omega_I$. The parameters $A_k, B_{k\pm}$ are the secular and pseudo-secular hyperfine coupling coefficients, respectively. The value of A_k is calculated in an analogous way to eq. (2.18), with one of the γ values being the gyromagnetic ratio of the electron.

The form of B_{k+} is given by [51]

$$B_{k+} = \frac{\mu_0}{4\pi} \frac{\gamma_k^{(I)} \gamma^{(S)} \hbar}{2r_k^3} \left(3 \sin(\Theta_k) \cos(\Theta_k) e^{-i\phi} \right),$$

where $\gamma^{(S)}$ is the electronic gyromagnetic ratio, r_k is the distance from the electron to a nuclear spin, Θ_k is the angle between the vector joining a nuclear spin to an electron, and the magnetic field, and ϕ is an azimuthal angle about the magnetic field. The absolute value of B_{k+} is independent of ϕ , and B_{k-} is a complex conjugate of B_{k+} . As described in chapter 1, SE-DNP relies on forbidden transitions. The pseudo-secular coupling makes the ZQ or DQ transitions weakly allowed; i.e. it introduces mixing between the corresponding states. Microwave radiation with a frequency centered at one of the SE-DNP resonance conditions drives one of these transitions.

The dissipator consists of the terms

$$\begin{aligned} & \Gamma_+^{(S)} \mathbf{D}[S_+] + \Gamma_-^{(S)} \mathbf{D}[S_-] + \Gamma_z^{(S)} \mathbf{D}[S_z] \\ & + \sum_k \Gamma_{k+}^{(I)} \mathbf{D}[I_{k+}] + \Gamma_{k-}^{(I)} \mathbf{D}[I_{k-}] + \Gamma_{kz}^{(I)} \mathbf{D}[I_{kz}]. \end{aligned} \quad (2.21)$$

The terms corresponding to rates $\Gamma_{kz}^{(I)}, \Gamma_z^{(S)}$ are responsible for modelling decoherence of nuclear spins, and electrons respectively. Since the nuclear thermal polarization is very low, even at temperatures approaching 1K, the rates $\Gamma_{k+}^{(I)}, \Gamma_{k-}^{(I)}$

approximately coincide. The electronic rates are weighted by the electron thermal polarization $\Gamma_{\pm}^{(S)} = \frac{R_1^{(S)}}{2}(1 \pm p_{\text{th}})$. The imbalance in value between these two rates is important for DNP; the electron flipping back to its ground state enables polarization of numerous nuclei.

The simulations are then carried out by propagating the density operator of the system, eq. (2.5) using eq. (2.13) at small time steps. It is worth noting that the steady-state result of such time-propagation will be independent of the choice of initial density operator. Polarization for each spin is obtained by taking a trace of the product of the density operator, at each time-step, with the operators \hat{I}_z or \hat{S}_z .

$$p^{(S)}(t) = Tr\left(\hat{\rho}\hat{S}_z\right) \quad p_k^{(I)}(t) = Tr\left(\hat{\rho}\hat{I}_{kz}\right).$$

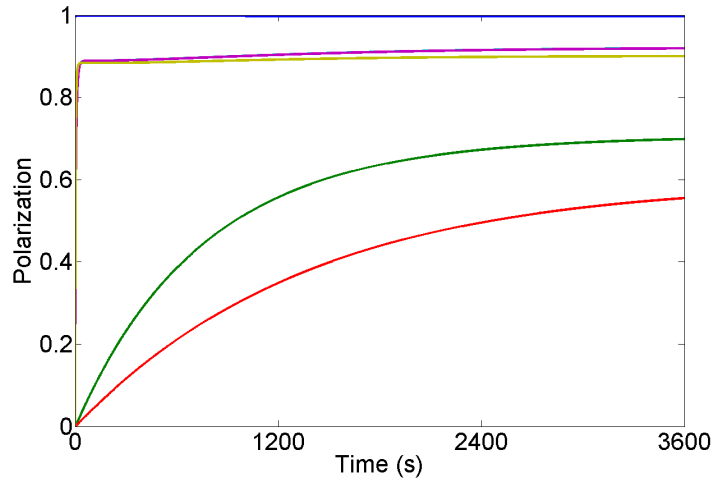


Figure 2.3: Example simulation for 5 nuclei surrounding 1 electron. The blue colour shows the electronic polarization. All curves are normalised to the electronic thermal polarization. The following parameters were used: $\omega_1 = 200$ kHz, $T = 1$ K, $B_Z = 3.4$ T, $T_1^{(S)} = 1$ ms, $T_2^{(S)} = 1$ μ s, $T_1^{(I)} = 1$ h, $T_2^{(I)} = 0.2$ ms, inter-spin separation = 5 \AA . The nuclei have the following $B_{k\pm}$ values: 1) – 13.9 kHz, 2) – 2.9 kHz, 3) – 0.91 MHz, 4) – 0.11 MHz, 5) – 0.82 MHz. Their polarization curves are as follows: 1) – green, 2) – red, 3) & 4) indistinguishable – magenta, 5) – yellow.

An example is shown in figure 2.3, where the polarization curves for each spin are shown in time. The blue curve is the electronic polarization, other curves correspond to the nuclear spins. The build-up rate and steady-state polarization levels depend in a complex way on the parameters of eqs. (2.20) and (2.21). The polarization levels of nuclei depend mostly on the pseudo-secular hyperfine coupling which leads to a direct transfer of polarization from the electron. The secular coupling strengths are also important as high A_k values reduce efficiency

of polarization transport. Nuclei with the high $B_{k\pm}$ values reach high polarization values (nuclei 3,4,5). Nuclei 1 and 2 reach lower polarization levels due to weaker pseudo-secular coupling, however the relatively strong dipolar coupling to the remaining nuclei leads to these two still having a decent polarization level. Nuclei 3 and 4 have a very strong dipolar coupling of ~ 1 kHz hence equalise making their polarization curves indistinguishable. It is expected that as time $\rightarrow \infty$, the nuclear polarizations would all equalise.

2.3 Theory of cross effect DNP

This section focuses on the theory of CE-DNP on a microscopic scale. This mechanism is most pronounced at temperatures of a few tens of Kelvin, typically in the region of liquid nitrogen temperature, and is most relevant to bi-radical solutions or mono-radical solutions of higher concentrations. This is currently the most efficient of the DNP mechanisms. It requires significant inhomogeneous broadening of the electron EPR line, and the dipolar interaction strength between the electrons should be relatively strong. This chapter will be focused on the static case of CE-DNP for a simple case of two electron radicals surrounded by nuclear spins.

2.3.1 Cross effect

The cross effect mechanism is a three-spin process, acting between two electrons and a nucleus. There is strong coupling between the two electrons, and the electron pairs are usually found in the form of bi-radical molecules or mono-radical molecules in close proximity. For this mechanism to be dominant, the inhomogeneous broadening (η) of the EPR spectrum should be greater than the nuclear Larmor frequency (ω_I). The homogeneous broadening (ζ) on the other hand should be less than the nuclear Larmor frequency; $\eta > \omega_I > \zeta$. With a greater inhomogeneous broadening, a higher number of electron pairs where the difference between their Larmor frequencies matches the CE-DNP resonance condition, would likely be encountered.

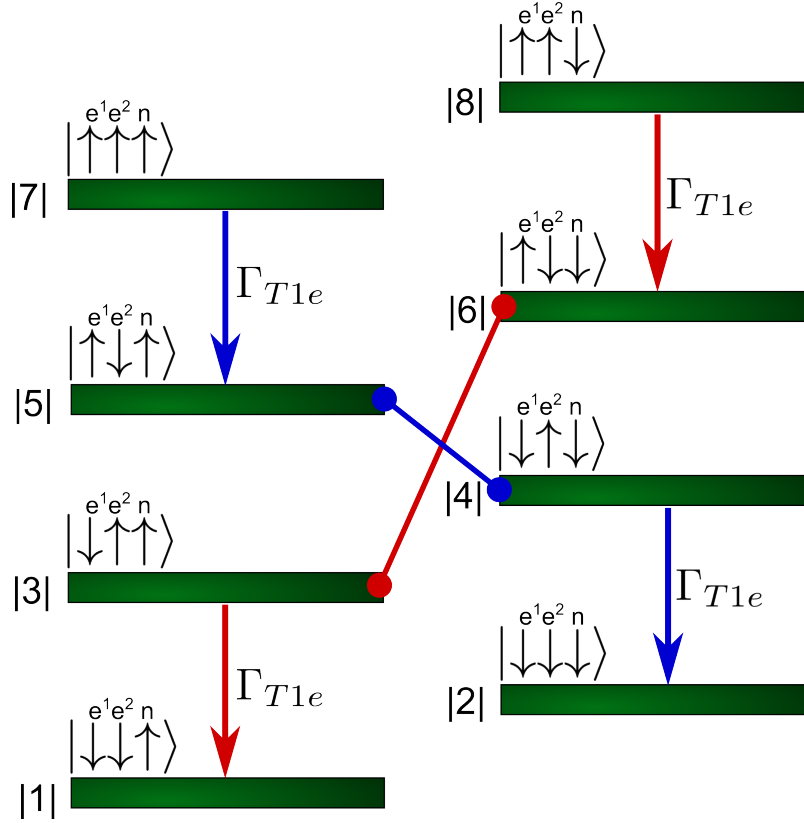


Figure 2.4: Schematic of the energy level diagram for CE-DNP, for two electrons and one nuclear spin. Depending on which CE resonance condition is met ($\Delta\omega_S = \pm\omega_I$), degeneracies will be seen in the energy levels. The energy levels are subject to all possible relaxation transitions analogous to those seen in the case of SE-DNP (fig. 2.2), however for the sake of clarity they have been omitted from this diagram. When $\Delta\omega_S = \omega_I$, a degeneracy between levels marked as |4| and |5| is seen in the system. Electronic relaxation, marked by blue arrows, leads to a population difference between eigenstates of the nucleus, leading to a notable polarization. In the case of $\Delta\omega_S = -\omega_I$, a degeneracy between levels marked as |3| and |6| is seen instead, and electronic relaxation, marked by red arrows leads to a nuclear polarization increase.

If however the homogeneous broadening in a sample was large, this would imply the sample has a strongly coupled dipolar network of electron radicals, leading to the thermal mixing mechanism being active. The resonance condition for CE-DNP is $\Delta\omega_S = \omega_{S2} - \omega_{S1} = \pm\omega_I$, i.e. the difference between the electronic Larmor frequencies should be equal to the absolute value of the nuclear Larmor frequency. As was the case with SE-DNP, the polarization transfer is mediated through the hyperfine coupling between the electrons and a nucleus. In contrast to SE-DNP, CE-DNP does not rely on driving forbidden transitions, it relies instead on degeneracies (fig. 2.4) of electronic eigenstates and a population equalisation between them. This is in addition aided by electronic relaxation and leads to a favourable population difference of nuclear eigenstates. As shown in fig. (2.4), at

the resonance condition $\Delta\omega_S = \omega_I$ the states numbered as |4| and |5|, linked in the diagram by a blue line, become degenerate, and the populations of those states will equalise. Electronic relaxation pathways for the second electron (marked by blue arrows) lead to the depopulation of states |7|, then |4| and |5|, causing an increased population of state |2|, thus resulting in a large population difference between the nuclear eigenstates, and resulting in nuclear state $|\downarrow\rangle$ being more populated. At the resonance condition $\Delta\omega_S = -\omega_I$ the states numbered as |3| and |6|, linked in the diagram by a red line, become degenerate, and the populations of those states will equalise. Electronic relaxation pathways for the second electron (marked by red arrows) lead to the depopulation of states |8|, then |3| and |6|, leading to an increased population of state |1|, thus causing a large population difference of the nuclear eigenstates, and resulting in the nuclear state $|\uparrow\rangle$ being populated.

2.3.2 Hamiltonian

The microscopic model is based on an electron pair surrounded by nuclear spins. The Hamiltonian is analogous to that seen in SE-DNP, eq. (2.16), with the addition of an electronic dipolar coupling term

$$\hat{H} = \hat{H}_Z + \hat{H}_{SS} + \hat{H}_{IS} + \hat{H}_{II} + \hat{H}_{mw}. \quad (2.22)$$

In the presence of a magnetic field, each spin has a Zeeman energy resulting in the Zeeman Hamiltonian of the system

$$\hat{H}_Z = \omega_S^{(1)} \hat{S}_z^{(1)} + \omega_S^{(2)} \hat{S}_z^{(2)} + \omega_I \sum_k \hat{I}_{kz}.$$

The cross effect mechanism relies on each electron having a different g-anisotropy [23] (introduction chapter), leading to a significant difference in their Larmor frequencies. The mechanism is most efficient when the difference between the Larmor frequencies of the two electrons is approximately equal to the nuclear Larmor frequency $|\omega_S^{(1)} - \omega_S^{(2)}| \approx \omega_I$. The electronic dipolar coupling present in the system is crucial for the mechanism to function, it allows the energy levels to become degenerate, as described in chapter 1. The form of the dipolar coupling is analogous to the dipolar coupling between nuclear spins. In the presence of a magnetic field, the dipolar Hamiltonian has the secular form

$$\hat{H}_{SS} = D \left(2\hat{S}_z^{(1)}\hat{S}_z^{(2)} - \frac{1}{2}\hat{S}_+^{(1)}\hat{S}_-^{(2)} - \frac{1}{2}\hat{S}_-^{(1)}\hat{S}_+^{(2)} \right),$$

where the coupling parameter D is

$$-\frac{\mu_0}{4\pi} \frac{\gamma^{(S_1)} \gamma^{(S_2)} \hbar}{2R^3} (3 \cos(\Theta_S) - 1).$$

The angle Θ_S is the angle between the vector joining the electron spins, and the magnetic field vector \bar{B}_Z . The parameter D is maximised for a given separation R , when $\Theta_S = 0^\circ$ or 180° , i.e. the vector joining the two spins is parallel or anti-parallel to \bar{B}_Z . The secular, electronic dipolar Hamiltonian is invariant under rotation, therefore it is unaltered when proceeding to the rotating frame of reference of the microwave radiation. The nuclear dipole-dipole Hamiltonian is identical to the SE-DNP case. The hyperfine, and microwave Hamiltonians are also analogous extensions to the SE-DNP case; each electron is influenced by the microwave field, and each electron has hyperfine coupling to surrounding nuclei. In the presence of microwave radiation it is necessary to proceed to the rotating frame of reference, as described in section 2.2.3.

2.3.3 CE-DNP master equation

The rotating frame of reference CE-DNP Hamiltonian is written as

$$\begin{aligned} \hat{H} = & \Delta_1 \hat{S}_z^{(1)} + \Delta_2 \hat{S}_z^{(2)} + \sum_k \omega_I \hat{I}_{kz} + D \left(2\hat{S}_z^{(1)} \hat{S}_z^{(2)} - \frac{1}{2} \hat{S}_+^{(1)} \hat{S}_-^{(2)} - \frac{1}{2} \hat{S}_-^{(1)} \hat{S}_+^{(2)} \right) \\ & + \sum_j \sum_k \left(A_k^{(j)} \hat{I}_{kz} + B_{k+}^{(j)} \hat{I}_{k+} + B_{k-}^{(j)} \hat{I}_{k-} \right) \hat{S}_z^{(j)} \\ & + \sum_{kk'} d_{kk'} \left(2\hat{I}_{kz} \hat{I}_{k'z} - \frac{1}{2} \hat{I}_{k+} \hat{I}_{k'-} - \frac{1}{2} \hat{I}_{k-} \hat{I}_{k'+} \right) + \frac{\omega_1}{2} \left(\hat{S}_+^{(1)} + \hat{S}_-^{(1)} + \hat{S}_+^{(2)} + \hat{S}_-^{(2)} \right). \end{aligned} \quad (2.23)$$

The parameters Δ_1, Δ_2 are the offset terms for each electron. The CE-DNP mechanism is most efficient when one of the electrons is on-resonance with the microwave radiation, and the other electron is at an offset of $\pm\omega_I$; $\Delta_1 \approx 0$, $\Delta_2 \approx \pm\omega_I$. This leads to the degeneracies in energy levels of the system, combined with relaxation resulting in polarization enhancements of the surrounding nuclei. In the case of cross effect DNP, the enhancement scales with magnetic field strength as B_Z^{-1} , this is most likely related to the fact that the separation between energy levels increases linearly with increasing field strength.

The dissipator contains all the terms that are present in SE-DNP, eq. (2.21). In addition, processes of both longitudinal and transverse cross-relaxation are possible between the electron pair due to the action of the environment. These have

the form

$$\Gamma_{+-}^{(SS)} \mathbf{D} \left[\hat{S}_+^{(1)} \hat{S}_-^{(2)} \right] + \Gamma_{-+}^{(SS)} \mathbf{D} \left[\hat{S}_-^{(1)} \hat{S}_+^{(2)} \right]$$

for longitudinal cross-relaxation, and

$$\Gamma_z^{(SS)} \mathbf{D} \left[\hat{S}_z^{(2)} - \hat{S}_z^{(1)} \right],$$

for transverse cross-relaxation. The CE-DNP system dissipator is then

$$\begin{aligned} & \Gamma_+^{(S_1)} \mathbf{D} \left[S_+^{(1)} \right] + \Gamma_-^{(S_1)} \mathbf{D} \left[S_-^{(1)} \right] + \Gamma_z^{(S_1)} \mathbf{D} \left[S_z^{(1)} \right] + \Gamma_+^{(S_2)} \mathbf{D} \left[S_+^{(2)} \right] \\ & + \Gamma_-^{(S_2)} \mathbf{D} \left[S_-^{(2)} \right] + \Gamma_z^{(S_2)} \mathbf{D} \left[S_z^{(2)} \right] + \Gamma_{+-}^{(SS)} \mathbf{D} \left[\hat{S}_+^{(1)} \hat{S}_-^{(2)} \right] + \Gamma_{-+}^{(SS)} \mathbf{D} \left[\hat{S}_-^{(1)} \hat{S}_+^{(2)} \right] \\ & + \Gamma_z^{(SS)} \mathbf{D} \left[\hat{S}_z^{(2)} - \hat{S}_z^{(1)} \right] + \sum_k \Gamma_{k+}^{(I)} \mathbf{D} \left[I_{k+} \right] + \Gamma_{k-}^{(I)} \mathbf{D} \left[I_{k-} \right] + \Gamma_{kz}^{(I)} \mathbf{D} \left[I_{kz} \right]. \end{aligned} \quad (2.24)$$

As previously mentioned, the terms corresponding to rates $\Gamma_{kz}^{(I)}$, $\Gamma_z^{(S_1)}$, $\Gamma_z^{(S_2)}$ are responsible for modelling decoherence of nuclear spins and electrons, respectively. Since the nuclear thermal polarization is very low, even at temperatures approaching 1K, the rates $\Gamma_{k+}^{(I)}$, $\Gamma_{k-}^{(I)}$ approximately coincide. The electronic rates are weighted by the electron thermal polarization $\Gamma_{\pm}^{(S_j)} = \frac{R_1^{(S_j)}}{2} (1 \pm p_{\text{th}})$. The system density operator is propagated using eqs. 2.13, 2.23, 2.24. Polarization for each spin is then obtained by taking a trace of the product of the density operator at each time-step and \hat{I}_z or $\hat{S}_z^{(j)}$ operator

$$p^{(S_j)}(t) = \text{Tr} \left(\hat{\rho} \hat{S}_z^{(j)} \right) \quad p_k^{(I)}(t) = \text{Tr} \left(\hat{\rho} \hat{I}_{kz} \right).$$

2.4 Adiabatic elimination

The work in this chapter follows the original derivation by A. Karabanov, and has been previously published by us in [52].

As discussed in section 2.1.1, the density operator dimension in DNP, or in fact any quantum-mechanical simulations, scales as 4^n , for n system constituents. Such unfavourable scaling limits simulations of spin systems to just a few spins. To date, systems with up to 10 spins [37] have been successfully simulated without any approximations. Any system larger than this would require very large amounts of memory, which is expensive and not feasible for wide-spread regular use.

There exist mathematical techniques that allow reduction of the effective subspace of the density operator, one such technique is called adiabatic elimination [50]. The method of adiabatic elimination allows for separating subspaces of the

density operator which evolve on different time-scales, such that slow dynamics can be separated from fast dynamics. In the context of quantum mechanics this process is somewhat analogous to proceeding to the rotating frame of reference, and the approximations that are taken to derive the Lindblad master equation in section 2.1.3, where the environment is assumed to evolve on a time-scale that is much faster than the time-scale over which the system evolves, hence the system dynamics are coarse grained.

In a simplified example, this can be illustrated by two coupled differential equations

$$\dot{\mathbf{L}}_0 = A \cdot \mathbf{L}_0 + B \cdot \mathbf{L}_1$$

$$\dot{\mathbf{L}}_1 = C \cdot \mathbf{L}_0 + D \cdot \mathbf{L}_1,$$

where \mathbf{L}_0 represents the system, coupled to a rapidly-evolving environment (\mathbf{L}_1), and A,B,C,D are linear coefficients. Approximate effective dynamics are found for the system involving a mean, coarse-grained effect of the environment on the system. In the case of adiabatic elimination applied to DNP we separate slow dynamics of the the density operator from the fast ones.

2.4.1 Mathematical procedure

The purpose of the adiabatic elimination is to separate the slow \mathbf{L}_0 , and the fast dynamics \mathbf{L}_1

$$\dot{\rho} = \mathbf{L}\rho = (\mathbf{L}_0 + \mathbf{L}_1) \rho.$$

For any linear system with constant coefficients

$$\dot{\hat{\rho}} = \mathbf{L}\hat{\rho},$$

defined in Hilbert space \mathcal{H} , we are interested in a reduced dimensions subspace $\mathcal{H}_0 \subset \mathcal{H}$.

Using Nakajima-Zwanzig projection operators [50], where \mathcal{P} is the projector onto the subspace of interest (\mathcal{H}_0), \mathcal{Q} is the complementary projector, we are effectively looking at the space decomposition $\mathcal{H} = \mathcal{H}_0 + \mathcal{H}_1$,

$$\begin{aligned} (\mathcal{P} + \mathcal{Q}) \dot{\rho} &= (\mathcal{P} + \mathcal{Q}) \mathbf{L} (\mathcal{P} + \mathcal{Q}) \rho \\ (\mathcal{P} + \mathcal{Q}) \dot{\rho} &= (\mathcal{P}\mathbf{L}\mathcal{P} + \mathcal{P}\mathbf{L}\mathcal{Q} + \mathcal{Q}\mathbf{L}\mathcal{P} + \mathcal{Q}\mathbf{L}\mathcal{Q}) \rho \\ \mathcal{P}\dot{\rho} &= (\mathcal{P}\mathbf{L}\mathcal{P} + \mathcal{P}\mathbf{L}\mathcal{Q}) \rho \\ \mathcal{Q}\dot{\rho} &= (\mathcal{Q}\mathbf{L}\mathcal{Q} + \mathcal{Q}\mathbf{L}\mathcal{P}) \rho \end{aligned}$$

defining now

$$\begin{aligned}\mathbf{L}_{00} &= \mathcal{P}\mathbf{L}\mathcal{P} & \mathbf{L}_{01} &= \mathcal{P}\mathbf{L}\mathcal{Q} \\ \mathbf{L}_{11} &= \mathcal{Q}\mathbf{L}\mathcal{Q} & \mathbf{L}_{10} &= \mathcal{Q}\mathbf{L}\mathcal{P},\end{aligned}$$

two coupled differential equations are formed

$$\dot{\hat{\rho}}_0 = \mathbf{L}_{00}\hat{\rho}_0 + \mathbf{L}_{01}\hat{\rho}_1 \quad (2.25)$$

$$\dot{\hat{\rho}}_1 = \mathbf{L}_{11}\hat{\rho}_1 + \mathbf{L}_{10}\hat{\rho}_0. \quad (2.26)$$

The general solution to eq. (2.26) with respect to $\hat{\rho}_1$, in time is

$$\hat{\rho}_1(t) = e^{\mathbf{L}_{11}t}\hat{\rho}_1(0) + e^{\mathbf{L}_{11}t} \int_0^t e^{-\mathbf{L}_{11}\tau} \mathbf{L}_{10}\hat{\rho}_0(\tau) d\tau,$$

where frequently the boundary condition $\rho_1(0) = \mathcal{Q}\rho = 0$ will usually apply. Substituting into eq. (2.25), dynamics enclosed in \mathcal{H}_0 are obtained

$$\dot{\hat{\rho}}_0 = \mathbf{L}_{00}\hat{\rho}_0 + \int_0^t \mathbf{L}_{01}e^{\mathbf{L}_{11}(t-\tau)} \mathbf{L}_{10}\hat{\rho}_0(\tau) d\tau$$

$$\dot{\hat{\rho}}_0 = \mathbf{L}_{00}\hat{\rho}_0 + \int_0^t \mathbf{K}(t-\tau)\hat{\rho}_0(\tau) d\tau. \quad (2.27)$$

The three-part product here is the kernel:

$$\mathbf{K}(t-\tau) = \mathbf{L}_{01}e^{\mathbf{L}_{11}(t-\tau)} \mathbf{L}_{10}.$$

The Laplace transform of both sides of equation 2.27 is taken; both sides are multiplied by $e^{-\epsilon t}$, and integrated between 0 and ∞ with respect to t .

LHS

Integration by parts is used

$$\int u'v = uv - \int v'u$$

$$\int_0^\infty e^{-\epsilon t} \dot{\hat{\rho}}_0(t) dt = \hat{\rho}_0(t)e^{-\epsilon t} \Big|_0^\infty - \int_0^\infty -\epsilon e^{-\epsilon t} \hat{\rho}_0(t) dt = -\hat{\rho}_0(0) + \epsilon \int_0^\infty e^{-\epsilon t} \hat{\rho}_0(t) dt.$$

RHS

$$-\hat{\rho}_0(0) + \epsilon \int_0^\infty \hat{\rho}_0(t) dt = \int_0^\infty e^{-\epsilon t} \mathbf{L}_{00} \hat{\rho}_0 + \int_0^\infty \int_0^t e^{-\epsilon t} \mathbf{K}(t-\tau) \hat{\rho}_0(\tau) d\tau dt.$$

In principle, the kernel can be written in a diagonalised frame in which it acts as a sum of eigenfunctions. This could be achieved by writing \mathbf{L}_{11} in a diagonal basis. Analytically this would be difficult, even for a 2-spin problem, however in principle there exists such diagonal form:

$$\mathbf{K}(t-\tau) \equiv \sum_k \mathbf{K}_k e^{\epsilon_k(t-\tau)}.$$

The kernel term has the form of a convolution function. As with the Fourier Transform, a Laplace Transform of a convolution function is the product of the individual functions in the space of eigenvalues. Thus

$$\int_0^\infty \int_0^t e^{-\epsilon t} \mathbf{K}(t-\tau) \rho_0(\tau) d\tau dt = l_{\mathbf{K}}(\epsilon) \cdot l_{\rho_0}(\epsilon).$$

Proof

$$\int_0^\infty e^{-\epsilon t} \left(\int_0^t \mathbf{K}(t-\tau) \hat{\rho}_0(\tau) d\tau \right) dt = \sum_k \int_0^\infty e^{(\epsilon_k - \epsilon)t} \left(\int_0^t e^{-\epsilon \tau} \mathbf{K}_k \hat{\rho}_0(\tau) d\tau \right) dt$$

this is integrated by parts, to find a bound solution, defining for clarity

$$\begin{aligned} u &= \frac{e^{(\epsilon_k - \epsilon)t}}{\epsilon_k - \epsilon} & u' &= e^{(\epsilon_k - \epsilon)t} & v &= \sum_k \int_0^t e^{-\epsilon \tau} \mathbf{K}_k \hat{\rho}_0(\tau) d\tau \\ v' &= \sum_k \left(e^{-\epsilon_k t} \mathbf{K}_k \hat{\rho}_0(t) \cdot \frac{d}{dt} t - e^0 \mathbf{K}_k \hat{\rho}_0(0) \cdot \frac{d}{dt} 0 + \int_0^t \frac{\partial}{\partial t} e^{-\epsilon \tau} \mathbf{K}_k \hat{\rho}_0(\tau) \right) \dots \\ & & v' &= \sum_k (e^{-\epsilon_k t} \mathbf{K}_k \hat{\rho}_0(t)), \end{aligned}$$

where for v' a standard mathematical property concerning derivation of integrals is used.

$$\begin{aligned} uv &= \left[\sum_k \frac{e^{(\epsilon_k - \epsilon)t}}{\epsilon_k - \epsilon} \int_0^t e^{-\epsilon_k \tau} \mathbf{K}_k \hat{\rho}_0(\tau) d\tau \right]_{t=0}^{t=\infty} = \dots \\ &= \sum_k \frac{e^{(\epsilon_k - \epsilon)\infty}}{\epsilon_k - \epsilon} \int_0^\infty e^{-\epsilon_k \tau} \mathbf{K}_k \hat{\rho}_0(\tau) d\tau - \sum_k \frac{1}{\epsilon_k - \epsilon} \int_0^0 e^{-\epsilon_k \tau} \mathbf{K}_k \hat{\rho}_0(\tau) d\tau = 0. \end{aligned}$$

$$-\int v'u = -\sum_k \int_0^\infty \frac{e^{(\epsilon_k - \epsilon)t}}{\epsilon_k - \epsilon} (e^{-\epsilon_k t} \mathbf{K}_k \hat{\rho}_0(t)) = -\sum_k \int_0^\infty \frac{e^{-\epsilon t}}{\epsilon_k - \epsilon} (\mathbf{K}_k \hat{\rho}_0(t)),$$

therefore

$$\begin{aligned} \sum_k \int_0^\infty e^{(\epsilon_k - \epsilon)t} \left(\int_0^t e^{-\epsilon \tau} \mathbf{K}_k \hat{\rho}_0(\tau) d\tau \right) dt &= \sum_k \frac{\mathbf{K}_k}{\epsilon_k - \epsilon} \cdot \int_0^\infty e^{-\epsilon t} \hat{\rho}_0(t) dt \\ &\equiv l_{\mathbf{K}}(\epsilon) \cdot l_{\hat{\rho}_0}(\epsilon). \end{aligned}$$

The following Laplace transforms are defined:

$$\begin{aligned} l_{\hat{\rho}_0}(\epsilon) &= \int_0^\infty e^{-\epsilon t} \hat{\rho}_0(t) dt \\ l_{\mathbf{K}}(\epsilon) &= \int_0^\infty e^{-\epsilon t} \mathbf{K}(t) dt = \sum_k \int_0^\infty e^{-\epsilon t} e^{\epsilon_k t} \mathbf{K}_k dt = \sum_k \frac{\mathbf{K}_k}{\epsilon - \epsilon_k} \end{aligned}$$

2.4.2 Effective dynamics

Hence, equation 2.27 is rewritten in the Laplace domain as

$$\begin{aligned} -\hat{\rho}_0(0) + \epsilon l_{\hat{\rho}_0}(\epsilon) &= \mathbf{L}_{00} l_{\hat{\rho}_0}(\epsilon) + l_{\mathbf{K}} l_{\hat{\rho}_0} \\ l_{\hat{\rho}_0}(\epsilon) &= (\mathbf{1}\epsilon - \mathbf{L}_{00} - l_{\mathbf{K}}(\epsilon))^{-1} \hat{\rho}_0(0). \end{aligned} \quad (2.28)$$

The initial value $\hat{\rho}_0(0)$ and the Laplace transform of the kernel $l_{\mathbf{K}}$ uniquely define the Laplace transform of the solution. The solution itself is then uniquely found by inversion of its Laplace transform.

It follows from eq. (2.27) that the solution at time t depends on its history in the time interval $[0, t]$. The integral kernel \mathbf{K} is often called *memory function*. Besides the memory effects, \mathbf{K} describes how dynamics in the complementary subspace \mathcal{H}_1 affect the dynamics in \mathcal{H}_0 .

If all eigenvalues, ϵ_k , of \mathbf{L}_{11} have negative real parts, which is expected in the system, then any solution to $\hat{\rho}_0(0)$ will rapidly tend to a steady-state

$$\hat{\rho}_0 \rightarrow \hat{\rho}_0^{ss} \quad t \rightarrow \infty.$$

Large negative eigenvalues of \mathbf{L}_{11} indicate a rapid decay of the dynamics in the complementary subspace \mathcal{H}_1 in comparison to the dynamics of $\hat{\rho}_0$. Under these assumptions, the form of the kernel in the time domain quickly reaches steady-state, and in consideration of time-scale of the dynamics of $\hat{\rho}_0$, the kernel can be

integrated to infinity

$$\int_0^\infty \mathbf{K}(t) dt = \sum_k \mathbf{K}_k \int_0^\infty e^{\epsilon_k t} dt = \sum_k \mathbf{K}_k \left[\frac{e^{\epsilon_k t}}{\epsilon_k} \right]_0^\infty = - \sum_k \frac{\mathbf{K}_k}{\epsilon_k} \equiv -\mathbf{L}_{01} \mathbf{L}_{11}^{-1} \mathbf{L}_{10}.$$

We assume the dynamics in the subspace $\hat{\rho}_1$ to evolve rapidly, and quickly be 'forgotten' by the system in the subspace $\hat{\rho}_0$, thus we require

$$\max(\text{eig}(\mathbf{L}_{01}, \mathbf{L}_{10})) \ll \min(\epsilon_k), \quad (2.29)$$

and hence we work in a regime where the eigenvalues of the effective system are small

$$\epsilon \ll \min(\epsilon_k)$$

i.e. slow dynamics in the subspace \mathcal{H}_0 .

Mathematically, the Laplace Transform of the kernel function

$$l_{\mathbf{K}}(\epsilon) = \sum_k \frac{\mathbf{K}_k}{\epsilon - \epsilon_k}$$

is expanded around $\epsilon \approx 0$, i.e. the region of slower dynamics with small eigenvalues, so in result we have the Maclaurin series

$$l_{\mathbf{K}}(\epsilon) \approx l_{\mathbf{K}}(0) + \frac{\partial l_{\mathbf{K}}(0)}{\partial \epsilon}(\epsilon) + \frac{\partial^2 l_{\mathbf{K}}(0)}{\partial \epsilon^2}(\epsilon^2/2) + \dots$$

If $\|\mathbf{L}_{01}\| \cdot \|\mathbf{L}_{10}\| \ll \epsilon_k^2$ then

$$-\frac{\partial l_{\mathbf{K}}(0)}{\partial \epsilon}(\epsilon) = - \sum_k \frac{\mathbf{K}_k}{\epsilon_k^2} \approx 0$$

and hence

$$l_{\mathbf{K}}(\epsilon) \approx l_{\mathbf{K}}(0) = - \sum_k \frac{\mathbf{K}_k}{\epsilon_k}.$$

The effect of $l_{\mathbf{K}}(0)$ can be rewritten as a superoperator \mathbf{M} . An inverse Laplace transform is then applied to obtain the solution eq. (2.28) in the time-domain

$$l_{\hat{\rho}_0}(\epsilon) = (\mathbf{1}\epsilon - \mathbf{L}_{00} - \mathbf{M})^{-1} \hat{\rho}_0(0). \quad (2.30)$$

Since the Laplace transform of a function $f(t) = e^{\alpha t}$ is $F(\epsilon) = \frac{1}{\epsilon - \alpha}$, the Laplace inverse of eq. 2.30 is

$$\hat{\rho}_0(t) = e^{(\mathbf{L}_{00} + \mathbf{M})t} \hat{\rho}_0(0),$$

and hence the form of the effective master equation is given in differential form as

$$\dot{\hat{\rho}}_0(t) = (\mathbf{L}_{00} + \mathbf{M}) \hat{\rho}_0(t). \quad (2.31)$$

Here the superoperator \mathbf{M} is approximated from $-\mathbf{L}_{01}\mathbf{L}_{11}^{-1}\mathbf{L}_{01}$.

Equation (2.31) does not contain any memory function. Its operator $\mathbf{L}_{00} + \mathbf{M}$ is time-independent. Fast dynamics in the complementary subspace \mathcal{H}_1 make the solution in \mathcal{H}_0 tend to the steady-state, rapidly “forgetting” its previous history.

Equation (2.31) is an adiabatic approximation for equation (2.27) – the complementary subspace \mathcal{H}_1 is adiabatically eliminated. The term ‘adiabatic’ means that we first separate fast motions in \mathcal{H}_1 from slow motions in \mathcal{H}_0 and then eliminate all information about the fast motions, not influencing the slow dynamics. Here the equation preserves its initial form of the linear system with constant coefficients. The technique is easily generalised to inhomogeneous systems and initial conditions outside the informative subspace \mathcal{H}_0 .

Such procedures are commonly used in condensed matter theory, quantum optics, quantum statistics and quantum information (among other fields), in cases where either external driving or an interaction with an environment are involved in such way that a non-resonant part of the dynamics becomes non-informative. If the dimension of the informative subspace \mathcal{H}_0 is much smaller than the dimension of the total space \mathcal{H} , this gives a significant reduction of the initial problem.

2.5 Kinetic Monte Carlo algorithm

In this section, the Monte Carlo (MC) algorithms applicable to Lindblad-type master equations are described. The background theory, and derivations are covered in detail in work by Plenio and Knight [53]. The algorithms are of a stochastic nature. They are applied in the Hilbert space of a system and rely on averaging over the different trajectories that a system can take in its evolution. Kinetic Monte Carlo (kMC) algorithms applicable to both quantum and classical systems exist. The quantum Monte Carlo algorithm describes the evolution of the system with quantum jumps (related to the Lindblad dissipator, eq. (2.11)), and the coherent evolution in between them. As such, the quantum MC algorithm faces the exponential scaling with respect to an increasing number of spins, since evolution of the entire system wavefunction must be considered, and the number of elements in the system wavefunction vector scales as $2^n \times 1$. As such, these algorithms are not necessarily more efficient than propagating the system with the Lindblad master equation in Liouville space, eq. (2.13), however they can be advantageous

in situations where the Lindblad master equation proves difficult to solve or is not strictly Markovian [54].

The classical kMC algorithm is suitable for systems where coherent evolution has been eliminated and only the dynamics of populations are simulated. The system dynamics are described entirely by quantum jump operations. These algorithms are very efficient, and are not subject to the exponential scaling of memory usage with an increasing number of spins. As the systems described are Markovian, only the information regarding the current state of the system has to be contained, therefore the memory usage with respect to an increasing number of spins tends to be linear or at worst polynomial.

2.5.1 Quantum Jump Monte Carlo

If the Lindbladian, eq. (2.10) is split into the 'sandwich' term $\mathbf{S} = \Gamma_k \hat{L}_k \hat{\rho} \hat{L}_k^\dagger$, and the commutator and anti-commutator parts $-i [\hat{H} \hat{\rho}] + \Gamma_k \left\{ \hat{\rho}, \hat{L}_k^\dagger \hat{L}_k \right\}$, where Γ_k is the jump rate, then the term \mathbf{S} can be integrated formally

$$\begin{aligned} \hat{\rho}(t) &= \exp [(\mathcal{L} - \mathbf{S}) t + \mathbf{S} t] \hat{\rho}(0) \\ &= \sum_m \int_0^t dt_m \int_0^{t_m} dt_{m-1} \dots \int_0^{t_2} dt_1 \\ &\times \left\{ e^{(\mathcal{L}-\mathbf{S})(t-t_m)} \mathbf{S} e^{(\mathcal{L}-\mathbf{S})(t_m-t_{m-1})} \mathbf{S} \dots \mathbf{S} e^{(\mathcal{L}-\mathbf{S})t_1} \hat{\rho}(0) \right\}, \end{aligned}$$

where

$$\left\{ e^{(\mathcal{L}-\mathbf{S})(t-t_m)} \mathbf{S} e^{(\mathcal{L}-\mathbf{S})(t_m-t_{m-1})} \mathbf{S} \dots \mathbf{S} e^{(\mathcal{L}-\mathbf{S})t_1} \hat{\rho}(0) \right\} \equiv \hat{\rho}_C(t),$$

is described by Carmichael [55] as the 'conditioned' density operator

$$\hat{\rho}_C(t) = |\Psi_C(t)\rangle \langle \Psi_C(t)|.$$

The component

$$\exp [(\mathcal{L} - \mathbf{S}) \Delta t]$$

propagates the conditioned density operator $\hat{\rho}_C(t)$ for a time Δt without a quantum jump occurring (those would occur due to the term \mathbf{S}):

$$|\Psi_C(t + \Delta t)\rangle = e^{-i\hat{H}\Delta t} |\Psi_C(t)\rangle.$$

The effective Hamiltonian is defined as

$$\hat{H}_{\text{eff}} = \hat{H} - i \sum_k \frac{\Gamma_k}{2} (\hat{L}_k^\dagger \hat{L}_k), \quad (2.32)$$

and is derived from $\mathcal{L} - \mathbf{S}$. At a time when a quantum jump occurs, the jump operator corresponding to that jump is applied to the wavefunction

$$|\Psi_C(t)\rangle' = \hat{L}_k |\Psi_C(t)\rangle.$$

Implementation

The implementation of the algorithm for quantum MC relies on the following steps:

1. The probabilities for all possible quantum jumps are calculated

$$\Delta P_k = \Gamma_k \delta t \langle \Psi | \hat{L}_k^\dagger \hat{L}_k | \Psi \rangle$$

2. A random number r_1 is obtained, where $0 < r_1 \leq 1$

3. If $r_1 < \sum_k \Delta P_k$, a quantum jump will occur.

- 3.1. Draw a second random number r_2 to choose which jump will occur, select rate corresponding to jump where

$$r_2 < \frac{\sum_1^k \Delta P_k}{\sum \Delta P (\forall_k)}$$

4. Otherwise if $r_1 > \sum_k \Delta P_k$, no quantum jump will occur, and the system evolves under the influence of the non-Hermitian effective Hamiltonian, eq. (2.32)

$$|\Psi\rangle \rightarrow \frac{\{1 - i\hat{H}_{\text{eff}}\Delta t\} |\Psi\rangle}{(1 - \sum \Delta P_k)^{1/2}}$$

5. Steps 1-4 are repeated until a desired time t is reached, to form an individual trajectory
6. Trajectories are averaged to approximate the time evolution of observables of interest.

2.5.2 Classical kinetic Monte Carlo

If the coherent evolution is eliminated, then the system dynamics are restricted to the populations, and are described entirely by jumps occurring in the system. These are described by terms of \mathbf{S} . Only knowledge of the current eigenstate of each system constituent needs to be known, in order to propagate the system in time and form a system trajectory. Since the form of the jump operators is known,

the associated rates connect classical system configurations. No re-normalisation of the system state is required.

The fixed time-step kMC algorithm can be summarised in the following steps

1. The effective rates, Γ_k , associated with the jump operations are calculated
2. Two uniformly-distributed random numbers r_1, r_2 are generated
3. A jump will be implemented in the system if

$$r_1 > e^{-\sum_k \Gamma_k \Delta t},$$

otherwise steps 2-3 are repeated

4. The effective rates are normalised in a vector, so that their cumulative sum adds to 1. A rate is then selected for which the normalised rate value is greater than the second random number r_2 , i.e. one finds the rate for which

$$r_2 < \frac{\sum_1^{k=i} \Gamma_k}{\sum_k \Gamma_k (\forall_k)},$$

the corresponding jump operation is then carried out

5. Steps 1-4 are repeated until a desired time τ is reached, to form a single trajectory of the system
6. Trajectories are averaged to approximate the time evolution of observables of interest.

The above algorithm relies on selecting an appropriate time step, and may be inefficient in cases where the time-step selected is too small. In such case, steps 2-3 would frequently be repeated with no jumps occurring in the system. If the time-step selected is too large, the dynamics might be under-sampled, and thus inaccurate. This would be the case if only one jump operation is carried out within a current time-step where numerous jumps should have been implemented.

Variable time-step kMC

A variable time-step kMC algorithm avoids the issues outlined above. Step 3 in the above algorithm is altered by setting $r_1 = e^{-\sum_k \Gamma_k \Delta t}$. The equation is rearranged to find the time step required between each jump operation in the system

$$\Delta t = \frac{-\log r_1}{\sum_k \Gamma_k}.$$

The remainder of the algorithm remains the same, as illustrated in figure 2.5.

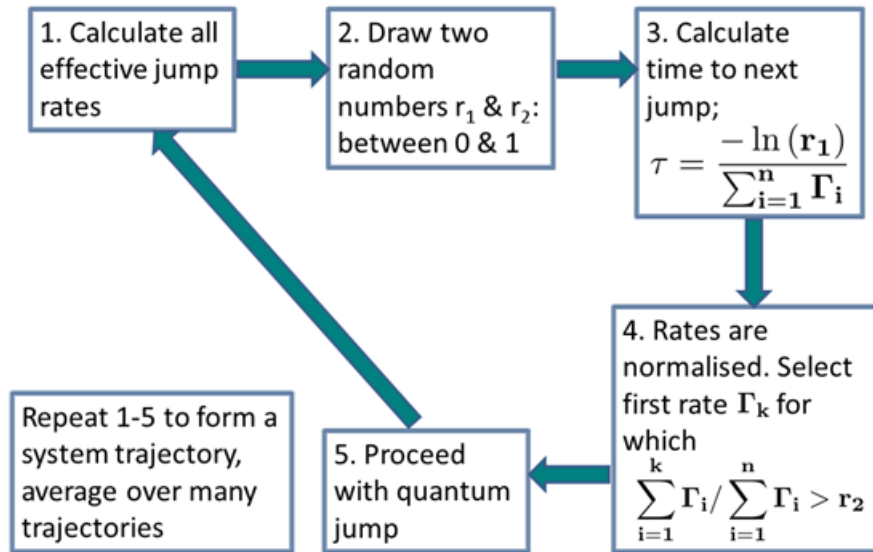


Figure 2.5: Graphical representation of the variable time-step kinetic Monte Carlo algorithm.

1. The effective rates, Γ_k , associated with the jump operations are calculated
2. Two uniformly-distributed random numbers r_1, r_2 are generated
3. The duration to the next time-step is calculated

$$\Delta t = \frac{-\log r_1}{\sum_k \Gamma_k}$$

4. A rate is then selected for which the normalised rate value is greater than the second random number r_2 ;

$$r_2 < \frac{\sum_1^{k=i} \Gamma_k}{\sum_k \Gamma_k (V_k)}$$

5. Steps 1-4 are repeated until a desired time τ is reached, to form a single trajectory of the system
6. Trajectories are averaged to approximate observable of interest.

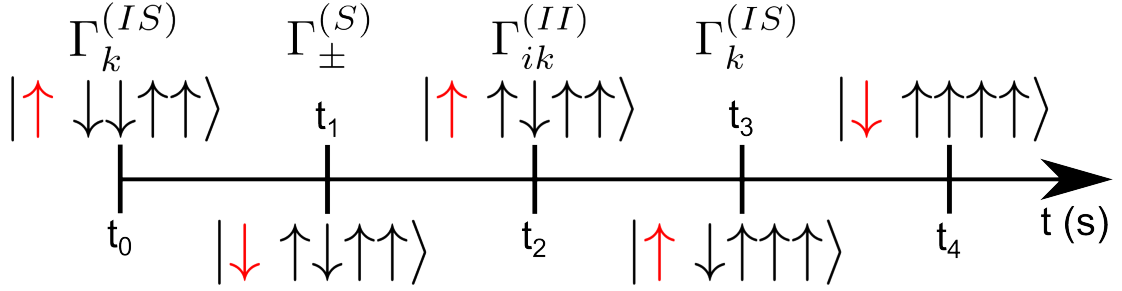


Figure 2.6: A graphical illustration of the implementation of the variable time-step kMC algorithm for a system of 5 spins; 1 electron (red arrow) and 4 nuclei (black arrows). At time t_0 , a flip-flop occurs between the electron and the first nuclear spin. This is possible due to the coupling between them and the microwave radiation driving the system. The spins 'exchange' states. At time t_1 , the electron flips back to its ground state. At time t_2 , a flip-flop occurs between nuclei 2 and 3, due to their dipolar coupling. Finally, at time t_3 , another flip-flop occurs between the electron and nucleus 2, leading to a fully polarized nuclear ensemble.

Evolution of a virtual system is illustrated in fig. 2.6. A trajectory is shown, where the starting-point nuclear ensemble consists of a number of spins in the $-\frac{1}{2}$ states equal to the number of nuclei in the $\frac{1}{2}$ states. Evolution of the system under the influence of microwave radiation driving the system, leads to an end state of a fully polarized nuclear ensemble. This is a simple description of the processes occurring in larger, more complicated spin systems, which leads to enhanced polarization.

An analogous variable time-step quantum Monte Carlo algorithm exists for cases where coherent evolution of the system is present.

Chapter 3

Solid Effect

3.1 Adiabatic elimination of Solid Effect dynamics

This chapter is focused on the derivation of the effective dynamics governing SE–DNP with the use of projection operators. This is followed by: a description of the derived effective rates and a comprehensive error analysis, spin diffusion studies in 1D systems, large spin ensemble simulations, fitting of the polarization curves, and finally scaling of the error and computational time with respect to the system size. Research described in this chapter is described in our publication [52].

3.1.1 Elimination of non–zero quantum coherences

The SE–DNP dynamics are projected onto the diagonal part of the density operator, the so–called Zeeman subspace, in a two–step process. The dynamics are first projected onto the zero–quantum subspace, and subsequently the Zeeman subspace of the zero–quantum subspace. In effect, the relevant subspace dimension of the density operator is reduced from $4^{(n+1)}$ to $2^{(n+1)}$ for n nuclear spins. The mathematical procedure of adiabatic elimination is explained in section 2.4. The SE–DNP Hamiltonian for a single electron and n nuclei is shown in eq. (2.20). For convenience, the rotating–frame of reference Hamiltonian can be separated into

four parts

$$\begin{aligned}
\hat{H}_Z &= \Delta \hat{S}_z + \sum_k \hat{I}_{kz} \\
\hat{H}_0 &= \lambda \hat{S}_z + \sum_k A_k \hat{S}_z \hat{I}_{kz} + \frac{\omega_1}{2} (\hat{S}_+ + \hat{S}_-) \\
&+ d_{kk'} \sum_{kk'} (2\hat{I}_{kz} \hat{I}_{k'z} - \frac{1}{2} \hat{I}_{k+} \hat{I}_{k'-} - \frac{1}{2} \hat{I}_{k-} \hat{I}_{k'+}) \\
\hat{H}_\pm &= \sum_k B_{k\pm} \hat{S}_z \hat{I}_{k\pm}.
\end{aligned}$$

The terms \hat{H}_Z , \hat{H}_0 keep dynamics of a particular subspace enclosed in that subspace. Terms \hat{H}_\pm , on the other hand, cause cross-overs between the different subspaces. At the SE resonance condition of either $\Delta = \pm\omega_I$, the Zeeman Hamiltonian becomes $\hat{H}_Z = \omega_I(\pm\hat{S}_z + \sum_k \hat{I}_{kz})$.

The system is also subject to dissipation. There is longitudinal relaxation (T_1) driving all spins back to their thermal equilibrium, as well as decoherence (T_2) processes. The dissipator for this system is written as

$$\begin{aligned}
\mathbf{\Gamma} &= \Gamma_+^{(S)} \mathbf{D}[\hat{S}_+] + \Gamma_-^{(S)} \mathbf{D}[\hat{S}_-] + \Gamma_z^{(S)} \mathbf{D}[\hat{S}_z] \\
&+ \sum_k \left(\Gamma_{k+}^{(I)} \mathbf{D}[\hat{I}_{k+}] + \Gamma_{k-}^{(I)} \mathbf{D}[\hat{I}_{k-}] + \Gamma_{kz}^{(I)} \mathbf{D}[\hat{I}_{kz}] \right),
\end{aligned}$$

with associated rates

$$\begin{aligned}
\Gamma_\pm^{(S)} &= \frac{R_1^{(S)}}{2} (1 \mp p_{\text{th}}) & \Gamma_z^{(S)} &= 2R_2^{(S)} \\
\Gamma_{k+}^{(I)} &= \Gamma_{k-}^{(I)} = \frac{R_1^{(I)}}{2} & \Gamma_{kz}^{(I)} &= 2R_2^{(I)}.
\end{aligned} \tag{3.1}$$

As outlined in section 2.1.3, the system dynamics are then described by

$$\dot{\hat{\rho}} = (-i\hat{H} + \mathbf{\Gamma})\hat{\rho}. \tag{3.2}$$

The Liouville state space can be decomposed as

$$\mathcal{L} = \sum \mathcal{L}_q,$$

where \mathcal{L}_q is the subspace of q -quantum coherences,

$$\hat{H}_Z \hat{\rho} = q\omega_I \hat{\rho}, \quad \hat{\rho} \in \mathcal{L}_q, \quad q = 0, \pm 1, \dots, \pm(n+1). \tag{3.3}$$

The case of $q = 0$, i.e. when $\hat{H}_Z \hat{\rho} = 0$ denotes the zero-quantum subspace. The subspace of interest is therefore the one that commutes with the Zeeman Hamiltonian. The dynamics in this subspace are a lot slower than the dynamics in the other subspaces, since

$$\omega_I \gg A_k, B_{k\pm}, d_{kk'}, \Gamma_z^{(S)}, \Gamma_{\pm}^{(S)}, \Gamma_{kz}^{(I)}, \Gamma_{k\pm}^{(I)}, \quad (3.4)$$

at high field, meaning the separation of these subspaces using adiabatic elimination is appropriate.

For a simple two-spin system, the density operator is

$$\rho = \rho_e \otimes \rho_n = \begin{pmatrix} a(S_z + \frac{1}{2}) & cS_+ \\ c^*S_- & b(S_z - \frac{1}{2}) \end{pmatrix} \otimes \begin{pmatrix} d(I_z + \frac{1}{2}) & eI_+ \\ e^*I_- & f(I_z - \frac{1}{2}) \end{pmatrix} = \dots$$

where a, b, c, d, e, f are linear coefficients. The elements of the zero-quantum subspace of the density operator are then easily written out

$$\begin{pmatrix} \alpha_1 (S_z + \frac{1}{2}) (I_z + \frac{1}{2}) & \alpha_2 (S_z + \frac{1}{2}) I_+ & \alpha_3 S_+ (I_z + \frac{1}{2}) & \alpha_4 S_+ I_+ \\ \alpha_5 (S_z + \frac{1}{2}) I_- & \alpha_6 (S_z + \frac{1}{2}) (I_z - \frac{1}{2}) & \alpha_7 S_+ I_- & \alpha_8 S_+ (I_z - \frac{1}{2}) \\ \alpha_9 S_- (I_z + \frac{1}{2}) & \alpha_{10} S_- I_+ & (\alpha_{11} S_z - \frac{1}{2}) (I_z + \frac{1}{2}) & \alpha_{12} (S_z - \frac{1}{2}) I_+ \\ \alpha_{13} S_- I_- & \alpha_{14} (I_z - \frac{1}{2}) S_- & \alpha_{15} (S_z - \frac{1}{2}) I_- & \alpha_{16} (S_z - \frac{1}{2}) (I_z - \frac{1}{2}) \end{pmatrix}. \quad (3.5)$$

Here elements existing in the zero-quantum subspace are marked in red, and for convenience $\frac{1}{2}$ is used to denote the identity matrix divided by 2. The symbols α_j ($1 \leq j \leq 16$) denote linear coefficients.

Letting the subspace \mathcal{H}_0 be the zero-quantum subspace, and \mathcal{H}_1 the complementary subspace

$$\mathcal{H}_0 = \mathcal{L}_0, \quad \mathcal{H}_1 = \sum_{q \neq 0} \mathcal{L}_q,$$

the relations

$$(-i\hat{H}_0 + \Gamma)\hat{\mathcal{L}}_q \subset \mathcal{L}_q, \quad \hat{H}_{\pm} \mathcal{L}_q \subset \mathcal{L}_{q\pm 1}$$

along with (3.3) give the following properties

$$\begin{aligned} \mathbf{L}_{00}\hat{\rho}_0 &= -i\hat{H}_0 + \Gamma\hat{\rho}_0, & \mathbf{L}_{10}\hat{\rho}_0 &= -i(\hat{H}_+ + \hat{H}_-)\hat{\rho}_0, \\ \mathbf{L}_{01}\mathcal{L}_{\pm 1} &= -i\hat{H}_{\mp}\mathcal{L}_{\pm 1}, & \mathbf{L}_{01}\mathcal{L}_q &= 0, \quad |q| > 1, \\ \mathbf{L}_{11}\mathcal{L}_{\pm 1} &= -(\pm i\omega_I \mathbf{1} + i\hat{H}_0 + i\hat{H}_{\pm} - \Gamma)\mathcal{L}_{\pm 1}, \\ \mathbf{L}_{11}\mathcal{L}_q &= -(iq\omega_I \mathbf{1} + i\hat{H}_0 + i\hat{H}_+ + i\hat{H}_- - \Gamma)\mathcal{L}_q, \quad |q| > 1. \end{aligned} \quad (3.6)$$

Due to the presence of relaxation, the eigenvalues of the superoperator \mathbf{L}_{11} have negative real parts, ζ_- , thus the solution in \mathcal{H}_1 rapidly tends to a steady-state. Therefore, the condition outlined in section 2.4 is satisfied, and the Kernel function is well approximated by its time-independent steady-state form. The zero-

quantum master equation is well approximated by

$$\dot{\hat{\rho}}_0 = (\mathbf{L}_{00} + \mathbf{M}) \hat{\rho}_0,$$

and $\mathbf{M} \equiv -\mathbf{L}_{01}\mathbf{L}_{11}^{-1}\mathbf{L}_{10}$.

3.1.2 Superoperator \mathbf{M}

In order to find the explicit form of \mathbf{M} the properties of superoperators summarised in eq. (3.6) were used. Superoperator \mathbf{L}_{01} acting on $\hat{\rho}_0$ leaves the dynamics in the first quantum coherence subspace $\mathcal{L}_{\pm 1}$

$$\mathbf{L}_{10}\hat{\rho}_0 = -i(\hat{H}_+ + \hat{H}_-)\hat{\rho}_0.$$

Letting $\hat{X} = \mathbf{L}_{11}^{-1}\mathbf{L}_{10}\hat{\rho}_0$, it is clear that

$$\mathbf{L}_{11}\hat{X} = \mathbf{L}_{10}\hat{\rho}_0 = -i(\hat{H}_+ + \hat{H}_-)\hat{\rho}_0.$$

Therefore, since $\omega_I \gg (\hat{H}_{0,\pm}, \mathbf{D})$, \hat{X} can be expanded as a rapidly-converging power series, truncated to second order

$$\hat{X} = \frac{x^{(1)}}{\omega_I} + \frac{x^{(2)}}{\omega_I^2} + 0\left(\frac{x^{(3)}}{\omega_I^3}\right).$$

Each term in the series expansion of \hat{X} can also be separated according to the coherence subspace order. We have from eq. (3.6)

$$\begin{aligned} \mathbf{L}_{11}\mathcal{L}_{\pm 1} &= -\left(\pm i\omega_I\mathbf{1} + i\hat{H}_0 + i\hat{H}_{\pm} - \mathbf{\Gamma}\right)\mathcal{L}_{\pm 1}, \\ \mathbf{L}_{11}\mathcal{L}_q (|q| > 1) &= -\left(\pm iq\omega_I\mathbf{1} + i\hat{H}_0 + i\hat{H}_+ + i\hat{H}_- - \mathbf{\Gamma}\right)\mathcal{L}_q, \end{aligned}$$

hence only focusing on coherence subspaces up to $q = 2$

$$\begin{aligned} \mathbf{L}_{11}\hat{X} &= -\left(i\omega_I\mathbf{1} + (i\hat{H}_0 - \mathbf{\Gamma}) + i\hat{H}_+\right)\hat{X}_{+1}, \\ &\quad -\left(-i\omega_I\mathbf{1} + (i\hat{H}_0 - \mathbf{\Gamma}) + i\hat{H}_-\right)\hat{X}_{-1}, \\ &\quad -\left(2i\omega_I\mathbf{1} + (i\hat{H}_0 - \mathbf{\Gamma}) + i\hat{H}_+ + i\hat{H}_-\right)\hat{X}_{+2}, \\ &\quad -\left(-2i\omega_I\mathbf{1} + (i\hat{H}_0 - \mathbf{\Gamma}) + i\hat{H}_- + i\hat{H}_-\right)\hat{X}_{-2}, \end{aligned}$$

$$\equiv -i \left(\hat{H}_+ + \hat{H}_- \right) \hat{\rho}_0.$$

The equations can then be rewritten according to coherence order

$$- \left(i\omega_I \hat{X}_{+1} + (i\hat{H}_0 - \mathbf{\Gamma}) \hat{X}_{+1} + i\hat{H}_- \hat{X}_{+2} \right) = -i\hat{H}_+ \rho_0, \quad (3.7)$$

$$- \left(-i\omega_I \hat{X}_{-1} + (i\hat{H}_0 - \mathbf{\Gamma}) \hat{X}_{-1} + i\hat{H}_+ \hat{X}_{-2} \right) = -i\hat{H}_- \rho_0, \quad (3.8)$$

$$- \left(2i\omega_I \hat{X}_{+2} + (i\hat{H}_0 - \mathbf{\Gamma}) \hat{X}_{+2} + i\hat{H}_+ \hat{X}_{+1} \right) = 0, \quad (3.9)$$

$$- \left(-2i\omega_I \hat{X}_{-2} + (i\hat{H}_0 - \mathbf{\Gamma}) \hat{X}_{-2} + i\hat{H}_- \hat{X}_{-1} \right) = 0. \quad (3.10)$$

Each coherence order term of \hat{X} is then expanded as a power series with respect to ω_I . First taking eqs. (3.9, 3.10), keeping terms of same order with respect to ω_I

$$\left(2i\omega_I \frac{x_{+2}^{(1)}}{\omega_I} + 0 \right) = 0, \quad \left(-2i\omega_I \frac{x_{-2}^{(1)}}{\omega_I} + 0 \right) = 0$$

thus $x_{+2}^{(1)} = 0$, $x_{-2}^{(1)} = 0$.

Equation (3.7) kept to first order of ω_I gives

$$- \left(i\omega_I \frac{x_{+1}^{(1)}}{\omega_I} \right) = -i \left(\hat{H}_+ \hat{\rho}_0 \right)$$

$$x_{+1}^{(1)} = \hat{H}_+ \hat{\rho}_0,$$

and the second order term of \hat{X}_{+1} is found as

$$- \left(i\omega_I \frac{x_{+1}^{(2)}}{\omega_I^2} + (i\hat{H}_0 - \mathbf{\Gamma}) \frac{x_{+1}^{(1)}}{\omega_I} + i\hat{H}_- \frac{x_{+2}^{(1)}}{\omega_I} \right) = 0$$

$$i \frac{x_{+1}^{(2)}}{\omega_I} + (i\hat{H}_0 - \mathbf{\Gamma}) \frac{x_{+1}^{(1)}}{\omega_I} = 0$$

$$x_{+1}^{(2)} = \frac{-1}{i} \left(i\hat{H}_0 - \mathbf{\Gamma} \right) x_{+1}^{(1)}$$

$$x_{+1}^{(2)} = i \left(i\hat{H}_0 - \mathbf{\Gamma} \right) \hat{H}_+ \hat{\rho}_0.$$

Equation (3.8) kept to first order of ω_I gives

$$- \left(-i\omega_I \frac{x_{-1}^{(1)}}{\omega_I} + 0 \right) = -i \left(\hat{H}_- \rho_0 \right)$$

$$x_{-1}^{(1)} = -\hat{H}_- \rho_0,$$

second order term is

$$\begin{aligned}
& - \left(-i\omega_I \frac{x_{-1}^{(2)}}{\omega_I^2} + (i\hat{H}_0 - \Gamma) \frac{x_{-1}^{(1)}}{\omega_I} + i\hat{H}_+ \frac{x_{-2}^{(1)}}{\omega_I} \right) = 0 \\
& -i \frac{x_{-1}^{(2)}}{\omega_I} + (i\hat{H}_0 - \Gamma) \frac{x_{-1}^{(1)}}{\omega_I} = 0 \\
& ix_{-1}^{(2)} = (i\hat{H}_0 - \Gamma) x_{-1}^{(1)} \\
& x_{-1}^{(2)} = i (i\hat{H}_0 - \Gamma) \hat{H}_- \hat{\rho}_0.
\end{aligned}$$

For completeness, the second order terms of eqs. (3.9), (3.10) are included:

$$\begin{aligned}
2i\omega_I \frac{x_{+2}^{(2)}}{\omega_I^2} + (i\hat{H}_0 - \Gamma) \frac{x_{+2}^{(1)}}{\omega_I} + i\hat{H}_+ \frac{x_{+1}^{(1)}}{\omega_I} &= 0 \\
2x_{+2}^{(2)} + \hat{H}_+ x_{+1}^{(1)} &= 0 \\
x_{+2}^{(2)} &= -\frac{1}{2} \hat{H}_+ \hat{H}_+ \hat{\rho}_0,
\end{aligned}$$

and

$$\begin{aligned}
-2i\omega_I \frac{x_{-2}^{(2)}}{\omega_I^2} + (i\hat{H}_0 - \Gamma) \frac{x_{-2}^{(1)}}{\omega_I} + i\hat{H}_- \frac{x_{-1}^{(1)}}{\omega_I} &= 0 \\
2x_{-2}^{(2)} + \hat{H}_- x_{-1}^{(1)} &= 0 \\
x_{-2}^{(2)} &= -\frac{1}{2} \hat{H}_- \hat{H}_- \hat{\rho}_0.
\end{aligned}$$

However, given the property written down in eq. (3.6), which dictates $\mathbf{L}_{01} \mathcal{L}_q = 0$, $|q| > 1$ – the terms $x_{\pm 2}^{(2)} = -\frac{1}{2} \hat{H}_{\pm} \hat{H}_{\pm} \hat{\rho}_0$ are neglected.

Hence the superoperator \mathbf{M} is found as the series

$$\mathbf{M} = \omega_I^{-1} \mathbf{M}_1 + \omega_I^{-2} \mathbf{M}_2 + \dots \quad (3.11)$$

converging exponentially fast

$$\mathbf{M} - \sum_{k=1}^m \omega_I^{-k} \mathbf{M}_k \sim \epsilon^{m+1} \quad (\epsilon \ll 1),$$

with terms

$$\mathbf{M}_1 = -i[\hat{H}_+, \hat{H}_-], \quad \mathbf{M}_2 = -\hat{H}_+(i\hat{H}_0 - \Gamma)\hat{H}_- - \hat{H}_-(i\hat{H}_0 - \Gamma)\hat{H}_+, \quad \dots \quad (3.12)$$

It follows from (3.6) that

$$\zeta_- > |\omega_I|, \quad \|\mathbf{L}_{01}\| \leq \max \|\hat{H}_\pm\|, \quad \|\mathbf{L}_{10}\| \leq 2 \max \|\hat{H}_\pm\|.$$

Hence, because of eq. (3.4), equation (3.2) can be replaced by its adiabatic approximation

$$\dot{\hat{\rho}} = \mathbf{L}_0 \hat{\rho} \quad (3.13)$$

with

$$\mathbf{L}_0 = \mathbf{L}_{00} + \mathbf{M} = \mathbf{M}_0 + \omega_I^{-1} \mathbf{M}_1 + \omega_I^{-2} \mathbf{M}_2,$$

where

$$\mathbf{M}_0 = -i\hat{H}_0 + \Gamma.$$

3.1.3 Elimination of non-Zeeman spin orders

Following the procedure from the initial Liouvillian \mathbf{L} , eq. (3.2), to the Liouvillian \mathbf{L}_0 , in eq. (3.13), a master equation accurately describing the dynamics closed in the subspace \mathcal{H}_0 is obtained. In this section, the procedure of projection of the dynamics within zero-quantum subspace onto the Zeeman subspace is described. This projection results in classical-like dynamics involving the diagonal elements of the density operator. In the illustrative case of a 2-spin system, the non-Zeeman zero-quantum subspace elements are the off-diagonal elements shown in red, in eq. (3.5).

The zero-quantum subspace is decomposed as

$$\mathcal{L}_0 = \mathcal{L}_Z + \mathcal{L}_C,$$

where

$$\mathcal{L}_Z = \text{span}\{\hat{\mathbf{I}}, \hat{S}_z, \hat{\mathbf{I}}_{kz}, \hat{S}_z \hat{\mathbf{I}}_{kz}, \hat{\mathbf{I}}_{kz} \hat{\mathbf{I}}_{k'z}, \dots\},$$

is the subspace of Zeeman spin orders, and \mathcal{L}_C the complementary subspace consisting of non-Zeeman zero-quantum coherences.

The commutation character of the notation $\hat{O} \equiv [\hat{O}, \cdot]$ implies that the superoperator \mathbf{M}_1 is a commutation:

$$\mathbf{M}_1 = -i\hat{H}_1, \quad \hat{H}_1 = [\hat{H}_+, \hat{H}_-] = \hat{H}_{1,0} + \hat{H}'_1,$$

$$\hat{H}_{1,0} = \frac{\omega_1^2}{2} \hat{S}_z + \frac{1}{8} \sum B_{k+} B_{k-} \hat{\mathbf{I}}_{kz}, \quad \hat{H}'_1 = -\frac{\omega_1}{4} \sum (B_{k+} \hat{\mathbf{I}}_{k+} \hat{S}_- + B_{k-} \hat{\mathbf{I}}_{k-} \hat{S}_+).$$

The mathematical proof is shown in appendix A.1.

We have also

$$\hat{H}_0 = \hat{H}_{0,0} + \hat{H}'_0, \quad \mathbf{\Gamma} = \mathbf{\Gamma}_0 + \mathbf{\Gamma}',$$

where

$$\begin{aligned} \hat{H}_{0,0} &= \lambda \hat{S}_z + \sum_k A_k \hat{I}_{kz} \hat{S}_z + \sum_{k < k'} 2d_{kk'} \hat{I}_{kz} \hat{I}_{k'z}, \\ \hat{H}'_0 &= \sum_{k < k'} -\frac{d_{kk'}}{2} \left(\hat{I}_{k+} \hat{I}_{k'-} + \hat{I}_{k-} \hat{I}_{k'+} \right), \\ \mathbf{\Gamma}_0 &= R_2^{(S)} \mathbf{D}[\hat{S}_z] + \sum R_2^{(I)} \mathbf{D}[\hat{I}_{kz}], \\ \mathbf{\Gamma}' &= \frac{R_1^{(S)}}{2} (1 - p_{\text{th}}) \mathbf{D}[\hat{S}_+] + \frac{R_1^{(S)}}{2} (1 + p_{\text{th}}) \mathbf{D}[\hat{S}_-] + \sum_k \frac{R_1^{(I)}}{2} \left(\mathbf{D}[\hat{I}_{k+}] + \mathbf{D}[\hat{I}_{k-}] \right). \end{aligned} \tag{3.14}$$

In agreement with previous notation, [2.4](#),

$$\mathbf{L}_{0,kj} = \pi_k \mathbf{L}_0 \pi_j, \quad k, j = 0, 1,$$

$$\pi_0 = \mathcal{P}_Z, \quad \pi_1 = \mathcal{Q}_C,$$

where $\mathcal{P}_Z, \mathcal{Q}_C$ are projections onto the subspaces $\mathcal{L}_{Z,C}$ respectively.

The superoperators $\hat{H}_{0,0}, \hat{H}_{1,0}, \mathbf{\Gamma}_0$ trivially act on \mathcal{L}_Z . Within the accuracy of $\sim \omega_I^{-1}$, only the superoperators \hat{H}'_0, \hat{H}'_1 contribute to $\mathbf{L}_{0,10}, \mathbf{L}_{0,01}$, since

$$\mathcal{P}_Z \mathbf{M}_2 \mathcal{Q}_C, \quad \mathcal{Q}_C \mathbf{M}_2 \mathcal{P}_Z \cong \frac{\omega_A |B_{\pm}| (R_2 + \lambda)}{8\omega_I^2},$$

thus the terms that scale as ω_I^{-2} are negligible in comparison to \hat{H}'_1 , since

$$\frac{\omega_A |B_{\pm}|}{4\omega_I} \gg \frac{\omega_A |B_{\pm}| (R_2 + \lambda)}{8\omega_I^2} \implies 1 \gg \frac{R_2 + \lambda}{2\omega_I}.$$

The same applies to $\mathcal{Q}_C \mathbf{M}_2 \mathcal{Q}_C$, hence the superoperator

$$\mathbf{X} = -i\hat{H}'_{0,0} + \mathbf{\Gamma}_0$$

maps \mathcal{L}_C to itself with eigenvalues ζ'_k satisfying

$$\text{Re } \zeta'_k < 0, \quad |\zeta'_k| > \min\{2R_2^{(I)}, R_2^{(S)} + R_2^{(I)}\}.$$

Thus, while

$$\min \left\{ \left(2R_2^{(I)} \right)^2, \left(R_2^{(S)} + R_2^{(I)} \right)^2 \right\} \gg \max \left\{ \frac{|d_{kj}^2|}{4}, \frac{|\omega_1 B_k|^2}{16|\omega_I|^2}, \left(R_1^{(S)} \right)^2, \left(R_1^{(I)} \right)^2 \right\}, \quad (3.15)$$

conditions in eq. (2.29) are satisfied and the subspace \mathcal{L}_C is adiabatically eliminated. The adiabatic approximation to eq. (3.13) is then obtained,

$$\dot{\hat{\rho}}_Z = \mathbf{L}_Z \hat{\rho}_Z, \quad \mathbf{L}_Z = \mathbf{L}_{0,00} - \mathbf{L}_{0,01} \mathbf{L}_{0,11}^{-1} \mathbf{L}_{0,10} \quad (3.16)$$

closed in the Zeeman subspace \mathcal{L}_Z . Using conditions, (3.15), it can be shown that the right-hand side of (3.16) is well approximated as

$$\begin{aligned} \mathbf{L}_{0,00} &= -\mathbf{\Gamma}' - \mathbf{\Gamma}'', \\ \mathbf{L}_{0,01} \mathbf{L}_{0,11}^{-1} \mathbf{L}_{0,10} &= \sum_{k < k'} \hat{C}'_{kk'} \hat{X}'_{kk'} + \sum_k \hat{D}'_k \hat{Y}'_k. \end{aligned} \quad (3.17)$$

The detailed derivation of the effective dynamics is illustrated for a 2-spin, electron-nuclear coupled system in appendix A.2.

The term \mathbf{L}_{00} is given by eq. (3.14), and

$$\mathbf{\Gamma}'' = \frac{\omega_1^2 R_2^{(S)}}{2\omega_I^2} \left(\mathbf{D}[\hat{S}_+] + \mathbf{D}[\hat{S}_-] \right) + \sum_k \frac{B_{k+} B_{k-} R_2^{(I)}}{8\omega_I^2} \left(\mathbf{D}[\hat{I}_{k+}] + \mathbf{D}[\hat{I}_{k-}] \right). \quad (3.18)$$

The operators $\hat{X}'_{kk'}$, \hat{Y}'_k , and the associated coefficients are

$$\begin{aligned} \hat{X}'_{kk'} &= \frac{d_{kk'}}{2} (\hat{I}_{k+} \hat{I}_{k'-} + \hat{I}_{k-} \hat{I}_{k'+}), \\ \hat{Y}'_k &= \frac{|B_{k+}| \omega_1}{4\omega_I} (\hat{I}_{k+} \hat{S}_- + \hat{I}_{k-} \hat{S}_+), \end{aligned} \quad (3.19)$$

$$\begin{aligned} \hat{C}'_{kk'} &= \frac{2R_2^{(I)}}{\left(2R_2^{(I)} \right)^2 + \hat{C}_{kk'}^2}, \quad \hat{D}'_k = \frac{R_2^{(S)} + R_2^{(I)}}{\left(R_2^{(S)} + R_2^{(I)} \right)^2 + \hat{D}_k^2}, \\ \hat{C}_{kk'} &= (A_k - A_{k'}) \hat{S}_z + \frac{1}{8\omega_I} (B_{k+} B_{k-} - B_{k'+} B_{k'-}) \hat{1}, \\ \hat{D}_k &= \lambda \hat{1} + \sum_{s \neq k} A_s \hat{I}_{sz} + \frac{1}{8\omega_I} (4\omega_1^2 - B_{k+} B_{k-}) \hat{1}. \end{aligned} \quad (3.20)$$

The advantage of formula (3.17) is that it reduces the inversion $\mathbf{L}_{0,11}^{-1}$ in the subspace \mathcal{L}_C to the much simpler problem of inversions \hat{C}'_{kj} , \hat{D}'_k of Zeeman operators. The latter are defined in the 2^{n+1} -dimensional Hilbert space and are diagonal in the Zeeman basis.

3.1.4 The Lindblad form

Utilizing the double-commutator, it is straightforward to re-write the right-hand side of the Zeeman projected equation (3.16) in the purely Lindblad form, eq. (2.11)

$$\begin{aligned} \mathbf{L}_Z = & \Gamma_+^{(S)} \mathbf{D}(\hat{S}_+) + \Gamma_-^{(S)} \mathbf{D}(\hat{S}_-) + \sum_k \Gamma_{k\pm}^{(I)} \left(\mathbf{D}(\hat{I}_{k+}) + \mathbf{D}(\hat{I}_{k-}) \right) \\ & + \sum_k \hat{\Gamma}_k^{(IS)} \mathbf{D}(\hat{Y}_k) + \sum_{k < k'} \hat{\Gamma}_{kk'}^{(II)} \mathbf{D}(\hat{X}_{kk'}). \end{aligned} \quad (3.21)$$

The constant rates

$$\Gamma_{\pm}^{(S)} = \frac{1 \mp P_0}{2} R_1^{(S)} + \frac{\omega_1^2}{2\omega_I^2} R_2^{(S)}, \quad (3.22)$$

$$\Gamma_{k\pm}^{(I)} = \frac{1}{2} \left(R_1^{(I)} + \frac{|B_k|^2}{4\omega_I^2} R_2^{(I)} \right), \quad (3.23)$$

are related to the single-spin jump operators \hat{S}_{\pm} , $\hat{I}_{k\pm}$, and the operator rates

$$\hat{\Gamma}_k^{(IS)} = \frac{\omega_1^2 |B_{k+}|^2}{8\omega_I^2 (R_2^{(S)} + R_2^{(I)})} (1 + \hat{D}_k^2)^{-1}, \quad (3.24)$$

$$\hat{\Gamma}_{kk'}^{(II)} = \frac{d_{kk'}^2}{4R_2^{(I)}} (1 + \hat{C}_{kk'}^2)^{-1}, \quad (3.25)$$

are related to the two-spin jump operators $\hat{X}_{kk'}$, and \hat{Y}_k ;

$$\hat{X}_{kk'} = \hat{I}_{k+} \hat{I}_{k'-} + \hat{I}_{k-} \hat{I}_{k'+},$$

$$\hat{Y}_k = \hat{I}_{k+} \hat{S}_- + \hat{I}_{k-} \hat{S}_+.$$

The re-written operator-valued coefficients \hat{D}_k , $\hat{C}_{kk'}$ are:

$$\hat{D}_k = \frac{\lambda \hat{1} + \sum_{s \neq k} A_s \hat{I}_{sz} + \frac{1}{8\omega_I} (4\omega_1^2 - |B_{k+}|^2) \hat{1}}{R_2^{(S)} + R_2^{(I)}}, \quad (3.26)$$

$$\hat{C}_{kk'} = \frac{(A_k - A_{k'}) \hat{S}_z + \frac{1}{8\omega_I} (|B_{k+}|^2 - |B_{k'+}|^2) \hat{1}}{2R_2^{(I)}}. \quad (3.27)$$

It is worth noting that for the operator-valued coefficient $\hat{C}_{kk'}$, eq. (3.27), the second part, $\frac{1}{8\omega_I} (|B_{k+}|^2 - |B_{k'+}|^2) \hat{1}$ is negligible in comparison to the first, hence

the rate $\Gamma_{kk'}^{(II)}$ is approximately state-independent, as

$$\hat{C}_{kk'}^2 \approx \frac{[(A_k - A_{k'})\hat{S}_z]^2}{(2R_1^{(I)})^2} = \frac{(A_k - A_{k'})^2}{16 R_1^{(I)2}}.$$

The situation is similar for eq. (3.26), where the term $\frac{1}{8\omega_I} (4\omega_1^2 - |B_{k+}|^2)$ is small in comparison to the rest of terms, hence effectively eq. (3.26) can be approximated to

$$\hat{D}_k \approx \frac{\lambda\hat{1} + \sum_{s \neq k} A_s \hat{I}_{sz}}{R_2^{(S)} + R_2^{(I)}}.$$

To implement the Zeeman-projected master equation, eq. (3.21), in the computationally convenient form of eq. (2.12), a correct treatment of the operator rates, $\hat{C}_{kk'}, \hat{D}_k$ must be implemented. This procedure is described in appendix A.3.

3.1.5 Analysis of SE-DNP effective dynamics

The effective dynamics, outlined in eqs. (3.22 - 3.25) provide insight into the dynamics of SE-DNP, with much more clarity than the starting master equation, eq. (3.2). The transfer of polarization from an electron to surrounding nuclei, polarization transport between nuclei and dissipative processes are all well described by the four terms of the Lindbladian.

Electron relaxation

Equation (3.22) describes longitudinal relaxation of the central electron spin. This is governed by spin-flips 'up' (+) and 'down' (-). The longitudinal relaxation rate is weighted by the thermal electron polarization of the two states to ensure that the electron relaxes back to thermal equilibrium. A comparison to eq. (3.1) shows a perturbative, second order correction to the longitudinal relaxation of this spin. This is a consequence of the applied microwave field; it relies on the microwave field amplitude, ω_1 , the nuclear Larmor frequency ω_I , and the electronic transverse relaxation time $R_2^{(S)}$. The driving microwave field effectively tilts the quantization axis of the electron away from the Zeeman axis. The perturbative correction corrects for this, approximating dynamics in a diagonal frame.

Nuclear relaxation

Equation (3.23) describes longitudinal relaxation of the nuclear spins. Since even at low temperatures the thermal polarization of nuclear spins is very low, these rates approximately coincide, and without any driving the nuclear spins will relax to a state of no thermal polarization. A comparison to eq. (3.1) shows that

nuclear longitudinal relaxation also has a perturbative, second order correction. This is a consequence of the pseudo–secular coupling to the electron spin, and thus predominantly affects nuclei close to the electron. It relies on the pseudo–secular coupling coefficient $B_{k\pm}$, the nuclear Larmor frequency ω_I , and the nuclear transverse relaxation rate $R_2^{(I)}$. Coupling to the electron shifts the quantization axis of the nuclei, and the second order correction term compensates for this.

Electron–nuclear interaction rate

This is the rate underlying the process of SE–DNP, and clearly shows diffusive dynamics between the electron and the nuclei. Eq. (3.24), shows this rate is operator–valued; its value depends on the state of the entire nuclear spin ensemble. Such operator–valued rates are often referred to as kinetically constrained [56], [57]. Other than the operator–valued coefficient, this rate also depends on the microwave field amplitude ω_1 squared, the absolute value of the pseudo–secular coupling strength squared – $B_{k\pm}$, the inverse of the nuclear Larmor frequency ω_I squared, and the transverse relaxation rates of the electron and nucleus, $R_2^{(S)}$ and $R_2^{(I)}$, respectively. The dependence on the transverse relaxation rates indicates that even though the effective dynamics are classical, the underlying process is quantum–mechanical, and is mediated by coherences.

The operator–valued coefficient in eq. (3.26), has eigenvalues dependent on the polarization level of the nuclear ensemble. It depends on the offset parameter λ , ($\lambda = 0$ corresponds to SE–DNP resonance condition) and the sum $\sum_{s \neq k} A_s I_{sz}$. The sum of nuclear polarizations is close to 0 when the degree of nuclear polarization is low, and increases when the ensemble becomes more polarized, meaning the rate in eq. (3.24) will be reduced in value. It is also clear that \hat{D}_k will be dominated by terms with the strongest A_k couplings.

What follows is that hypothetically λ could be 'tuned' to compensate for the increase in the polarization of the nuclear ensemble. Setting $\lambda = -\sum_{s \neq k} A_s I_{sz}$ would increase the rate $\Gamma_k^{(IS)}$ following an increase in polarization of the nuclei closest to the electron.

Nuclear–nuclear interaction rate

Transport of polarization within the ensemble of nuclear spins is governed by spin diffusion – the rate in eq. (3.25). The rate of polarization transfer between two nuclei is proportional to the square of their dipolar coupling coefficient $d_{kk'}$. It is also inversely proportional to the transverse relaxation rate of the nuclei $R_2^{(I)}$. This rate is approximately state–independent, as demonstrated in section 3.1.4, it does however depend on the difference of the secular couplings of the two nuclei. This

is a consequence of the coupling to the electron shifting the Larmor frequencies of the nuclei. If the difference between the frequencies of the two nuclei becomes significant, then the interaction between them becomes ineffective. In such case the rate, eq. (3.25) becomes quenched and very little or no polarization transfer takes place.

3.2 Error testing of Zeeman projection in SE–DNP

The effective SE–DNP dynamics are an approximation to the dynamics in a diagonal frame. It is important to know when the assumptions underlying the projection are valid. The conditions for the Zeeman projection are outlined in eq. (3.15).

For the rate $\Gamma_k^{(IS)}$, we require

$$1 \gg \frac{|\omega_1||B_k|^2}{16(\omega_I)^2(R_2^{(S)} + R_2^{(I)})^2}.$$

For a hydrogen nucleus, in a modest magnetic field of $B_Z = 3.4$ T, $\omega_I = 144.8$ MHz. Setting the transverse relaxation rates to: $R_2^{(I)} = 10^4$ (s⁻¹), $R_2^{(S)} = 10^5$ (s⁻¹), the above condition is satisfied for example parameters of $\omega_1 = 500$ kHz, $B_{k\pm} = 30$ MHz, giving

$$\frac{|\omega_1||B_k|^2}{16(\omega_I)^2(R_2^{(S)} + R_2^{(I)})^2} \sim 0.012 \ll 1.$$

For the rate $\Gamma_{kk'}^{(II)}$, we require

$$1 \gg \frac{(d_{kk'})^2}{8(R_2^{(I)})^2}$$

Selecting again $R_2^{(I)} = 10^4$, the above is satisfied for $d_{kk'}$ on the order of a few kilohertz. For $d_{kk'} = 4$ kHz,

$$\frac{(d_{kk'})^2}{8(R_2^{(I)})^2} \sim 0.02 \ll 1.$$

In order to verify the accuracy of the Zeeman projection more carefully, a more systematic approach was taken. The virtual system pictured in fig. 3.1 was used with variable separation a (for $2 \text{ \AA} \leq a \leq 10 \text{ \AA}$). The nuclear coordinates are given in table (3.1). Since the coupling strength between spins is not affected by azimuthal rotations, most of the spins are placed in the y - z plane.

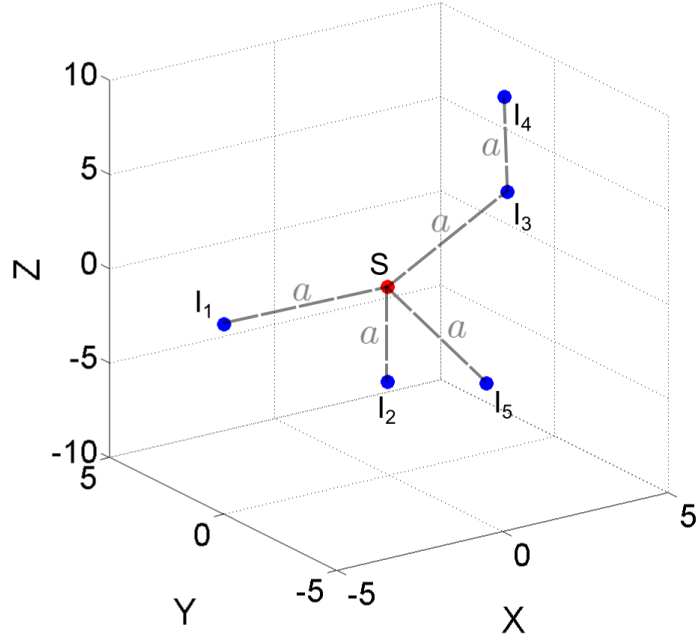


Figure 3.1: Test system, consisting of 5 nuclei (blue dots) surrounding an electron (red dot). The nuclear coordinates are given in the table below.

Spin	x	y	z
S	0	0	0
I ₁	$-a$	0	0
I ₂	0	0	$-a$
I ₃	$\frac{a}{\sqrt{2}}$	0	$\frac{a}{\sqrt{2}}$
I ₄	$\frac{a}{\sqrt{2}}$	0	$a(1 + \frac{\sqrt{2}}{2})$
I ₅	0	$-a\frac{\sqrt{3}}{2}$	$-\frac{a}{2}$

Table 3.1: Coordinate table.

Based on the separation a , the dipolar coupling strength $d_{kk'}$, secular coupling A_k , and pseudo-secular coupling $B_{k\pm}$ will vary accordingly. The simulations were carried out using the gyromagnetic ratio of a ^1H nucleus, and a magnetic field of 3.4 T. In order to generate a significant nuclear polarization enhancement, it was necessary to use a microwave field amplitude of 500 kHz for an inter-spin separation of $a = 2\text{\AA}$. Such microwave field strength would be very difficult to generate experimentally without a resonance cavity. The remaining simulation parameters were: $T = 1\text{ K}$, $T_1^{(S)} = 1\text{ ms}$, $T_1^{(I)} = 1\text{ h}$, $T_2^{(S)} = 200\text{ ns}$, $T_2^{(I)} = 0.2\text{ ms}$. The simulation duration (build-up time) was 1h. These parameters were

consistently used for a separations of 2–5 Å.

The error testing was performed by comparing results obtained using the full Liouvillian, eq. (3.2), and the Liouvillian projected into the Zeeman subspace – eq. (3.21). In each case, the polarization curves of the nuclei are normalised to the electronic thermal equilibrium polarization.

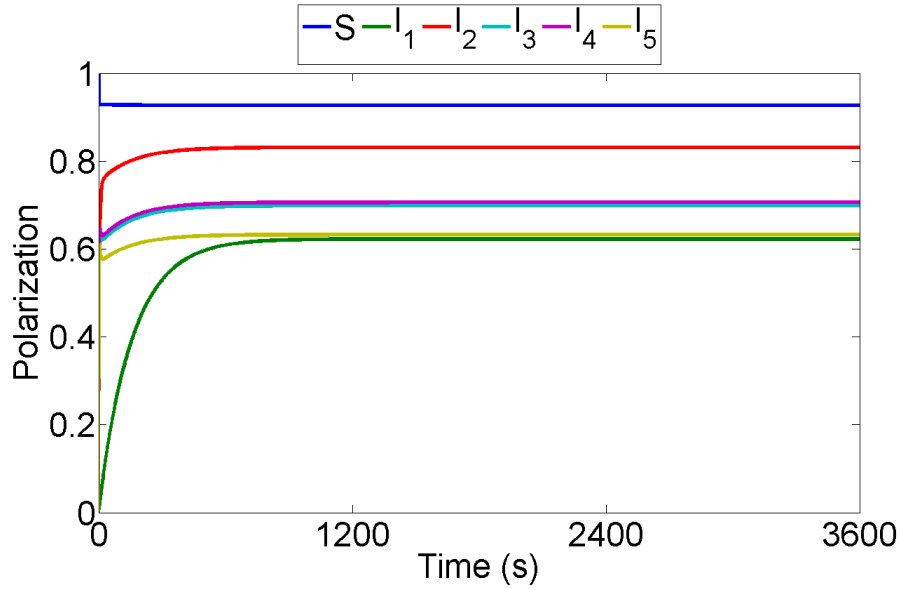


Figure 3.2: Nuclear polarization curves for $a = 2\text{Å}$. The spins are numbered in the legend in the same order as shown in table 3.1.

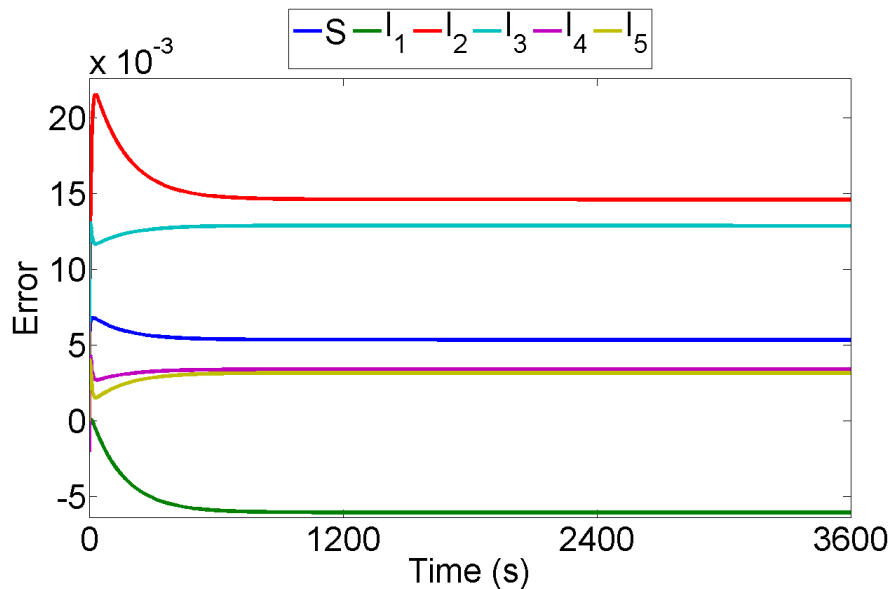


Figure 3.3: Error between full Liouvillian and Zeeman-projected master equation at $a = 2\text{Å}$. A maximum error of 2.2 % is seen in the early stages of the simulation, and this falls to 1.5 % at steady-state.

Polarization curves for the system in fig. 3.1, when $a = 2 \text{ \AA}$ are shown in figure 3.2. It can be seen that most of the nuclei in the system very quickly reach steady-state. Nuclei with very weak pseudo-secular coupling (e.g. I_1), take longer to reach a steady-state, as would be expected. At approximately 800 s, all spins are at steady-state.

Figure 3.3 shows a maximum error of approximately 2.2 % for a spin separation of 2 \AA . This error falls below 1.5 % at steady-state. The error is seen to be lower at larger spin-spin separations, as can be seen in figs. 3.4 – 3.7.

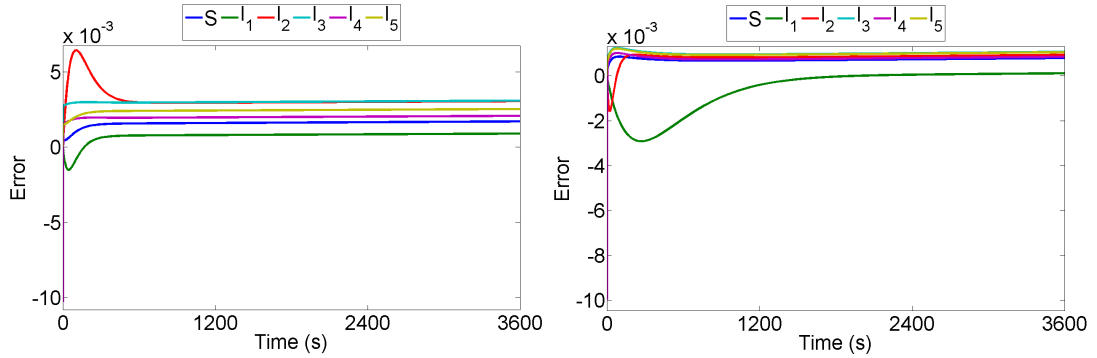


Figure 3.4: Error for $a = 3 \text{ \AA}$ (LHS) and 4 \AA (RHS). The error never exceeds 1 %.

At separations of $a = 3 \text{ \AA}$ and 4 \AA the error is around 1 % in the very early dynamics, and falls to 0.3 % and $\sim 0.1 \text{ %}$ respectively, at steady state. For separations of $a = 5\text{--}10 \text{ \AA}$, the microwave field amplitude was reduced to an experimentally more realistic strength of 200 kHz, and the electronic transverse relaxation time constant $T_2^{(S)}$ was increased 5-fold to $T_2^{(S)} = 1 \mu\text{s}$. For $a = 5 \text{ \AA}$ there is an error of 0.15 % in the early dynamics, and this value falls as the system approaches steady-state.

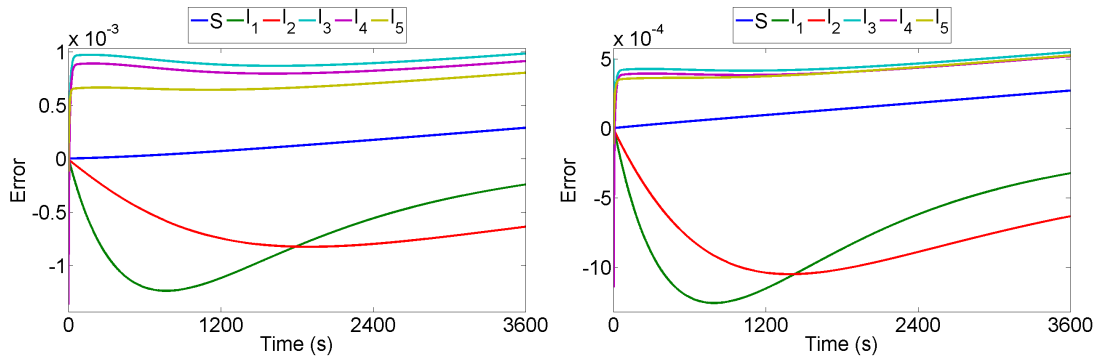


Figure 3.5: Error for $a = 5 \text{ \AA}$ (LHS) and 6 \AA (RHS).

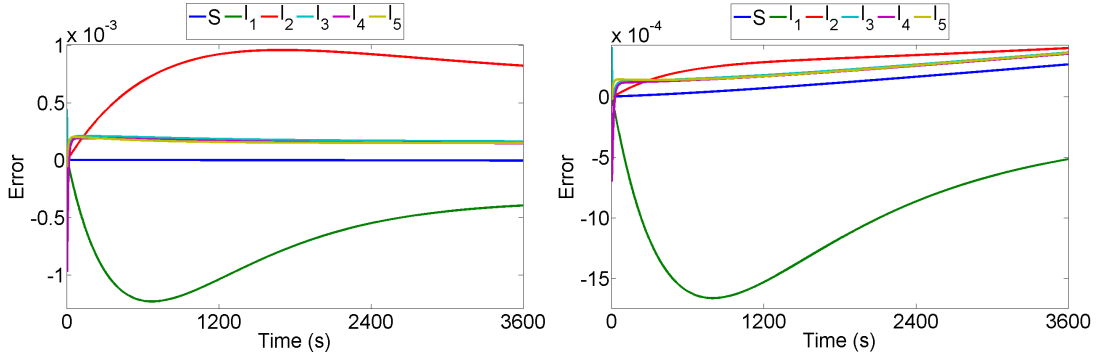


Figure 3.6: Error for $a = 7 \text{ \AA}$ (LHS) and 8 \AA (RHS).

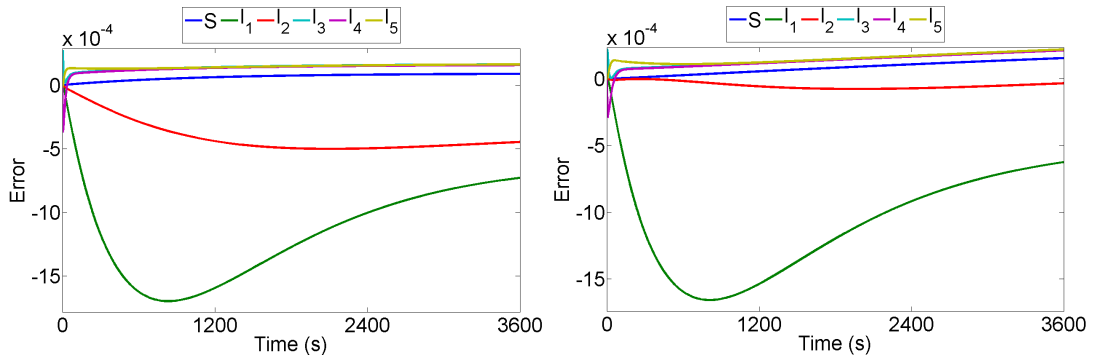


Figure 3.7: Error for $a = 9 \text{ \AA}$ (LHS) and 10 \AA (RHS).

Figures 3.5 – 3.7 show the error to rarely exceed 1 % for larger spin–spin separations.

A very good agreement is seen between the full master equation and the Zeeman–projected one, eqs. (3.2) and (3.21), respectively, for a wide range of parameters – selected to reflect realistic experimental conditions. However, there will be parameter regimes where the error is likely to be greater than shown here, if the conditions in eq. (3.15) are not satisfied. In particular the dynamics in spin systems with very small average distances ($< 2 \text{ \AA}$), long transverse relaxation time constants, or systems with extremely short $T_2^{(S)}$ and $T_1^{(S)}$ times will not be well approximated by the Zeeman–projected effective master equation.

With the accuracy of the Zeeman projection for SE–DNP verified, the greatest advantage of the form of the effective dynamics of eq. (3.21) is that they allow the use of classical kinetic Monte Carlo algorithms. The general kMC algorithm is described in detail in section 2.5.

The algorithm is applied with the effective, Zeeman subspace dynamics as follows: The Lindblad rates (eqs. (3.22) – (3.25)) are first calculated based on the sys-

tem parameters. The rate for the flip–flop interaction between an electron and a nucleus (eq. (3.24)) is state–dependent and hence is initiated using the thermal equilibrium state. Next, two random numbers r_1 and r_2 are generated. The time required for the next event to take place is calculated using a natural logarithm of the first random number and the inverse of the sum of all rates of jumps that are possible in the system. In the next step it is decided which type of jump will be carried out. For this purpose all rates are normalised to sum up to 1, and arranged in a cumulative sum array. An element in this array is identified which is higher in value than the second random number. The operation corresponding to that rate in the array element is then carried out. Accordingly, operations with higher rate values are statistically more likely to occur than events with low rates. Once the operation or jump is carried out, the effective rates for the flip flop jump between a nucleus and the electron (eq. (3.24)) are re–calculated based on the current system state. The steps outlined are repeated until a desired time is reached in the trajectory. Many trajectories are computed and averaged to approximate the polarization dynamics of the system. As previously discussed; the method does not require vast amounts of memory since only an $(n + 1)$ –element binary array is required that stores the current orientation of the z –component (spin state) of each individual spin.

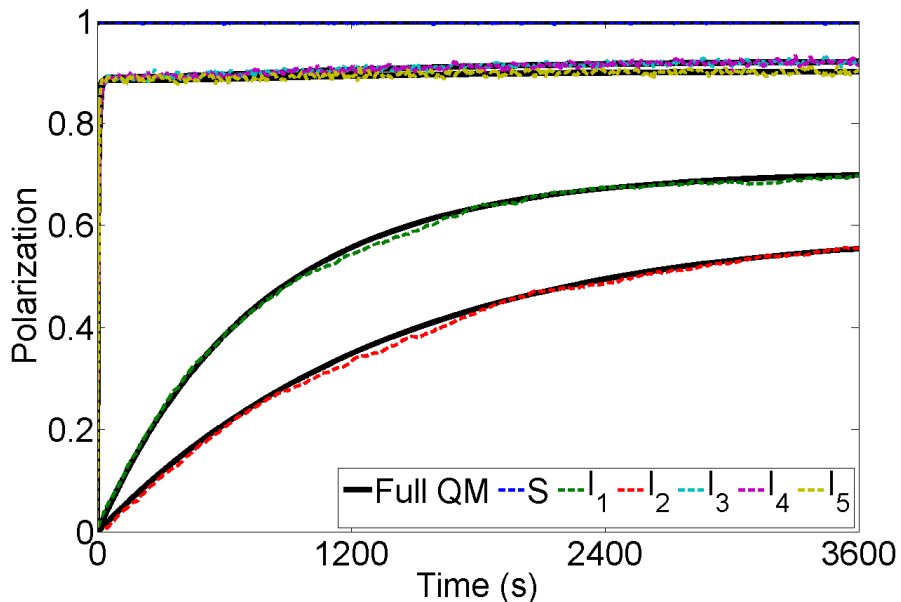


Figure 3.8: Comparison of polarization curves computed using eq. (3.21) – solid black lines, to the polarization curves approximated using kinetic Monte Carlo algorithms – dashed coloured lines. A good fit is seen between the two. The polarization curves estimated using kMC show an inherent random error that is reduced with averaging over a higher number of trajectories. The labelling of nuclear spins corresponds to the labelling used in table 3.1.

Figure 3.8 illustrates a comparison between the polarization curves calculated using the Zeeman-projected master equation, and the polarization curves approximated using kMC. Solid black lines correspond to the Liouvillian closed in the Zeeman subspace, and dashed colour lines correspond to the kMC algorithm. An excellent agreement is seen between the two, as is expected, there is, however, a random error seen in the polarization curves computed using kMC. This is inherent with all Monte Carlo approaches, and is reduced if a larger number of trajectories is used in the approximation. The random error associated with kMC and its scaling, are described in more detail in section 3.5.

3.3 Spin diffusion studies

The use of kMC algorithms allows simulations of SE-DNP in large spins systems. Since only the current eigenstates of spins are kept in memory, this approach avoids the exponential growth of memory usage with respect to an increasing number of spins.

Long 1-D spin chains were simulated with the aim of investigating the role of the nuclear dipolar interactions, and understanding the mechanism of polarization transport to the bulk in SE-DNP. A similar study has been reported by Hovav et al. in [38]. In the authors' investigation, small chain system simulations were conducted using a full master equation. Their results show a very weak dependence of polarization build-up rates on the nuclear dipolar couplings between the nuclei further away (bulk) from the electron, suggesting there is a direct transfer of polarization from the electron to all nuclei, through mixing of the multi-nuclear product states.

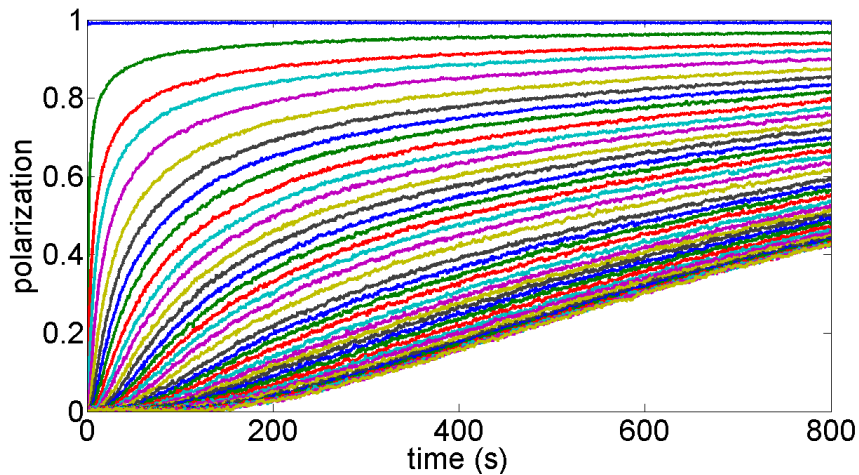


Figure 3.9: Polarization curves for a spin chain of 40 ^{13}C nuclei.

To explore this, simulations of 1-D ^{13}C chains were implemented, with spin chain lengths ranging from 30 – 50 nuclear spins. In each simulation the spin chain was placed at an angle of 45° to the magnetic field vector, B_Z .

Figure 3.9 illustrates the polarization build-up curves for each of the nuclear spins in the chain. The parameters were chosen in accordance with parameters selected by the authors in ref. [38]. There is a slight delay in time between the build-up of each successive spin in the chain, indicating behaviour characteristic of spin-diffusion.

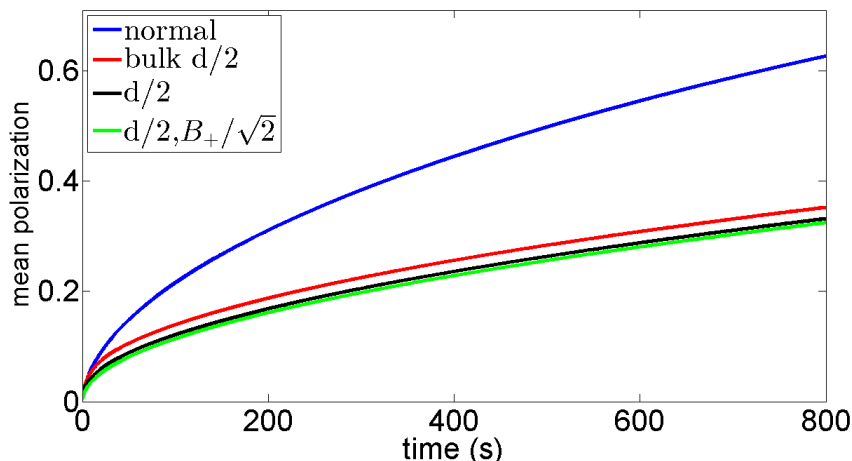


Figure 3.10: The dependence of mean nuclear polarization on coupling parameters in the spin chain.

In figure 3.10 the polarization build-up trajectories shown in fig. 3.9 are averaged, to give the mean nuclear polarization build-up in time – blue line. A comparison is then made for a variety of coupling parameters. The nucleus closest to the electron is referred to as the core nucleus, the remainder of nuclei are treated as the bulk. The red line shows the difference in polarization build-up if the nucleus-nucleus coupling parameter $d_{kk'}$ for the bulk nuclei is halved. A large drop in polarization is observed, and the polarization build-up rate is much slower. The black line shows outcome if all of the nuclear dipolar coupling parameters $d_{kk'}$ are halved. The difference between the red and black lines is small in comparison to the difference between the blue and red lines. The green line shows the polarization build-up seen if in addition to halving $d_{kk'}$ values, the pseudo-secular coupling parameter B_{k+} of the core nucleus is reduced by $\sqrt{2}$. The difference between the black and green lines is negligible.

It is thus clearly seen in fig. 3.10 that the rate of polarization transport across the chain shows a large dependence on the dipolar coupling parameters. This further strengthens the argument spin diffusion is the mechanism of polarization transport to the bulk. This is in contrast to the conclusions drawn in [38], where the

authors have concluded a DNP-assisted process to be responsible for transport of polarization to the bulk, rather than spin diffusion. The discrepancy is most likely due to edge effects, particularly severe for short spin chains, and due to a different treatment of relaxation superoperator. A detailed analysis of the difference of the relaxation treatment by us and Hovav et al. has been discussed in detail [39].

3.3.1 Mathematical treatment of spin diffusion

In figure 3.9 the blue curve shows the electronic polarization which rapidly reaches steady-state. The green line corresponds to the 'core' nucleus – nucleus closest to the electron. The core nucleus also rapidly reaches a steady-state; it does so significantly faster than other nuclei. Therefore the first nuclear spin can be treated as an effective polarization source for the remaining nuclei. The effective electron–nuclear interaction, eq. (3.24) in the spin chain is much greater in magnitude than the rate of eq. (3.25), between the core nucleus and the first bulk nucleus. Consequently the electron and core nucleus act as a system detached from the bulk nuclei, and thus the rate limiting step for the whole spin chain is the interaction between nuclei 2 and 3. Polarization is distributed along the chain with a diffusion rate relating to the effective coupling strength between neighbouring bulk nuclei. Due to the difference in magnitudes between nearest–neighbour coupling, ($\Gamma_{kk'}^{(II)} \sim r_{kk'}^{-6}$) and next–to–nearest–neighbour coupling; effectively only the nearest–neighbour interactions need to be considered.

Assuming, in addition, that the polarization transfer rates between nuclear spins in the bulk are approximately the same i.e.

$$\Gamma_{k,k+1} \sim \Gamma_{k,k-1}$$

the following coupled, linear rate equations can be used to describe the polarization dynamics in the spin chain

$$\begin{aligned} \dot{p}_0 &= r_0(1 - p_0) + \Gamma_1(p_1 - p_0) \\ \dot{p}_1 &= -r_{p1} + \Gamma_1(p_0 - p_1) \\ \dot{p}_k &= -r_{pk} - \Gamma_{nn}(p_k - \frac{1}{2}p_{k-1} - \frac{1}{2}p_{k+1}), \quad k \in \{2, \dots, n-2\}, \end{aligned}$$

where p_0 is the polarization of the electron, p_1 is the polarization of the core nucleus, and p_k are polarizations of nuclei in the bulk. With the assumption that

rate of polarization transfer between bulk nuclei is constant along the chain;

$$\dot{p}_k = -r_{pk} - \Gamma_{nn} (p_k - p_{k-1}).$$

The nuclear polarization at thermal equilibrium is negligible, and generally in SE-DNP $\Gamma_1 \gg \Gamma_{nn}$, $\Gamma_1 \gg r_0$, $\Gamma_{nn} \gg r_p$. It is therefore reasonable to assume in the derivation that the polarization of the core nucleus is constant in time and close in value to the electron quasi-steady-state polarization.

$$p_1(t) \sim 1 = \text{const}$$

The above assumptions work only if relaxation of nuclear spins in the system is weak. Including dissipative contributions makes it difficult to solve the above rate equations analytically. Neglecting edge effects and assuming the chain is semi-infinite, in which case polarization is measured along a continuous spatial coordinate 'x', the equation describing polarization transfer from the core nucleus to the rest of the nuclei can be written as

$$a_k^2 \frac{\partial^2 p}{\partial x^2} \approx \frac{1}{2} p_{k-1} + \frac{1}{2} p_{k+1} - p_k,$$

with a_k being the effective separation between nuclei in the bulk. Since

$$\frac{\partial p}{\partial t} = \Gamma_{nn} (\frac{1}{2} p_{k-1} + \frac{1}{2} p_{k+1} - p_k),$$

the diffusion equation is recovered

$$\frac{\partial p}{\partial t} = D \frac{\partial^2 p}{\partial x^2}, \quad (3.28)$$

where $D = a_k^2 \Gamma_{nn}$. The solution to eq. (3.28) for the imposed initial conditions $p_{t=0, x>0} = 0$, $p_{t=0, x=0} \approx 1$ is

$$p(x, t) = \text{erfc} \left(\frac{x}{2\sqrt{Dt}} \right), \quad (3.29)$$

where erfc is the complimentary error function

$$\text{erfc}(x) = \frac{2}{\sqrt{\pi}} \int_x^\infty e^{-\epsilon^2} d\epsilon.$$

Setting eq. (3.29) equal to erfc(1), the diffusion length is obtained

$$x = 2\sqrt{Dt}. \quad (3.30)$$

Equations (3.29), (3.30) can be used to approximate the diffusion constant D from the simulation data by the following optimization problems

$$\begin{aligned} \|P^*(t, x) - p(t, x)\| &\rightarrow \min \\ \left\| x^*(t) - 2\sqrt{Dt} \right\| &\rightarrow \min. \end{aligned}$$

The asterisk indicates data from a simulation, and $p(x,t)$ is obtained from equation (3.29). The diffusion constant values obtained from the minimization problem can be compared against the diffusion constant obtained directly from the effective rate in eq. (3.25)

$$D_k = \frac{4R_2^{(I)} d_{kk'}^2 a_k^2}{(4R_2^{(I)})^2 + (A_k - A_{k'})^2}. \quad (3.31)$$

Due to the small randomization in position of the nuclear spins, the diffusion constant in eq. (3.31) can vary slightly between spin pairs. The average diffusion coefficient is obtained by averaging over all D_k in a spin system

$$\bar{D} = \frac{1}{n-1} \sum_k^{n-1} D_k.$$

This constant describes the diffusive transport between neighbouring nuclei. It will be quenched if the nuclear transverse relaxation rate $R_2^{(I)}$ is large, or there is a large difference between the A_k values of two spins, thus presence of an electron in close vicinity of a nucleus reduces its rate of polarization diffusion to other nuclei.

Having calculated the effective diffusion constant \bar{D} from the rates $\Gamma_{kk'}^{(II)}$ in a linear chain system; the diffusion length itself, eq. (3.30), can be compared to simulation data. Simulations were carried out for ^{13}C spin chains, placed at an angle of 45° with respect to the magnetic field vector, as a result reducing the strength of the inter-nuclear dipolar coupling. The following simulation parameters were chosen: spin-spin separation $a_k = 5 \text{ \AA}$, $B_Z = 3.4 \text{ T}$, $T = 1 \text{ K}$, $T_1^{(S)} = 1 \text{ s}$, $T_2^{(S)} = 10 \text{ \mu s}$, $T_1^{(I)} = 10^8 \text{ s}$, $T_I^{(I)} = 100 \text{ \mu s}$. A long nuclear T_1 time was chosen to eliminate dissipation processes for the purpose of spin diffusion analysis. Eq. (3.30) was compared against a 2-D contour plot of the spin-system polarization, as a function of distance from the effective source, and time. The contours show a constant level of polarization across time and space, and therefore correspond to paths of polarization transport across the chain in time. The results for a spin chain of 30 nuclei is shown in fig. 3.11.

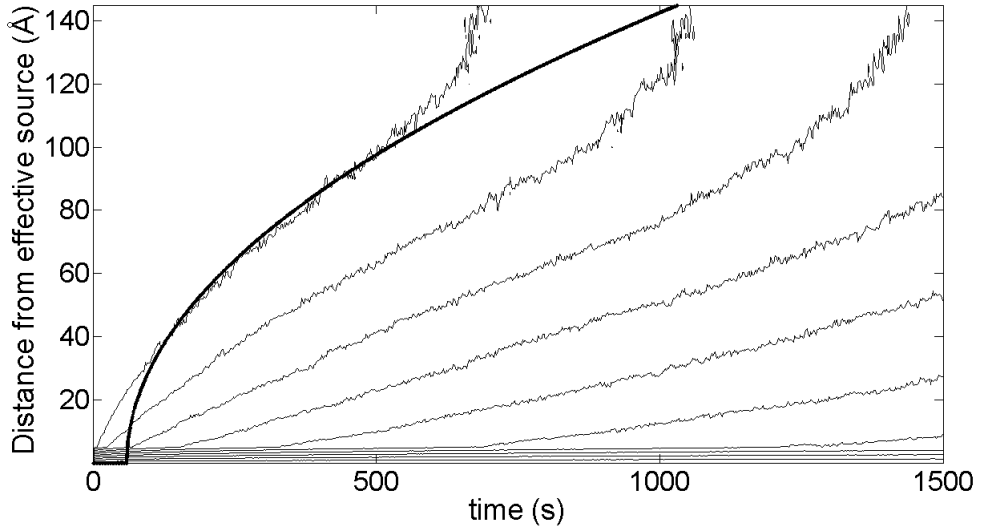


Figure 3.11: Polarization contours shown for a 30–spin linear chain of ^{13}C nuclei. The first polarization contour marks a polarization level of 7 %, and this is the contour the solution to eq. (3.30), marked by a black solid line, is fitted to. The polarization level contours increase from left to right in increments of $\sim 7\%$. A good fit is seen in the early stages, but the contour and solid line are later seen to diverge.

As is clearly seen, the diffusion length, $\langle x \rangle = 2\sqrt{Dt}$, overlaps with the early–time polarization contour very well, however, at later times and greater distance from the source the solution to eq. (3.30) diverges from the contour and intercepts other contour lines. The fit is also not very good at very early times, this is likely due to the fact that there is a finite time taken for the core nucleus to build–up its polarization, causing a delay across the entire chain.

The deviation of the contour lines from the diffusion length is due to the approximations used to derive eq. (3.29). The fact is that the spin chain is not semi–infinite but has a well–defined boundary. Polarization reaching the last nucleus (furthest from the electron) is ‘reflected’ and transported back across the chain towards the electron spin. To account for this, the solution presented in eq. (3.29) was modified; a solution involving a reflective boundary at the end of the spin chain was used instead, as outlined on pages 13 – 16 in [58]. Considering a finite chain of length l with polarization as a finite quantity transported across it; a reflection of polarization is expected to occur when the polarization ‘wave’ reaches the end of the chain. The solution is thus a superposition of two polarization waves that travel down the spin chain in opposite directions

$$p(x, t) = \operatorname{erfc}\left(\frac{x}{2\sqrt{Dt}}\right) + \operatorname{erfc}\left(\frac{2l - x}{2\sqrt{Dt}}\right), \quad (3.32)$$

and in such case the level curve corresponding to the diffusion length is found by numerically solving

$$\operatorname{erfc}\left(\frac{x}{2\sqrt{Dt}}\right) + \operatorname{erfc}\left(\frac{2l-x}{2\sqrt{Dt}}\right) = \operatorname{erfc}(1), \quad (3.33)$$

as there is no analytical solution.

The solution to eq. (3.33) is shown in comparison to eq. (3.30) for a spin chain with 30 nuclei in figure 3.12. Other than at the very early stages of the dynamics, the fit of reflective boundary solution (red line) to the polarization contour is very good. The red line follows the contour shape much more closely than the black line.

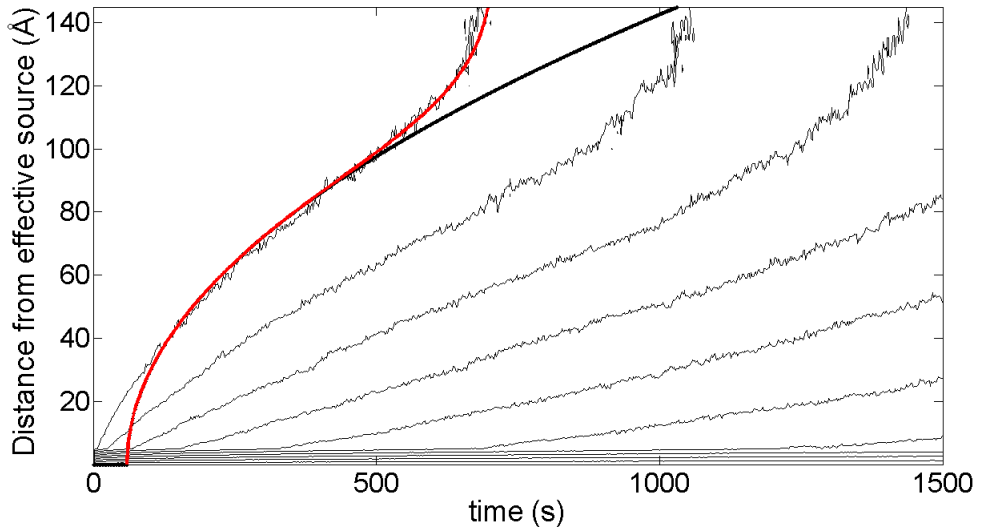


Figure 3.12: Polarization contours shown for a 30–spin linear chain of ^{13}C nuclei. The first polarization contour marks a polarization level of 7 %, and the polarization level contours increase from left to right in increments of ~ 7 %. The black line marks the solution to eq. (3.30). The reflective boundary solution, eq. (3.33), is shown in red. The reflective boundary solution matches the polarization contour much more closely, indicating that a semi–infinite chain treatment is not suitable.

The same is seen for a slightly longer spin chain in fig. 3.13, where the spin chain consists of 1 electron and 40 ^{13}C nuclear spins. Again, the red line, eq. (3.33), matches the shape of the polarization contours much more closely.

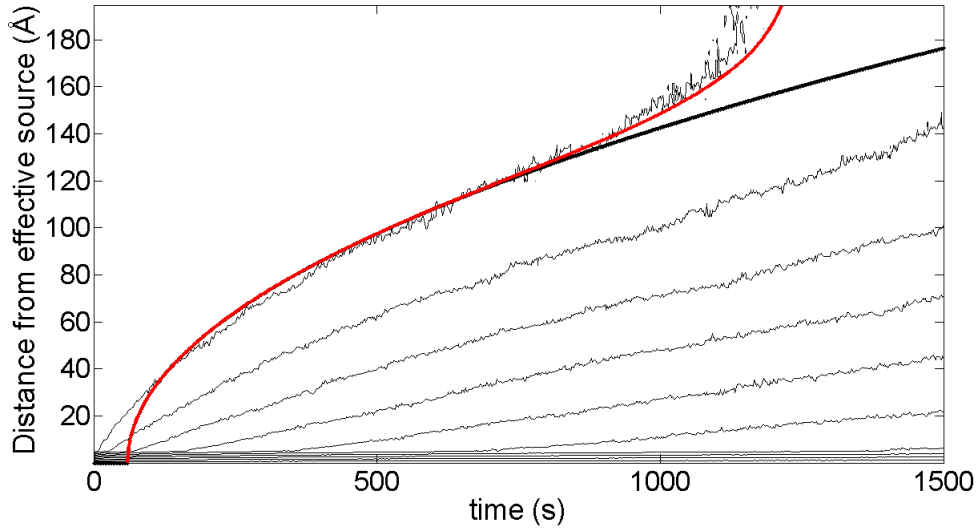


Figure 3.13: Polarization contours shown for a 40–spin linear chain of ^{13}C nuclei. The contours show polarization level increments of 7.5 %. As previously the black line corresponds to the solution of eq. (3.30), and the red line corresponds to a reflective boundary condition. The red line is clearly seen to fit more closely to the polarization contours.

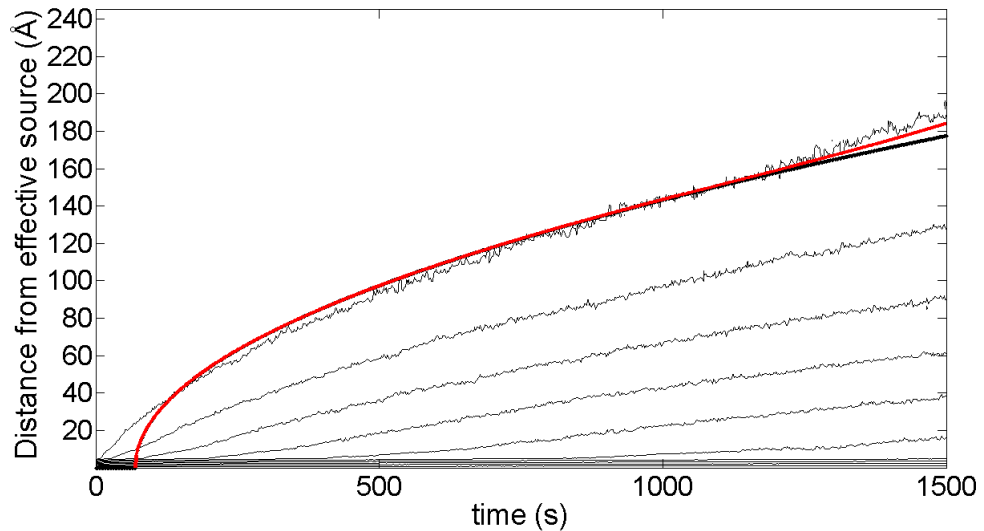


Figure 3.14: Polarization contours shown for a 50–spin linear chain of ^{13}C nuclei. The contours show polarization level increments of 7.5 %. As previously the black line corresponds to the solution of eq. (3.30), and the red line corresponds to a reflective boundary condition. Here it is seen that both solutions fit more closely to one another. This implies that for a spin chain of 50 nuclear spins the finite–edge effects are less severe and the approximation of a semi–infinite linear chain is accurate.

For even longer spin chains, such as the one shown in fig. 3.14, there is still a decent fit of the reflective boundary solution to the polarization contours, however

it can be seen that the fit is not as close as in fig. (3.12), for example. It is also clear that the solutions to eqs. (3.30, 3.33) match each other much more closely, thus indicating that the role of the reflective boundary becomes less important for longer spin chains. The general fit being slightly worse than that seen in fig. 3.12 or fig. 3.9 is likely to be due to the randomization in spin position, leading to a slight deviation of diffusion constant values across the chain from the average diffusion coefficient value.

Our findings strongly suggest, therefore, that the transport of polarization to bulk nuclei in SE-DNP is governed by spin diffusion. This work would not be possible without the use of the effective dynamics and kMC. Moreover it is clear that small spin-system simulations suffer quite severely from finite-boundary effects. This signifies the advantage and necessity of using large-scale many body simulations for understanding the physics of DNP.

3.4 Large spin ensemble calculations

The classical form of the equations governing the dynamics of SE-DNP, eqs. (3.22 – 3.25), enables efficient numerical treatment with the use of kinetic Monte Carlo algorithms, in order to simulate and study large spin ensembles. The spin systems in figures 3.11 – 3.14 are already far beyond the capability of the full master equation, eq. (3.2), and therefore can already be considered large spin ensembles. In this section, large spin system simulations of 3D cubic lattices are shown, to demonstrate the capability of the effective treatment, and the insight it provides.

The parameters constant across all simulations are the temperature $T = 1$ K, magnetic field strength, $B_Z = 3.4$ T, and offset from the ZQ transition frequency $\lambda = 0$.

3.4.1 Hydrogen nuclei

A 5x5x5 cubic lattice was simulated with a lattice constant of 30 Å, making the nearest-neighbour separation between nuclei 6 Å. This value is close to the mean proton-proton separation expected in DNP juice¹. A 5 % uniform randomization in the position of the spins was additionally applied to make the simulation more realistic. A total of 124 ¹H nuclei surround the central electron spin. The following relaxation times were chosen: $T_1^{(S)} = 1$ s, $T_2^{(S)} = 10$ μs, $T_1^{(I)} = 1$ h, and $T_2^{(I)} =$

¹60/30/10 : d₈-glycerol/D₂O/H₂O (vol %)

100 μs . The microwave field amplitude ω_1 was set to 160 kHz. A build-up time of 2000 s was simulated, using a total of 10080 averaged kMC trajectories. The output is shown in fig. 3.15.

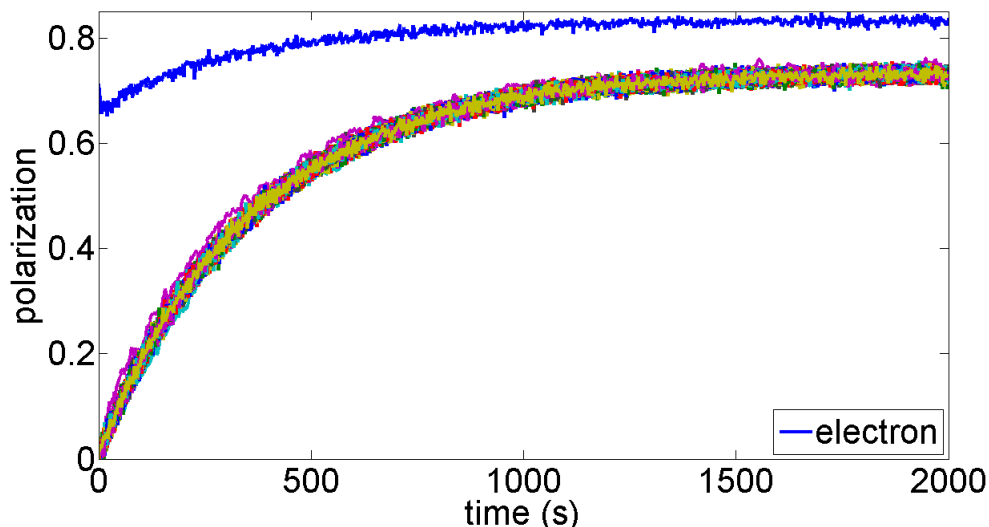


Figure 3.15: Polarization build-up curves in a cube of 125 ^1H spins. The blue line shows polarization of the electron. The coloured lines show the various nuclei in the system. Due to the nuclei having relatively strong dipolar coupling, their polarization levels equalise. After 2000 s the system is close to steady-state.

A rapid build-up of nuclear polarization is seen within the first few minutes of the simulation. Steady-state is reached before the set duration of 2000 s. All of the curves are relatively close together – this is due to the strong nuclear dipolar coupling, leading to a quick equalisation of nuclear polarization. The 3D representation in fig. 3.16 illustrates this quite well; time shots of the polarization levels of each spin in space are shown. The third quartile in the x-y plane has been removed from the 3D plot for clarity in displaying results. The colour bar scale represents the amount of polarization as a percentage of the electronic thermal equilibrium polarization.

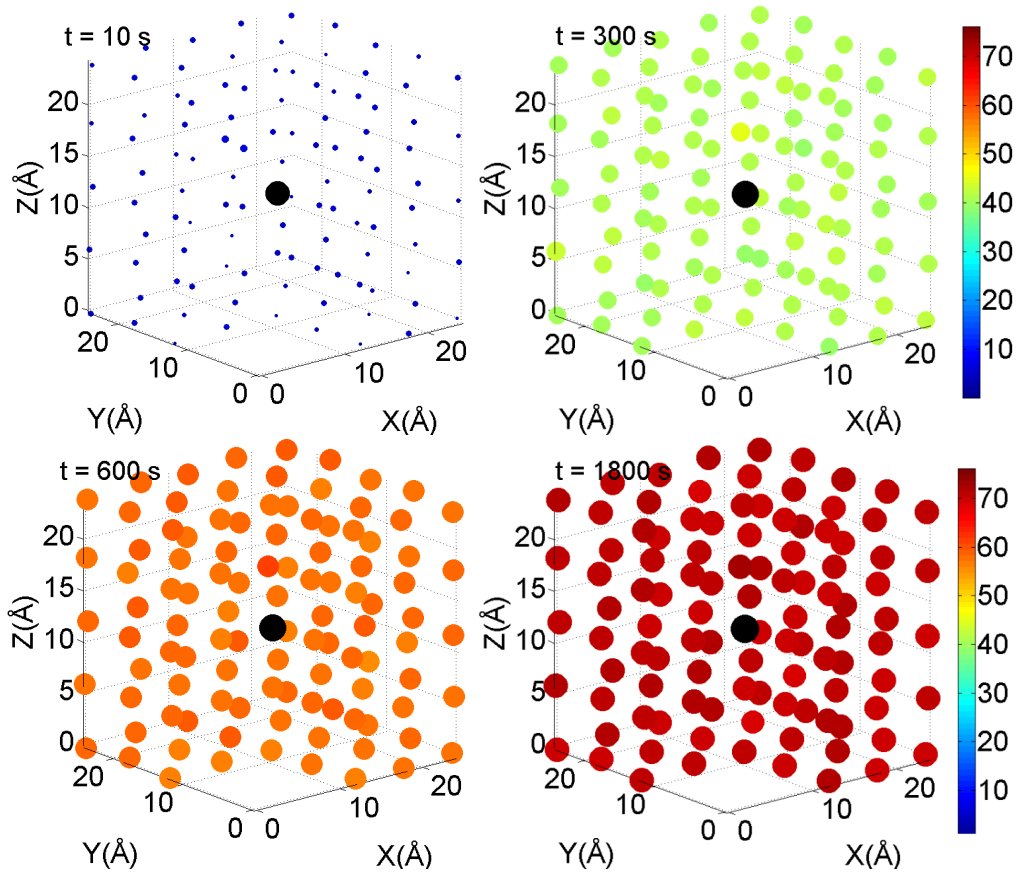


Figure 3.16: Evolution of the polarization of the 124 ^1H nuclear spins. The black dot in the centre marks the position of the electron. Colour and dot size are used to indicate the polarization level of the nuclei. Time shots at 10 s, 300 s, 600 s, and 1800 s are shown.

3.4.2 Carbon-13 nuclei

The lattice seen in figure 3.16 was then simulated with ^{13}C nuclei instead of ^1H nuclei. The spin-spin separation was set to 10.3 Å, with a 5% uniform randomization in position. For the purpose of comparison to figs. 3.15, 3.16, the relaxation parameters were kept the same as above. The microwave field amplitude ω_1 was set to 100 kHz in this case. A build-up time of 4000 s seconds was simulated, and a total of 100 000 trajectories were averaged. A quick comparison between figures 3.15 and 3.17 clearly shows that the build-up for ^{13}C is much slower, the nuclei reach a lower polarization level at steady-state, and the system takes longer to reach steady-state. This is expected since the interactions between ^{13}C spins are much weaker, due to ^{13}C having a lower gyromagnetic ratio. The gyromagnetic ratio of ^{13}C is approximately 4 times smaller than that of ^1H , making the effective interaction strengths of eqs. (3.24), (3.25) ~ 16 , and $\sim 16^2$ times weaker, respectively. The expected separation between the ^{13}C nuclei is also significantly greater

than that of ^1H , weakening the effective dipolar interaction further by a factor of $\sim (10.3/6)^6$.

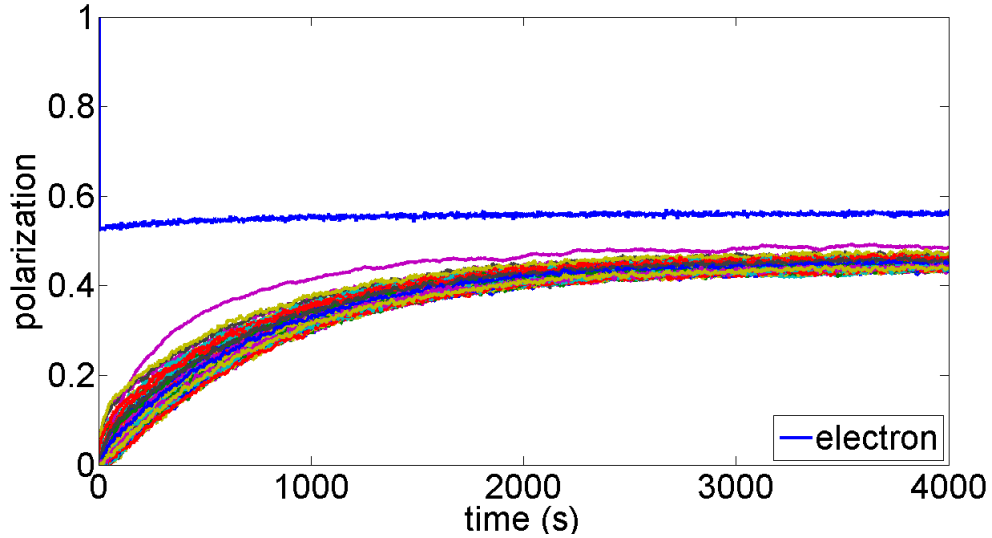


Figure 3.17: Polarization build-up curves for a cube of 125 ^{13}C nuclei. The blue line shows polarization of the electron. The coloured lines show the various nuclei in the system. In ^{13}C , the dipolar coupling is weaker than in ^1H , hence the nuclear polarization levels do not equalise as well. After 4000 s the system is close to steady-state.

The microwave field amplitude ω_1 chosen to produce the simulation in fig. 3.15 was 60 % higher than that for fig. 3.17. This is due to the fact that the ^1H nuclei are coupled to the electron more effectively and depolarize the electron more efficiently, thus the electron does not saturate. In figure 3.17 it is evident that the electron polarization level is much lower, due to ^{13}C coupling to the electron being much weaker. The ^{13}C nuclei do not depolarize the electron spin as efficiently, hence it is closer to saturation by the the microwave field. A higher microwave field amplitude ω_1 would not be beneficial in this case. It is very likely it would have a negative effect instead. The fact that the ^{13}C - ^{13}C coupling is much weaker manifests itself in fig. 3.17 – the polarization curves show a lot more spread than those in fig. 3.15. This is also shown more clearly in the 3D figures, 3.18. The plots clearly show that nuclei closer to the electron (with greatest $B_{k\pm}$ values) have a higher degree of polarization than nuclei at the edge of the lattice. It is clear that the spin-diffusion rate is much slower for ^{13}C nuclei.

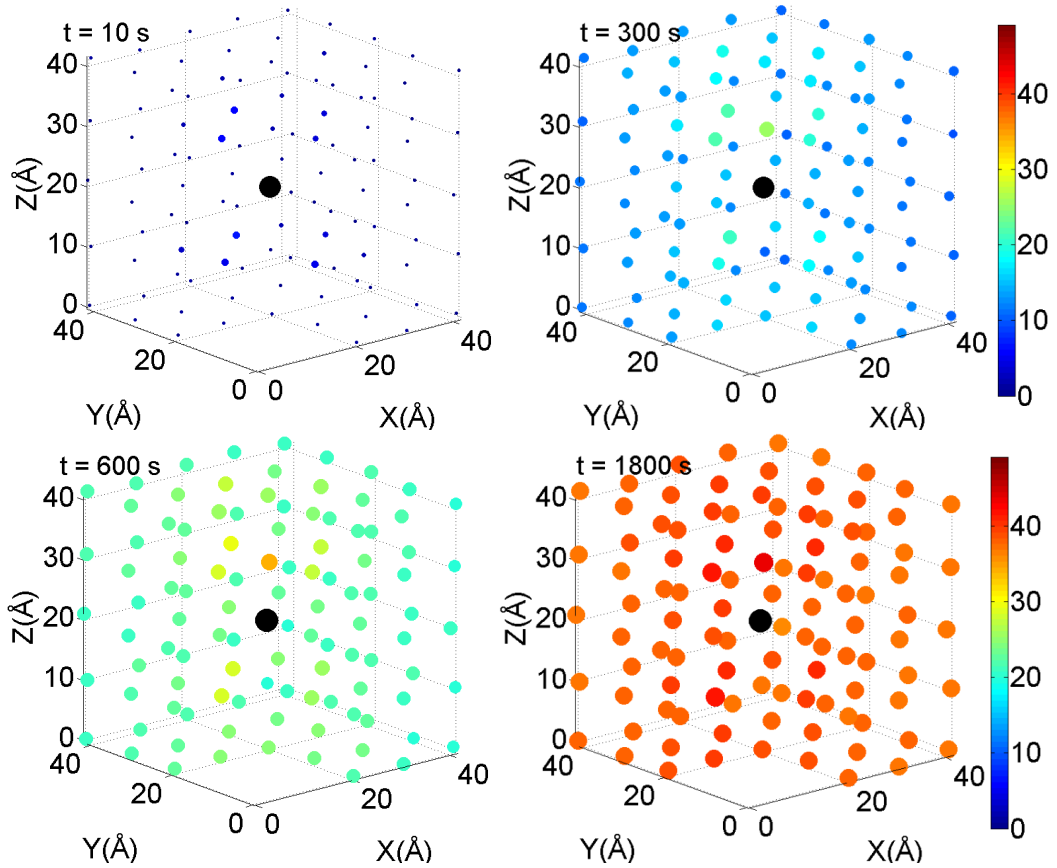


Figure 3.18: Evolution of polarization of the $125\ ^{13}\text{C}$ nuclear spins. The black dot in the centre marks the position of the electron. Colour and dot size are used to indicate the polarization level of the nuclei. Time shots at 10 s, 300 s, 600 s, and 1800 s are shown, as a comparison against figure 3.16.

3.4.3 Carbon-13 – large spin system simulations

Following the simulations shown in figs. 3.15 – 3.18, cubic lattices with 7^3 , 9^3 , and 11^3 spins were simulated. Odd numbers were always chosen for the dimension size in order to place the electron radical exactly in the centre of the lattice. For all cases, the microwave field amplitude ω_1 was ~ 100 kHz. The following relaxation parameters apply to all three cases: $T_1^{(S)} = 1$ s, $T_2^{(S)} = 10\ \mu\text{s}$, $T_2^{(I)} = 100\ \mu\text{s}$. The separation between nuclei was set to be $\sim 10\ \text{\AA}$; with 5 % randomization in position. A build-up time of 4000 s was simulated in each case. For the spin systems with 7^3 , and 9^3 ; $T_1^{(I)} = 1$ h. For the lattice with 11^3 nuclear spins, $T_1^{(I)} = 1$ h. Polarization dynamics were approximated by averaging over 100 000 trajectories, 20 000 trajectories, 10 000 trajectories for the spin systems with: 343 spins, 729 spins, and 1331 spins respectively.

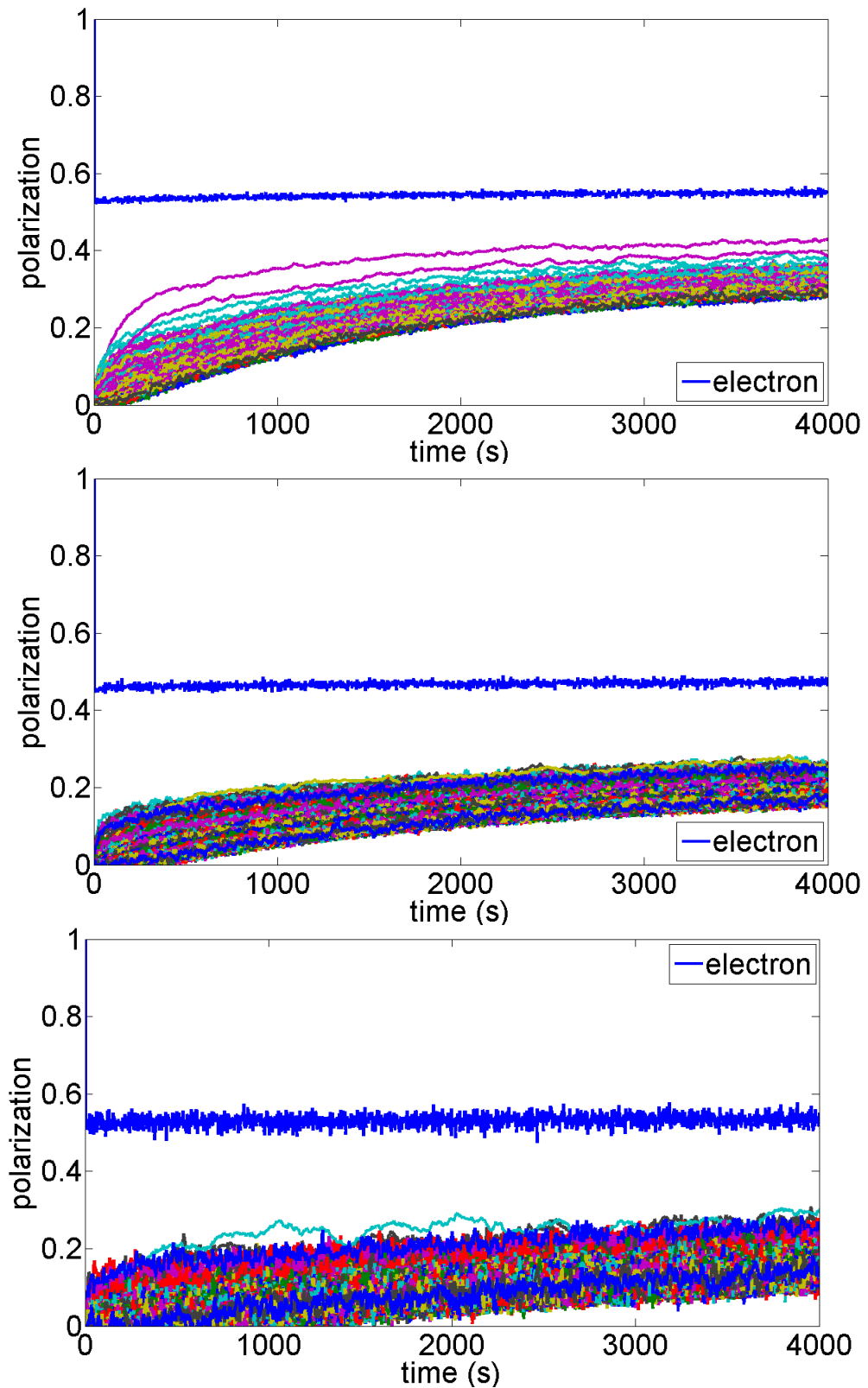


Figure 3.19: Polarization build-up curves for cubic systems of ^{13}C nuclear spins. From top to bottom are shown the systems with 343 (top), 729, and 1331 (bottom) nuclear spins respectively. The top blue line shows the electron polarization, all other lines correspond to nuclear polarization.

The lower numbers of trajectories averaged was due to the long times² needed to simulate the latter cases. The results are shown in fig. 3.19. Figure 3.19 makes it very apparent that for larger spin systems the build-up time and the time taken to reach steady-state are significantly longer. It also appears that the steady-state polarization values the nuclear spins reach are lower. Given the conclusion from section 3.3.1, it is expected the last subplot of figure 3.19 suffers from edge effects the least, and corresponds most closely to the build-up that would be expected in a realistic experimental set-up. The spread in nuclear polarization values in fig. 3.19 is much greater than that seen for a smaller system with similar parameters – figure 3.17. The limiting factor is clearly the weak interaction between ¹³C nuclei, leading to an inefficient transport of polarization. This figure illustrates the importance of using large-scale system simulations in understanding the dynamics that govern DNP. The polarization dynamics seen in figs. 3.15 – 3.19 would not be reflected in small spin systems – this applies particularly to the distribution of polarization among spins, the polarization build-up rates, and the steady-state polarization values reached. All of these properties are visibly affected by the number of spins interacting in the system, and seem especially important in cases where the inter-nuclear interactions are relatively weak due to large separations of spins, small gyromagnetic ratios, or both.

A close look at figure 3.20 shows that some nuclei further from the electron have unusually high polarization values i.e. higher than their surrounding neighbours. This phenomenon is purely down to the random noise in the system, and is affected by the number of trajectories averaged to approximate the polarization curves of each spin. It is clear then, when looking at this figure, that a larger number of trajectories would be beneficial for a more accurate solution. The amplitude of the noise is very likely to be due to the weak interactions in the system. If there are weak interactions present in the system, these are dominated by other interactions which have a higher probability of occurring as an event. Consequently the weak interactions are not sampled enough in the 10 000 trajectory course of the simulation. This under-sampling causes a significant error for nuclei further from the electron. This discovery suggests that the error magnitude approximation for the kMC method may depend on the number of spins in the system. This was investigated, and the results are described in the next section.

²for 1331 spins, the total simulation run-time was ~ 26 days, on a dual processor 20-core workstation. The processors in use were Intel Xeon E5-2690 v2 3.00 GHz.

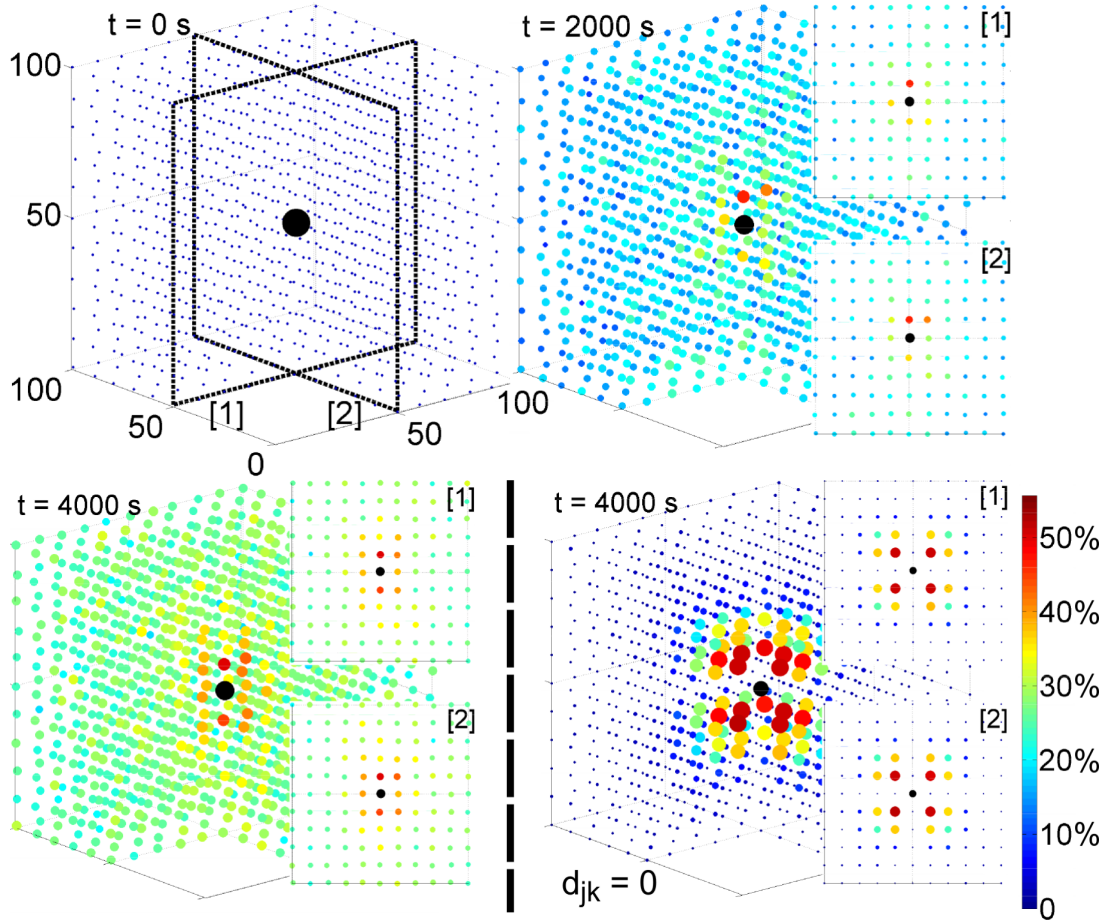


Figure 3.20: Time–shots showing polarization of nuclear spins arranged in a cubic, regular lattice ($11 \times 11 \times 11$). The black dot in the centre is the electron. Polarization build–up is fastest for nuclei that are close to the electron and at an angle of $\pi/4$ with respect to B_z . The contribution of spin–diffusion is shown in the bottom figure. The bottom–right figure shows a system with no nuclear dipolar interactions in comparison to the normal case in the bottom–left. Spins within one quarter of the cube are hidden for better visibility. The inserts show polarization of nuclei in the planes marked in the top–left part of the figure.

The bottom part of figure 3.20 shows the importance of dipolar interactions, and spin diffusion in the system. A simulation was carried out for a system without any nuclear dipole interactions. On the RHS part of this figure, nuclei close to the electron reach much greater levels of polarization, but there is no transport to the bulk. In the LHS, the same core electrons are at a lower polarization level due to transport of polarization to the bulk.

3.4.4 Fitting of polarization curves

The polarization build–up curves of individual nuclei are subject to random error. Other than increasing the number of trajectories to average over in the kMC simulations, the random error can be reduced by fitting the polarization curves

to an analytical function. This section describes the fitting approaching that has been implemented – with some success. A suitable function for modelling the build–up of polarization is

$$p(t) = p_{ss}(1 - e^{-t/\tau}),$$

where τ is the polarization build–up time constant, and p_{ss} is the polarization reached at steady–state ($t \rightarrow \infty$). Another possibility is to use a bi–exponential fit of the form

$$p(t) = p_{ss}(1 - e^{-t/\tau_1}) + p'_{ss}(1 - e^{-t/\tau_2}).$$

This fit now has two time–constants τ_1, τ_2 , and each corresponds to a different process contributing to build–up of polarization of a particular spin. Most likely, in the case of the systems studied, this would include contributions of polarization due to spin–diffusion, and direct contributions from the electron – applicable to nuclei close to the electron. Polarization curves of nuclei further away from the electron should fit a mono–exponential function quite well. A comparison to the output of figure 3.17 is shown first, in figure 3.21. The bi–exponential function was used for fitting in this case.

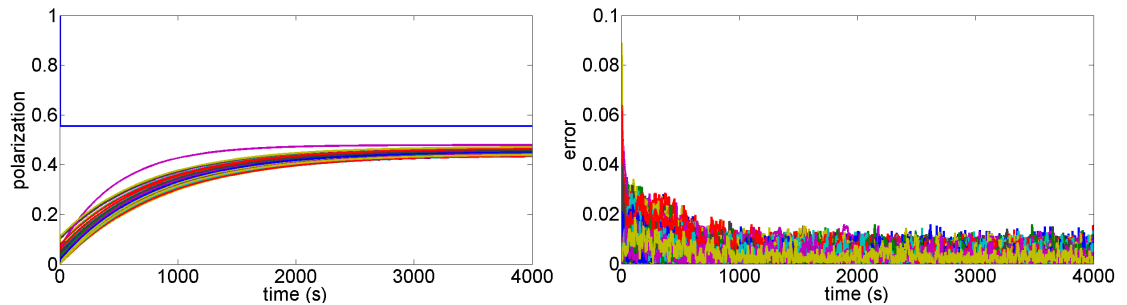


Figure 3.21: Polarization curves fitted to the output of figure 3.17 – a bi–exponential fit is used. On the right the fitting error, found by taking an absolute difference between the two figures. This was done to clearly illustrate the maximum error. Other than at the very early time of the simulation, the RHS plot shows the random error associated with kMC algorithms.

Other than at very early times of the simulation, the fit is very accurate, and the error rarely exceeds 2 %. The adjusted R^2 value rarely falls below 0.995. Next, the fits to the polarization curves in figure 3.19 are shown.

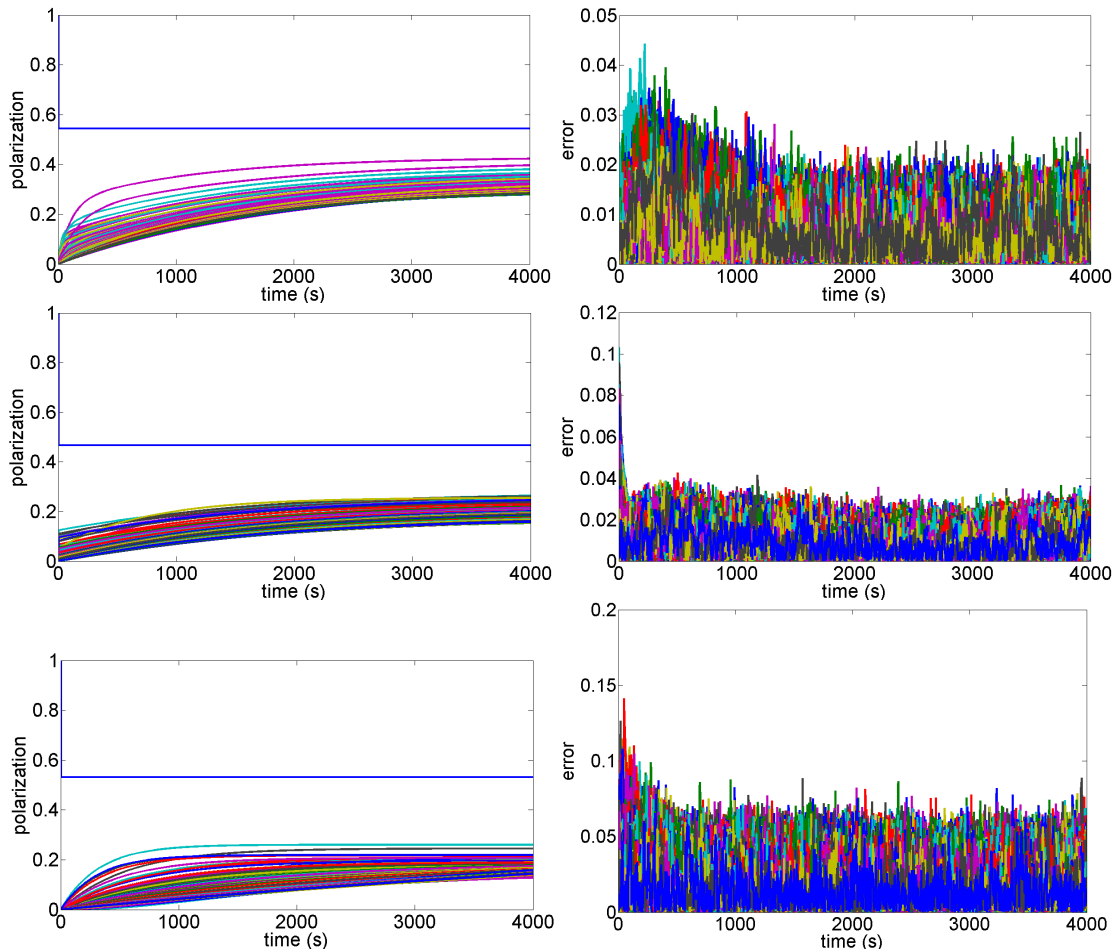


Figure 3.22: Polarization curves fitted to the output of figure 3.19, and on the right, the fitting error, found by taking an absolute difference between the figures. The absolute value is taken for clarity to illustrate maximum error. With increasing spin system the random error clearly increases, as well as the error in the very early stages of the simulation.

The top figure corresponds to the simulation of the spin system with 343 spins. The fit to the polarization curves is overall very good, with an adjusted R^2 value averaging at 0.995, and the error rarely exceeding 3 %. The middle part of figure 3.22 corresponds to the spin lattice with 729 nuclei. The fit is rather bad at the very early stages of the simulation with the error reaching 10 %. This error does, however, fall rapidly in time and stays below 4 % for the most part of the polarization build-up. The adjusted R^2 value averages at 0.97, indicating a good quality fit overall. Considering, 20 000 trajectories were used for this simulation in comparison to 100 000 in fig. 3.21, and the top part of fig. 3.22, this is a good fit. It could be used for extrapolation to determine steady-state polarization values of each spin.

The fit is much worse for the bottom part of fig. 3.22, where only 10 000 trajectories have been averaged. The adjusted R^2 value averages around 87 % for

the spins. As was the case in figures 3.21 and 3.22 (middle and top), the error is larger in the early stages of polarization build-up, and then falls at later times. Typically, the error stays at a maximum of around 6 % for some of the the spins.

Fitting to a higher number of terms

The figures showing a poorer fit, i.e. the middle and bottom parts of fig. 3.22 were then fitted to a function consisting of four exponential terms:

$$p(t) = p_{ss}(1 - e^{-t/\tau_1}) + p'_{ss}(1 - e^{-t/\tau_2}) + p''_{ss}(1 - e^{-t/\tau_3}) + p'''_{ss}(1 - e^{-t/\tau_4}).$$

Whereas it is difficult to explain the presence of four different processes, each acting over a different time-scale, the use of a quad-exponential fitting function significantly improves the fit quality to the polarization build-up curves of the spin system of 728 nuclei, as shown in fig. 3.23 below.

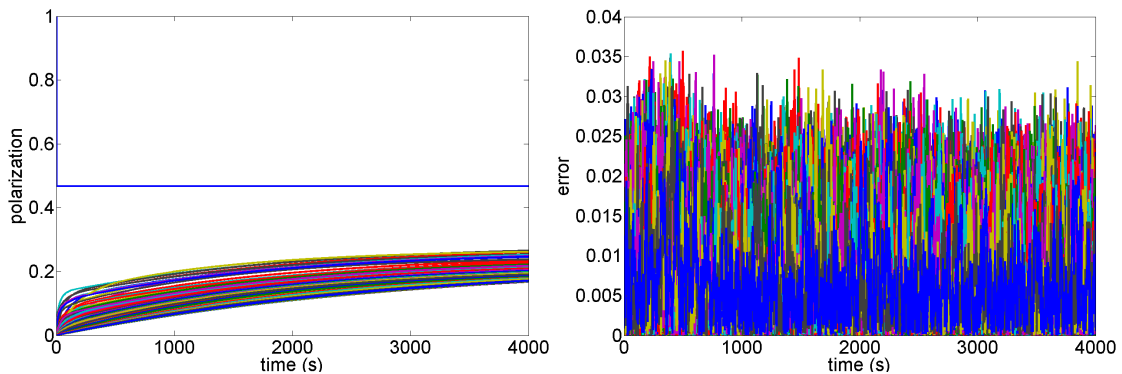


Figure 3.23: Fitting of the polarization curves from figure 3.19 (middle part), and associated error. The fit is made using a function containing four exponential terms. An absolute value of the error is taken. A much closer fit is found than in figure 3.22.

The fitting to a higher number of terms removes the error previously seen in the early times of polarization build-up. The error due to the fitting does not exceed 3.5 %, which is on the scale of random error expected from using kMC algorithms.

In the case of the 1331-spin simulation, a fit with four terms reduces the large error seen in the early stages of the simulation. The error during the rest of the polarization build-up is not affected significantly.

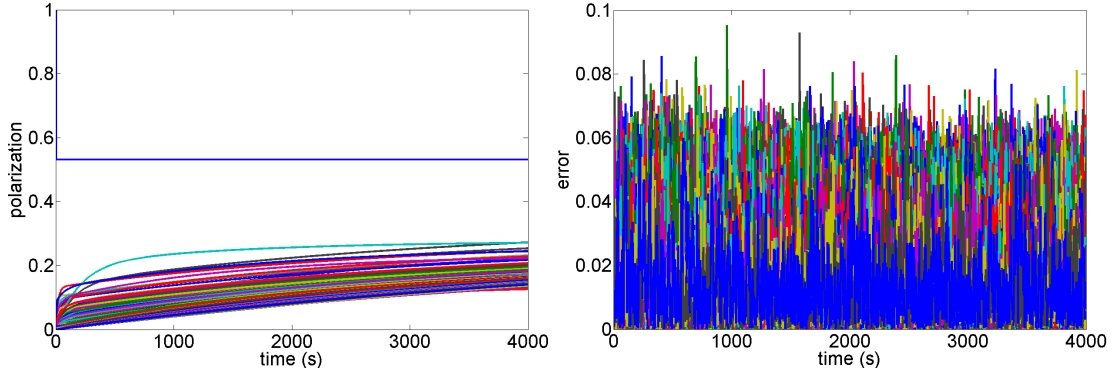


Figure 3.24: Fitting of the polarization curves from figure 3.19 (bottom part), and associated error. The fit is made to a function containing four exponential terms, and again an absolute value of the error is taken. A comparison to figure 3.22 shows the early-stage error is reduced and thus a much better fit is found, with only the random error remaining. An increase in the maximum kMC random error is seen for larger spin systems.

It can be seen that the error is in the vicinity of 6 % for some nuclei. The mean error (averaged over spins) is approximately 1.4 %. The fit can be considered quite accurate, with the deviation from the lines of best fit being due to the random error, which is inherent in all Monte Carlo algorithms. The fitting described in this section can thus be effectively used to remove the random error of simulations relying on the kMC algorithm.

A more comprehensive error analysis is described in the next section.

3.5 Monte Carlo scaling and error analysis

In this section the error associated with kMC algorithms is analysed more carefully. The scaling of the random error with respect to an increasing number of trajectories is verified. The scaling of the error with respect to an increasing number of spins in the system is then shown. In the last part of this section, the scaling of simulation duration is shown with respect to an increasing system size.

3.5.1 Scaling of error with number of spins

The analysis was mostly carried out using results from three simulations, carried out for cubic systems containing ^{13}C nuclei, with a uniform spin-spin separation – subject a to a small degree of uniform randomization in spin position. The same parameters were used in each simulation; $B_Z = 3.4$ T, $T = 1$ K, $T_1^{(S)} = 1$ s, $T_2^{(S)} = 10$ μs , $T_1^{(I)} = 1$ h, $T_2^{(I)} = 100$ μs , spin-spin separation = 10.3 \AA . The cubic lattices contained $3 \times 3 \times 3$, $5 \times 5 \times 5$, and $7 \times 7 \times 7$ spins respectively. A 20 000

trajectory–simulation was used as a baseline in each case, since in each simulated case the result of a 20 000 trajectory–simulation appeared to have converged to the true value. A comparison against a simulation with 100 000 trajectories did not show a significant difference.

The error expected for kMC simulations is given as

$$\delta_{\text{kMC}} \approx \frac{a}{\sqrt{N_{tr}}}, \quad (3.34)$$

where a is a linear constant, which turned out to be dependent on the number of spins in the system.

The error was calculated by first calculating the variance from the baseline, p_b

$$\text{var} = (p - p_b)^2,$$

then approximated as

$$\delta_{\text{kMC}} = \sqrt{\frac{1}{n_s} \sum_{i=1}^{i=n_s} \max(\text{var}_i(t))}.$$

The variance is first calculated for all spins, at all time points. A point of maximum variance, in time is then found for each spin. The variance values are then averaged over the number of spins, and a square root is taken.

For a cubic lattice of 27 ^{13}C spins, the following error values were calculated

N_{tr}	δ
10	0.9670
100	0.3045
1000	0.1005
10 000	0.0384

Fitting this data to eq. (3.34), gives a value of $a = \mathbf{3.06} \pm \mathbf{0.03}$. The error was approximated using the MATLAB curve fit tool.

For 125 spins, the following values were calculated

N_{tr}	δ
10	1.0359
100	0.3348
1000	0.1085
10 000	0.0419

giving a value of $a = \mathbf{3.29} \pm \mathbf{0.03}$.

Finally, for 343 spins, the following values were calculated

N_{tr}	δ
10	1.2105
100	0.5060
1000	0.1344
10 000	0.0538

Fitting this data to eq. (3.34), gives a value of $a = \mathbf{3.9} \pm \mathbf{0.3}$. It is also worth noting that the error approximated this way is likely to be exaggerated. Figure 3.25 illustrates the value of a coefficients as a function of the number of spins in the system, for the three cubic lattices.

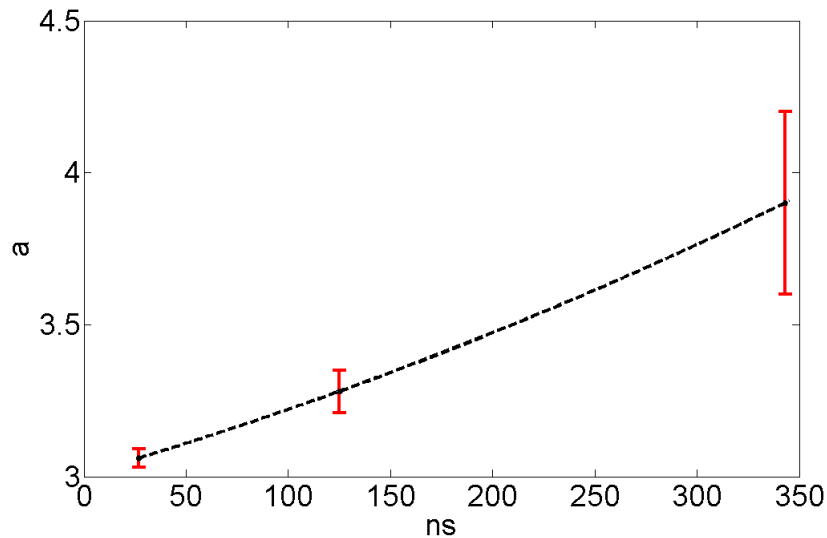


Figure 3.25: Coefficient a from eq. 3.34 shown as a function of the number of spins. It is seen here that with an increasing number of spins in the system, the error associated with the kMC algorithm will also increase. The data here fits a second order polynomial equation, indicating a quadratic scaling of the error with respect to the number of spins.

The relationship of error as a function of the number of spins fits a quadratic polynomial perfectly – with SSE = 0, and $R^2 = 1$.

A simple extrapolation of the fit for a cubic lattice with 729 spins would suggest a should be around ~ 5 . The value of a in the actual simulation results seemed to decrease instead. This was investigated. For each simulation, histograms were plotted showing the distribution of error values for different numbers of trajectories averaged. First the histograms for the 27–spin simulation were plotted for varying numbers of trajectories – 20 bins were used for histogram plotting.

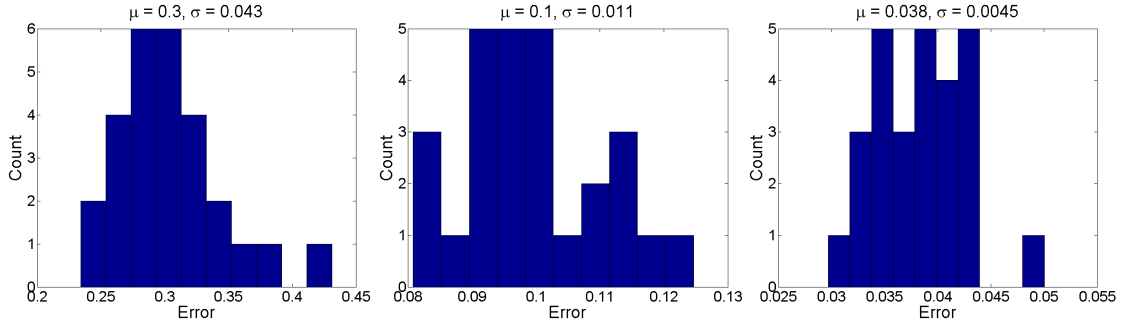


Figure 3.26: Distribution of errors for a cubic lattice of 27 spins. From left to right; 100 trajectories, 1000 trajectories, 10 000 trajectories were used respectively.

Next, the histograms for the 125 spin simulation were plotted (30 bins used for histograms):

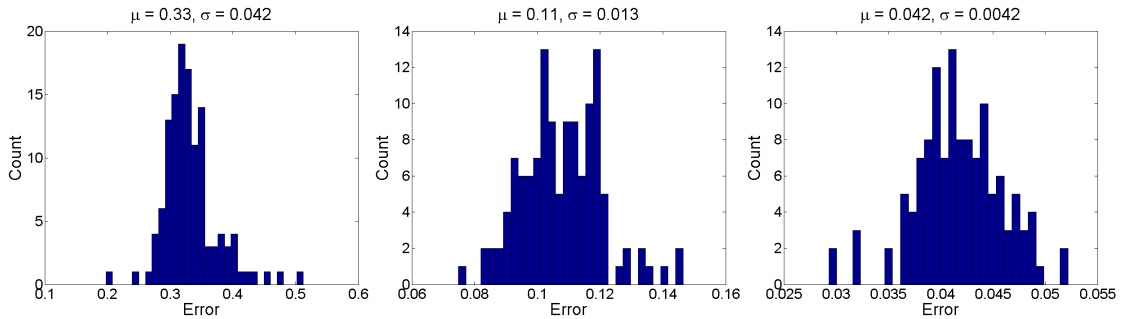


Figure 3.27: Distribution of errors for a cubic lattice of 125 spins. From left to right; 100 trajectories, 1000 trajectories, 10 000 trajectories.

Followed by the histograms for the 343 spin simulation (30 bins used for histograms).

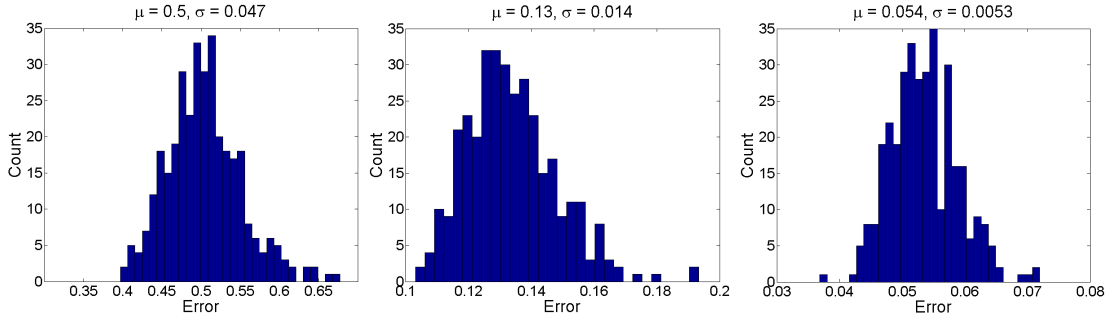


Figure 3.28: Distribution of errors for a cubic lattice of 343 spins. From left to right; 100 trajectories, 1000 trajectories, 10 000 trajectories.

For each histogram the mean error in the polarization values, as well as the standard deviation of the distribution are included above the histogram plot. Generally, in each of the cases of figs. 3.26 – 3.28, with an increasing number of trajectories averaged over, the mean error as well as the standard deviation of errors are reduced. This is expected from eq. (3.34). What is also apparent when comparing the 10 000 trajectory outputs, is that with an increasing number of spins the mean error as well as the standard deviation of errors increase; this is also in agreement with fig. 3.25.

The new insight gained from these histogram plots is that for a greater numbers of spins, and for higher numbers of trajectories, the shapes of the histograms resemble a normal distribution more closely. This implies that there is some small statistical probability for the error in the polarization value of a particular spin to be greater than would generally be expected. Finally, histograms for a 729–spin simulation are shown.

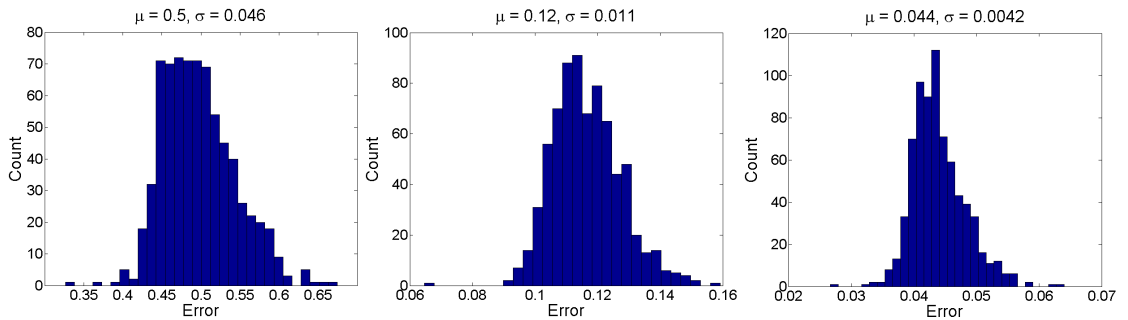


Figure 3.29: Distribution of errors for a cubic lattice of 729 spins. From left to right; 100 trajectories, 1000 trajectories, 10 000 trajectories.

As with figure 3.28, the shape of the distribution can be reasonably compared to a normal distribution, albeit a small degree of asymmetry is seen. The mean error and standard deviation fall as the number of trajectories is increased. However, a comparison between figures 3.28 and 3.29 shows that the mean error and

distribution of errors are generally lower for the 729–spin simulation. It is expected that the middle and RHS plots of fig. 3.29 are closer to the baseline than the corresponding case in fig. 3.28. Rather than the solutions for the 729 spin lattice being more accurate, they fit closer to a baseline, which in this case is further away from the correct solution. In the case of this spins system, a solution with more averaged trajectories would have to be used as a baseline.

It is expected that for simulations with even greater spin numbers, such as the simulation with 1331 spins in fig. 3.20, a number of spins will have an error greater than generally anticipated (3.5 %) for 10 000 averaged trajectories – as seen for example in fig. 3.8. This also explains the error seen in some of the polarization curves. The probability of the error being greater than this value is small (regions far from the mean of the Gaussian), hence the number of spins with a large error is expected to be small.

The nature of the random error associated with the Monte Carlo algorithms relies on choosing an optimal number of trajectories to be averaged. If the number is too small, the accuracy of the solution will be insufficient, on the other hand, too large a number of trajectories is a waste of computational time. In accordance with eq. (3.34) increasing the number of trajectories by ten–fold will increase the simulation run–time by a factor of 10, but the error will only be reduced by a factor of $\sqrt{10}$.

If one is only interested in the mean ensemble polarization of a system, then a lower number of trajectories can be used. The random nature of the errors means that ensemble averaging of the polarization of spins will lead to averaging out of the individual errors.

3.5.2 Scaling of simulation duration

As mentioned in section 2.5 – describing implementation of the kMC algorithm, use of this algorithm circumvents the exponential scaling of memory usage with respect to the number of spins. When using the kMC algorithm only the current state of the system, coupling parameters, and effective rates are kept in memory. The state of the system, as well as rates in eq. (3.23), (3.24) all scale linearly with respect to an increasing number of spins. The rate in eq. (3.25) scales quadratically with respect to an increasing number of spins. Thus, the memory scaling with respect to an increasing number of spins is described by a second–order polynomial. The CPU usage with an increasing number of spins is more tricky to determine. This was analysed by measuring the time taken for 10 000 trajectories in simulations of systems depicted in figs. 3.18 and 3.19. The result is shown below in figure 3.30.

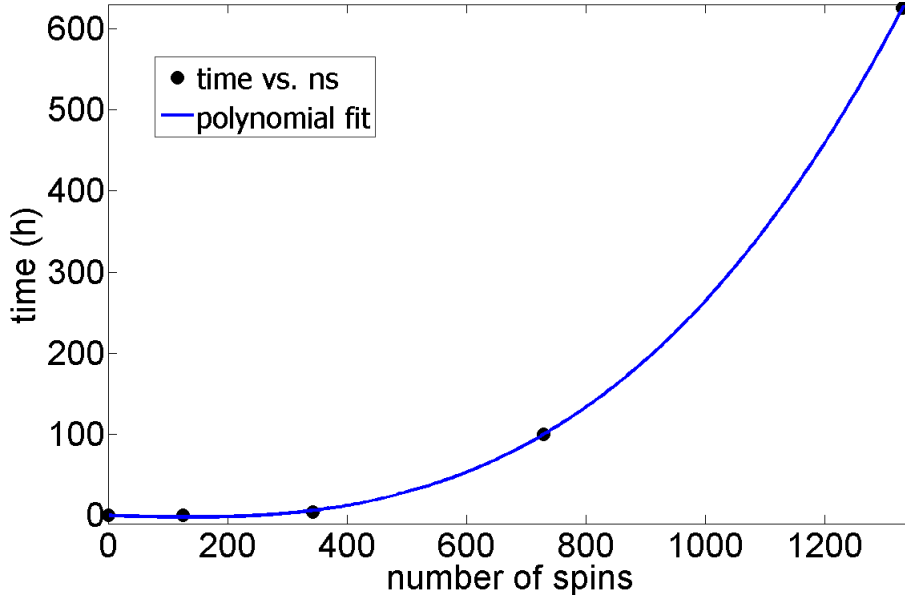


Figure 3.30: Time taken for simulations of spin systems with an increasing number of spins. The point of 0 spins would naturally take no time. The times for the cubic ^{13}C spin lattices are as follows: 125 spins – 0.5 h, 343 spins – 4.43 h, 729 spins – 100 h, 1331 spins, 626 hours. The points fit a third order polynomial. The simulation duration also depends on the dipolar coupling parameter strengths, thus varying the spacing between the spins will also vary the computational time.

The line of best fit follows a third–order polynomial equation, with no offset

$$f(n_s) = b(n_s)^3 + c(n_s)^2 + d(n_s),$$

very closely. The terms b, c, d are constant coefficients with values of $b = 2.51 \times 10^{-7}$ ($\pm 31\%$), $c = 3.85 \times 10^{-5}$ ($\pm 100\%$), $d = -2.5 \times 10^{-2}$ ($\pm 100\%$). It is clear then that for larger spin systems (eg. $13 \times 13 \times 13$), the time such a simulation would take makes it unfeasible without the use of a supercomputer cluster.

3.6 Adiabatic elimination of Solid Effect dynamics for hetero–nuclear spins

The adiabatic elimination projection of the SE–DNP dynamics onto the Zeeman subspace can be carried out for a system consisting of hetero–nuclear spins, provided these are relatively close in frequency. One such example is a system consisting of protons and fluorine nuclei. The projection is carried out in a similar manner to that described in section 3.1. An offset from the SE–DNP resonances for the nuclear spins is introduced - δ . For example, if the projection was to be carried out for protons, all the ^1H nuclei would have $\delta = 0$, and the second species

(e.g. fluorine) will have an offset of $\delta = {}_1H\omega_I - {}_{19}F\omega_I$.

For the zero-quantum subspace projection the strict mathematical requirement is that ${}_1H\delta \ll \omega_I$. Formally the condition for this projection is then

$$\omega_I \gg A_k, B_{k\pm}, d_{kk'}, \delta_k, \Gamma_z^{(S)}, \Gamma_{\pm}^{(S)}, \Gamma_{kz}^{(I)}, \Gamma_{k\pm}^{(I)}. \quad (3.35)$$

The relaxation superoperator is unaltered. The system Hamiltonian becomes

$$\begin{aligned} \hat{H}_Z &= \Delta \hat{S}_z + \sum_k \hat{I}_{kz} \\ \hat{H}_0 &= \lambda \hat{S}_z + \sum_k \delta_k \hat{I}_{kz} + \sum_k A_k \hat{S}_z \hat{I}_{kz} + \frac{\omega_1}{2} (\hat{S}_+ + \hat{S}_-) \\ &\quad + d_{kk'} \sum_{kk'} (2\hat{I}_{kz} \hat{I}_{k'z} - \frac{1}{2} \hat{I}_{k+} \hat{I}_{k'-} - \frac{1}{2} \hat{I}_{k-} \hat{I}_{k'+}) \\ \hat{H}_{\pm} &= \sum_k B_{k\pm} \hat{S}_z \hat{I}_{k\pm}. \end{aligned}$$

The projection onto the Zeeman subspace is carried out exactly as before; subject to the same conditions as described in eq. (3.15).

The effective dynamics are written in the Lindblad form, shown in eq. (2.11)

$$\begin{aligned} \mathbf{L}_Z &= \Gamma_+^{(S)} \mathbf{D}(\hat{S}_+) + \Gamma_-^{(S)} \mathbf{D}(\hat{S}_-) + \sum_k \Gamma_{k\pm}^{(I)} \left(\mathbf{D}(\hat{I}_{k+}) + \mathbf{D}(\hat{I}_{k-}) \right) \dots \\ &\quad + \sum_k \hat{\Gamma}_k^{(IS)} \mathbf{D}(\hat{Y}_k) + \sum_{k < k'} \hat{\Gamma}_{kk'}^{(II)} \mathbf{D}(\hat{X}_{kk'}). \end{aligned} \quad (3.36)$$

The constant rates

$$\Gamma_{\pm}^{(S)} = \frac{1 \mp P_0}{2} R_1^{(S)} + \frac{\omega_1^2}{2\omega_I^2} R_2^{(S)}, \quad (3.37)$$

$$\Gamma_{k\pm}^{(I)} = \frac{1}{2} \left(R_1^{(I)} + \frac{|B_k|^2}{4\omega_I^2} R_2^{(I)} \right), \quad (3.38)$$

are related to the single-spin jump operators \hat{S}_{\pm} , $\hat{I}_{k\pm}$. These are identical to the homo-nuclear case, eqs. (3.22), (3.23). The operator rates

$$\hat{\Gamma}_k^{(IS)} = \frac{\omega_1^2 |B_{k+}|^2}{8\omega_I^2 (R_2^{(S)} + R_2^{(I)})} (1 + \hat{D}_k^2)^{-1}, \quad (3.39)$$

$$\hat{\Gamma}_{kk'}^{(II)} = \frac{d_{kk'}^2}{4R_2^{(I)}} (1 + \hat{C}_{kk'}^2)^{-1}, \quad (3.40)$$

are related to the two-spin jump operators $\hat{X}_{kk'}$, and \hat{Y}_k ;

$$\hat{X}_{kk'} = \hat{I}_{k+}\hat{I}_{k'-} + \hat{I}_{k-}\hat{I}_{k'+},$$

$$\hat{Y}_k = \hat{I}_{k+}\hat{S}_- + \hat{I}_{k-}\hat{S}_+.$$

The operator-values coefficients $D_k, C_{kk'}$ appearing in the above equations are:

$$\hat{D}_k = \frac{(\lambda - \delta_k)\hat{1} + \sum_{s \neq k} A_s \hat{I}_{sz} + \frac{1}{8\omega_I} (4\omega_1^2 - |B_{k+}|^2) \hat{1}}{R_2^{(S)} + R_2^{(I)}}, \quad (3.41)$$

$$\hat{C}_{kk'} = \frac{(\delta_k - \delta_{k'})\hat{1} + (A_k - A_{k'})\hat{S}_z + \frac{1}{8\omega_I} (|B_{k+}|^2 - |B_{k'+}|^2)\hat{1}}{2R_2^{(I)}}. \quad (3.42)$$

It is worth noting that for the operator-valued coefficient $\hat{C}_{kk'}$, eq. (3.42), the last part, $\frac{1}{8\omega_I} (|B_{k+}|^2 - |B_{k'+}|^2) \hat{1}$ is as previously negligible in comparison to the first two terms

$$\hat{C}_{kk'}^2 \approx \frac{\left[(\delta_k - \delta_{k'}) + (A_k - A_{k'})\hat{S}_z \right]^2}{(2R_1^{(I)})^2}.$$

3.6.1 Analysis of hetero-nuclear SE-DNP effective dynamics

Electron-nuclear interaction rate

The addition of an offset parameter δ_k in the state-dependent coefficient \hat{D}_k , in eq. (3.41), means this coefficient will typically be large for large δ_k . For a magnetic field of 3.4 T, and at the proton resonance; the δ_k for fluorine nuclei is ~ 8.5 MHz. This value would likely dominate the terms in eq. (3.41) and cause the rate $\Gamma_k^{(IS)}$ to be quenched for fluorine nuclei.

Nuclear-nuclear interaction rate

The form of the rate $\Gamma_{kk'}^{(II)}$ for a heteronuclear system depends on the difference between the offsets δ_k in the coefficient $\hat{C}_{kk'}$ – eq. (3.42) – of any two nuclei. This implies that the effective internuclear interaction is efficient between spins of the same species, but becomes inefficient between spins of different nuclei.

On the other hand, there exists a possibility for the offset difference $\delta_k - \delta_{k'}$ to cancel with $A_k - A_{k'}$, or at least collectively reduce the magnitude of $\hat{C}_{kk'}$. Thus cross-polarization under DNP for hetero-nuclear systems appears to be feasible, even for the simplest of DNP mechanisms; SE-DNP.

3.6.2 Error testing

For error testing, a small spin system was chosen consisting of 1 electron 2 hydrogen nuclei, and 2 fluorine-19 nuclei. The electron was placed at the origin, the ^1H spins were placed at coordinates $(a/\sqrt{2}, 0, a/\sqrt{2})$, $(a/\sqrt{2} + a, 0, a/\sqrt{2})$, and the two fluorine nuclei at coordinates $(a/\sqrt{3}, a/\sqrt{3}, a/\sqrt{3})$, $(a/\sqrt{2}, -a, a/\sqrt{2})$. The constant a was set to 3.6 Å, and a 2 % randomization was applied in the positions of all spins. The distance of 3.6 Å is the average proton spin-spin separation that can be expected in a sample of mixed toluene and fluorobenzene in a volume ratio of 75:25 (toluene:fluorobenzene).

Three simulations were then carried out; one at the ZQ transition frequency of ^1H , one at the ZQ transition frequency of ^{19}F , and one where the system is irradiated in the middle; between the resonances of the two nuclear spins. The magnetic field B_Z was set to 3.4 T, the microwave field amplitude was 50 kHz, and the relaxation parameters were $R_1^{(S)} = 1$ s, $R_2^{(S)} = 10$ μs , $R_1^{(I)} = 10$ min., $R_2^{(I)} = 0.5$ ms. Build-up was simulated for 1000 s. The error was calculated by taking a difference between the full quantum mechanical simulation, and the Zeeman projected one in eq. (3.36).

Proton resonance

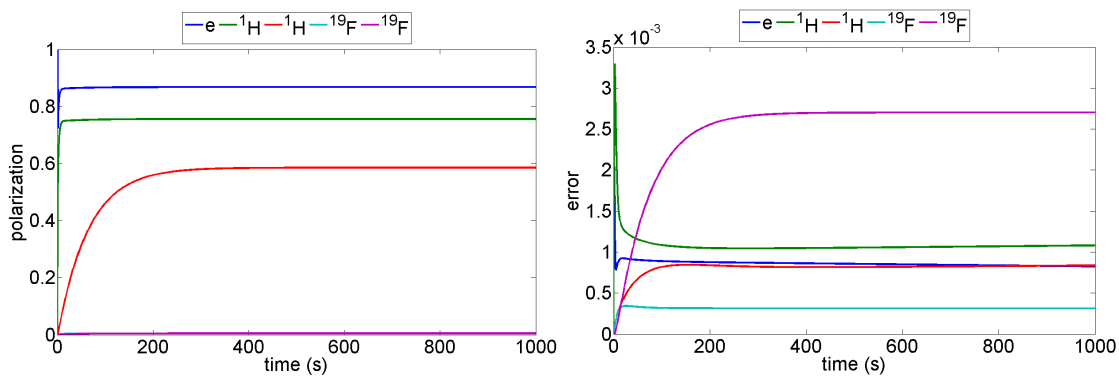


Figure 3.31: Polarization curves (LHS) and error plot (RHS) for a system irradiated at the proton ZQ transition frequency. The legend shows which polarization curve corresponds to which nucleus in the system. There is a build-up of polarization for protons, for fluorine nuclei on the other hand the build-up is non-existent. The error is shown to be negligible for all spins.

The error in figure 3.31 is seen to be less than 1 % for all spins, during the whole duration of the simulation.

Fluorine resonance

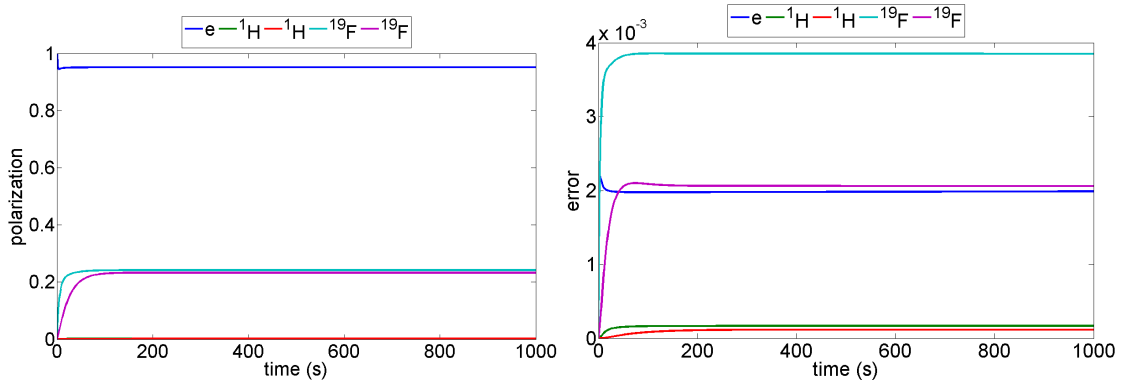


Figure 3.32: Polarization curves (LHS) and error plot (RHS) for a system irradiated at the fluorine ZQ transition frequency. The legend shows which polarization curve corresponds to which nucleus in the system. There is a decent build-up of polarization for fluorine nuclear spins, and for hydrogen nuclei the build-up is non-existent. The error is negligible for all spins.

The error in figure 3.32 is seen to be less than 1 % for all spins, during the whole duration of the simulation.

Midpoint between the two resonances

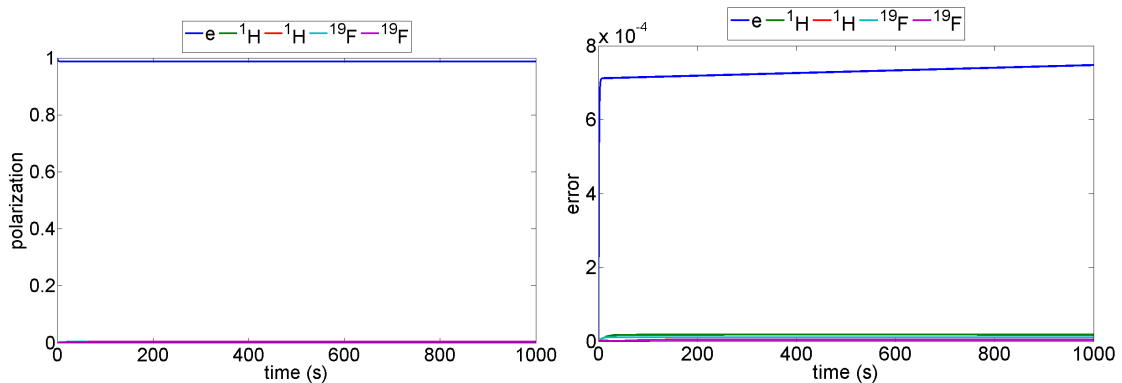


Figure 3.33: Polarization curves (LHS) and error plot (RHS) for a system irradiated at the midpoint between the proton and fluorine ZQ transition frequencies. There is a negligible build-up of polarization for both the protons and fluorine nuclei in this case, and it is no surprise then that the error is close to zero for nuclear spins and negligible for the electron spin.

The error in figure 3.33 is seen to be less than 0.1 % for all spins, during the whole duration of the simulation. The largest error is seen for the electron spin.

The nuclei in this system have no polarization build-up during the course of the simulation, in which case the error should be 0.

3.6.3 Large heteronuclear spin system simulations

Following the establishment of the accuracy of the effective dynamics for a heteronuclear spin system containing protons and fluorine nuclei, a large spin-system simulation was carried out. A cubic lattice of 125 spins was simulated with a nearest spin spacing of 3.6 Å, and a 2 % randomization in position. The microwave field amplitude was set to 50 kHz, and the relaxation parameters were: $R_1^{(S)} = 0.5$ s, $R_2^{(S)} = 10$ μs, $R_1^{(I)} = 500$ s, $R_2^{(I)} = 0.5$ ms. The magnetic field strength was again 3.4 T. Out of the 124 nuclear spins, 9 (~ 1 in 14) spins were randomly set to be fluorine nuclei. The first simulation was carried out at the proton SE-DNP resonance condition – the result is seen in figure 3.34. In 300 s of build-up the mean proton polarization is seen to reach about 23 %. A slight build-up of polarization can be seen for the fluorine – ~ 1.5 %. The mechanism solely responsible for the polarization of fluorine nuclei is polarization diffusion from the protons. This was verified by setting the rates $\Gamma_{kk'}^{(II)}$ for all fluorine nuclei to 0, in which case no build-up at all was seen.

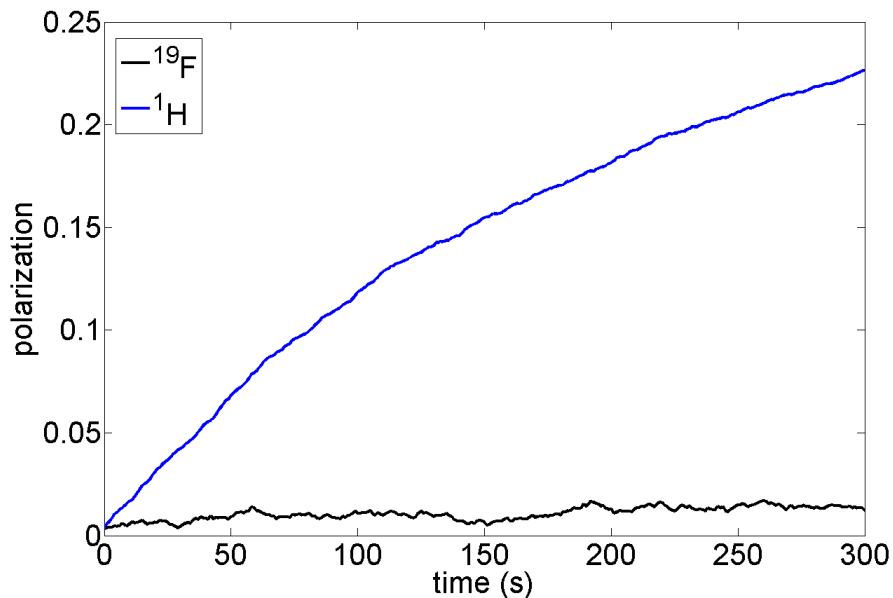


Figure 3.34: Build-up of polarization for a heteronuclear system of 115 ^1H spins, 9 ^{19}F spins, and one central electron. The blue curve shows polarization averaged over the 115 ^1H spins, the black curve is the polarization level averaged over 9 ^{19}F . The system is irradiated at the proton SE-DNP resonance. After 300 s ^1H nuclei reach 23 % of polarization, The ^{19}F nuclei show a small degree of polarization – approximately 1.5 % is reached.

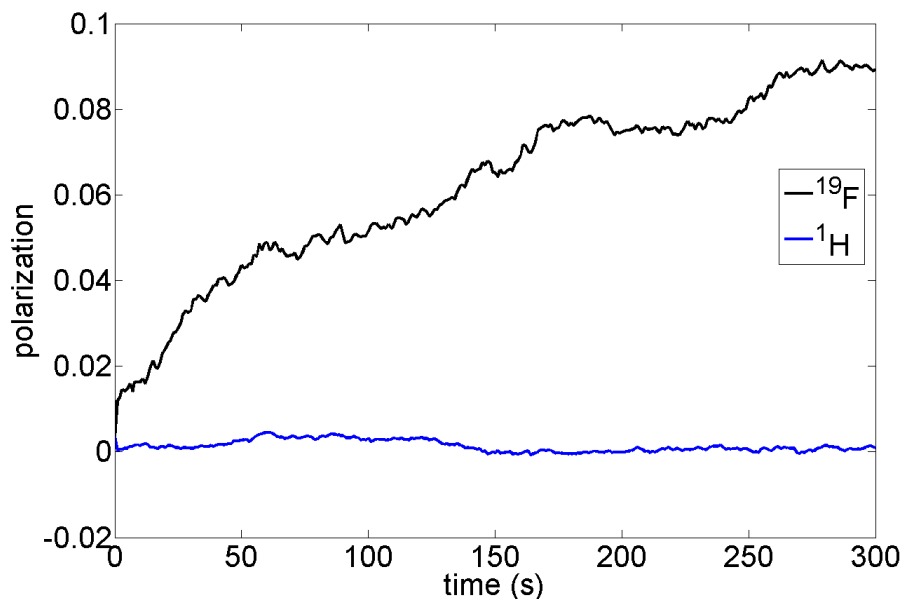


Figure 3.35: Build-up of polarization for a heteronuclear system of 115 ^1H spins, 9 ^{19}F spins, and one central electron. The blue curve shows polarization averaged over the 115 ^1H spins, the black curve is the polarization level averaged over 9 ^{19}F . The system is irradiated at the fluorine SE-DNP resonance. The ^{19}F nuclei reach 9 % polarization after 300 s. The level of polarization of ^1H is negligible.

Figure 3.35 shows the case where the fluorine SE-DNP resonance is irradiated. Approximately a 9 % polarization level is reached by the fluorine nuclei after 300 s of build-up. The fluorine curve is noisy as only 1000 trajectories were averaged (due to a long simulation run-time) and the polarization curves are only averaged over the 9 spins present. This is probably also the reason why the level of polarization reached by fluorine in figure 3.35 is much lower than the level of polarization of protons in figure 3.34 – the fluorine nuclei are a lot more sparse, and are placed at random positions. Some of the nuclei in the system will likely be quite far away from one another; leading to weak effective dipolar interactions $-\Gamma_{kk'}^{(II)}$. This is also likely the explanation for no proton polarization in figure 3.35. It is expected that for systems containing more electrons and exhibiting CE-DNP or TM-DNP, this situation would change and polarization build-up of both spin species could be seen.

3.7 Linear rate equation approach for simulating SE-DNP

The mathematical derivation described in this section was carried out by A. Karabanov.

The SE–DNP dynamics enclosed in the zero–quantum subspace of the density operator – master equation in eq. (3.13) are projected onto the subspace of spin polarizations, in a manner similar to that seen in section 3.1.3.

The subspace of Zeeman orders covers terms

$$\mathcal{L}_Z = \text{span}\{\hat{1}, \hat{S}_z, \hat{I}_{kz}, \hat{S}_z \hat{I}_{kz}, \hat{I}_{kz} \hat{I}_{k'z}, \dots\},$$

and \mathcal{L}_C then covers the complimentary subspace. The subspace containing the polarization dynamics is a $(n+1)$ –dimensional single–spin Zeeman–order subspace – in other words it is a subspace within the Zeeman subspace concerning single–spin coherence orders.

$$\mathcal{L}_P = \text{span}\left\{\hat{S}_z, \hat{I}_{kz}, \hat{I}_{k'z}, \dots\right\} \subset \mathcal{L}_Z.$$

3.7.1 Projection onto the polarization subspace

The relevant projection superoperator onto the polarization subspace is \mathcal{P}_P , and \mathcal{Q}_P is the complimentary projection superoperator. The action of the superoperator \mathbf{L}_{00} is enclosed in \mathcal{L}_P , and acts on operators \hat{S}_z, \hat{I}_{kz} as follows

$$\mathbf{L}_{00} \hat{S}_z = -\frac{R_1^{(S)}}{2} \hat{S}_z, \quad \mathbf{L}_{00} \hat{I}_{kz} = -\frac{R_1^{(I)}}{2} \hat{I}_{kz},$$

the action of $\mathcal{P}_P \mathbf{M}_2 \mathcal{P}_P$ leads to second order correction terms resulting in

$$\Gamma' = -\frac{R_2^{(S)} \omega_1^2}{2\omega_I^2} \hat{S}_z - \frac{R_2^{(I)} |B_{k\pm}|^2}{8\omega_I^2},$$

analogous to the relaxation term seen originally for the Zeeman–projected dynamics, shown in eq. (3.14) and (3.18). In the same manner as with the Zeeman–subspace projection, the dynamics of \hat{H}'_1 and \hat{H}_0 were projected onto the polarization subspace \mathcal{L}_P

$$\begin{aligned} \mathbf{L}_{10} &= -i \mathcal{Q}_P \left(\hat{H}'_0 + \hat{H}'_1 \right) \mathcal{P}_P, \\ \mathbf{L}_{01} &= -i \mathcal{P}_P \left(\hat{H}'_0 + \hat{H}'_1 \right) \mathcal{Q}_P, \\ \mathbf{L}_{11} &= -i \left(\hat{H}_{0,0} + \hat{H}_{1,0} \right) + \Gamma'. \end{aligned}$$

Acting on terms in the polarization subspace these give

$$\begin{aligned}\mathbf{L}_{10}\hat{S}_z &= \frac{i\omega_1}{4\omega_I} \sum_k \left(B_{k+}\hat{I}_{k+}\hat{S}_- - B_{k-}\hat{I}_{k-}\hat{S}_+ \right), \\ \mathbf{L}_{10}\hat{I}_{kz} &= \frac{i\omega_1}{4\omega_I} \sum_k \left(B_{k-}\hat{I}_{k-}\hat{S}_+ - B_{k+}\hat{I}_{k+}\hat{S}_- \right) + \frac{i}{2} \sum_{k<k'} d_{kk'} \left(\hat{I}_{k+}\hat{I}_{k'-} - \hat{I}_{k-}\hat{I}_{k'+} \right),\end{aligned}$$

thus it is accurate to calculate the action of \mathbf{L}_{11} on the operators $\hat{I}_{k\pm}\hat{S}_{\mp}$, $\hat{I}_{k\pm}\hat{I}_{k'\mp}$,

$$\begin{aligned}\mathbf{L}_{11} \left(\hat{I}_{k\pm}\hat{S}_{\mp} \right) &= \hat{P}_{k\pm}\hat{I}_{k\pm}\hat{S}_{\mp}, & \hat{P}_{k\pm} &= \pm i\lambda \pm i \sum_{s \neq k} A_s \hat{I}_{sz} - (R_2^{(I)} + R_2^{(S)}), \\ \mathbf{L}_{11} \left(\hat{I}_{k\pm}\hat{I}_{k'\mp} \right) &= \hat{P}_{kk'}\hat{I}_{k\pm}\hat{I}_{k'\mp}, & \hat{P}_{kk'} &= i(A_k - A_{k'})\hat{S}_z - 2R_2^{(I)}.\end{aligned}$$

Immediately a resemblance to the form of the effective rates for the Zeeman-subspace master equation – eq. (3.20) can be seen. In addition, the superoperator \mathbf{L}_{11} acts trivially on $\hat{P}_{k\pm}$ and $\hat{P}_{kk'}$, hence

$$\begin{aligned}(\mathbf{L}_{11})^m \left(\hat{I}_{k\pm}\hat{S}_{\mp} \right) &= (\hat{P}_{k\pm})^m \hat{I}_{k\pm}\hat{S}_{\mp}, \\ (\mathbf{L}_{11})^m \left(\hat{I}_{k\pm}\hat{I}_{k'\mp} \right) &= (\hat{P}_{kk'})^m \hat{I}_{k\pm}\hat{I}_{k'\mp},\end{aligned}$$

for $m = 1, 2, 3, \dots$, and as follows from linear algebra properties

$$\begin{aligned}e^{\mathbf{L}_{11}} \left(\hat{I}_{k\pm}\hat{S}_{\mp} \right) &= e^{\hat{P}_{k\pm}t} \hat{I}_{k\pm}\hat{S}_{\mp}, \\ e^{\mathbf{L}_{11}} \left(\hat{I}_{k\pm}\hat{I}_{k'\mp} \right) &= e^{\hat{P}_{kk'}t} \hat{I}_{k\pm}\hat{I}_{k'\mp}.\end{aligned}$$

The operators \hat{I}_{kz} commute with each other. From the properties of these operators, and that of \hat{S}_z , we get that

$$\begin{aligned}e^{\hat{P}_{k\pm}t} &= e^{(\pm i\lambda - R_2^{(I)} - R_2^{(S)})t} \prod_{k' \neq k} \left[\cos \left(\frac{A_{k'}t}{2} \right) \pm 2i \sin \left(\frac{A_{k'}t}{2} \right) \hat{I}_{k'z} \right], \\ e^{\hat{P}_{kk'}t} &= e^{(-R_2^{(I)} - R_2^{(S)})t} \left[\cos \left(\frac{(A_k - A_{k'})t}{2} \right) \pm 2i \sin \left(\frac{(A_k - A_{k'})t}{2} \right) \hat{S}_z \right].\end{aligned}$$

The result of the action of \mathbf{L}_{01} must belong to \mathcal{L}_Z hence;

$$\mathbf{L}_{01}e^{\mathbf{L}_{11}t}\hat{I}_{k\pm}\hat{S}_{\mp} = e^{\hat{P}_{k\pm}t}\mathbf{L}_{01}\hat{I}_{k\pm}\hat{S}_{\mp}, \quad \mathbf{L}_{01}e^{\mathbf{L}_{11}t}\hat{I}_{k\pm}\hat{I}_{k'\mp} = e^{\hat{P}_{kk'}t}\mathbf{L}_{01}\hat{I}_{k\pm}\hat{I}_{k'\mp}.$$

Using the formulas

$$\mathbf{L}_{01}\hat{I}_{k\pm}\hat{S}_{\mp} = \pm \frac{i\omega_1 B_{k\pm}}{4\omega_I} \left(\hat{S}_z - \hat{I}_{kz} \right), \quad \mathbf{L}_{01}\hat{I}_{k\pm}\hat{I}_{k'\mp} = \pm \frac{id_{kk'}}{2} \left(\hat{I}_{kz} - \hat{I}_{k'z} \right),$$

one obtains

$$\mathbf{L}_{01}e^{\mathbf{L}_{11}t}\mathbf{L}_{10}\hat{S}_z = -\frac{\omega_1^2}{16\omega_I^2}\sum_k|B_k|^2\left(e^{\hat{P}_{k+t}}+e^{\hat{P}_{k-t}}\right)\left(\hat{S}_z-\hat{I}_{kz}\right) \quad (3.43)$$

$$\begin{aligned} \mathbf{L}_{01}e^{\mathbf{L}_{11}t}\mathbf{L}_{10}\hat{I}_{kz} &= \frac{\omega_1^2}{16\omega_I^2}|B_k|^2\left(e^{\hat{P}_{k+t}}+e^{\hat{P}_{k-t}}\right)\left(\hat{S}_z-\hat{I}_{kz}\right) \\ &- \frac{1}{4}\sum_{k'\neq k}\left(e^{\hat{P}_{k'k}t}+e^{\hat{P}_{kk'}t}\right)\left(\hat{I}_{kz}-\hat{I}_{k'z}\right) \end{aligned} \quad (3.44)$$

Furthermore,

$$e^{\hat{P}_{k'k}t}+e^{\hat{P}_{kk'}t}=2e^{-2R_2^{(I)}t}\cos\left(\frac{(A_k-A_{k'})t}{2}\right),$$

hence the terms resulting in dipolar flip-flops, i.e. terms proportional to $d_{kk'}^2$ are enclosed in \mathcal{L}_P . The terms proportional to $|B_k|^2$ are not. Higher Zeeman orders are generated due to the presence of the factors

$$\left(e^{\hat{P}_{k+t}}+e^{\hat{P}_{k-t}}\right).$$

This is avoided if the negative eigenvalues of \mathbf{L}_{11} are large due to decoherence rates; $R_2^{(I)}$ and $R_2^{(S)}$. Under the assumptions required for the projection onto the Zeeman subspace, eq. (3.15) this issue will be avoided, and the dynamics will remain within the polarization subspace \mathcal{L}_P of the Zeeman subspace \mathcal{L}_Z ;

$$\dot{\hat{\rho}}=\mathbf{L}_P\hat{\rho}.$$

The result is a set of linear rates describing polarization build-up for nuclear spins, and the depolarization of the electron spin. The dynamics for each spin are described analytically as follows

$$\mathbf{L}_P\hat{S}_z=-\frac{R_1^{(S)}}{2}\hat{S}_z-\frac{R_2^{(S)}\omega_1^2}{2\omega_I^2}\hat{S}_z-\sum_k\frac{\omega_1^2|B_k|^2}{8\omega_I^2}D_k\left(\hat{S}_z-\hat{I}_{kz}\right), \quad (3.45)$$

$$\begin{aligned} \mathbf{L}_P\hat{I}_{kz} &= -\frac{R_1^{(I)}}{2}\hat{I}_{kz}-\frac{R_2^{(I)}|B_k|^2}{8\omega_I^2}\hat{I}_{kz}+\frac{\omega_1^2|B_k|^2}{8\omega_I^2}D_k\left(\hat{S}_z-\hat{I}_{kz}\right) \\ &- \frac{1}{2}\sum_{kk'}d_{kk'}^2C_{kk'}\left(\hat{I}_{kz}-\hat{I}_{k'z}\right). \end{aligned} \quad (3.46)$$

The coefficients $C_{kk'}$ and D_k are given as

$$C_{kk'}=\int_0^\infty e^{-2R_2^{(I)}t}\cos\left(\frac{(A_k-A_{k'})t}{2}\right)dt, \quad (3.47)$$

$$D_k=\int_0^\infty e^{-(R_2^{(I)}+R_2^{(S)})t}\cos(\lambda t)\prod_{k'\neq k}\cos\left(\frac{A_{k'}t}{2}\right)dt. \quad (3.48)$$

For the coefficient C_{kk} , nuclei with a significant coupling strength $d_{kk'}$ will not have a difference in secular coupling strengths A_k that is larger than $2R_2^{(I)}$, hence this coefficient will rapidly tend to a steady-state value. The effective rate of inter-nuclear dipolar flip flops will have the same form as $\Gamma_{kk'}^{(II)}$ in eq. (3.23), which has previously been shown to be state-independent.

The story is slightly different for the coefficient D_k . This coefficient is to compensate for the state-dependence of rate $\Gamma_k^{(IS)}$ in eq. (3.22), manifested in the state-dependent coefficient, shown in eq. (3.26). There exist systems where A_k can exceed $R_2^{(I)} + R_2^{(S)}$.

The product part of eq. (3.48)

$$\prod_{k' \neq k} \cos\left(\frac{A_{k'} t}{2}\right), \quad (3.49)$$

causes D_k to be time-dependent due to the oscillatory behaviour of the product of cosine functions. Using properties of trigonometric functions it can be shown that the fastest-oscillating part of the product in eq. (3.49) will oscillate with a frequency of $\sim \sum_{k' \neq k} \frac{|A_{k'}|}{2}$. Thus as an upper-bound on the oscillation frequencies of the product in eq. (3.49) is it reasonable to take $\sum_k \frac{A_k}{2}$, and if this term is much greater than $R_2^{(I)} + R_2^{(S)}$, then the coefficient D_k will have a significant time-dependence in the early stages of the simulation, and its decay to a steady-state will not be quick enough.

The conditions in eq. (3.15) have to be met to make the projection onto the polarization subspace accurate, but in addition, the error will likely be large if

$$\frac{\sum_k |A_k|}{2(R_2^{(I)} + R_2^{(S)})} \gg 1. \quad (3.50)$$

This has to be avoided in a system of choice.

3.7.2 Error testing against Zeeman projection

With the accuracy of the Zeeman projection established in section 3.2, the linear rate equation approach was compared to the simulations implemented with the use of kMC algorithms; for the purpose of an error analysis. A cubic system of 125 spins was chosen, with the electron spin in the centre. The separation between the nearest-neighbour spins a was varied between 6 Å and 10 Å. Simulations were carried out for both ^{13}C and ^1H nuclear spins. A 5 % randomization in the position of spins was applied. The magnetic field B_Z was set to 3.4 T, the relaxation parameters were $R_1^{(S)} = 1$ s, $R_2^{(S)} = 10$ μs , $R_1^{(I)} = 1$ h, $R_2^{(I)} = 0.1$ ms.

The microwave field amplitude ω_1 was set to 50 kHz unless otherwise stated. For a spacing of 10 Å the error is negligible – figure 3.36 A, and the fraction on the LHS of eq. (3.50) is equal to ~ 8.8 . A inter-spin spacing of 9 Å results in a slightly larger but still acceptable error, seen in figure 3.36 B. The fraction in eq. (3.50) is 12.4 in this case. For spacings of 8 Å and 7 Å respectively the error increases each time – figure 3.36 C & D. The sum of secular coupling strengths, divided by the decoherence rates are in this case 17.6 and 26.1 respectively, thus more than an order of magnitude greater than 1, and the regime outlined by the inequality in eq. (3.50) is reached.

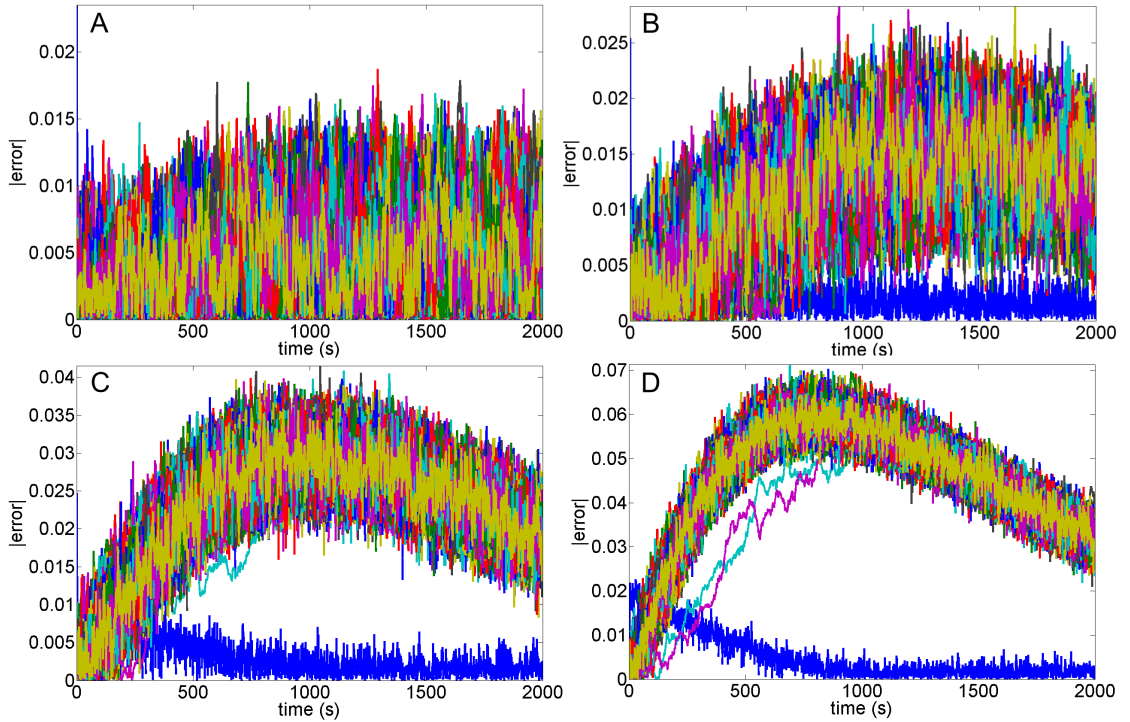


Figure 3.36: Errors analysis was carried out for a cube of 124 ^{13}C spins surrounding an electron spin. The inter-spin spacing, a is varied. Part A) – $a = 10$ Å, Part B) – $a = 9$ Å, Part C) – $a = 8$ Å, Part D) – $a = 7$ Å. The error for each individual spin is shown. The blue line corresponds to the electron, which typically has the lowest error. The error is seen to increase for stronger spin-spin coupling.

As expected, the error gets worse when the separation is reduced to 6 Å, in figure 3.37 A, where the ratio of the sum of secular coupling strengths to the decoherence rates is 41.9. This is then compared to a simulation of the same system with hydrogen nuclei, where $\omega_1 = 160$ kHz. Protons have a much higher gyromagnetic ratio than ^{13}C nuclei, hence the error in figure 3.37 B is even higher. The ratio of the sum of the secular coupling strengths to $R_2^{(S)} + R_2^{(I)}$ is 165.2 in this case.

Figure 3.37 C shows the simulation outcome for ^{13}C nuclei with $a = 6 \text{ \AA}$, but the decoherence rate $R_2^{(S)}$ increased to $10^6 \text{ (s}^{-1}\text{)}$, as a comparison to figure 3.37 A. The error falls below 2 % for all spins other than the electron, as the ratio from eq. (3.50) is now reduced from 41.9 to 4.6.

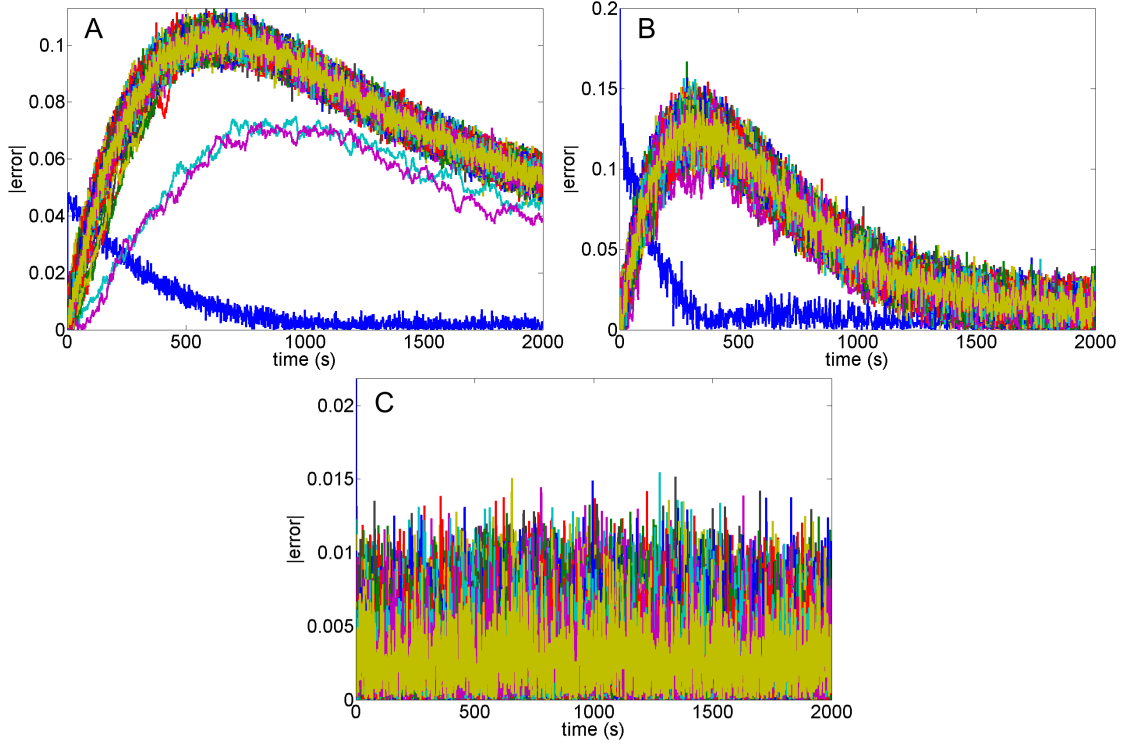


Figure 3.37: Error analysis carried out for cubic lattices of 124 ^1H or ^{13}C nuclear spins surrounding a central electron. The error for each spin is shown; the blue line corresponds to the the electron spin and the rest corresponds to the nuclear spins. Part A) simulation for ^{13}C where $a = 6 \text{ \AA}$, Part B) simulation for ^1H where $a = 6 \text{ \AA}$ $\omega_1 = 160 \text{ kHz}$. For ^1H nuclei, which have stronger coupling, the error is significantly larger. Part C) simulation for ^{13}C with $a = 6 \text{ \AA}$ and the rate of electronic decoherence increased ($T_2^{(S)} = 1 \mu\text{s}$). For shorter decoherence times the error is reduced as the condition in eq. (3.50) is met again.

3.7.3 Very large spin–system simulations

Having established the parameter region where the formalism of the linear effective rates is accurate; a simulation was carried out on a spin system containing 9261 spins. The model system is a cube of dimension $21 \times 21 \times 21$. A spacing of 10 \AA was set between nearest spins, with a 5 % randomization in position of all spins. The magnetic field B_z was set to 3.4 T, the microwave field amplitude $\omega_1 = 250 \text{ kHz}$, and the following relaxation parameters were chosen: $T_1^{(S)} = 20 \text{ ms}$, $T_2^{(S)} = 10 \mu\text{s}$, $T_1^{(I)} = 1 \text{ h}$, $T_2^{(S)} = 0.1 \text{ ms}$.

The simulation took 450 seconds, thus illustrating the power and efficiency of the linear rate formalism, in eqs. (3.45), (3.46).

Nuclear polarization is normalised to the electronic thermal polarization. The system in figure 3.38 is seen to reach an average level of 11 % of polarization after 1 hour of microwave irradiation. The time–shot parts of figure 3.38 show the diffusive transport of polarization to the bulk, and the high level of polarization reached by the core. A spin system of this size is expected to suffer a lot less from a reflective boundary, and in addition, periodic boundary conditions to imitate a sample with a number of spins on the order of Avogadro’s constant could most likely be considered.

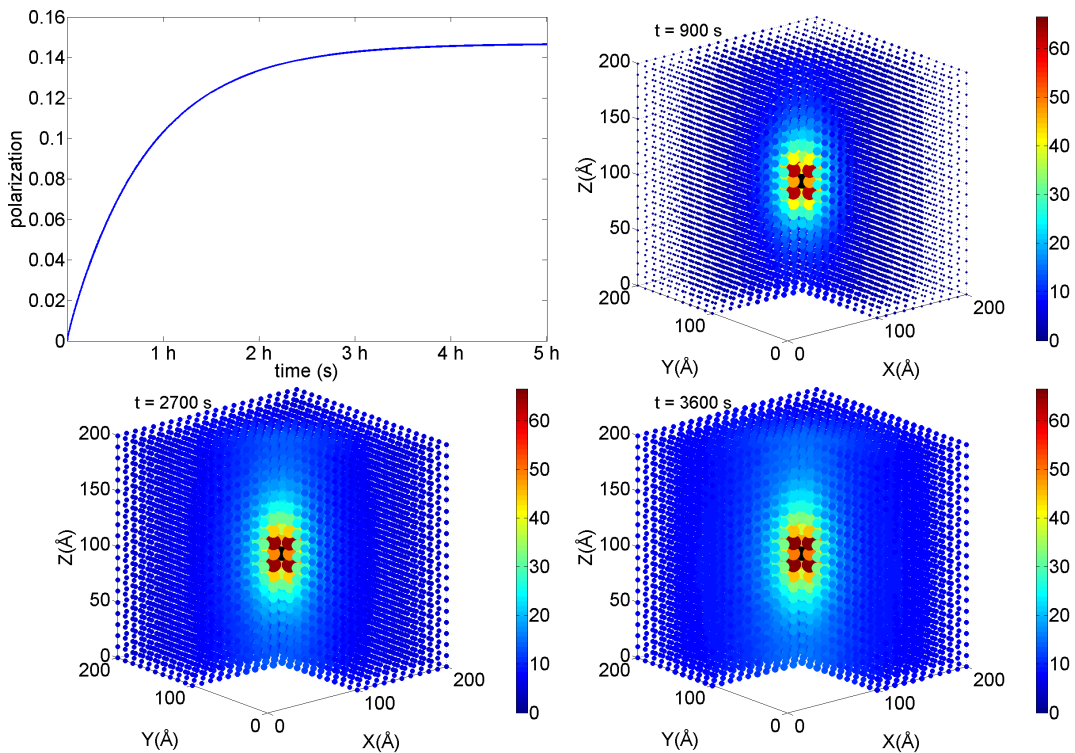


Figure 3.38: Large spin system simulation showing the build–up of polarization for a cubic lattice of 9260 ^{13}C nuclei surrounding a central electron spin. The first part shows the mean nuclear polarization as a function of time. The system is seen to reach steady–state after a time of 5 h, with a polarization level of $\sim 15\%$. Time shots illustrating polarization of individual spins, at 900 s, 1800 s, and 3600 s are also shown. These clearly demonstrate diffusive transport from core nuclei to the bulk.

Chapter 4

Radical design

In this chapter the dependence of nuclear polarization during DNP build-up on the geometrical configuration of the system is studied. The study is carried out using a model central spin system, consisting of an electron surrounded by many nuclei and exhibiting SE-DNP. It's made feasible by the use of the kinetic Monte Carlo method, which allows one to significantly increase the number of spins considered in the model system. Our findings demonstrate that increasing the minimal distance between nuclei and electrons leads to a rise of the nuclear bulk polarization. These observations therefore have implications for the design of radicals that can lead to improved bulk nuclear spin polarization.

This chapter largely follows the work published by us in [59].

4.1 Introduction

The formalism described in section 3.1 opens up the possibility of analysing polarization transport in systems of up to a few thousand coupled spins. The focus of this chapter is on the insight that such simulations can provide in understanding the dynamics of large, uncoupled spin ensembles during DNP. In particular, it is shown how the bulk polarization level crucially depends on the immediate molecular environment of the unpaired electron spin.

The effective rates can be used to distinguish between bulk and core nuclei. Comparison between the two rates ($\Gamma_k^{(IS)}$ and $\Gamma_{kk'}^{(II)}$) for each nucleus determines whether it belongs to the core or to the bulk. In the case that the effective hyperfine rate, eq. (3.24), is greater than the effective nuclear dipolar rate ($\Gamma_k^{(IS)} > \Gamma_{kk'}^{(II)}$), eq. (3.25), the interaction with the electron will be dominating, indicating a core nucleus. The opposite would be true ($\Gamma_k^{(IS)} < \Gamma_{kk'}^{(II)}$) for a bulk nucleus.

4.2 Model spin system

Large spin-system simulations were carried out in order to gain further insight into the optimal conditions for SE-DNP, for achieving the highest nuclear spin polarization and the fastest build-up rate of nuclear polarization. This kind of analysis provides important information for a tailored radical design in which radical compounds would be synthesized with desired properties. In this context, that would correspond to an optimal separation between the electron radical, and the nuclear spins closest to it, as well as on the geometry of the molecule containing the electron radical. In order to analyse the spin dynamics during SE-DNP, a system of one central electron surrounded by ^{13}C nuclear spins arranged in a $5 \times 5 \times 5$ cubic grid was chosen – thus consisting of a total of 124 nuclear spins. The nearest neighbour separation between nuclear spins was set to 4 \AA , and a 1% uniform randomization in position of each spin was applied. Such an average distance between nuclei corresponds to 26 M of a ^{13}C labelled molecule or in other words – it is slightly shorter than the average distance between ^{13}C nuclei in free pyruvic acid (4.8 \AA) [60]. The magnetic field was set to be 3.4 T, the temperature was set 1K, and a microwave field amplitude of 20 kHz was chosen to approximate realistic experimental conditions (without the use of a gyrotron microwave source or a resonance cavity). The relaxation parameters were set to be: $T_1^{(S)} = 0.5 \text{ s}$, $T_2^{(S)} = 10 \text{ }\mu\text{s}$, $T_1^{(I)} = 1 \text{ h}$, $T_2^{(I)} = 0.5 \text{ ms}$. The polarization dynamics during one hour of microwave irradiation were simulated using our effective rate formalism and a kMC algorithm.

In order to better understand the dependence on polarization build-up on the coupling parameters, these were plotted as a function of position in space. Figs. 4.1 and 4.2 show the spatial dependence of the secular and pseudo-secular hyperfine interaction strengths A_k and B_k for the 124 ^{13}C nuclei. The rate in eq. (3.24) shows a squared dependence on $B_{k\pm}$ i.e. the pseudo-secular hyperfine coupling strength. It is therefore reasonable to expect that nuclei with the highest $B_{k\pm}$ values will have the highest effective rate $\Gamma_k^{(IS)}$ values.

On the other hand, nuclei with the highest A_k will be shifted in frequency the most, due to the interaction with the electron. The rate in eq. (3.25) will be lower between nuclei that have a large difference in their secular coupling strengths. The efficiency of SE-DNP for the nuclear ensemble, seen in terms of build-up duration and steady-state polarization level, will rely on a delicate interplay between these two processes.

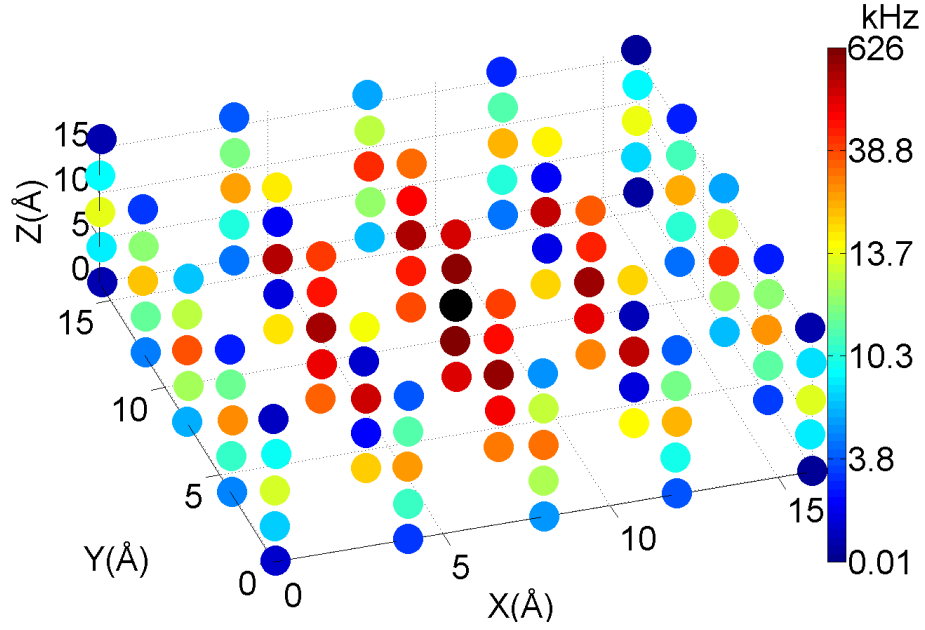


Figure 4.1: Strength of the secular hyperfine interaction A_k between the central electron (black) and the 124 ^{13}C nuclei. The colour scale indicates the coupling strength in kHz. Note the non-uniform scale of the colour bar.

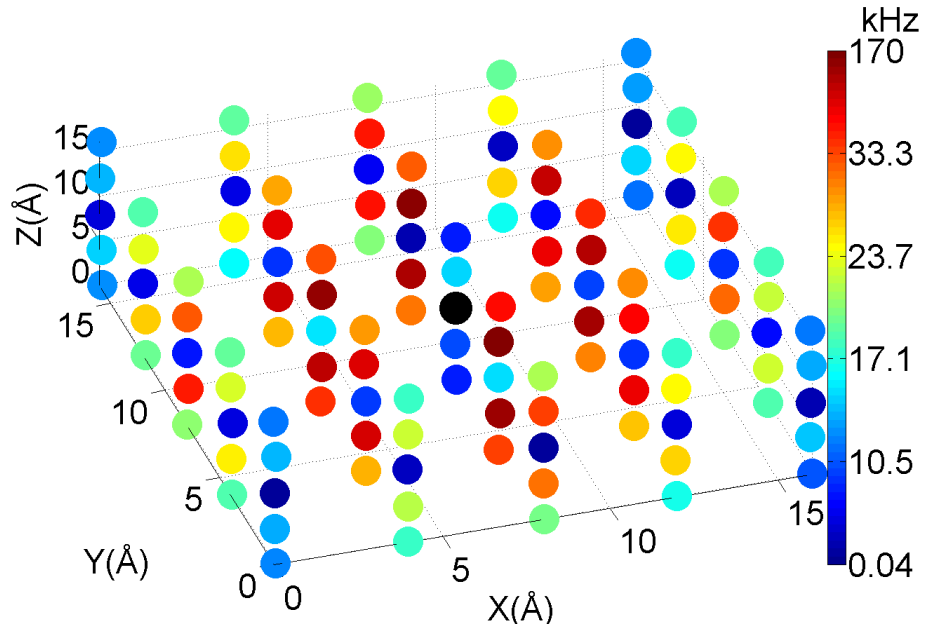


Figure 4.2: Strength of the pseudo-secular hyperfine interaction B_k between the central electron (black) and the 124 ^{13}C nuclei. The colour scale indicates the coupling strength in kHz. Note the non-uniform scale of the colour bar.

The magnitudes of the secular part and the pseudo-secular part of the hyperfine interaction (previously shown in 2.2) are given by

$$A_k = \left| \frac{\mu_0 \gamma_S \gamma_I \hbar}{4\pi r_k^3} (1 - 3 \cos^2 \theta_k) \right|,$$

$$B_{k\pm} = \left| -\frac{\mu_0}{4\pi} \frac{3}{2} \frac{\gamma_S \gamma_I \hbar}{r_k^3} \sin \theta_k \cos \theta_k \right|.$$

The strength of the secular part of the hyperfine interaction A_k is strongest for nuclei at positions with angle $\theta = 0$ or $\theta = \pi$. Conversely, the strength of the pseudo-secular part of the hyperfine interaction is zero at these positions and strongest at positions characterized by $\theta = \pi/4$ or $\theta = 3\pi/4$. The interaction strength is also affected by the separation between spins. It scales as r_k^{-3} , hence it decays relatively quickly with an increasing distance between nuclei and the electron.

By calculating the effective rates, eq. (3.24), for the flip-flop jumps between the electron S and the nucleus I_k and comparing them to the effective rates with which the nucleus I_k can carry out flip-flop jumps with adjacent nuclei, eq. (3.25), it is possible to determine the nuclei that will predominately interact with the electron. The nuclei where $\Gamma_k^{(IS)} > \Gamma_{kk'}^{(II)}$ are from hereon referred to as core nuclei. All the remaining nuclei belong to the bulk (Fig. 4.3).

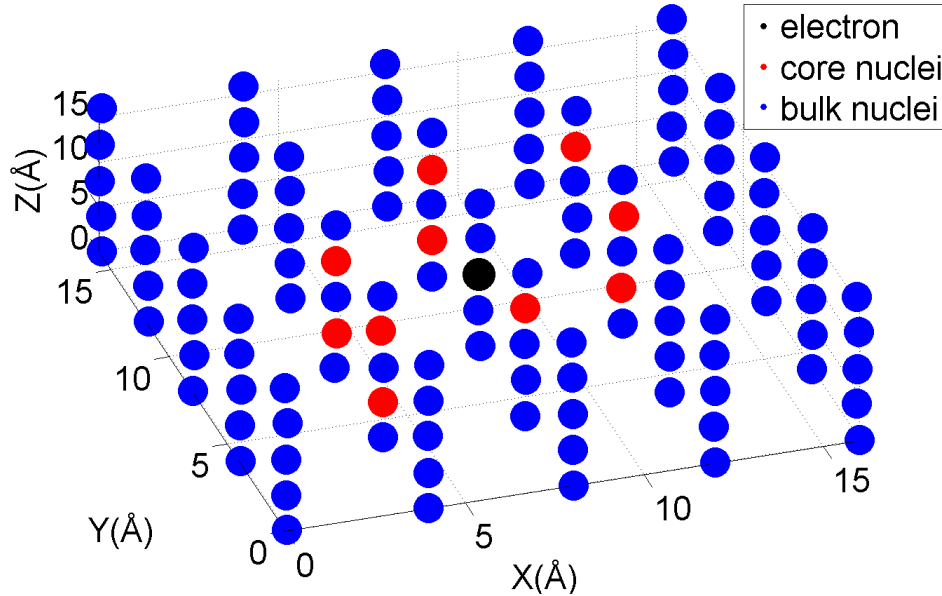


Figure 4.3: The nuclei in the ensemble around the central electron belong either to the core or bulk. Core nuclei are marked with red colour. These are the nuclei for which the effective rate of flip-flop jumps between electron and nucleus, eq. (3.24), is higher than any of the effective inter-nuclear flip-flop rates, eq. (3.25). Bulk nuclei are marked with blue colour, and for these nuclei the effective rate in eq. (3.24) is smaller than effective rate in eq. (3.25). Note that because of the 1% uniform randomization of the position the configuration is not fully symmetric.

As is expected, the nuclei with the strongest pseudo-secular coupling $B_{k\pm}$ belong to the group of core nuclei, this is clearly seen in the comparison between figures 4.2 and 4.3. Generally the number of core nuclei is relatively small, since the spacing between spins is very small, thus leading to very strong nuclear dipole-dipole interactions. The 1 % randomization in position leads to a significant, visible asymmetry in the system.

The build-up of nuclear polarization, at various points in time, for the described system is seen in fig. 4.4. This figure is analogous to the output of a previous simulation carried out on a large spin ensemble, shown in figure 3.20. As expected, the highest polarization increase is for nuclei with the greatest pseudo-secular interaction strength, $B_{k\pm}$. The polarization is then distributed by spin diffusion to regions where $B_{k\pm}$ is small. In this system, the effective dipolar interactions distribute polarization to the bulk well, as it can be seen that the polarization levels remain relatively equal between nuclear spins, throughout time (figure 4.4 A) – C).

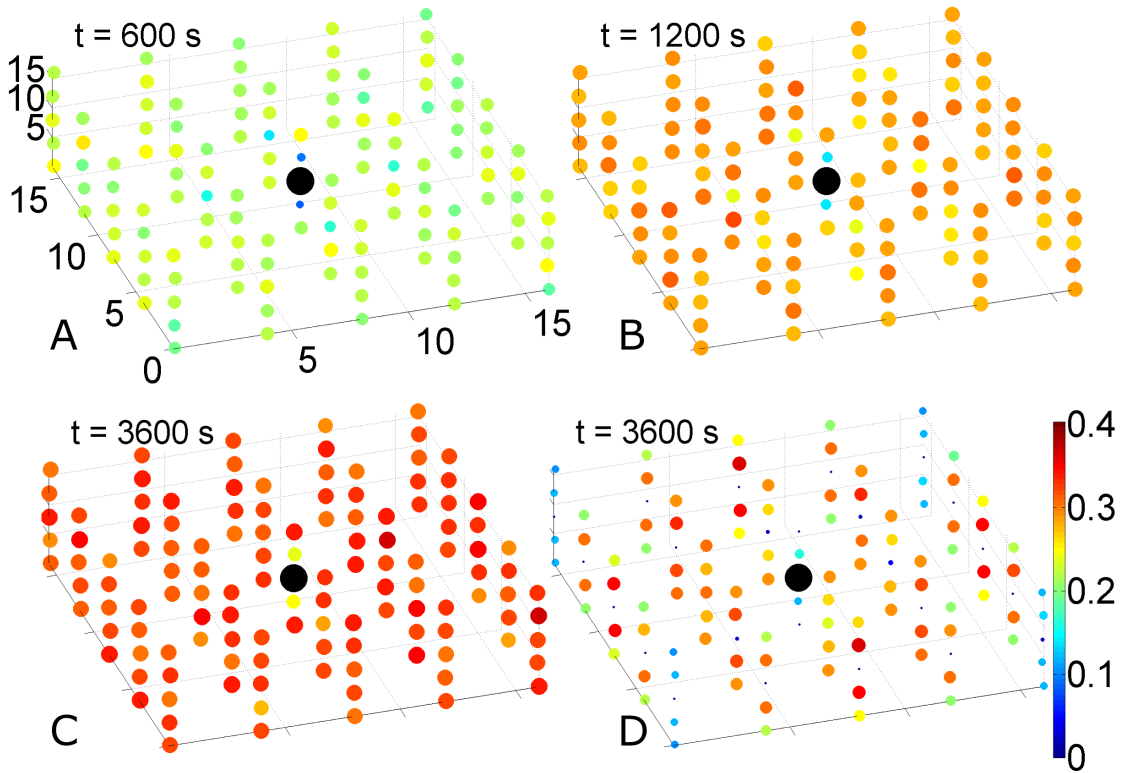


Figure 4.4: A) – C) The distribution of the nuclear spin polarization at times of 600 s, 1200 s, and 3600 s during the buildup. A careful comparison with fig. 4.2 reveals that the nuclei with the strongest $B_{k\pm}$ values have in the initial phase the highest polarization. D) Nuclear steady-state polarization if the nuclear dipolar interaction coefficients $d_{kk'}$ are set to zero. Here, the nuclear spins are only polarized via the pseudo-secular part of the hyperfine interaction and no spin diffusion takes place.

Several nuclei closest to the electron clearly show a lower polarization level than the remainder. These are the nuclei with the highest secular coupling strength (see figure 4.1). Part B) of figure 4.4 shows that the two nuclei directly above and below the electron have a much lower polarization level. These two nuclei have the highest A_k values. The remaining 4 closest nuclei in plane with the electron have a secular value 2 times smaller than that, yet they still show a lower degree of polarization in comparison to the bulk. It thus becomes clear that nuclei with low $B_{k\pm}$ values and high A_k are a hindrance to the mechanism of polarization transport to the bulk. The contributions of the effective dipolar rate $\Gamma_{kk'}^{(II)}$ can be seen in figure 4.4 D). There the effective rate for internuclear flip-flops was set to zero during the course of the simulation. In such case only nuclei in regions with $B_{k\pm} \neq 0$ receive significant electronic polarization during SE DNP.

4.3 Influence of nuclei close to the electron

The result in figure 4.4 shows that some nuclei might be reducing the efficiency with which polarization is transferred to the bulk. In our study we analysed the effect on the average bulk polarization under changes to the configuration of this model system. The six nuclei which are the nearest neighbours to the electron spin, hence ones with the highest secular hyperfine interaction strength (A_k) were first removed in succession. The simulation was re-run starting from the initial thermal equilibrium state, upon removal of each nucleus from the system, in order to study the effect this had on the bulk polarization. The polarization level at steady-state, so after 1 hour of build-up was calculated each time. Following removal of the nearest neighbouring nuclei, further nuclei adjacent to the electron were subsequently removed. A study as such would of course not be possible without many-body system simulations, made possible by the effective Zeeman-subspace master equation and efficient kMC algorithms. The idea here is to understand the role of the secular and pseudo-secular terms of the hyperfine interaction of nuclei in immediate proximity of the electron on spin-diffusion and hence on the bulk nuclear polarization. Fig. 4.5 shows the order and the position of the removed nuclei. The dependence of the mean nuclear spin polarization per nucleus at steady state, on the number of removed nuclei is summarized in fig. 4.6. The nuclei are removed in the sequence depicted in figure 4.5. The first data point (black) represents the average nuclear spin polarization in the system without removal of any nuclei. The next six data points (dark blue) indicate the average nuclear spin polarization if the six nuclei with the strongest secular hyperfine interaction strength A_k are successively removed.

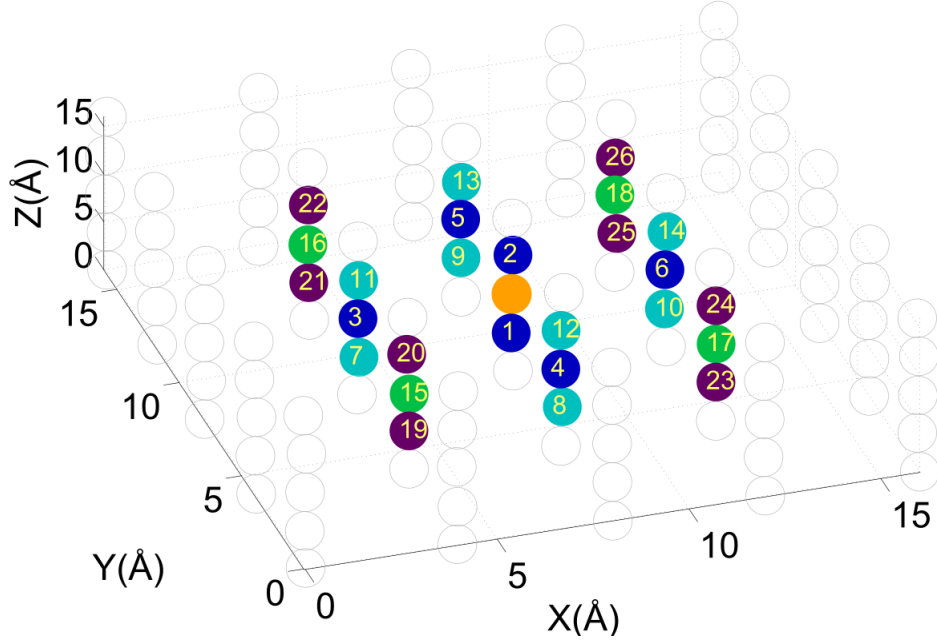


Figure 4.5: The order by which the layer of nuclei adjacent to the electron was removed in successive simulations is indicated by the numbers. Different colour coding was used to group nuclei in four groups: The first six nuclei with strong secular hyperfine interaction and weak pseudo-secular hyperfine interaction (dark blue), eight nuclei with relatively strong pseudo-secular interaction (light blue). Four nuclei with strong secular hyperfine interaction and weak pseudo-secular hyperfine interaction strength (green) and eight nuclei with relatively strong pseudo-secular interaction strength (purple). The orange dot is the central electron.

These are the nuclei just directly above and below the electron and next to the electron in the xy -plane in which the electron is located (see fig. 4.5 for the position of the removed nuclei and fig. 4.1 for the A_k values). The pseudo-secular interaction strengths B_k of these six nuclei are all very low (see fig. 4.2) and none of the removed nuclei belong to the core nuclei group, characterized by high effective transfer rates of polarization from the electron (fig. 4.3). The average nuclear spin polarization improves by a factor of more than 2 due to the removal of these nuclei, and the largest improvement is seen when the last of the nuclei from this subgroup (index 6) is removed from the system. Eq. 3.27 is clearly reduced in magnitude between nuclei with a large difference in A_k values, thus removal of these six nuclei means removal of nuclei that are inefficient at diffusing polarization into the bulk.

The next eight nuclei that were successively removed (light blue colour) have the highest pseudo-secular interaction strength B_k but also relatively high A_k values (see see figs. 4.5, 4.1 and 4.2). Removal of these nuclei decreases the average nuclear spin polarization by about 15 %, as would be expected since seven of these eight nuclei belong to the core nuclei group and thus had some of the highest $\Gamma_k^{(IS)}$

rates.

The next four nuclei (green) that were removed have high A_k values and low B_k values. The removal of these nuclei increases again the average nuclear spin polarization of the ensemble. Following the removal of these nuclei, the nuclei left remaining in the system have more efficient polarization exchange rates, $\Gamma_{kk'}^{(II)}$. Compared to the polarization level of the last bright blue data point (spin index number 14) the increase is more than 30 %.

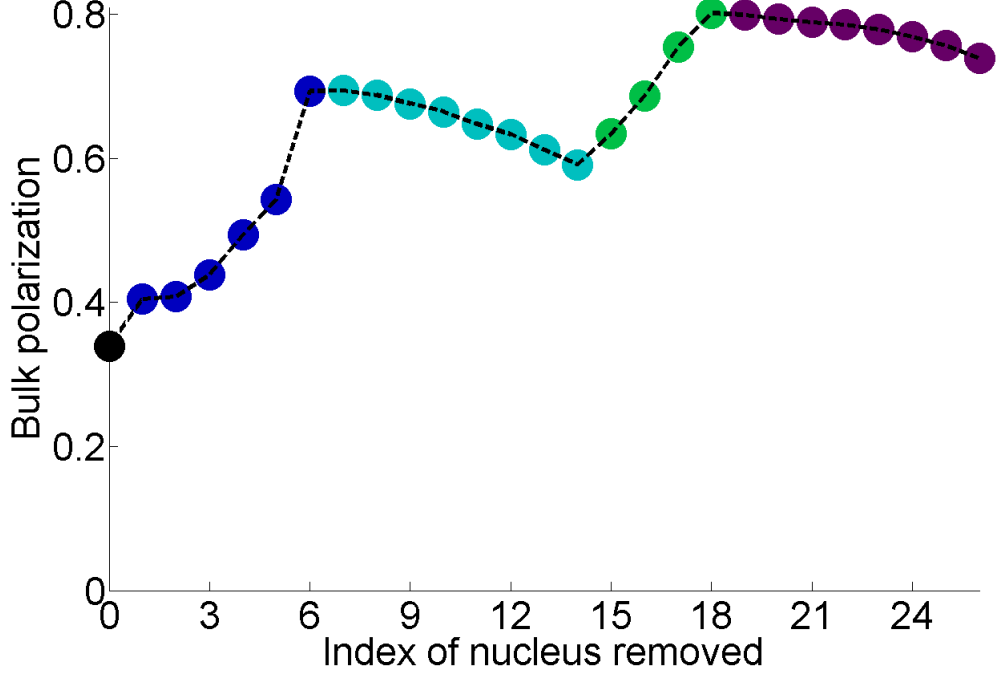


Figure 4.6: Mean polarization per nucleus versus the number of nuclei removed from the model system. The colour coding is identical to the one used in fig. 4.5. The first data point corresponds to the mean polarization without any nuclei removed (black). The next six data points (dark blue) correspond to the mean polarization if the six nuclei with strongest secular hyperfine interaction strength A_k are removed. The next eight data points (light blue) correspond to the mean polarization if nuclei with strong pseudo-secular interaction strength are removed (B_k). The next four data points again correspond to removal of nuclei with high A_k values and the final eight data points (purple) correspond to removal of nuclei with high B_k values. The broken black line has been added as a visual guide.

This polarization level compared to the average polarization for the reference system without any nuclei removed, shows that the polarization of this system (marked by spin index number 19 in figure 4.5) is increased by more than a factor of 2.3. The last eight nuclei that were removed have high B_k values and the average nuclear spin polarization level decreases by about 10%.

In order to interpret these results it is instructive to analyse the distribution of frequencies which are characteristic for SE-DNP. The effect of the nuclei with

strong secular hyperfine interaction (high A_k values) is a splitting of the frequencies $\omega_S \pm \omega_I$ at which SE–DNP is mediated by an excitation of ZQ or DQ transitions [61, 37]. The splitting of these frequencies for each nucleus I_k can be calculated by using [61, 37]

$$\omega_{I_k}^{DNP} = \omega_S \pm \omega_I - \frac{1}{2} \sum_{i \neq k} s_i A_i, \quad s_i = \pm 1, \quad (4.1)$$

where s_i is a sum implying that one needs to add up over both of the possible permutations. In order to calculate the splitting frequencies for a given nucleus, one needs to sum over all permutations of all other spins. This means that for a system of n nuclei the total number of DNP frequencies is $124 \times 2^{(n-1)}$ – a number that is not computationally feasible. Because the number of transition frequencies, resulting from the coupling of 124 nuclei to the electron is extremely high, we have selected only 25 nuclei to calculate these frequencies. These were chosen by ordering all nuclei according to secular coupling strength, A_k , in a decreasing order. The first 25 nuclei with the highest A_k values were then selected each time, reducing the number of frequencies to a more feasible value. The distributions of frequencies calculated using eq. (4.1) are shown in histograms (see fig. 4.7). The histograms are plotted for systems with 0, 2, 6, 14, 18, and 24 nuclei removed, respectively. In these histograms the fractional number of transition frequencies at which nucleus–electron flip–flops occur are plotted against the frequency offset with respect to the ZQ frequency $\omega_S + \omega_I$.

With the removal of the first six nuclei the distribution becomes significantly narrower – these have the largest effect on the width of the distribution of the SE–DNP frequencies. Further removal of nuclei reduces the width of the distribution less significantly, until the A_k values of the removed nuclei are so weak that no further significant change is observed. From fig. 4.7 we can conclude that initially the successive removal of nuclei with strong secular coupling causes a larger number of nuclei to have transition frequencies closer to the microwave carrier frequency, set to $\omega_S + \omega_I$ and hence SE–DNP will be more efficient. However, while this has a positive effect on the average nuclear spin polarization, removal of nuclei with high B_k values that can transfer polarization to the bulk by spin diffusion, does have a negative effect on the average nuclear spin polarization. These considerations show the delicate interplay between the various parameters in the spin ensemble, controlled by the geometry of the system.

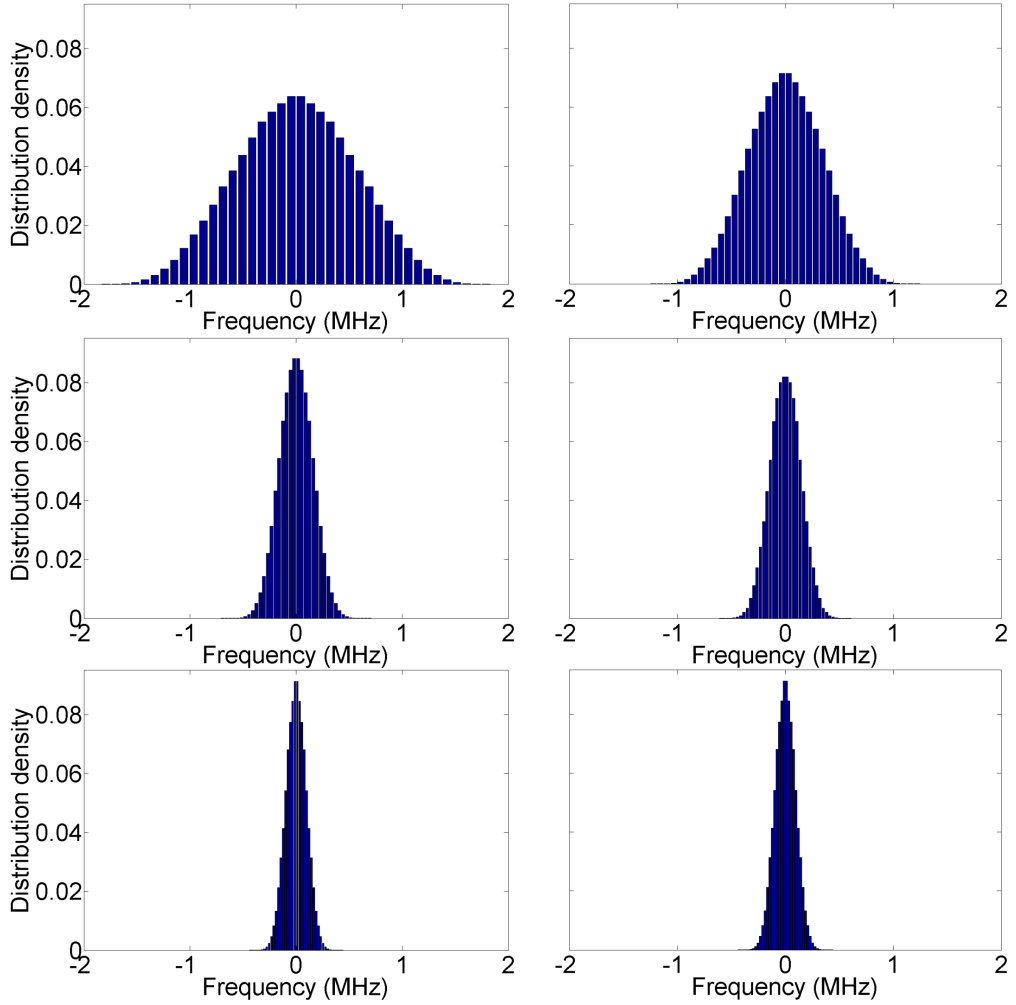


Figure 4.7: Histograms show the distribution of frequencies for ZQ transitions that occur in the model spin ensemble. The frequencies are given as offset frequencies in respect to the ZQ transition $\omega_S + \omega_I$. The nuclei are successively removed (none, 2, 6, 14, 18 and 24 removed) and the frequencies for ZQ transitions are calculated. The first two nuclei with the strongest secular hyperfine interaction A_k were removed, leading to a significant narrowing of the distribution. Removal of the next 4 nuclei then very visibly narrows the distribution of frequencies further. Additional nuclei were then subsequently removed, in an order of descending secular hyperfine interaction strength. Fig 4.5 shows the positions of the removed nuclei. Generally the width of the distribution becomes narrower with increasing numbers of nuclei removed. However, the six nuclei that were removed at the end have only very weak A_k values, and there is no significant change between the last two histograms.

Our simulation results demonstrate that the average nuclear spin polarization is more than 2 times higher if the 26 nuclei adjacent to the central electron are removed. The removal of the nuclei means that nearest distance between nuclei and electron has increased by a factor of 2. The separation between the electron and nearest nuclei is now 8 \AA , while the separation between neighbouring nuclear

spins is still 4 Å. This is somewhat analogous to increasing the volume occupied by the molecule containing the electron radical. The expulsion volume for nuclei could be implemented by designing radical molecules with additional functional groups.

If further layers of nuclei were removed it is to be expected that the average nuclear spin polarization would decrease to levels below the initial level, i.e. that of the system without any nuclei removed, since the pseudo-secular interaction strength would become too weak for an efficient polarization transfer between the central electron and the interacting nuclei. From these considerations it is clear that there must be a set of parameters that gives the optimum DNP efficiency; parameters for which the build-up time would be the shortest, and for which the nuclear spin polarization will reach its highest level. Such an optimum does depend in a complex way on all parameters including the microwave irradiation strength, the average distance between the nuclei, the nearest distance between nuclei and the central electron, and the various R_1, R_2 relaxation parameters.

4.4 Radical design

The simulations and the results presented in this work point to a possible explanation why the trityl radical, currently in frequent use for ^{13}C dissolution DNP, seems to perform particularly well [62, 63]. The explanation is based on the assumption that there is also an optimal distance for CE-DNP between the electron and the nuclei.

The bulky aromatic groups of the trityl compound keep the molecules that carry the ^{13}C -label (e.g. [1- ^{13}C] pyruvate) at an appreciable distance to the electron (analysis for ^1H nuclei was carried out in [64]). The relatively large separation between ^{13}C nuclei and the electron results in a relatively narrow distribution of the possible DNP transition frequencies in the nuclear spin ensemble. The ^{13}C nuclei are, however, still near enough to ensure a high pseudo-secular interaction between the first layer of nuclei and the electron. Furthermore, the large separation between the electron spin and the nearest layer of nuclei will result in a lower difference between the secular hyperfine interaction strengths of adjacent nuclei as opposed to a case of a radical with a smaller steric factor – allowing nuclei to get very close to the electron spin. This in turn will lead to more efficient spin diffusion (rate eq. (3.25)) between nuclei closest to the electron and those in the next layer – further away – meaning polarization will be transported through the lattice more rapidly. These considerations demonstrate that the performance of DNP is critically dependent on the immediate molecular environment of the

paramagnetic centre and that improvements in the performance of DNP could be obtained by a precise radical design.

Chapter 5

Cross Effect

5.1 Effective Cross Effect dynamics

This chapter focuses on cross effect DNP. The theory is already described in chapter 2. In this section the adiabatic elimination and projection of the CE-DNP dynamics onto the Zeeman subspace of the density operator is described - the original derivation of the effective dynamics was carried out by A. Karabanov. The effective dynamics and the parameters they depend on are then described in great detail. This is followed by a comprehensive error analysis, spin diffusion studies in 1D systems, optimisation studies for bi-radicals, and finally large spin ensemble simulations. The research described in this chapter is not yet published as of the time of writing.

It is also to be noted that the relaxation rates of T_1 and T_2 for both electron spins have been chosen to be identical, however this is not a requirement and can be altered at will. The same applies to the relaxation rates for the nuclei - there can be variation in $T_1^{(I)}$ and $T_2^{(I)}$ values of the system.

5.1.1 Elimination of non-zero quantum coherences

The CE-DNP dynamics are projected onto the diagonal part of the density operator, the so-called Zeeman subspace, in a two-step process. The resonance condition for the cross effect, outlined in 2.3.1 indicates that the mechanism of transfer of polarization to the nuclear spins is optimal when one of the electrons has their EPR transition saturated; i.e. the microwave radiation is on resonance with its Larmor frequency.

Thus by projecting the dynamics at the CE-DNP resonance condition, the dynamics are projected onto the zero-quantum subspace of the off-resonance electron and the nuclear spins. Subsequently the derived dynamics are then projected onto the

Zeeman subspace of this zero-quantum subspace. In effect, the relevant subspace dimension of the density operator is reduced from $4^{(n+2)}$ to $2^{(n+2)}$ for n nuclear spins. The general mathematical procedure of adiabatic elimination is explained in great detail in section 2.4.

The CE-DNP Hamiltonian for a single electron pair and n nuclei is shown in 2.22. For convenience, the rotating-frame Hamiltonian is separated into four parts

$$\hat{H} = \hat{H}_Z + \hat{H}_0 + \hat{H}_+ + \hat{H}_-,$$

where

$$\begin{aligned}\hat{H}_Z &= \Delta_1 \hat{S}_z^{(1)} + \Delta_2 \hat{S}_z^{(2)} + \sum_k \omega_I \hat{I}_{kz} \\ \hat{H}_0 &= \lambda_2 \hat{S}_z^{(2)} + \lambda_1 \left(\hat{S}_z^{(1)} + \hat{S}_z^{(2)} \right) + 2D \hat{S}_z^{(1)} \hat{S}_z^{(2)} + \sum_k A_k^{(1)} \hat{I}_{kz} \hat{S}_z^{(1)} \\ &+ \frac{\omega_1}{2} \left(\hat{S}_+^{(1)} + \hat{S}_-^{(1)} \right) + \sum_k A_k^{(2)} \hat{I}_{kz} \hat{S}_z^{(2)} + \sum_{k < k'} \left(2\hat{I}_{kz} \hat{I}_{k'z} - \hat{I}_k \cdot \hat{I}_{k'} \right) \\ \hat{H}_\pm &= \frac{\omega_1}{2} \hat{S}_\pm^{(2)} - \frac{D}{2} \hat{S}_\pm^{(2)} \hat{S}_\mp^{(1)} + \frac{1}{2} \sum_{j,k}^{2,n} B_{k\pm}^{(j)} \hat{I}_{k\pm} \hat{S}_z^{(j)},\end{aligned}$$

with offset terms Δ_1, Δ_2 , which are $\Delta_j = \omega_S^{(j)} - \omega_{\mu w}$, i.e. the difference between the Larmor frequency of an electron and the microwave field frequency.

At the CE-DNP resonance, $\Delta_1 \approx 0$ and $\Delta_2 \approx \pm \omega_I$, hence the Zeeman Hamiltonian becomes $\hat{H}_Z = \omega_I \left(\pm \hat{S}_z^{(2)} + \sum_k \hat{I}_{kz} \right)$. The offset terms from this CE-DNP resonance condition are λ_1, λ_2 . Their form is $\lambda_1 = \Delta_1$, $\lambda_2 = \Delta_2 - \Delta_1 - \omega_I$.

The terms \hat{H}_Z, \hat{H}_0 keep dynamics of a particular subspace enclosed in that subspace. Terms \hat{H}_\pm , on the other hand, cause cross-overs between the different subspaces.

The system is also subject to dissipation. There is longitudinal relaxation driving all spins back to their thermal equilibrium, and there are also decoherence processes. The dissipator for this system is written as

$$\begin{aligned}\mathbf{\Gamma} &= \sum_j \left(\Gamma_+^{(S)} \mathbf{D}[\hat{S}_+^{(j)}] + \Gamma_-^{(S)} \mathbf{D}[\hat{S}_-^{(j)}] + \Gamma_z^{(S)} \mathbf{D}[\hat{S}_z^{(j)}] \right) \\ &+ \sum_k \left(\Gamma_{k+}^{(I)} \mathbf{D}[\hat{I}_{k+}] + \Gamma_{k-}^{(I)} \mathbf{D}[\hat{I}_{k-}] + \Gamma_{kz}^{(I)} \mathbf{D}[\hat{I}_{kz}] \right),\end{aligned}$$

with associated rates

$$\begin{aligned}\Gamma_{\pm}^{(S)} &= \frac{R_1^{(S)}}{2}(1 \mp p_{\text{th}}) & \Gamma_z^{(S)} &= 2R_2^{(S)} \\ \Gamma_{k+}^{(I)} &= \Gamma_{k-}^{(I)} = \frac{R_1^{(I)}}{2} & \Gamma_{kz}^{(I)} &= 2R_2^{(I)}.\end{aligned}\quad (5.1)$$

The evolution of the system is then described by the Liouville von Neumann equation

$$\dot{\hat{\rho}} = (-i\hat{H} + \mathbf{\Gamma})\hat{\rho}. \quad (5.2)$$

The Liouville state space can be decomposed as

$$\mathcal{L} = \sum \mathcal{L}_q,$$

where \mathcal{L}_q is the subspace of q -quantum coherences,

$$\hat{H}_Z \hat{\rho} = q\omega_I \hat{\rho}, \quad \hat{\rho} \in \mathcal{L}_q, \quad q = 0, \pm 1, \dots, \pm(n+1). \quad (5.3)$$

The case of $q = 0$, i.e. when $\hat{H}_Z \hat{\rho} = 0$ denotes the zero-quantum subspace of the electron (at offset $\Delta_2 = \omega_I$) and the nuclear spins. The subspace of interest is therefore the one that commutes with the Zeeman Hamiltonian. The dynamics in this subspace are a lot slower than the dynamics in the other subspaces, since at high field

$$\omega_I \gg D, A_k, B_{k\pm}, d_{kk'}, \Gamma_z^{(S)}, \Gamma_{\pm}^{(S)}, \Gamma_{kz}^{(I)}, \Gamma_{k\pm}^{(I)}. \quad (5.4)$$

Letting the subspace \mathcal{H}_0 be the zero-quantum subspace, and \mathcal{H}_1 the complementary subspace

$$\mathcal{H}_0 = \mathcal{L}_0, \quad \mathcal{H}_1 = \sum_{q \neq 0} \mathcal{L}_q,$$

the relations

$$(-i\hat{H}_0 + \mathbf{\Gamma})\mathcal{L}_q \subset \mathcal{L}_q, \quad \hat{H}_{\pm} \mathcal{L}_q \subset \mathcal{L}_{q\pm 1}$$

along with (5.3) give the following properties

$$\begin{aligned}\mathbf{L}_{00}\hat{\rho}_0 &= -i\hat{H}_0 + \mathbf{\Gamma}\hat{\rho}_0, & \mathbf{L}_{10}\hat{\rho}_0 &= -i(\hat{H}_+ + \hat{H}_-)\hat{\rho}_0, \\ \mathbf{L}_{01}\mathcal{L}_{\pm 1} &= -i\hat{H}_{\mp}\mathcal{L}_{\pm 1}, & \mathbf{L}_{01}\mathcal{L}_q &= 0, \quad |q| > 1, \\ \mathbf{L}_{11}\mathcal{L}_{\pm 1} &= -(\pm i\omega_I \mathbf{1} + i\hat{H}_0 + i\hat{H}_{\pm} - \mathbf{\Gamma})\mathcal{L}_{\pm 1}, \\ \mathbf{L}_{11}\mathcal{L}_q &= -(iq\omega_I \mathbf{1} + i\hat{H}_0 + i\hat{H}_+ + i\hat{H}_- - \mathbf{\Gamma})\mathcal{L}_q, \quad |q| > 1.\end{aligned}\quad (5.5)$$

Due to the presence of relaxation, the eigenvalues of the superoperator \mathbf{L}_{11} have negative real parts, ζ_- , thus the solution in \mathcal{H}_1 rapidly tends to a steady-state. Therefore, the condition outlined in section 2.4 is satisfied, and the Kernel func-

tion is well approximated by its time-independent steady-state form. The zero-quantum master equation is well approximated by

$$\dot{\hat{\rho}}_0 = (\mathbf{L}_{00} + \mathbf{M}) \hat{\rho}_0,$$

where $\mathbf{M} \equiv -\mathbf{L}_{01}\mathbf{L}_{11}^{-1}\mathbf{L}_{10}$.

5.1.2 Superoperator \mathbf{M}

In order to find the explicit form of \mathbf{M} , the properties of superoperators summarised in eq. (5.5) were used. Superoperator \mathbf{L}_{01} acting on $\hat{\rho}_0$ leaves the dynamics in the first quantum coherence subspace $\mathcal{L}_{\pm 1}$

$$\mathbf{L}_{10}\hat{\rho}_0 = -i(\hat{H}_+ + \hat{H}_-)\hat{\rho}_0.$$

Letting $\hat{X} = \mathbf{L}_{11}^{-1}\mathbf{L}_{10}\hat{\rho}_0$, it is clear that

$$\mathbf{L}_{11}\hat{X} = \mathbf{L}_{10}\hat{\rho}_0 = -i(\hat{H}_+ + \hat{H}_-)\hat{\rho}_0.$$

Therefore, since $\omega_I \gg (\hat{H}_{0,\pm}, \mathbf{D})$, \hat{X} can be expanded as a rapidly-converging power series, truncated to second order. This is carried out in a similar fashion to that in the case of SE-DNP, shown in section 3.1.2.

As before, the superoperator \mathbf{M} is found as a series

$$\mathbf{M} = \omega_I^{-1}\mathbf{M}_1 + \omega_I^{-2}\mathbf{M}_2 + \dots \quad (5.6)$$

converging exponentially fast

$$\mathbf{M} - \sum_{k=1}^m \omega_I^{-k}\mathbf{M}_k \sim \epsilon^{m+1} \quad (\epsilon \ll 1),$$

with terms

$$\mathbf{M}_1 = -i[\hat{H}_+, \hat{H}_-], \quad \mathbf{M}_2 = -\hat{H}_+(i\hat{H}_0 - \mathbf{\Gamma})\hat{H}_- - \hat{H}_-(i\hat{H}_0 - \mathbf{\Gamma})\hat{H}_+, \quad \dots \quad (5.7)$$

It follows from (5.5) that

$$\zeta_- > |\omega_I|, \quad \|\mathbf{L}_{01}\| \leq \max \|\hat{H}_{\pm}\|, \quad \|\mathbf{L}_{10}\| \leq 2 \max \|\hat{H}_{\pm}\|.$$

Hence, because of eq. (5.4), equation (5.2) can be replaced by its adiabatic approximation

$$\dot{\hat{\rho}} = \mathbf{L}_0\hat{\rho} \quad (5.8)$$

with

$$\mathbf{L}_0 = \mathbf{L}_{00} + \mathbf{M} = \mathbf{M}_0 + \omega_I^{-1}\mathbf{M}_1 + \omega_I^{-2}\mathbf{M}_2,$$

where

$$\mathbf{M}_0 = -i\hat{H}_0 + \mathbf{\Gamma}.$$

5.1.3 Elimination of non-Zeeman spin orders

Following the procedure from the initial Liouvillian \mathbf{L} , eq. (5.2), to the Liouvillian \mathbf{L}_0 , in eq. (5.8), a master equation accurately describing the dynamics closed in the subspace \mathcal{H}_0 is obtained. In this section, the procedure of projection of the dynamics within zero-quantum subspace onto the Zeeman subspace is described. This projection results in classical-like dynamics concerning the diagonal elements of the density operator.

The zero-quantum subspace is decomposed as

$$\mathcal{L}_0 = \mathcal{L}_Z + \mathcal{L}_C,$$

where

$$\mathcal{L}_Z = \text{span}\{\hat{1}, \hat{S}_z^{(1)}, \hat{S}_z^{(2)}, \hat{I}_{\text{kz}}, \hat{S}_z^{(1)}\hat{S}_z^{(2)}, \hat{S}_z^{(1)}\hat{I}_{\text{kz}}, \dots\},$$

is the subspace of Zeeman spin orders, and \mathcal{L}_C the complementary subspace consisting of non-Zeeman, zero-quantum coherences.

The commutation character of the notation $\hat{O} \equiv [\hat{O}, \cdot]$ implies that the super-operator \mathbf{M}_1 is a commutation (mathematical proof in appendix A.1):

$$\mathbf{M}_1 = -i\hat{H}_1, \quad \hat{H}_1 = [\hat{H}_+, \hat{H}_-] = \hat{H}_{1,0} + \hat{H}'_1,$$

$$\begin{aligned} \hat{H}_{1,0} &= \frac{\omega_1^2}{2}\hat{S}_z^{(2)} + \omega_I \sum_k \left(b_{k0} + b_{k1}\hat{S}_{1z}\hat{S}_{2z} \right) \hat{I}_z + \frac{D^2}{4} \left(\hat{S}_{2z} - \hat{S}_{1z} \right) \\ \hat{H}'_1 &= -\frac{\omega_1}{4} \left(B_{k+}^{(2)}\hat{S}_-^{(2)}\hat{I}_{k+} + B_{k-}^{(2)}\hat{S}_+^{(2)}\hat{I}_- \right) - \frac{D\omega_1}{2} \left(\hat{S}_+^{(1)} + \hat{S}_-^{(1)} \right) \hat{S}_z^{(2)} \\ &\quad + \frac{D}{4} \left[\left(B_+^{(2)} - B_+^{(1)} \right) \hat{S}_+^{(1)}\hat{S}_-^{(2)}\hat{I}_{k+} + \left(B_-^{(2)} - B_-^{(1)} \right) \hat{S}_-^{(1)}\hat{S}_+^{(2)}\hat{I}_{k-} \right], \end{aligned}$$

where b_{k0} and b_{k1} are:

$$b_{k0} = \frac{1}{8\omega_I} \left(\left| B_k^{(1)} \right|^2 + \left| B_k^{(2)} \right|^2 \right), \quad b_{k1} = \frac{1}{2\omega_I} \left(B_{k+}^{(1)}B_{k-}^{(2)} + B_{k-}^{(1)}B_{k+}^{(2)} \right).$$

We have also

$$\hat{H}_0 = \hat{H}_{0,0} + \hat{H}'_0, \quad \mathbf{\Gamma} = \mathbf{\Gamma}_0 + \mathbf{\Gamma}',$$

where

$$\begin{aligned}\hat{H}_{0,0} &= \lambda_1 \hat{S}_z^{(1)} + (\lambda_1 + \lambda_2) \hat{S}_z^{(2)} + 2D \hat{S}_z^{(1)} \hat{S}_z^{(2)} + \sum_{j,k} A_k^{(j)} \hat{S}_z^{(j)} \hat{I}_{kz} + 2 \sum_{k,k'} d_{k,k'} \hat{I}_{kz} \hat{I}_{k'z} \\ \hat{H}'_0 &= \frac{\omega_1}{2} \left(\hat{S}_+^{(1)} + \hat{S}_-^{(1)} \right) - \frac{d_{kk'}}{2} \left(\hat{I}_{k+} \hat{I}_{k'-} + \hat{I}_{k-} \hat{I}_{k'+} \right),\end{aligned}$$

and

$$\begin{aligned}\Gamma_0 &= \sum_j R_2^{(S)} \mathbf{D}[\hat{S}_z^{(j)}] + \sum_k R_2^{(I)} \mathbf{D}[\hat{I}_{kz}], \\ \Gamma' &= \sum_j \left\{ \frac{R_1^{(S)}}{2} (1 - p_{\text{th}}) \mathbf{D}[\hat{S}_+^{(j)}] + \frac{R_1^{(S)}}{2} (1 + p_{\text{th}}) \mathbf{D}[\hat{S}_-^{(j)}] \right\} \\ &\quad + \sum_k \frac{R_1^{(I)}}{2} \left(\mathbf{D}[\hat{I}_{k+}] + \mathbf{D}[\hat{I}_{k-}] \right).\end{aligned}\tag{5.9}$$

In agreement with previous notation, [2.4](#),

$$\mathbf{L}_{0,kj} = \pi_k \mathbf{L}_0 \pi_j, \quad k, j = 0, 1,$$

$$\pi_0 = \mathcal{P}_Z, \quad \pi_1 = \mathcal{Q}_C,$$

where $\mathcal{P}_Z, \mathcal{Q}_C$ are projections onto the subspaces $\mathcal{L}_Z, \mathcal{L}_C$ respectively.

The superoperators $\hat{H}_{0,0}, \hat{H}_{1,0}, \Gamma_0$ trivially act on \mathcal{L}_Z . Within the accuracy of $\sim \omega_I^{-1}$, only the superoperators \hat{H}'_0, \hat{H}'_1 contribute to $\mathbf{L}_{0,10}, \mathbf{L}_{0,01}$, since

$$\mathcal{P}_Z \mathbf{M}_2 \mathcal{Q}_C, \quad \mathcal{Q}_C \mathbf{M}_2 \mathcal{P}_Z \ll \hat{H}'_0, \hat{H}'_1$$

and thus the terms that scale as ω_I^{-2} are negligible. The same applies to $\mathcal{Q}_C \mathbf{M}_2 \mathcal{Q}_C$, hence the superoperator

$$\mathbf{X} = -i \hat{H}'_{0,0} + \Gamma_0$$

maps \mathcal{L}_C to itself with eigenvalues ζ'_k satisfying

$$\text{Re } \zeta'_k < 0, \quad |\zeta'_k| > \min\{2R_2^{(I)}, R_2^{(S)} + R_2^{(I)}\}.$$

Thus, under the conditions

$$\begin{aligned}1) \quad & \max \left(\text{eig}(\hat{T}_0) \cdot \text{eig}(\hat{Y}_0) \right) \ll 1, \quad 2) \quad \max \left(\text{eig}(\hat{T}_{2k}) \cdot \text{eig}(\hat{Y}_{2k}) \right) \ll 1, \\ 3) \quad & \max \left(\text{eig}(\hat{T}_{3k}) \cdot \text{eig}(\hat{Y}_{3k}) \right) \ll 1, \quad 4) \quad \max \left(\text{eig}(\hat{T}_{kk'}) \cdot \text{eig}(\hat{Y}_{kk'}) \right) \ll 1,\end{aligned}\tag{5.10}$$

the subspace \mathcal{L}_C is adiabatically eliminated and we come then to the approximation for eq. (5.8),

$$\dot{\hat{\rho}}_Z = \mathbf{L}_Z \hat{\rho}_Z, \quad \mathbf{L}_Z = \mathbf{L}_{0,00} - \mathbf{L}_{0,01} \mathbf{L}_{0,11}^{-1} \mathbf{L}_{0,10}, \quad (5.11)$$

closed in the Zeeman subspace \mathcal{L}_Z . Using the fact that $\|\omega_I^{-1} \hat{H}_{0,\pm}\|, \|\omega_I^{-1} \mathbf{\Gamma}\| \ll 1$, and assuming conditions (5.10), it can be shown that the right-hand side of (5.11) is well approximated as

$$\begin{aligned} \mathbf{L}_{0,11} &= \mathbf{\Gamma}' + \mathbf{\Gamma}'', \\ -\mathbf{L}_{0,01} \mathbf{L}_{0,11}^{-1} \mathbf{L}_{0,10} &= \hat{T}_0 \hat{Y}_0^2 \sum_k \left(\hat{T}_{2k} \hat{Y}_{2k}^2 + \hat{T}_{3k} \hat{Y}_{3k}^2 \right) + \sum_{k < k'} \hat{T}_{kk'} \hat{Y}_{kk'}^2, \end{aligned} \quad (5.12)$$

where $\mathbf{\Gamma}'$ is given by eq. (5.9), and $\mathbf{\Gamma}''$ is obtained from $\mathcal{P}_Z \mathbf{M}_2 \mathcal{P}_Z$;

$$\begin{aligned} \mathbf{\Gamma}'' &= \frac{\omega_1^2 R_2^{(S)}}{2\omega_I^2} \left(\mathbf{D}[\hat{S}_+] + \mathbf{D}[\hat{S}_+] \right) + \frac{R_2^{(S)} D^2}{\omega_I^2} \left(\mathbf{D}[\hat{K}_+] + \mathbf{D}[\hat{K}_-] \right) \\ &\quad + \frac{R_2^{(I)}}{\omega_I} \sum_k \left(b_{k0} + b_{k1} \hat{S}_z^{(1)} \hat{S}_z^{(2)} \right) \left(\mathbf{D}[\hat{I}_{k+}] + \mathbf{D}[\hat{I}_{k-}] \right), \end{aligned} \quad (5.13)$$

and

$$\begin{aligned} \hat{Y}_0 &= \frac{\omega_1}{2} \left(1 - \frac{D}{\omega_I} \hat{S}_z^{(2)} \right) \left(\hat{S}_+^{(1)} + \hat{S}_-^{(1)} \right), \\ \hat{Y}_{2k} &= -\frac{\omega_1}{4\omega_I} \left(B_{k+}^{(2)} \hat{S}_-^{(2)} \hat{I}_{k+} + B_{k-}^{(2)} \hat{S}_+^{(2)} \hat{I}_- \right), \\ \hat{Y}_{3k} &= \frac{D}{4\omega_I} \left[\left(B_+^{(2)} - B_+^{(1)} \right) \hat{S}_+^{(1)} \hat{S}_-^{(2)} \hat{I}_{k+} + \left(B_-^{(2)} - B_-^{(1)} \right) \hat{S}_-^{(1)} \hat{S}_+^{(2)} \hat{I}_{k-} \right], \\ \hat{Y}_{kk'} &= \frac{d_{kk'}}{2} \left(\hat{I}_{k+} \hat{I}_{k'-} + \hat{I}_{k-} \hat{I}_{k'+} \right), \end{aligned} \quad (5.14)$$

$$\begin{aligned} \hat{T}_0 &= \frac{R_2^{(S)}}{\left(R_2^{(S)} \right)^2 + \hat{P}_0^2}, & \hat{T}_{2k} &= \frac{R_2^{(I)} + R_2^{(S)}}{\left(R_2^{(I)} + R_2^{(S)} \right)^2 + \hat{P}_{2k}^2}, \\ \hat{T}_{3k} &= \frac{R_2^{(I)} + 2R_2^{(S)}}{\left(R_2^{(I)} + 2R_2^{(S)} \right)^2 + \hat{P}_{3k}^2}, & \hat{T}_{kk'} &= \frac{2R_2^{(I)}}{\left(2R_2^{(I)} \right)^2 + \hat{P}_{kk'}^2}, \end{aligned}$$

with the state-dependent coefficients written out explicitly as

$$\begin{aligned}
\hat{P}_0 &= \lambda_1 - \frac{D^2}{4\omega_I} + 2D\hat{S}_z^{(2)} + \sum_k \left(A_k^{(1)} + b_{k1}\hat{S}_z^{(2)} \right) \hat{I}_{kz}, \\
\hat{P}_{2k} &= \lambda_1 + \lambda_2 + \frac{2\omega_1^2 + D^2}{4\omega_I} - b_{k0} + \left(2D - A_k^{(1)} \right) \hat{S}_z^{(1)} + \sum_{s \neq k} A_s^{(2)} \hat{I}_{sz}, \\
\hat{P}_{3k} &= \lambda_2 + \frac{\omega_1^2 + D^2}{2\omega_I} - b_{k0} + \frac{b_{k1}}{4} + \sum_{s \neq k} \left(A_s^{(2)} - A_s^{(1)} \right) \hat{I}_{sz}, \\
\hat{P}_{kk'} &= b_{k0} - b_{k'0} + (b_{k1} - b_{k'1}) \hat{S}_z^{(1)} \hat{S}_z^{(2)} + \sum_{j=1}^2 \left(A_k^{(j)} - A_{k'}^{(j)} \right) \hat{S}_z^{(j)}.
\end{aligned} \tag{5.15}$$

The advantage of formulas (5.12), (5.14) is that they reduce the inversion of $\mathbf{L}_{\mathbf{0},\mathbf{11}}^{-1}$ in the subspace \mathcal{L}_C to the much simpler problem of inversions of the Zeeman operators $\hat{T}_0, \hat{T}_{2k}, \hat{T}_{3k}, \hat{T}_{kk'}$. The latter are defined in the 2^{n+1} -dimensional Hilbert space and are diagonal in the Zeeman basis.

5.1.4 The Lindblad form

Utilizing the double-commutator, it is straightforward to re-write the right-hand side of the Zeeman-projected equation (5.11) in the purely Lindbladian form, eq. (2.11)

$$\begin{aligned}
\mathbf{L}_Z &= \sum_j \left(\Gamma_+^{(S_j)} \mathbf{D}(\hat{S}_+) + \Gamma_-^{(S_j)} \mathbf{D}(\hat{S}_-) \right) + \sum_k \left(\hat{\Gamma}_{k+}^{(I)} \mathbf{D}(\hat{I}_{k+}) + \hat{\Gamma}_{k-}^{(I)} \mathbf{D}(\hat{I}_{k-}) \right) \\
&\quad + \Gamma^{(SS)} \left(\mathbf{D}(\hat{K}_+) + \mathbf{D}(\hat{K}_-) \right) + \sum_k \hat{\Gamma}_k^{(IS)} \mathbf{D}(\hat{Y}_k) \\
&\quad + \sum_{k < k'} \hat{\Gamma}_{kk'}^{(II)} \mathbf{D}(\hat{X}_{kk'}) + \sum_k \hat{\Gamma}_k^{(ISS)} \mathbf{D}(\hat{Z}_k).
\end{aligned} \tag{5.16}$$

Single spin processes

The rates

$$\hat{\Gamma}_{\pm}^{(S_1)} = \frac{1 \mp P_0}{2} R_1^{(S)} + \frac{\omega_1^2}{2} \left(1 - \frac{D}{\omega_I} \hat{S}_z^{(2)} \right) \hat{T}_0, \tag{5.17}$$

$$\Gamma_{\pm}^{(S_2)} = \frac{1 \mp P_0}{2} R_1^{(S)} + \frac{\omega_1^2}{2\omega_I^2} R_2^{(S)}, \tag{5.18}$$

$$\hat{\Gamma}_{k\pm}^{(I)} = \frac{R_1^{(I)}}{2} + \frac{R_2^{(I)}}{\omega_I} \left(b_{k0} + b_{k1} \hat{S}_z^{(1)} \hat{S}_z^{(2)} \right), \tag{5.19}$$

are all related to the single-spin jump operators $\hat{S}_{\pm}^{(j)}, \hat{I}_{k\pm}$.

Two–spin processes

The operator rates

$$\hat{\Gamma}_k^{(IS)} = \frac{\omega_1^2 |B_{k+}|^2 (R_2^{(S)} + R_2^{(I)})}{8\omega_I^2} ((R_2^{(S)} + R_2^{(I)})^2 + \hat{P}_{2k}^2)^{-1}, \quad (5.20)$$

$$\hat{\Gamma}_{kk'}^{(II)} = d_{kk'}^2 R_2^{(I)} ((2R_2^{(I)})^2 + \hat{P}_{kk'}^2)^{-1}, \quad (5.21)$$

$$\Gamma^{(SS)} = \frac{R_2^{(S)} D^2}{2\omega_I^2}, \quad (5.22)$$

are all associated with the two–spin jump operators

$$\hat{Y}_k = \hat{S}_-^{(2)} \hat{I}_{k+} + \hat{S}_+^{(2)} \hat{I}_{k-}, \quad \hat{X}_{kk'} = \hat{I}_{k+} \hat{I}_{k'-} + \hat{I}_{k-} \hat{I}_{k'+}, \quad K_{\pm} = \hat{S}_{\pm}^{(2)} \hat{S}_{\mp}^{(1)}.$$

Three–spin processes

The three spin rate

$$\hat{\Gamma}_k^{(ISS)} = \frac{D^2 |B_k^{(2)} - B_k^{(1)}|^2 (R_{2k}^{(I)} + 2R_2^{(S)})}{8\omega_I^2} \left((R_{2k}^{(I)} + 2R_2^{(S)})^2 + \hat{P}_{3k}^2 \right)^{-1} \quad (5.23)$$

and corresponding jump operator

$$\hat{Z}_k = \hat{S}_+^{(1)} \hat{S}_-^{(2)} \hat{I}_{k+} + \hat{S}_-^{(1)} \hat{S}_+^{(2)} \hat{I}_{k-},$$

describe the cross effect mechanism.

To implement the Zeeman–projected master equation, eq. (5.16), the rates are treated as described in appendix A.3.

5.1.5 Analysis of CE–DNP effective dynamics

The effective dynamics, governed by eqs. (5.17 – 5.23), provide a lot of insight into the mechanism of CE–DNP and give much more clarity than the starting, full master equation – eq. (5.2). The transfer of polarization from the electron pair to surrounding nuclei, the effect analogous to SE–DNP between the second electron (at resonance condition $\Delta_2 = \pm\omega_I$) and nuclei, polarization transport between nuclei, effective cross–relaxation between electrons, and the dissipative processes for all spins are all well described by these seven effective rates. As was the case with the Zeeman projection for SE–DNP, some of the effective rates are state–dependent, i.e. kinetically constrained [56], [57].

Each of the processes underlying CE–DNP is described in detail in this section.

Relaxation of the first electron

Equation (5.17) describes dissipation processes of the first electron spin – this is the spin at the resonance condition of $\Delta_1 \approx 0$. The dissipative process is governed by single-spin flips 'up' (+) and 'down' (-). The first part of this rate describes the relaxation of this spin back to its thermal equilibrium. This process is weighted by the longitudinal relaxation constant $R_1^{(S)}$, and the thermal polarization value of the electrons P_0 . This part is identical to that seen in eq. (5.1). In the absence of a driving field, and if $P_0 = 0$ the 'down' (-) rate will dominate.

The second part of rate (5.17) is a consequence of this electron being on-resonance with the microwave field, and it describes the saturation of this electron. This part relies on the microwave field amplitude ω_1 squared and thus at moderate to high microwave power values, this term will dominate leading to 'up' and 'down' rates being roughly equal and having a significantly large value – resulting in rapid spin flips of this electron. This part of the rate also depends on the strength of the coupling to the second electron D , and the operator-valued coefficient \hat{T}_0 . Both of these terms will consequently reduce the efficiency of saturation of this electron. The coefficient \hat{T}_0 also depends on the coupling strength to the second electron, in addition it relies on the transverse electronic relaxation rate $R_2^{(S)}$, the offset parameter λ_1 (indicating how close the microwave radiation is in frequency to this electron), the secular coupling strengths A_k of the nuclei to this electron, as well as the pseudo-secular coupling strengths B_k between both electrons and the surrounding nuclei. In short, strong coupling of any spins to this electron will lead to a less efficient saturation process.

Relaxation of the second electron

Equation (5.18) describes relaxation of the second electron spin – that is the spin on resonance with the nuclear Larmor frequency ($\Delta_2 \approx \pm\omega_I$). The first part again drives this electron back to its thermal equilibrium through longitudinal relaxation processes governed by $R_1^{(S)}$. A comparison to eq. (5.1) shows a perturbative, second order correction to the relaxation of this spin. This is a consequence of the applied microwave field; it relies on the microwave field amplitude, ω_1 , the nuclear Larmor frequency ω_I , and the electronic transverse relaxation time $R_2^{(S)}$. The driving microwave field effectively tilts the quantization axis of the electron away from the Zeeman axis. The perturbative correction corrects for this, approximating dynamics in a diagonal frame. It is worth noting that the form of this rate is identical to the relaxation rate for the central electron in SE-DNP, as shown in eq. (3.22).

Nuclear relaxation

Equation (5.19) describes relaxation of the nuclear spins. Given that the thermal polarization of nuclear spins is very small even at low temperatures; the flip 'up' and flip 'down' rates approximately coincide and without any driving the nuclear spins will relax to a state of no polarization. A comparison to eq. (5.1) shows that the nuclear spin relaxation rate also has a perturbative, second order correction. This is a consequence of the pseudo-secular coupling of nuclei to the electron spins and therefore affects nuclei closest to the electron the most, and it is indirectly effected by the interaction between the electron spins. Because of this interaction between the electron radical pair this rate is also dependent on the electronic states. It relies on the pseudo-secular coupling coefficients $B_{k\pm}^{(1)}, B_{k\pm}^{(2)}$, the nuclear Larmor frequency ω_I , the nuclear transverse relaxation rate $R_2^{(I)}$, and the states of electrons $\hat{S}_z^{(1)}, \hat{S}_z^{(2)}$. Coupling to the electrons shifts the quantization axis of the nuclei, thus the second order correction term is to compensate for this.

Electron-nuclear interaction rate

This is the rate, eq. (5.20), corresponding to the interaction between the second electron (off-resonance with respect to the microwave frequency) and the nuclear ensemble, showing diffusive dynamics. The form of this rate is analogous to the electron-nuclear rate governing the solid effect – eq. (3.24). In fact, if the first (on-resonance) electron is moved far away from the ensemble in which case $D, A_k^{(1)}, B_k^{(1)} \rightarrow 0$, the exact form of the SE-DNP effective rate is recovered. The presence of this rate shows that the mechanism of SE-DNP is also present in the case of CE-DNP.

The rate depends on the microwave field amplitude ω_1 squared, the inverse of the nuclear Larmor frequency ω_I squared, the pseudo-secular coupling $B_k^{(2)}$ between the second electron and a nucleus, the transverse relaxation rates of the electron and nuclei – $R_2^{(S)}, R_2^{(I)}$ respectively, and the operator-valued coefficient \hat{P}_{2k} . The dependence on the transverse relaxation rates indicates that even though the effective dynamics are classical, the underlying process is quantum-mechanical, and is mediated by coherences.

The value of \hat{P}_{2k} , eq. (5.15), depends on the state of the entire nuclear spin ensemble, more precisely, it has eigenvalues dependent on the polarization level of each nuclear spin. This term also depends on the offset parameters $\lambda_1 + \lambda_2$ – which is equivalent to $\Delta_2 - \omega_I$, i.e. the offset from the SE-DNP condition for the second electron, the microwave field amplitude squared, the electronic dipolar coupling D squared, the nuclear Larmor frequency, the pseudo-secular couplings $B_k^{(1)}, B_k^{(2)}$ to both electrons, and the secular coupling strength $A_k^{(1)}$ to the first electron.

Therefore it is clear that the rate in eq. (5.20) will be reduced in value as the nuclear spin ensemble becomes more polarized. It is also clear that \hat{P}_{2k} will be dominated by terms with the strongest A_k couplings. If the coupling between the electrons is strong then the mechanism driving SE–DNP will be quenched quite severely.

Nuclear–nuclear interaction rate

Transport of polarization within the ensemble of nuclear spins is governed by spin diffusion – the rate in eq. (5.21). The rate of polarization transfer between two nuclei is proportional to the square of their dipolar coupling coefficient $d_{kk'}$, it is inversely proportional to the transverse relaxation rates of the nuclei $R_2^{(I)}$, and it is inversely proportional to the square of the state–dependent coefficient $\hat{P}_{kk'}$. This rate is analogous to the effective rate of interaction between nuclei seen in the case of SE–DNP (eq. (3.25)), with the addition of dependence on the coupling strengths to the first (on–resonance) electron.

The state–dependent coefficient $\hat{P}_{kk'}$ depends on the differences of the secular $A_k^{(1)}, A_k^{(2)}$, and pseudo–secular $B_k^{(1)}, B_k^{(2)}$ coupling coefficients between two nuclei, for each electron. This introduces a state–dependence on the electronic states $\hat{S}_z^{(1)}, \hat{S}_z^{(2)}$. Even though the coefficients b_{k0}, b_{k1} are significantly smaller, and can again (as in the case of SE–DNP) be discarded, the square of $P_{kk'}$ retains its state–dependence.

The dependence on the difference of the secular couplings of the two nuclei arises as a consequence of the coupling to an electron shifting the nuclei in frequency. If the difference between the frequencies of the two nuclei becomes large, then the interaction between them becomes ineffective; the rate in eq. (5.21) becomes quenched, and very little or no polarization transfer takes place between them. This is because of the fact that nuclei off–resonance with respect to one another do not interact very well.

Effective electron–electron interaction rate

Equation (5.22) describes a cross–relaxation dissipative mechanism between the electron pair, resulting from the projection of the dynamics onto the Zeeman subspace. This rate is constant, and is dependent on the transverse relaxation rate of the electrons $R_2^{(S)}$, the electronic dipolar coupling strength D squared, and the inverse of the nuclear Larmor frequency ω_I squared. The presence of this rate shows that even without introducing a phenomenological cross–relaxation dissipator between the electrons in the system, there will still exist an effective cross–relaxation mechanism as a consequence of the strong dipolar coupling between them, lead-

ing to flip–flop jumps between the two electrons. The presence of the transverse relaxation rate shows that this mechanism is mediated by the coherences of each of the electrons, and thus the underlying nature of this interaction is coherent.

Three–spin interaction rate

Equation (5.23) is the rate governing the three–spin interaction process characteristic of CE–DNP. The mechanism itself relies on spin flips between both of the electrons and a coupled nucleus. The form of the rate shows dependence on the square of the electronic dipolar coupling ' D ', the squared absolute difference between the pseudo–secular coupling coefficients $B_k^{(j)}$ of each electron, and it is inversely proportional to the nuclear Larmor frequency ω_I squared. The rate also depends on the sum of the nuclear and electronic transverse relaxation terms $R_2^{(I)}, R_2^{(S)}$. Although the rate is not visibly, directly affected by the microwave field amplitude ω_1 ; it is dependent on the operator–valued coefficient \hat{P}_{3k} .

The coefficient \hat{P}_{3k} depends on the offset term λ_2 – this is the offset from the CE–DNP resonance condition, it also depends on the dipolar coupling D , the microwave field amplitude ω_1 , the nuclear Larmor frequency ω_I , and the secular A_k as well as pseudo–secular $B_{k\pm}$ electron–nuclear coupling strengths.

This rate will be reduced in value if the offset term λ_2 is large. In addition this rate will be reduced due to the presence of nuclei that have a very large difference between the secular couplings to each electron (if $A_k^{(2)} - A_k^{(1)}$ is large), particularly as the ensemble becomes more polarized.

A comparison of eqs. (5.23) (5.20) – corresponding to the CE–DNP and SE–DNP effective rates respectively, provides insight into the superior efficiency of CE over SE. The SE rate depends on the microwave amplitude, where it is difficult to achieve high ω_1 values without using expensive microwave hardware. With very high microwave power the SE mechanism would be quenched, and in addition a significant heating of the sample would be expected from a large microwave flux. The three–spin rate depends instead on the electron–electron coupling D , which tends to be in the order of several MHz for bi–radicals (leading to $D^2 \gg \omega_1^2$), and thus causing the CE–DNP rate to be orders of magnitude greater than the SE–DNP rate. The presence of the term $\left| B_k^{(2)} - B_k^{(1)} \right|^2$ also makes it clear that this rate relies on an asymmetry in the pseudo–secular couplings to a nucleus. Thus for nuclei placed at an equal distance between the electrons this rate will be reduced severely. It will on the other hand have a large magnitude when $B_{k+}^{(1)} \gg B_{k+}^{(2)}$ or $B_{k+}^{(2)} \gg B_{k+}^{(1)}$.

A clear link has been established between the rate magnitude, and the fast nuclear polarization build–up as well as the high steady–state polarization of the bulk ex-

perienced in CE-DNP. It also enabled us to study ways of improving the build-up times and nuclear polarization in large spin ensembles. This has been shown in section 5.5. The operator-valued coefficients in eqs. (5.15), (5.23) suggest that the offset coefficients λ_1, λ_2 can be 'tuned' to give a more optimised polarization output.

5.2 Validity of assumptions

The CE-DNP projection onto the Zeeman subspace was tested extensively for a variety of parameters to try to determine the parameter regimes for which its accuracy holds. It was noticed that the error became large in the intermediate regime of D coupling strength, while it was small for either weakly or strongly coupled electron spins.

5.2.1 Testing the zero-quantum subspace master equation

The first step of the projection was tested to start with – the projection onto the zero-quantum subspace of the second electron spin and the nuclear ensemble. The error was obtained by calculating the polarization curves using the full master equation, and comparing those against the polarization curves obtained with the zero-quantum subspace master equation. Both were normalised with respect to the electronic thermal equilibrium polarization value, and hence the error was obtained by computing the difference between the two outputs:

$$\delta p = p - p_{zq}.$$

The error testing was carried out for a single nuclear spin coupled to an electron pair (with variable separation) as shown in figure 5.2. The result is seen in figure 5.1 below. The same analysis was carried out for the spin system shown in figure 5.3 with the same conclusion and no significant difference in error curves.

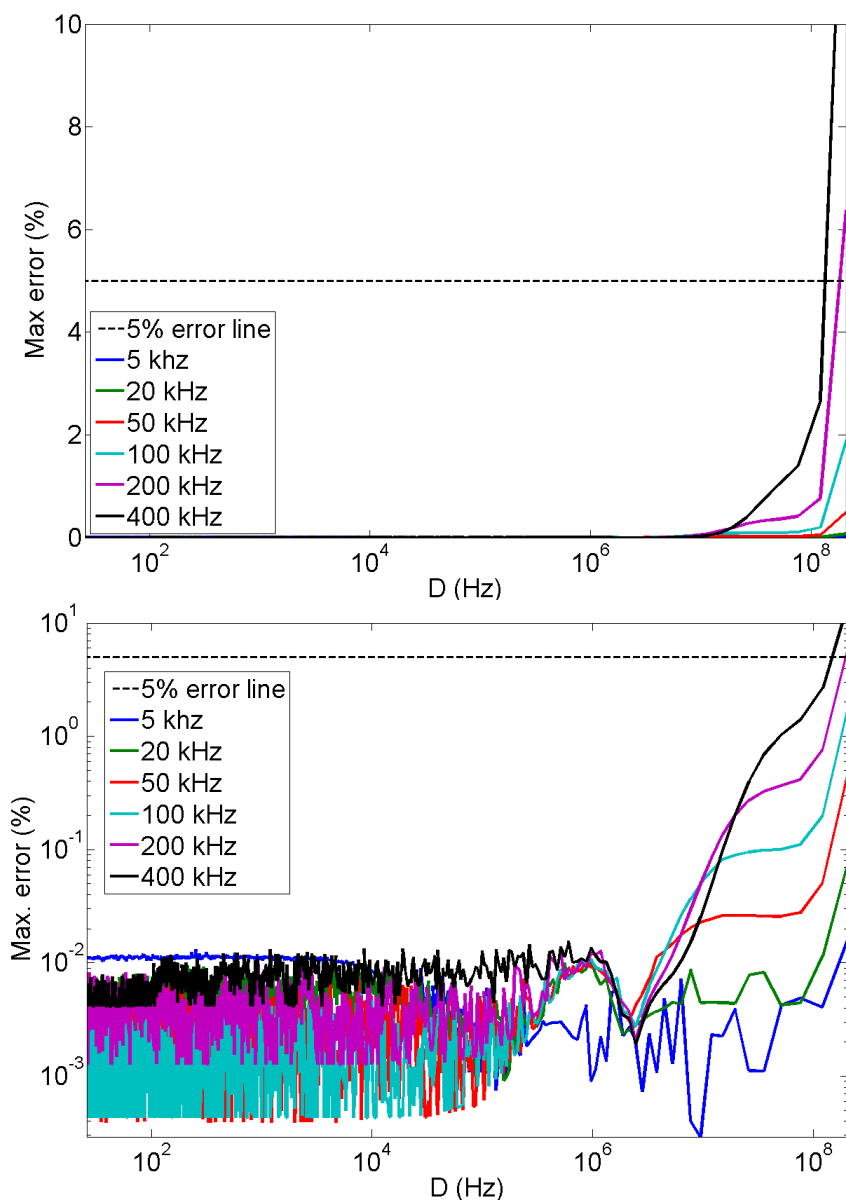


Figure 5.1: Testing the accuracy of the zero-quantum projection for CE-DNP dynamics. The bottom figure shows the error on a logarithmic scale. The error does not exceed 5 % until D is very high; For a microwave power of $\omega_1 = 400$ kHz (black solid line) the error is equal to 2.7 % for $D = 120$ MHz.

Figure 5.1 clearly shows that the zero-quantum projection is very accurate across a wide range of electron-electron coupling strengths. The error does not become large until D exceeds 100 MHz, and a large microwave field amplitude is chosen as well. In the case of bi-radicals with such extremely strong dipolar coupling, it is expected that the cross-effect mechanism would be quenched, hence the region where $D > 100$ MHz is not of interest.

5.2.2 Testing the Zeeman subspace projection

The error testing of the zero–quantum projected master equation gave very satisfactory results. The next step was the error testing of the projection onto the Zeeman subspace. In the adiabatic elimination procedure, 2.4 it is assumed that the Kernel function \mathbf{K} can be approximated by its time–independent value due to it rapidly reaching steady–state

$$\int_0^\infty \hat{K}(t) = \sum_k \hat{K}_k \left[\frac{e^{\epsilon_k t}}{\epsilon_k} \right]_0^\infty = - \sum_k \frac{\hat{K}_k}{\epsilon_k} \equiv -L_{Z,00} L_{00}^{-1} L_{00,Z},$$

in other words we assume the memory function decays quickly. Under this assumption the Laplace transform of the kernel function

$$l_{\hat{K}}(\epsilon) = \sum_k \frac{\hat{K}_k}{\epsilon - \epsilon_k}$$

is expanded around $\epsilon \approx 0$, so in result we have the Maclaurin series

$$l_{\hat{K}}(\epsilon) \approx l_{\hat{K}}(0) + \frac{\partial l_{\hat{K}}(0)}{\partial \epsilon}(\epsilon) + \frac{\partial^2 l_{\hat{K}}(0)}{\partial \epsilon^2}(\epsilon^2/2) + \dots$$

and if $\text{eig}(L_{00,Z} \cdot L_{Z,00}) \ll \epsilon_k^2$ then

$$-\frac{\partial l_{\hat{K}}(0)}{\partial \epsilon}(\epsilon) = - \sum_k \frac{\hat{K}_k}{\epsilon_k^2} \approx 0$$

and as a result

$$l_{\hat{K}}(\epsilon) \approx l_{\hat{K}}(0) = - \sum_k \frac{\hat{K}_k}{\epsilon_k}.$$

The assumption is valid, as long as the condition

$$-\frac{\partial l_{\hat{K}}(0)}{\partial \epsilon}(\epsilon) \equiv - \sum_k \frac{\hat{K}_k}{\epsilon_k^2} \approx 0$$

is satisfied. Otherwise the Zeeman–subspace master equation is non–Markovian, and higher–order terms of the above Maclaurin series would have to be considered. In the first derivative term $(-\sum_k \frac{\hat{K}_k}{\epsilon_k^2})$, the ϵ_k^2 part corresponds to squared eigenvalues of L_{00} . In order to check the validity of the Zeeman projection, the term

$$L_{Z,00} L_{00}^{-2} L_{00,Z}$$

was checked for a variety of coupling parameters strengths. It is required that the eigenvalues of the first derivative term should be very small ≈ 0 . This also follows

from the previous condition

$$\text{eig}(L_{00,Z} \cdot L_{Z,00}) \ll \epsilon_k^2.$$

Proceeding with the analysis described above, the eigenvalues of the triple-product Kernel were analysed for a variety of parameters. Error analysis was carried out for the system geometries shown in figures 5.2 and 5.3. A 0.5 % linear randomization in position was applied for all spins.

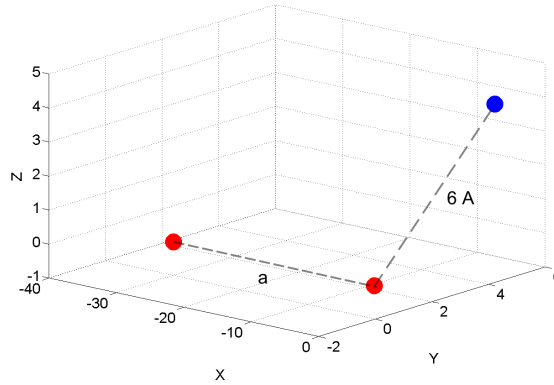


Figure 5.2: Basic system geometry used for error testing. The red dots are electrons, and the blue dot is a ^1H nucleus. The separation between the electrons 'a' was varied between 5\AA and 1000\AA .

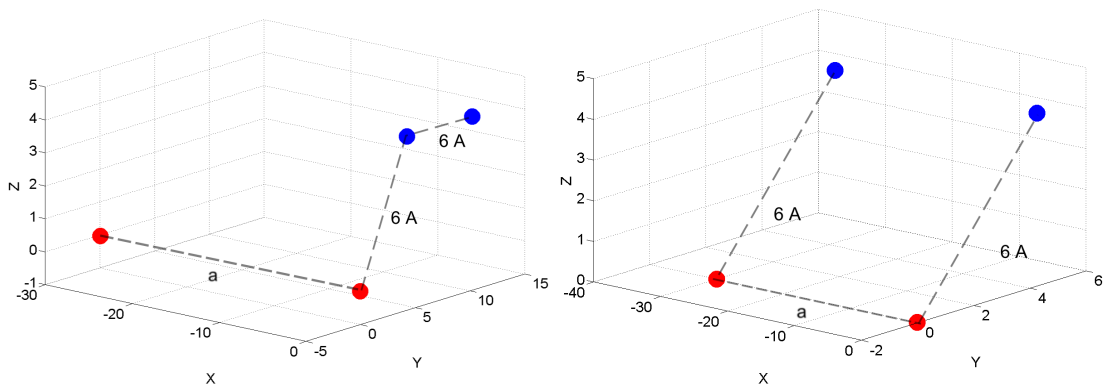


Figure 5.3: System geometry used for error testing. The red dots are electrons, and the blue dots are ^1H nuclei. The separation between the electrons 'a' was varied between 5\AA and 1000\AA . There are now two nuclear spins in the system. On the left, the further nucleus is placed behind the core nucleus thus acting as a bulk nucleus. On the right, the second nucleus is placed next to the first electron in a symmetric geometry.

Figure 5.4 shows the mean nuclear polarization as a function of D for the geometries depicted in figures 5.2 and 5.3, for microwave field amplitudes values of 5 kHz, 50 kHz, and 100 kHz.

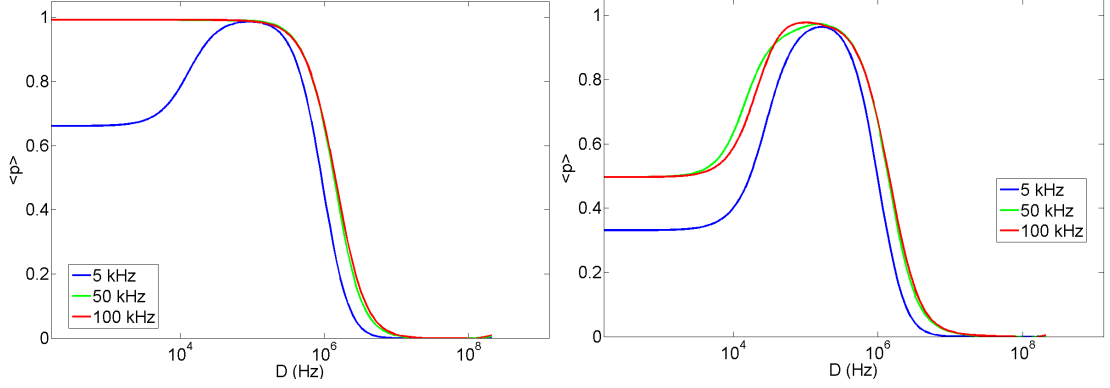


Figure 5.4: Mean nuclear polarization as a function of D . For very weak electronic dipolar coupling strengths the nuclear polarization build-up is due to SE–DNP. At moderate coupling strengths the CE–DNP mechanism becomes active. For strong D (tens of MHz) and the parameters chosen here, DNP is quenched. The LHS figure shows the polarization profiles for the geometries in figure 5.2 and LHS of figure 5.3. The RHS of this figure shows the polarization profile for the geometry in figure 5.3 RHS. There the nucleus coupled to the on–resonance electron has low polarization.

The Kernel eigenvalues were calculated for all geometries and were then plotted as a function of electronic dipolar coupling D , for varying microwave field amplitude values.

In the eigenvalue plots, a blue horizontal dashed line was used to mark an arbitrarily chosen threshold of 0.1 ($0.1 \ll 1$), where the first derivative of the Kernel is still negligible and can be ignored. The vertical dashed blue line is an aid to see the highest electron–electron dipolar coupling strength value at which the eigenvalue curve intersects the horizontal dashed threshold line. The error was calculated by taking a difference between the full master equation and Zeeman–projected master equation polarization curves; both normalised to the electron thermal equilibrium:

$$\delta p = p - p_z.$$

Both the steady–state and maximum simulation error were calculated for the Zeeman–projected master equation. The steady–state error was obtained after 1000 s of polarization build–up.

In the plot showing polarization and associated error, a horizontal black dashed line was used to mark the 5 % error threshold, which was chosen as a maximum acceptable value. The vertical dashed blue line is marked in the same position (D value) for both parts of the figure.

5 kHz

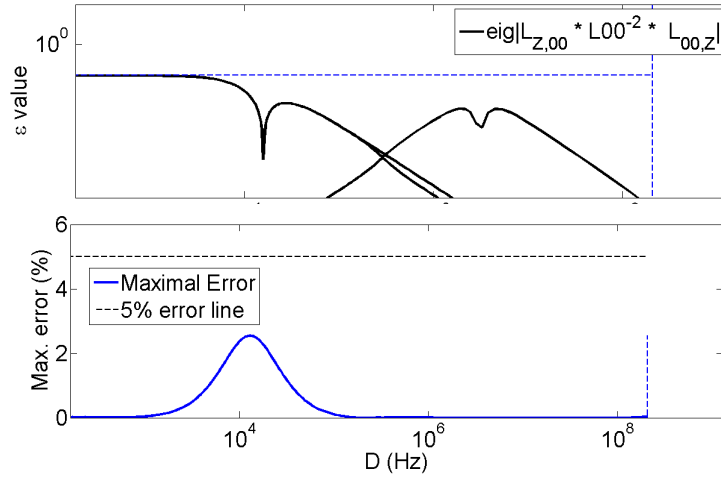


Figure 5.5: Eigenvalues and corresponding error calculated for the geometry in figure 5.2, for $\omega_1 = 5$ kHz. The horizontal dashed line is not intersected by the eigenvalue curve, and hence the corresponding error is not excessive - here it is less than 3 %.

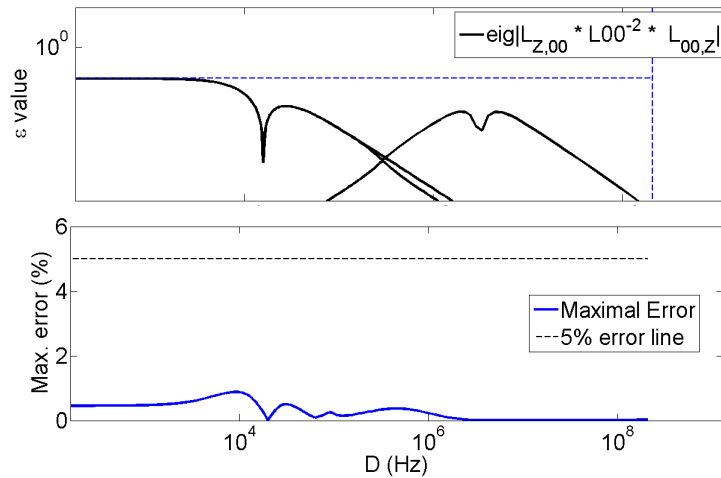


Figure 5.6: Eigenvalues and corresponding error calculated for the geometry in figure 5.3 (LHS), for $\omega_1 = 5$ kHz. The horizontal dashed line is not intersected by the eigenvalue curve, and the error does not exceed 1 %.

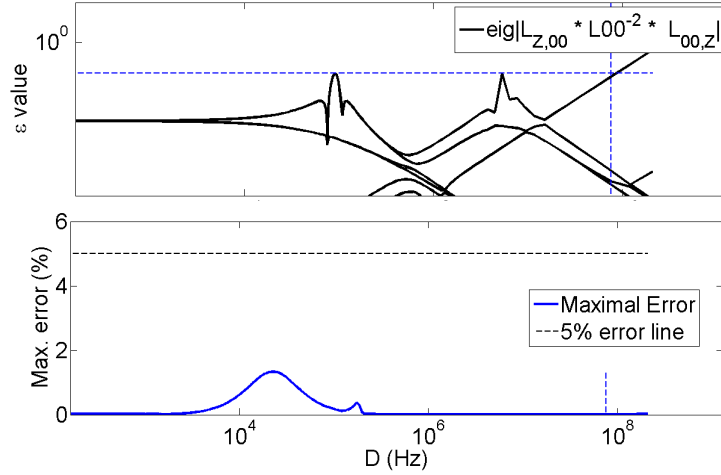


Figure 5.7: Eigenvalues and corresponding error calculated for the geometry in figure 5.3 (RHS), for $\omega_1 = 5$ kHz. The horizontal dashed line is not intersected by the eigenvalue curve until D is very high, at which point there is no nuclear polarization build-up (figure 5.4 RHS). The error does not exceed 2 % here.

For low microwave field amplitude values the eigenvalues of the kernel derivative are small, and remain below the threshold across the entire range of D – the electronic dipolar coupling strength. In this case, the corresponding error is never seen to be large – as illustrated in figures 5.5 – 5.7, the error remains well below the 5 % mark. The shape of the error curve varies slightly for the different geometries, however, the same conclusion can be drawn in each case.

50 kHz

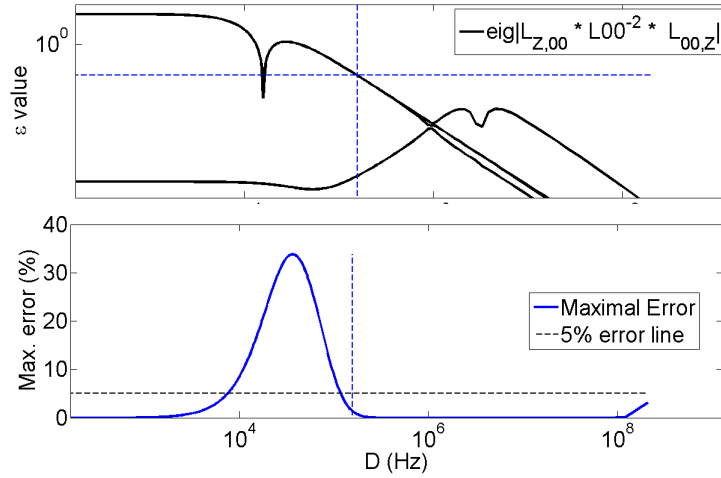


Figure 5.8: Eigenvalues of the three-part kernel product, and on the bottom the error between the Zeeman subspace master equation and the full master equation, calculated for the geometry in figure 5.2. Both are plotted as a function of D . The vertical dashed blue line indicates the point where the eigenvalues become too large, and where the error can be expected to increase.

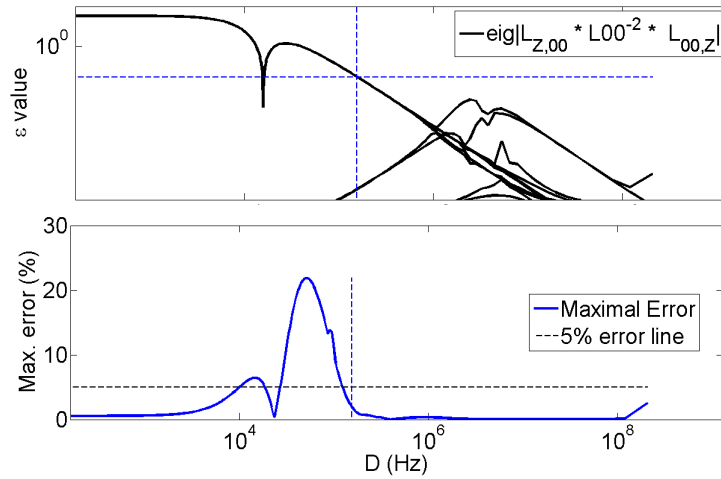


Figure 5.9: Eigenvalues of the three-part kernel product, and on the bottom the error between the Zeeman subspace master equation and the full master equation, calculated for the geometry in figure 5.3 (LHS). Both are plotted as a function of D . The vertical dashed blue line indicates the point where the eigenvalues become too large and thus where the error can be expected to increase.

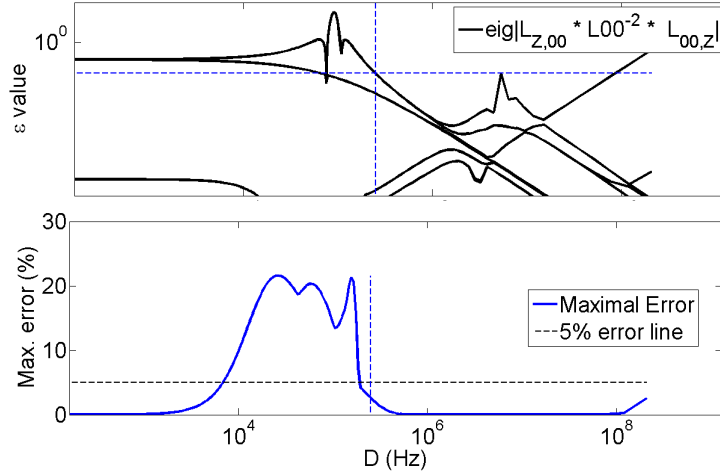


Figure 5.10: Kernel eigenvalues, and the corresponding error between the Zeeman subspace master equation and the full master equation, calculated for the geometry in figure 5.3 (RHS), and shown as a function of D . The vertical dashed blue line indicates the point where the eigenvalues become too large, and where the error can be expected to become large.

It can be clearly seen that the error at $\omega_A = 50$ kHz is significant for low–moderate D values. In this regime the eigenvalues of the first derivative of the Kernel become too large, resulting in a large error. The error curves vary significantly between the different geometries, and the maximal error seen in figure 5.9 is slightly lower than in figure 5.8. It also appears that the range of electron–electron dipolar coupling strengths for which the error exceeds 5 % is slightly narrower in figure 5.9, yet wider in figure 5.10. In general, however, it appears that there is a connection between the eigenvalue magnitude and the corresponding error magnitude in figures 5.8–5.10.

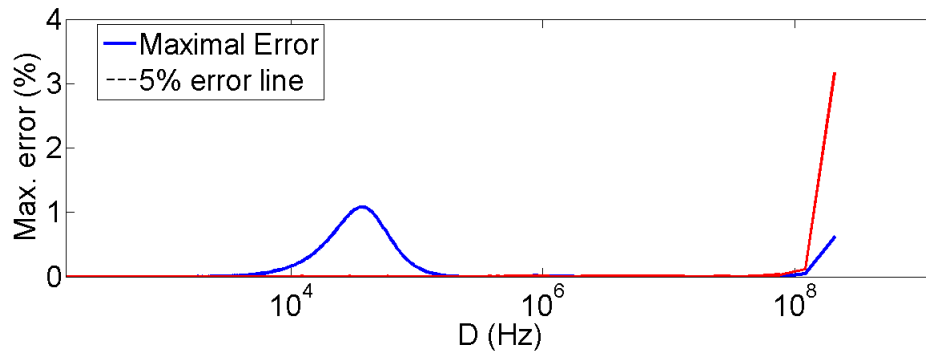


Figure 5.11: Steady–state error calculated after 1000 s of build–up corresponding for the geometry in figure 5.2. The microwave field amplitude is 50 kHz. A comparison to figure 5.8 indicates that at steady–state the error associated with the projection onto the Zeeman subspace decreases significantly.

Figure 5.11 shows the steady-state error for the geometry in figure 5.2. The error in polarization when the system reaches steady-state is very small in comparison to figure 5.8.

100 kHz

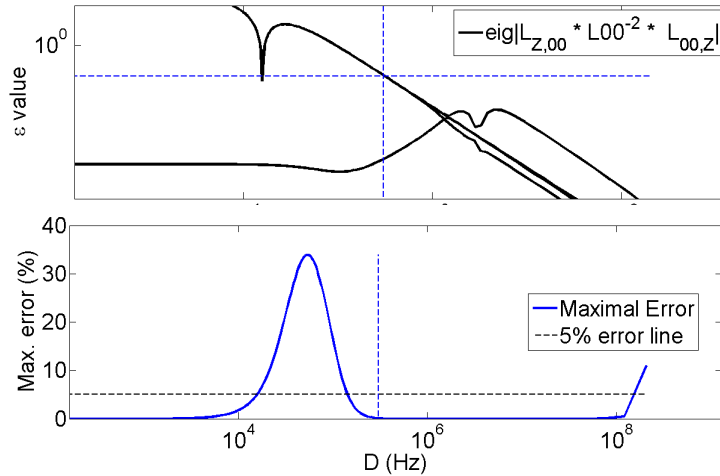


Figure 5.12: Eigenvalues and corresponding error for large microwave field amplitudes, calculated for the geometry in figure 5.2. The maximum error reaches higher values than previously – close to 40 % error. It can also be seen that the kernel eigenfunctions exceed the threshold at higher D values than was the case for lower ω_1 . The relationship between the kernel eigenvalues and corresponding error is seen to be much weaker here.

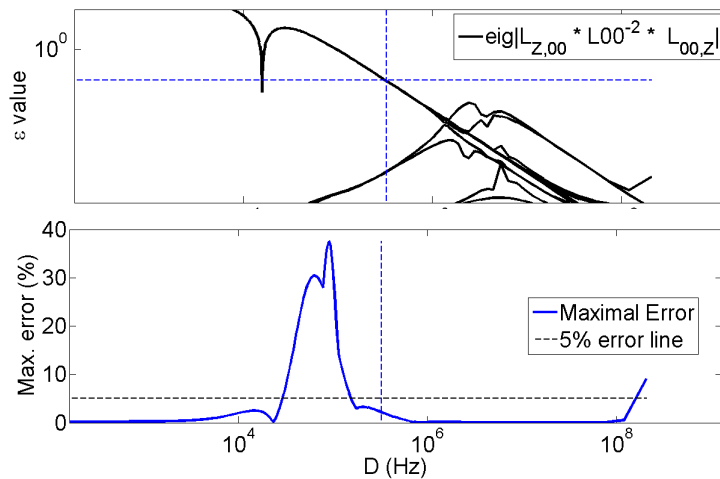


Figure 5.13: Eigenvalues and corresponding error for large microwave field amplitudes, calculated for the geometry in figure 5.3 (LHS). The relationship between the kernel eigenvalues and corresponding error is seen to be much weaker.

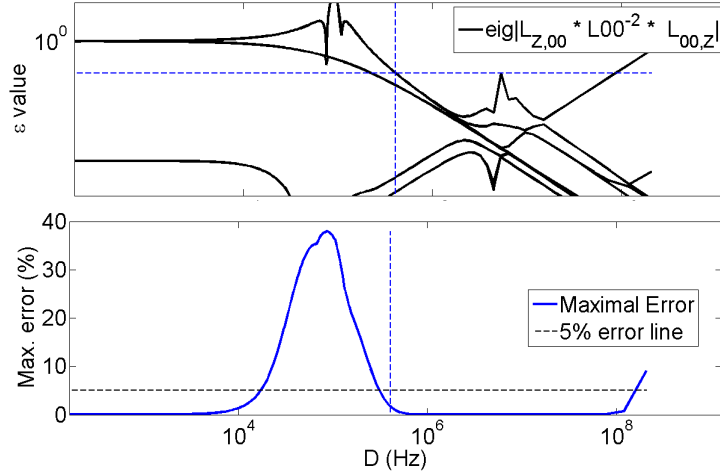


Figure 5.14: Eigenvalues and corresponding error for large microwave field amplitudes, calculated for the geometry in figure 5.3 (RHS).

At high microwave field amplitudes the maximum error increases and remains excessive for higher D values than was previously the case. In this case there is also less of a correlation between the error prediction based on eigenvalues, and the error curve itself.

5.2.3 Summary

Overall it can be seen that there is a link between the eigenvalues of the first derivative of the kernel function becoming too large to the error seen due to the projection onto the Zeeman subspace. However, what is more important is the knowledge of what causes the eigenvalues to become too large. The current treatment here is indicative but overall not completely sufficient for this purpose, and a more accurate rigorous, prediction of parameter regions of excessive error was needed.

In conclusion, finding the point at which the eigenvalues of the kernel triple-product become too large corresponds relatively well to the region of parameters where the error between the full master equation and Zeeman-projected master equation becomes large. Looking at the eigenvalues of the kernel can indicate the rough value of D , to estimate the boundary beyond which the approximations required for the Zeeman projection appear to break down.

5.3 Predicting regions of excessive error

The excessive error found for systems with moderate-strength electronic dipolar coupling (D on the order of 10 kHz – 100 kHz), and where the microwave power is

relatively high, has been attributed to one or more of the conditions in eq. (5.10) being violated. The Hamiltonian terms relevant to the Zeeman projection were separated in section 5.1.3 between ones that describe the exchange between the Zeeman and non-Zeeman subspaces; \hat{H}'_0, \hat{H}'_1 , from the terms that keep dynamics enclosed in either subspace; $\hat{H}_{0,0}, \hat{H}_{1,0}$.

The Hamiltonian terms \hat{H}'_0, \hat{H}'_1 when transferred to the Zeeman interaction frame of reference acquire a time-dependence resulting in an oscillating Hamiltonian

$$\hat{H}_{NZ} = e^{i(\hat{H}_{0,0} + \hat{H}_{1,0})t} \left(\hat{H}'_0 + \hat{H}'_1 \right) e^{-i(\hat{H}_{0,0} + \hat{H}_{1,0})t},$$

where it is required that the oscillation frequencies are much higher than the magnitude of the term they are applicable to, thus leading to the strict conditions for the Zeeman projection eq. (5.10). The conditions of 2–4 in eq. (5.10) are generally satisfied for parameters typical of CE-DNP. Condition 4 will not be satisfied if the inter-nuclear separation becomes too small, similarly to the condition in SE-DNP – eq. (3.15) – relating $R_2^{(I)}$ and $|d_{kk'}^2|/4$.

The first condition

$$\max \left(\text{eig}(\hat{T}_0) \cdot \text{eig}(\hat{Y}_0) \right) \ll 1, \quad (5.24)$$

however, is not satisfied in some cases where the microwave field amplitude ω_1 is significant in comparison to $R_2^{(S)}(\hat{P}_0^2 + (R_2^{(S)})^2)^{-1}$.

This can be used directly to predict regions where our effective formalism for CE-DNP will be incorrect, and can be done so quite quickly using numerical analysis for a system of choice – it does not suffer from the exponential scaling with respect to the number of spins in a system.

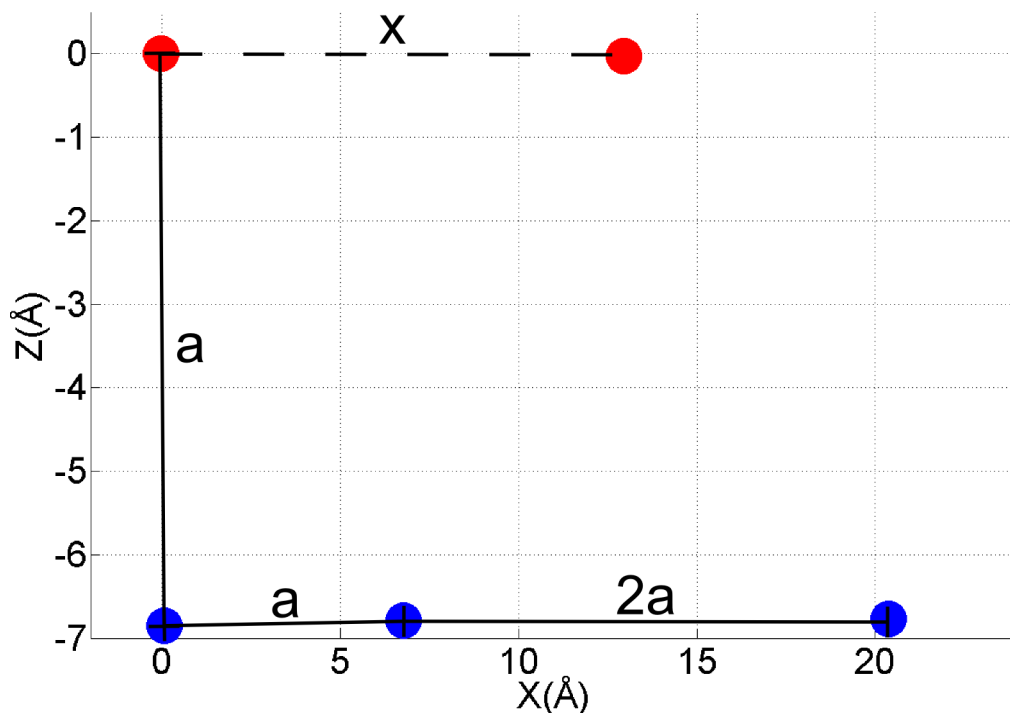


Figure 5.15: System geometry used for error testing of the Zeeman projection. The two red dots are electrons with a variable separation x between them, leading to D being varied. The three blue dots are nuclear spins. The parameter a is set to a separation of 6.8 \AA . A 1 uniform % randomization in the positions of spins was applied.

This approach was applied to an example system – shown in figure 5.15. The separation parameter a was set to be 6.8 \AA . The choice of the nearest-neighbour separation being 6.8 \AA between spins comes from calculating the average separation between protons in DNP juice.¹ The variable spacing parameter x was varied in the range of $5 \text{ \AA} \leq x \leq 1000 \text{ \AA}$. A 1 % uniform randomization in position of the spins was also applied. The electronic dipolar coupling D was thus varied between 26 Hz to 208 MHz.

The magnetic field B_Z was set to 3.4 T, polarization build-up was simulated for 1000 s, and the following relaxation parameters were set: $T_1^{(I)} = 600 \text{ s}$, $T_2^{(I)} = 0.5 \text{ ms}$, $T_1^{(S)} = 100 \mu\text{s}$, $T_2^{(S)} = 10 \mu\text{s}$ – parameters expected from a bi-radical at liquid nitrogen temperatures. The polarization curves were normalised to the electronic thermal equilibrium polarization. A difference was taken between the polarization curves of the full master equation, and the one restricted to the Zeeman subspace. The result is shown in figure 5.16.

¹60/30/10 d₈-glycerol/D₂O/H₂O (vol %)

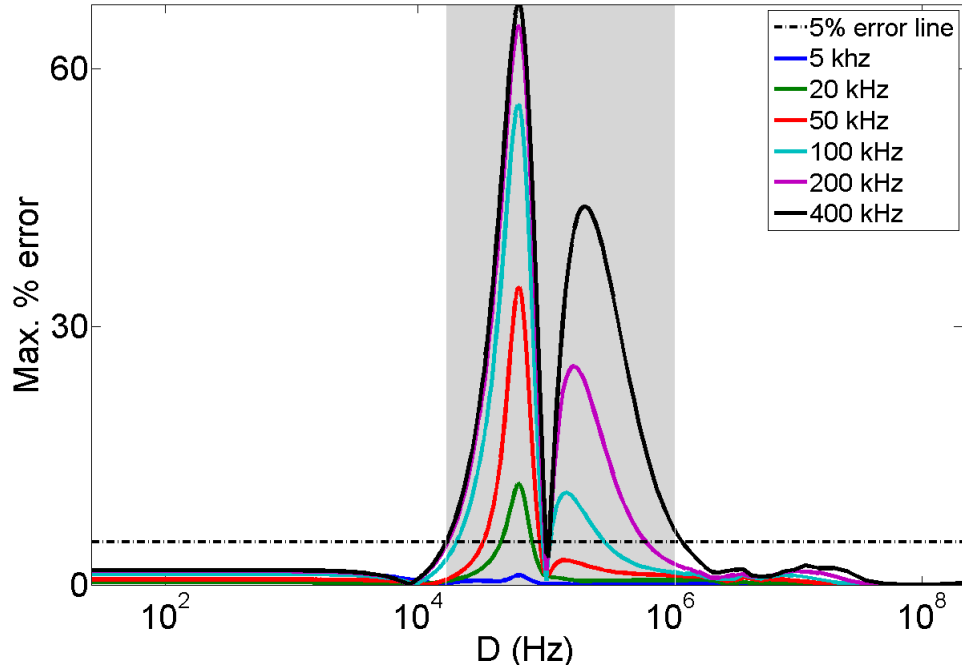


Figure 5.16: Zeeman subspace projection error for CE–DNP, shown as a function of D for several microwave amplitude values. Here a 5 % error has been selected as an upper limit on the acceptable error. The grey area highlights the range of D values where for $\omega_1 = 400$ kHz the error exceeds the acceptable upper limit.

It can be seen that the error becomes large, and is spread over a greater range of D for higher microwave field amplitude values, ω_1 . The area where the error exceeds 5 % for $\omega_1 = 400$ kHz has been shaded in light grey for the purpose of a visual aid – it covers roughly the range of $10 \text{ kHz} < D < 1 \text{ MHz}$ – and it has been decided to be outside the acceptable range of accuracy. The region where the error becomes too large can be predicted using the condition in eq. (5.24). Figure 5.17 shows the prediction corresponding to figure 5.16, calculated for the same parameters. The shaded grey region covers the same region in both figures. The regime where the output of eq. (5.24) increases beyond a certain threshold (arbitrarily chosen to be 0.1 in this case) indicates the region where the error will become too large (in figure 5.16). For lower D values the electrons become decoupled, and SE–DNP is recovered, hence the error decreases again.

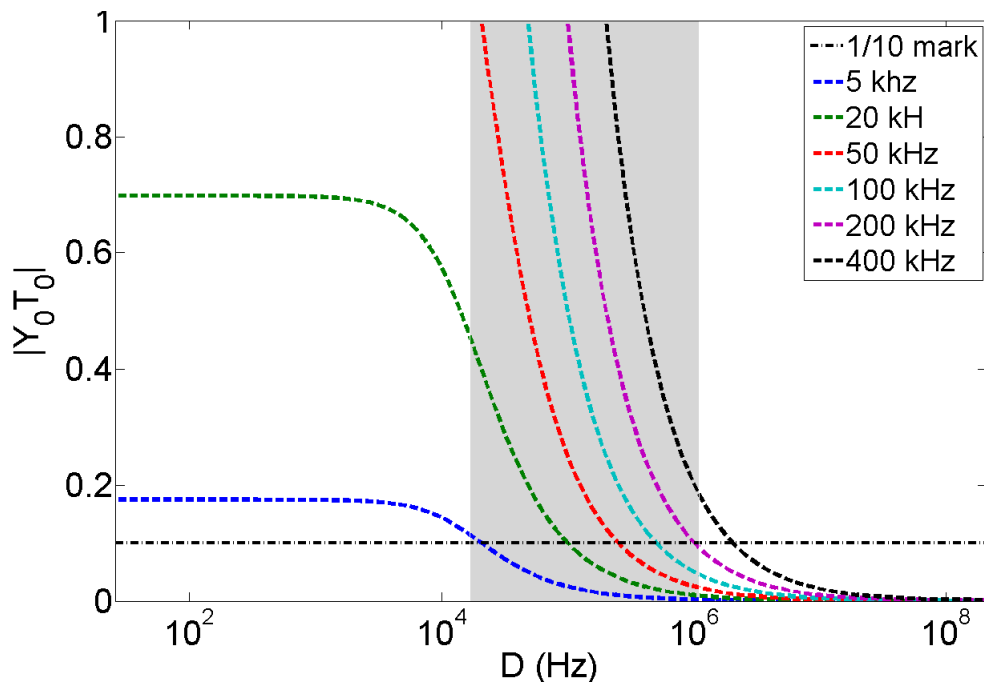


Figure 5.17: Prediction of regions of excessive error associated with the Zeeman projection for CE–DNP – predicted using eq. (5.24). The grey area highlights the range of D values where for $\omega_1 = 400$ kHz the error exceeds 5 %. The figure shows that where the product of $|Y_0 T_0|$ exceeds 0.1 the error becomes excessive. To the left of the shaded area D has low values, and SE–DNP is recovered, thus the error falls again.

Using the above figures it is apparent that even for very high microwave field amplitudes ($\omega_1 = 400$ kHz) our CE–DNP formalism is correct for electronic dipolar coupling strengths D exceeding 1 MHz. All bi–radicals currently, commonly in use exceed this coupling strength, meaning the CE–DNP formalism presented here is suitable for studying such systems. Griffin et al. report in [65] on the coupling strengths of several bi–radicals. Bi–radicals such as TOTAPOL and BTurea have D values of 23.2 MHz, and 35.2 MHz respectively; corresponding to separations of 13.1 Å and 11.4 Å between the electron spins. Even the BTnE ($n = 2,3,4$) series of bi–radicals have a coupling strength significantly larger than 1 MHz. Their dipolar coupling parameters are reported [65] to be 22.2 MHz (BT2E, 13.3 Å separation between electrons), 15.6 MHz (BT3E – 15 Å), and 11.6 MHz (BT4E – 16.5 Å). In a previous publication, [66] the same bi–radical family was reported to have D values of 11 MHz (BT2E), 5.2 MHz (BT3E), and 3.3 MHz (BT4E). These values still live comfortably outside the region of large error seen in figure 5.16.

5.3.1 Error under shorter decoherence times

The form of the state–dependent rate \hat{T}_0 in eq. (5.14) indicates that the condition in eq. (5.24) will be satisfied for a greater range of parameters if the decoherence

rate is increased, i.e. if $T_2^{(S)}$ is reduced. Figure 5.18 below shows the comparison to the output from figure 5.16 for $T_2^{(S)}$ reduced from $10 \mu\text{s}$ to $1 \mu\text{s}$.

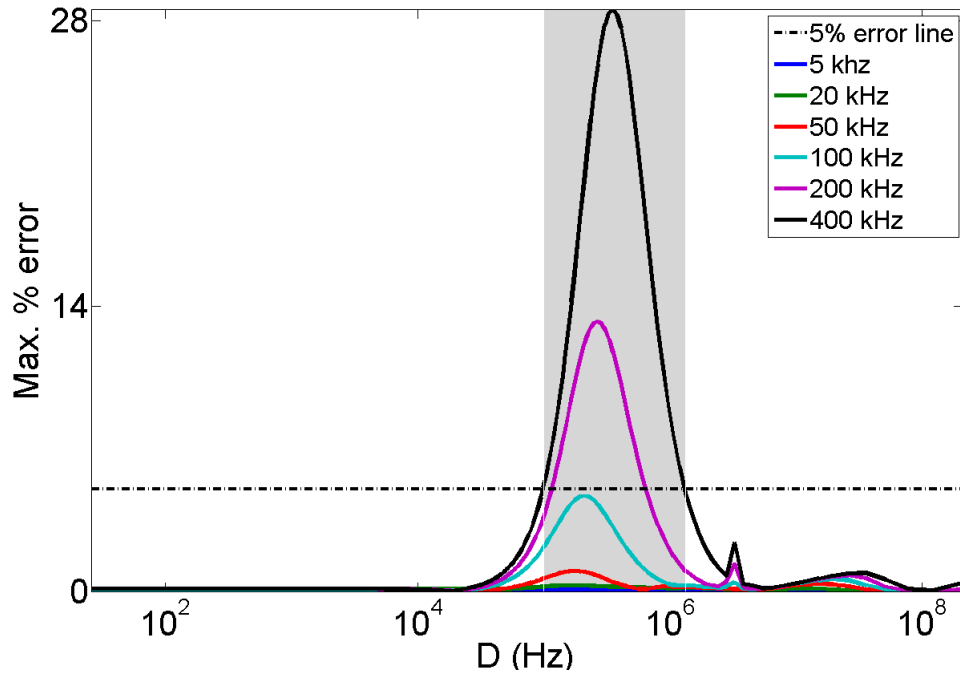


Figure 5.18: Zeeman subspace projection error for CE–DNP, shown as a function of D for several microwave amplitude values, $T_2^{(S)} = 1 \mu\text{s}$. As before a 5 % error has been selected as an upper limit on the acceptable error. The grey area highlights the range of D values where for $\omega_1 = 400 \text{ kHz}$ the error exceeds the acceptable upper limit. With a shorter decoherence time the error is reduced for all D values. For microwave field amplitude values of up to 100 kHz the error remains below 5 % across the entire range of D .

This is predicted again using the condition in eq. (5.24) for the outlined parameters, and is shown in figure 5.19. It is very clear that with shorter coherence times, and low–moderate ω_1 values (up to 100 kHz) – the error remains below 5 % for the entire range of D values. In figure 5.18 it can also be seen that the range over which the error exceeds 5 % is much more narrow than that which is seen in figure 5.16.

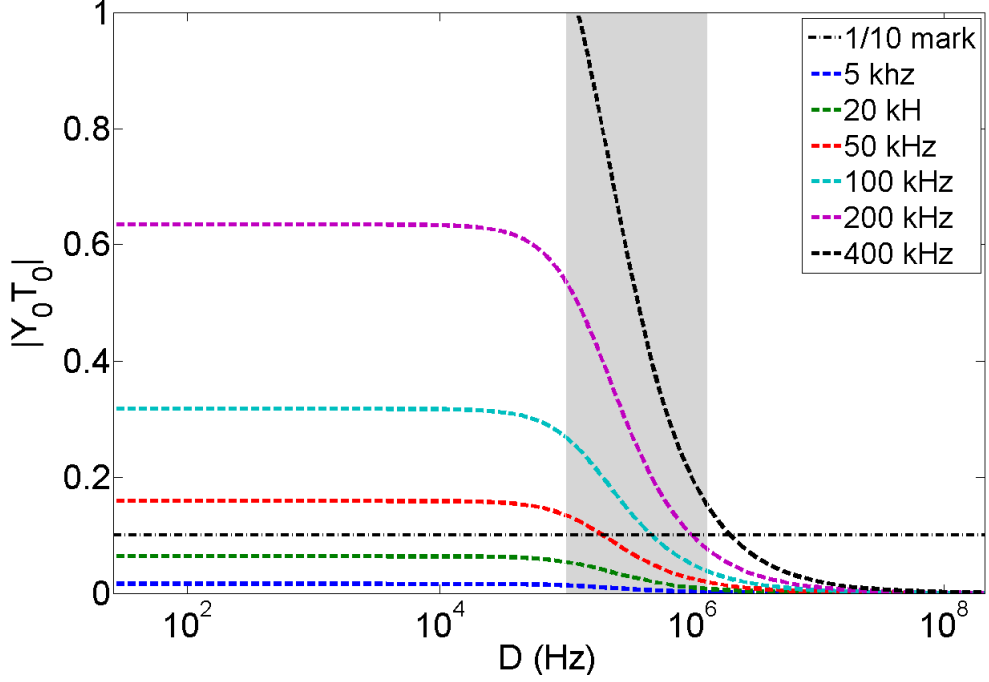


Figure 5.19: Prediction of regions of excessive error associated with the Zeeman projection for CE-DNP, with $T_2^{(S)} = 1 \mu\text{s}$ – calculated using eq. (5.24). The grey area highlights the range of D values where for $\omega_1 = 400 \text{ kHz}$ the error exceeds 5 %. In this figure the grey region is much more narrow. In addition, $|Y_0 T_0|$ values are lower for all ω_1 .

In order to establish the suitability of using a $T_2^{(S)}$ of $1 \mu\text{s}$ in simulations, literature references were compared. Values anywhere in the range of $0.5 \mu\text{s}$ to $20 \mu\text{s}$ are reported. In a theoretical study of transition between SE-DNP and CE-DNP, the authors in [36] varied $T_2^{(S)}$ between $0.5 \mu\text{s}$ to $20 \mu\text{s}$. In [67] an electron $T_2^{(S)}$ of $10 \mu\text{s}$ time was set as a "reasonable guess". An electronic $T_2^{(S)}$ time of $10 \mu\text{s}$ is also reported in [68]. A shorter $T_2^{(S)}$ time of $4 \mu\text{s}$ was reported by the authors in [69]. Decoherence time constants of $1 \mu\text{s}$ were reported in [70, 71], and in [72] the authors imply a direct measurement of $T_2^{(S)}$ – also to be $1 \mu\text{s}$.

Finally, the authors in [73] report measurements of $T_2^{(S)}$ for TOTAPOL and AMUPol at temperatures of 100 K , and magnetic fields of 3.4 T , 9.8 T . In some cases bi-exponential fitting was used. For TOTAPOL at 3.4 T the $T_2^{(S)}$ was measured at $0.1 \mu\text{s}$ (second time constant – $0.3 \mu\text{s}$), and $0.3 \mu\text{s}$ at 9.8 T .

For AMUPol the corresponding measurements were $0.7 \mu\text{s}$ and $0.8 \mu\text{s}$ respectively. It is worth noting that in some unusual, extreme cases the $T_2^{(S)}$ can be even shorter, as in the case of silicon nano-particles [74], where the electronic decoherence time constant can be on the order of tens of nanoseconds.

5.3.2 Error testing with shorter $T_1^{(S)}$ times

A study was then conducted relating the electronic longitudinal relaxation time, $T_1^{(S)}$ to the error seen in the formalism. Figures 5.16 and 5.18 show the error seen in the formalism for a $T_1^{(S)}$ time of 100 μs . Reducing the $T_2^{(S)}$ time by one order of magnitude reduces the error significantly, and it reduces the range over which the error is excessive. Increasing the electronic $T_1^{(S)}$ relaxation time is seen to reduce this error further.

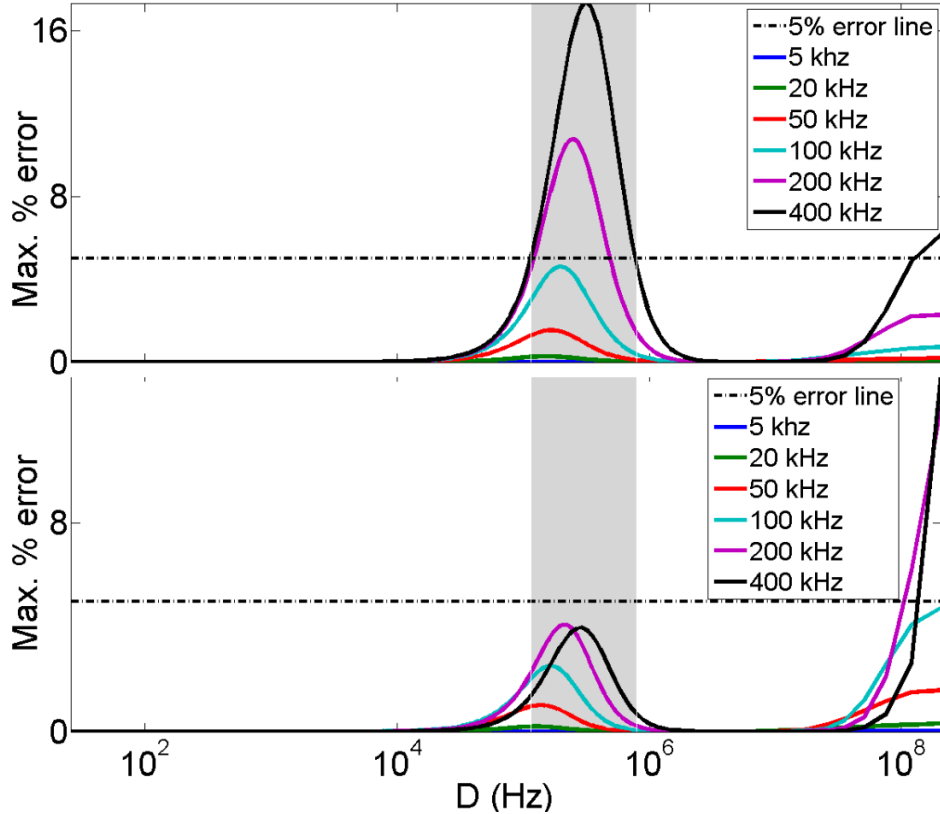


Figure 5.20: Zeeman subspace projection error for CE-DNP, shown as a function of D for several microwave amplitude values and $T_2^{(S)} = 1 \mu\text{s}$. Electronic $T_1^{(S)} = 50 \text{ ms}$ – top part, and 500 ms for the bottom part. As before a 5 % error has been selected as an upper limit on the acceptable error. The grey area highlights the range of D values where for $\omega_1 = 400 \text{ kHz}$, and $T_1^{(S)} = 50 \text{ ms}$ (top part) the error exceeds the acceptable upper limit. The grey region is left in the bottom figure for an easy comparison between the two.

The error in the top part of figure 5.20 is visibly reduced in magnitude for all ω_1 values when $T_1^{(S)}$ is increased to 50 ms. The range over which the error is excessive is, in addition, reduced in comparison to figure 5.18. Increasing $T_1^{(S)}$ further to 500 ms reduces this error such that for all values of ω_1 the maximum simulation error lies below the 5 % mark.

It is helpful to again relate the parameters used in the simulation to those reported

in the literature. The electronic $T_1^{(S)}$ is very temperature dependent. Depending on the temperature the experiments have been carried out at, the $T_1^{(S)}$ of radicals and bi-radicals have been reported to be anywhere in the range of 0.1 ms to a few hundreds of milliseconds. The authors in [70] carried out simulations where $T_1^{(S)}$ times as short as 100 μ s were used. In [71] the longitudinal relaxation time is set to 0.3 ms. One can assume that these values were to correspond to time constants realistic for samples at 100 K.

In [68] actual $T_1^{(S)}$ measurements were carried out on TEMPOL at temperatures of 10 K, 20 K and 40 K. The $T_1^{(S)}$ times the authors report are 17 ms, 5.3 ms, and 0.8 ms respectively. For TEMPOL, again, [67] the measurements at 20 K, 7 K, and 2.7 K yield $T_2^{(S)}$ times of 5.5 ms, 50 ms, and 240 ms. For TOTAPOL, $T_1^{(S)}$ measurements were carried out in [69]. There the $T_1^{(S)}$ times are shown for temperatures of 6 K – 40 K. These are as follows: 40 K: \sim 1 ms, 30 K: \sim 1 ms, 20 K: 10 ms, 10 K: 60 ms, and 5 K: 150 ms. In [73] the $T_1^{(S)}$ for TOTAPOL at 100 K was measured to be 10 μ s (second fitting constant 50 μ s) at 3.4 T, and 9 μ s (50 μ s for the second time constant) at 9.8 T.

For AMUPol the corresponding time constants were 50 μ s (160 μ s – second time constant) at 3.4 T, and 60 μ s (230 μ s for the second fitting constant) at 9.8 T.

Nuclear longitudinal relaxation times $T_1^{(I)}$ are reported to be anywhere in the range of seconds to minutes, whereas the transverse relaxation times $T_2^{(I)}$ are anywhere between 3 μ s to 1 ms, in publications [36], [67] – [72].

This shows that the parameters chosen by us for the simulations are reasonable and are within experimental measurements.

5.3.3 Error testing for nuclei with lower γ – ^{13}C

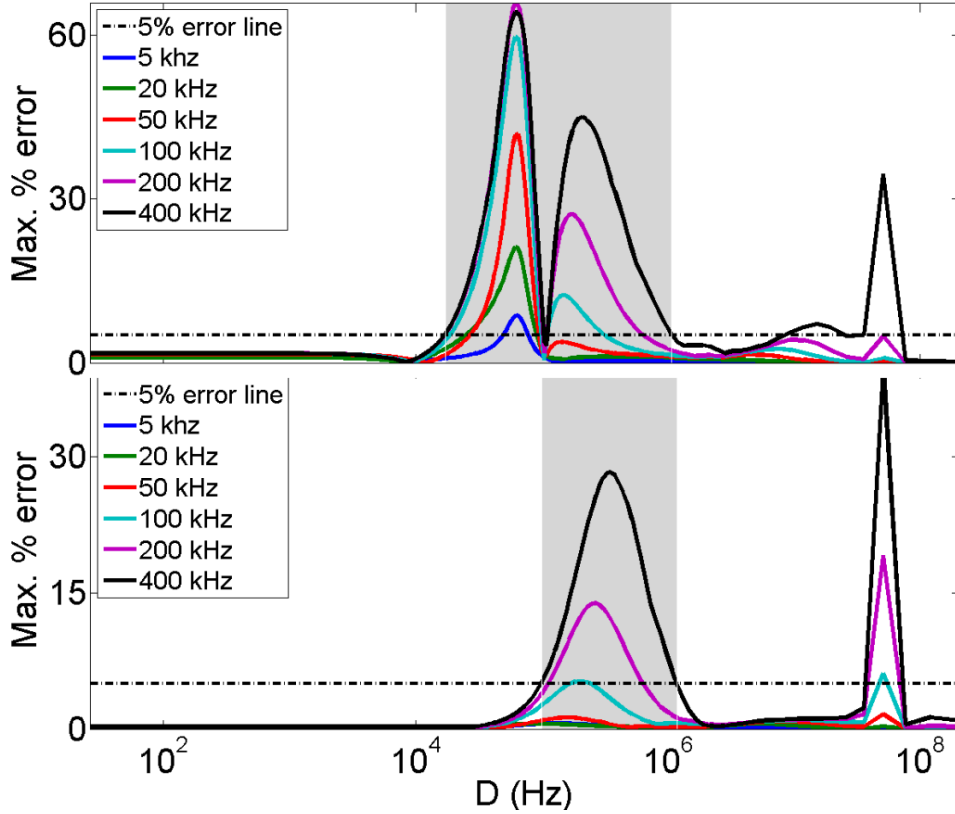


Figure 5.21: Zeeman subspace projection error for CE-DNP, for ^{13}C nuclei. The error is shown as a function of D for several microwave amplitude values. Top figure – $T_2^{(S)} = 10 \mu\text{s}$, bottom figure – $T_2^{(S)} = 1 \mu\text{s}$. A value of 5% has been selected as an upper limit on the acceptable error. The grey area highlights the range of D values where for $\omega_1 = 400 \text{ kHz}$ the error exceeds the acceptable upper limit. The results are similar to those for ^1H . A large error spike is seen at approximately 36 MHz. In this region, the condition for the projection onto the ZQ subspace (1st step adiabatic elimination) of the density operator is broken for ^{13}C nuclei.

The error seen for the CE-DNP formalism with systems consisting of ^{13}C nuclei instead of protons was carried out using the same geometry, shown in figure 5.15, with the same spacing between the spins. The results are shown in figure 5.21; they show similar characteristics to those seen in figures 5.16 and 5.18. The error is again seen to be quite large in the region of low-moderate D values. This error is reduced in magnitude (bottom part of figure 5.21) when the $T_2^{(S)}$ constant is reduced to $1 \mu\text{s}$, the range of D over which the error exceeds 5% also becomes narrower.

The crucial difference to the plots showing the error for protons is the appearance of a spike around $D = 36 \text{ MHz}$. This error is not reduced even when $T_2^{(S)}$ is reduced, because it is of a more fundamental origin than the Zeeman subspace

projection. The simulations were carried out at $B_Z = 3.4$ T, meaning the Larmor frequency ω_I of ^{13}C nuclei is approximately 34 MHz. The error spike for high D values appears due to a violation in the conditions of the projection of the dynamics into the zero-quantum subspace, shown in eq. (5.4). In order to avoid this issue, one can either carry out simulations for bi-radicals that do not exceed this electronic coupling strength, or the simulations could be carried out at a higher magnetic field, increasing ω_I .

5.3.4 Error testing summary

In summary the formalism is correct and suitable for simulations involving bi-radical molecules. For low-moderate microwave field amplitude values, studies can be accurately carried out on systems resembling two mono-radicals in close proximity at the CE-DNP resonance condition – for example at $\omega_1 = 100$ kHz, simulations can be carried out for separations between the electronic spins of ~ 40 Å or less.

There is a region of parameters corresponding to low-medium electronic coupling strength D where the error becomes large, and it is shown here that this error is reduced if the the electronic decoherence time is set to an experimentally reasonable and realistic value of of $1 \mu\text{s}$. It also helps if the $T_1^{(S)}$ time-constant is increased. Thus simulations in this range of D values can be carried out for bi-radicals with a larger distance separating the electron spins, studied at low temperatures – typically of a few Kelvin, where the $T_1^{(S)}$ times increase very significantly.

5.4 Spin diffusion studies

In order to study spin diffusion in 1-D chains of nuclear spins interacting with a bi-radical electron spin pair; a treatment similar to that applied in the case of SE-DNP (section 3.3.1) was implemented. The testing geometry is shown in figure 5.22.

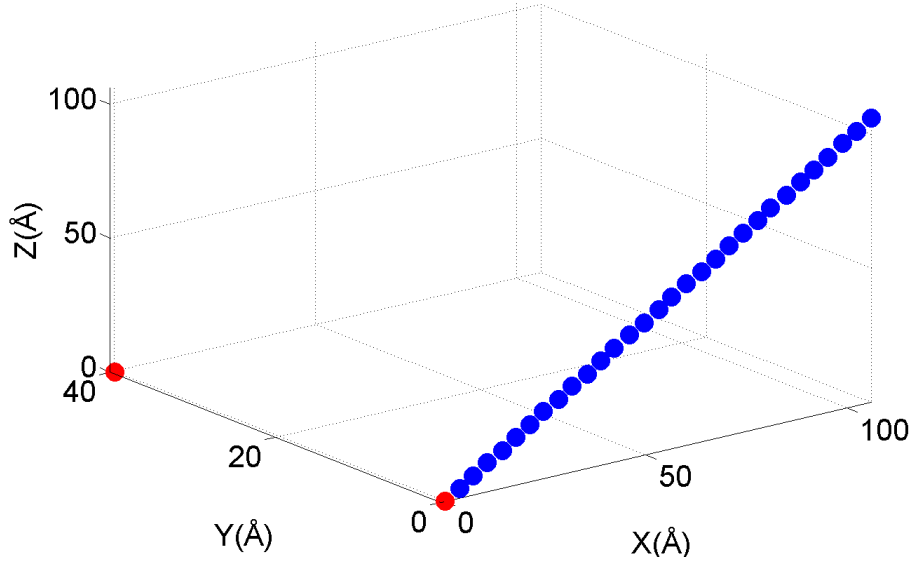


Figure 5.22: Spin chain of 30 ^{13}C nuclei (blue dots) next to an electron spin pair (red dots). The nuclear spin chain is at an angle of 45° to the magnetic field. The separation of the electron spins was set to 40 \AA , and the separation between the nuclear spins (and the distance between electron 2 and the nearest nucleus) was set to 5 \AA . A 5 % uniform randomization was applied to the position of all spins.

As in the case of SE-DNP, the first nucleus – treated and referred to as the core nucleus – is the effective source of polarization diffusing into the spin chain. The effective rate corresponding to the inter-nuclear flip-flops driving spin diffusion in eq. (5.13) shows dependence on the states of both electrons, of which there are a total of four possible permutations.

For simplicity of the diffusion analysis in the 1-D chain, the four effective dipolar interaction rates were averaged. The following parameters were used for the simulations: $\omega_1 = 50 \text{ kHz}$, $T_1^{(S)} = 14.3 \text{ ms}$, $T_2^{(S)} = 10 \text{ }\mu\text{s}$, $T_1^{(I)} = \infty$, $T_2^{(I)} = 100 \text{ }\mu\text{s}$, $B_Z = 3.4 \text{ T}$. The electronic spins were set to be separated by 40 \AA , the inter-nuclear separations, as well as the distance between the second electron to the core nucleus were set to 5 \AA . The nuclear spin chain was placed at an angle of 45° to B_Z . A uniform, 5 % randomization was applied to the position of each spin. Figure 5.16 shows that the parameters chosen here do not result in a large error and are reliable.

Figure 5.23 shows the polarization contours in the spin system, as a function of time and distance from the effective source, thus indicating the spin-diffusion pathways. A comparison to the early-time contours shows a good fit to the reflective-boundary solution to the diffusion equation (eq. (3.33)) – discussed in more detail in section 3.3.1. Unsurprisingly then the mechanism of polarization transport to the bulk in systems exhibiting CE-DNP is spin diffusion. One of the assumptions is that rate-limiting step is the transfer of polarization between the core nucleus to the bulk nuclei. This would imply that the rate of diffusion would

be the same for a given system regardless of whether the mechanism of nuclear polarization build-up is SE-DNP or CE-DNP – which tends to be more efficient.

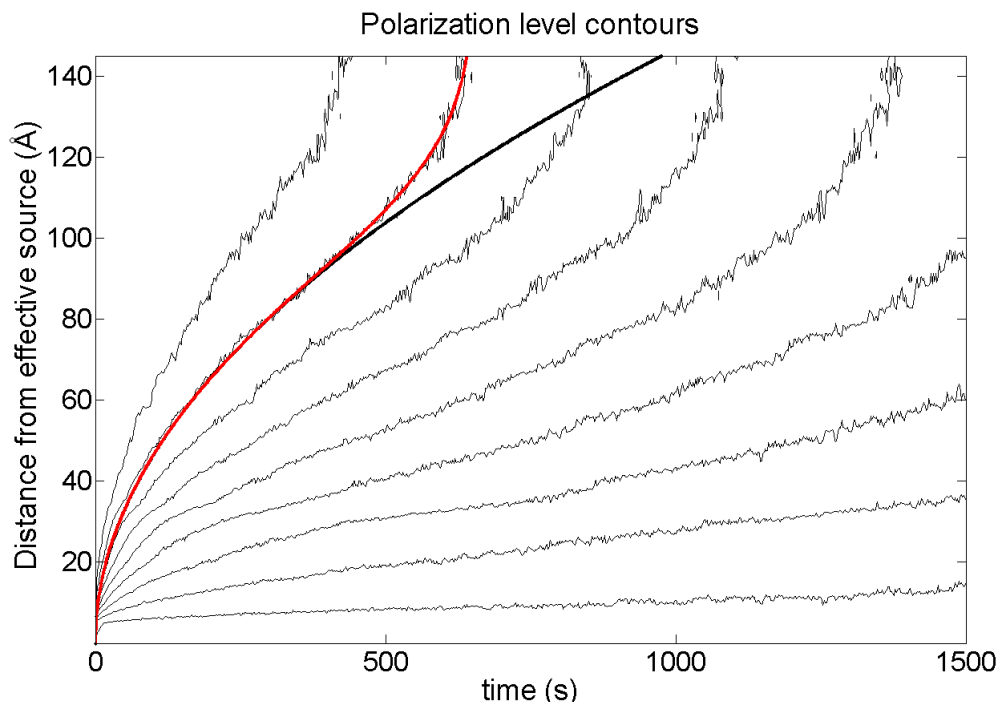


Figure 5.23: A comparison of polarization contours to solutions to the diffusion equation with a reflective boundary (red) and without (black), for the geometry seen in figure 5.22. An average over 100 000 trajectories was taken. The polarization contours correspond to polarization level increments of 8 %. There is a better fit of the reflective boundary solution to the polarization contour in the case of CE-DNP, than was seen for SE-DNP.

In order to verify this, a comparison was made to SE-DNP. The same system geometry (figure 5.22) was used with electron 1 (on-resonance to the microwave radiation) removed. The relaxation parameters and ω_1 were left unchanged. The result is shown in figure 5.24 – top part. The bottom part shows a comparison between the mean nuclear polarization in the chain during build-up for CE-DNP and SE-DNP. The polarization diffusion constant calculated in the cases of both CE-DNP and SE-DNP was the same at a value of $5.39 \text{ \AA}^2/\text{s}$. This is expected, however, a comparison between figures 5.23 and 5.24 shows a significant difference. The system exhibiting CE-DNP shows a quicker polarization build-up – particularly in the very early stages. In the bottom part of figure 5.24 it does however appear that the polarization levels would equalise after a long time; at steady-state. The polarization contours in figure 5.23 do fit the solution to the diffusion equation much more closely than in the top part of figure 5.24.

It appears that even though in both cases the exchange between the core and bulk nuclei is the rate-limiting step and the rates of diffusion are identical, the

exchange between the bi-radical and the core nucleus is much quicker and much more efficient than in the single-electron case (SE-DNP), leading to diffusion of 'more' polarization down the chain. In addition, the initial build-up in CE-DNP is much faster – this is particularly pronounced in the bottom part of figure 5.24 – leading to a 'jump' in early polarization levels.

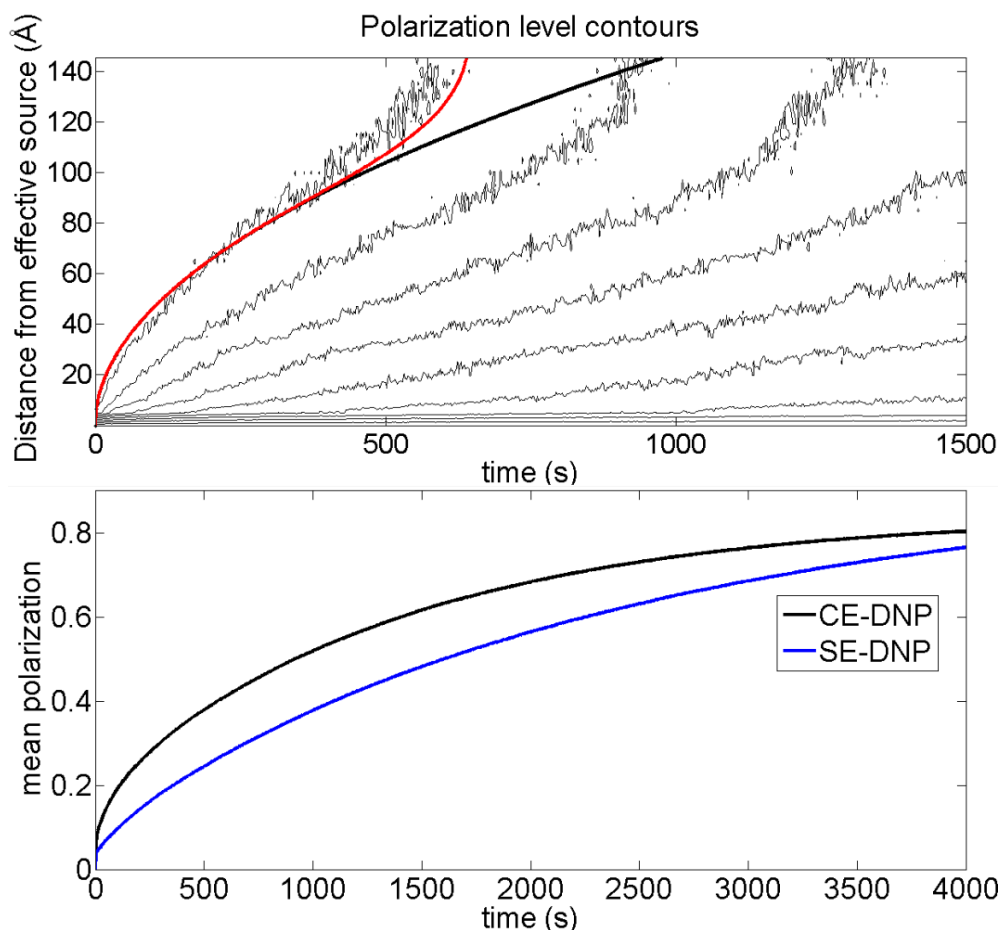


Figure 5.24: A comparison of polarization contours to solutions to the diffusion equation with a reflective boundary (red) and without (black) for SE-DNP, in the geometry seen in figure 5.22 – first electron is removed. The polarization contours correspond to polarization level increments of $\sim 7\%$. An average over 10 000 trajectories was taken. The bottom part of the figure shows comparison curves, averaged over the number of nuclei for the two mechanisms. The comparison illustrates that even though the rates of polarization diffusion across the chain are the same, the transport of polarization is more efficient in CE-DNP. At steady-state the two curves would reach the same level.

The efficiency of CE-DNP over SE-DNP is demonstrated and discussed further in the next sections.

5.5 Optimisation studies

The analytical form of the effective dynamics for CE–DNP in eq. (5.14) provides a clearer insight into the mechanism that leads to build–up of nuclear polarization. The form of the rates also provides a hint to the possibility of increasing the efficiency of the mechanism and making the process more optimised. For the CE–DNP mechanism to be efficient, the rates corresponding to operators \hat{Y}_0, \hat{Y}_{3k} in eq. (5.14) should be as large as possible. The rate corresponding to \hat{Y}_0 describes the process of saturation of the on–resonance electron, whereas the rate corresponding to \hat{Y}_{3k} describes the three–spin flip processes characteristic of the CE–DNP mechanism.

The state dependent coefficients \hat{P}_0, \hat{P}_{3k} reduce the magnitude of the respective rates. The presence of the offset terms λ_1 , and λ_2 in the respective coefficients points to a possibility of ‘tuning’ and reducing the magnitude of operators \hat{P}_0, \hat{P}_{3k} . The parameter \hat{P}_0 depends on $\omega_I, D, A_k^{(1)}$, and b_{k1} , which in turn depends on $B_{k\pm}^{(1)}, B_{k\pm}^{(2)}$. The secular and pseudo–secular coupling coefficients are geometry–dependent and thus vary between spins. The nuclear Larmor frequency and the electronic dipolar coupling are constants in the model spin systems, thus the magnitude of \hat{P}_0 can be reduced by setting λ_1 to $\lambda_1 = -D + \frac{D^2}{4\omega_I}$.

The coefficients \hat{P}_{3k} depend on $\omega_1, \omega_I, D, A_k^{(1)}, A_k^{(2)}, b_{k0}, b_{k1}$. The last two – b_{k0}, b_{k1} depend on the pseudo–secular coupling of a nucleus to the electron spins. Again, the secular and pseudo–secular couplings are dependent on the geometry and thus will vary between spins. The parameters ω_I, ω_1, D are constants in our spin systems, thus the magnitude of \hat{P}_{3k} is reduced by setting $\lambda_2 = -\frac{\omega_1^2 + D^2}{2\omega_1}$.

Going back to the definition of λ_2 ($\lambda_2 = \Delta_2 - \Delta_1 - \omega_I$), this would imply that the exact CE–DNP resonance condition is

$$\Delta_2 - \Delta_1 = \omega_I - \frac{\omega_1^2 + D^2}{\omega_I^2}.$$

In practice, it is likely that this exact resonance condition will be nearly impossible to target because of the dependence on ω_1 which will vary between experiments and experimental set–ups, and because of the fact that in experiments it is likely that – due to a distribution of orientations of bi–radicals – D will also vary.

What also follows is that the first electron should be irradiated at

$$\Delta_1 = -D + \frac{D^2}{4\omega_I},$$

and not directly on–resonance with the microwave radiation. This is much more realistic to achieve experimentally.

This was verified using the Zeeman master equation, eq. (5.16) for a range of

λ_1, λ_2 , where $-35 \text{ MHz} \leq \lambda_1, \lambda_2 \leq 35 \text{ MHz}$. The test was carried out for the geometry shown in figure 5.15, with the separation between electron spins set to 13.1 \AA (corresponding roughly to the separation in TOTAPOL). With the vector combining the electron spins being perpendicular to B_Z , the D value was approximately 11.6 MHz . One percent randomization in the position of all spins was applied, and the following parameters were used: $\omega_1 = 400 \text{ kHz}$, $B_Z = 3.4 \text{ T}$, $T_1^{(S)} = 100 \text{ } \mu\text{s}$, $T_2^{(S)} = 10 \text{ } \mu\text{s}$, $T_1^{(I)} = 10 \text{ mins.}$, $T_2^{(I)} = 0.5 \text{ ms}$. Polarization build-up was simulated for 1000 s . The result is shown in figure 5.25. It can be seen that the optimal value for λ_1 is just under -10 MHz . Given $D \sim 11.6 \text{ MHz}$, this would confirm that in fact $\lambda_1 = -D + \frac{D^2}{4\omega_1}$.

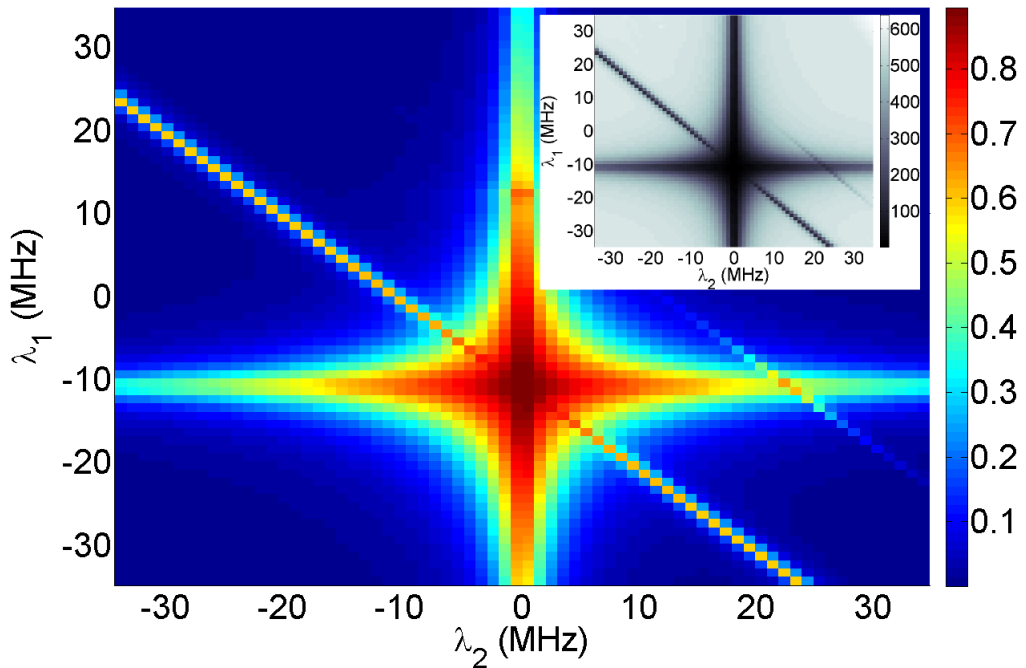


Figure 5.25: Mean steady-state nuclear polarization as a function of frequency offsets from the CE-DNP resonance condition; λ_1 and λ_2 . Nuclear polarization is normalised to the electronic thermal equilibrium polarization. The colour bar scale shows the corresponding polarization level. The insert shows the estimated polarization build-up time as a function of the same offsets. The calculation was carried out using the Zeeman-projected master equation. Offsets λ_1, λ_2 are varied in steps of 0.67 MHz .

The result is less obvious for λ_2 where the optimal point lies close to 0. Numerically evaluated for this simulation, the value of $\lambda_2 = -\frac{\omega_1^2 + D^2}{2\omega_1}$ is $\approx -0.47 \text{ MHz}$, which would be difficult to see with the resolution of figure 5.25. This result was then compared to the output seen from the full master equation (eq. (5.2)) using the same parameters, in order to verify the accuracy. The result is seen in figure 5.26. Using the definitions of offsets λ_1, λ_2 , it is clear to see that figure 5.26 shows the same results as figure 5.25, on a different grid. There is a transformation of

coordinates between the two figures.

There is an agreement between the simulation results, and the predictions from using the operator-valued coefficients \hat{P}_0, \hat{P}_{3k} in eq. (5.15).

It is, finally, also worth noting that adjusting the offset values to increase the efficiency of CE-DNP by setting $\lambda_1 = -D + \frac{D^2}{4\omega_I}$, $\lambda_2 = -\frac{\omega_1^2 + D^2}{2\omega_1}$ will very notably reduce the efficiency of the SE-DNP mechanism in the system, as the operator-valued coefficient \hat{P}_{2k} then has an offset $\lambda_1 + \lambda_2 = -D - \frac{2\omega_1^2 + D}{4\omega_I}$. This will increase the value of \hat{P}_{2k} by $\sim D$, hence in the cases of strong electronic dipolar coupling the rate $\Gamma_k^{(IS)}$ will be quenched.

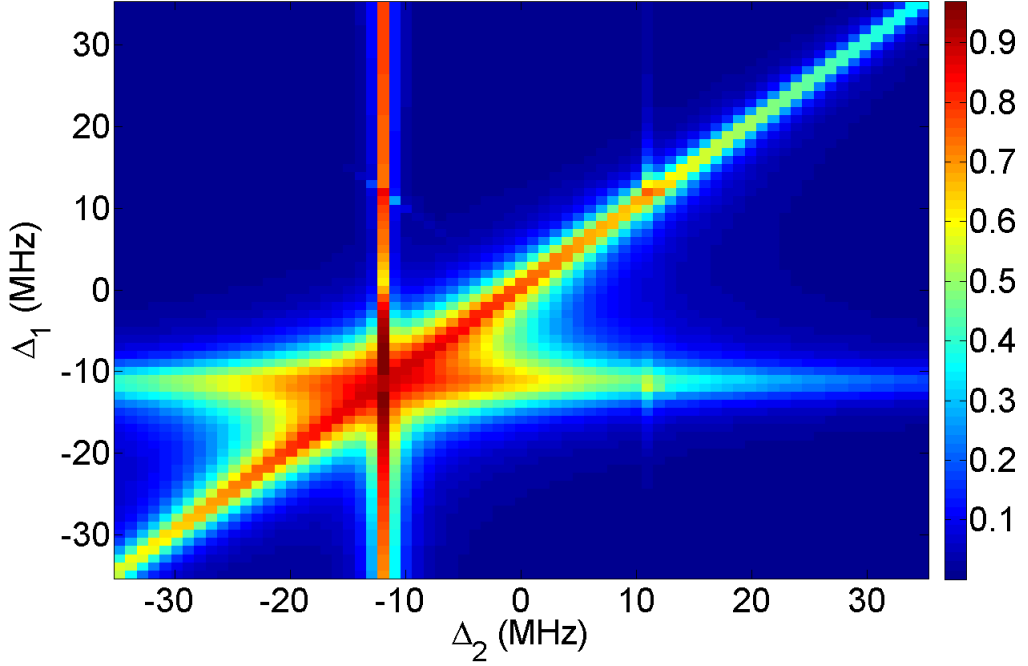


Figure 5.26: Mean steady-state nuclear polarization as a function of frequency offsets Δ_1 and Δ_2 , calculated using the full master equation. Nuclear polarization is normalised to the electronic thermal equilibrium polarization. Offsets Δ_1, Δ_2 are varied in steps of 0.67 MHz.

5.5.1 Optimising bi-radical coupling

The rate $\Gamma_k^{(ISS)}$ was plotted as a function of D with $\lambda_2 = 0$ – as it was mentioned before, it would be difficult to match the condition of $\lambda_2 = -\frac{\omega_1^2 + D^2}{2\omega_1}$ experimentally. The test system shown in figure 5.15 was used with the following parameters: $\omega_1 = 400$ kHz, $B_Z = 3.4$ T, $T_1^{(S)} = 100$ μ s, $T_2^{(S)} = 10$ μ s, $T_1^{(I)} = 10$ mins., $T_2^{(I)} = 0.5$ ms. In addition, the rate $\Gamma_k^{(IS)}$ corresponding to the SE-DNP mechanism was plotted on the same graph, as a function of D . The offset λ_1 in that rate was also set to 0. To establish where the CE-DNP mechanism is inefficient, the same rate was plotted in the case of electron 1 being removed from the system completely.

The results are shown in figure 5.27. The top part of the figure clearly shows the three-spin rate (red) decaying below the value of the rate $\Gamma_k^{(IS)}$ when $D < 1$ MHz. The black and blue lines are seen to overlap perfectly in the region where $D =$ a few tens of kHz. In this regime the electrons become decoupled and the CE-DNP mechanism is completely quenched.

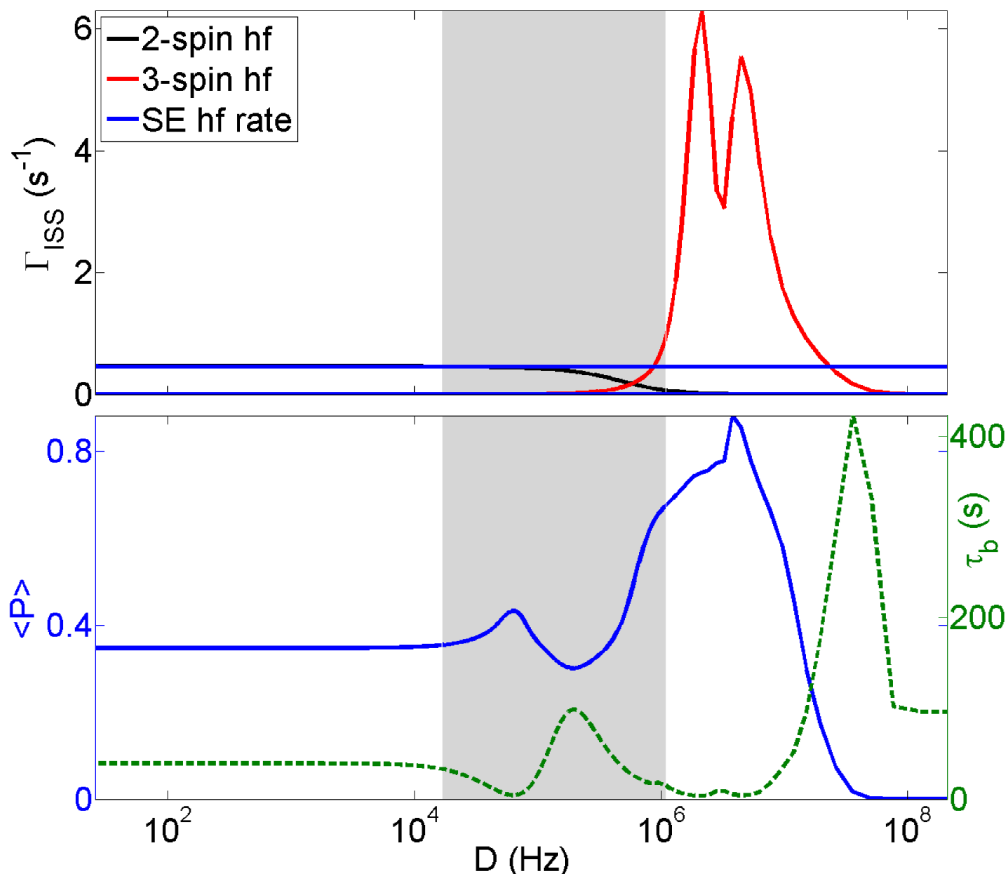


Figure 5.27: Top part – the effective three-spin interaction rate $\Gamma_k^{(ISS)}$ is plotted in red as a function of D , averaged over the 3 nuclear spins. The rate $\Gamma_k^{(IS)}$ corresponding to the two-spin interaction characteristic of SE-DNP is plotted in black. The blue line corresponds to the value of the rate $\Gamma_k^{(IS)}$ for a system where the first electron is removed altogether.

Bottom part – plot showing the mean nuclear polarization (in blue) as well as the build-up time (in green) as a function of D for the same system.

The grey shaded area covers the same region as that in figure 5.16, indicating the parameter region with excessive error. A link is seen between $\Gamma_k^{(ISS)}$ rate magnitude and polarization build-up efficiency.

Figure 5.27 (top part) shows the three spin rate ($\Gamma_k^{(ISS)}$) peak in the region of a few MHz. A comparison to the bottom part of that figure shows clearly that this corresponds to a region of D values resulting in the largest steady-state nuclear polarization (blue line) and the shortest build-up times (green line). Thus a clear link is established between the rate magnitude and polarization build-up

efficiency.

A dip is seen in the three-spin effective rate when averaging over three nuclei. A closer look at the operator-valued coefficient \hat{P}_{3k} points to the reason as to why this happens. It is likely that for one or more of the nuclei in fig. 5.15 at some positions of the first electron; the values of D and $B_{k\pm}^{(1)}$ lead to a high value of \hat{P}_{3k} and thus a reduced rate $\Gamma_k^{(ISS)}$. Plotting this rate for a cubic system of 120 nuclei shows this problem does not appear – figure 5.28.

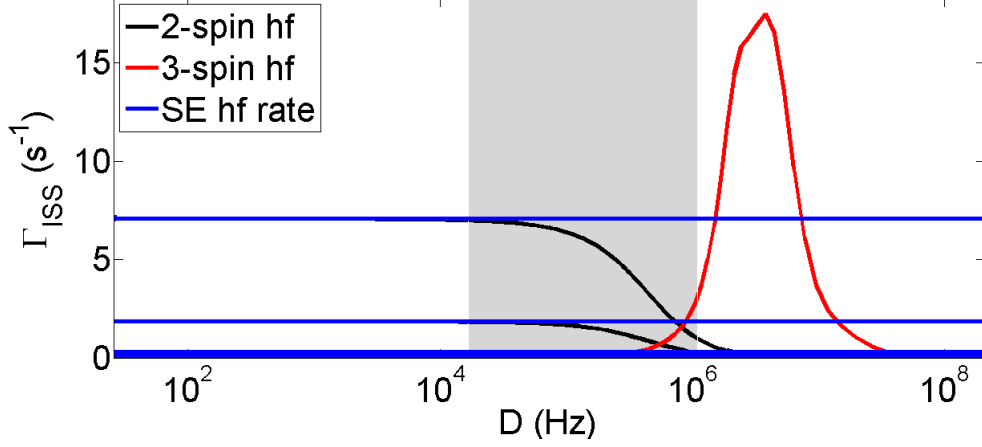


Figure 5.28: The effective three-spin interaction rate $\Gamma_k^{(ISS)}$ is plotted in red as a function of D , averaged over the 120 nuclear spins. The system is a cubic lattice with nearest neighbour separation of 6.8 Å, as previously. All other parameters are kept the same as in figure 5.27. Nuclear spins along the line where x is variable and $y, z = 0$ are removed, as the position of the first electron spin is varied.

The three-spin effective rate $\Gamma_k^{(ISS)}$ in eq. (5.14) was then recalculated as a function of D for $T_2^{(S)}$ reduced from 10 μs to 1 μs , with all other parameters being kept the same. The result is shown in figure 5.29.

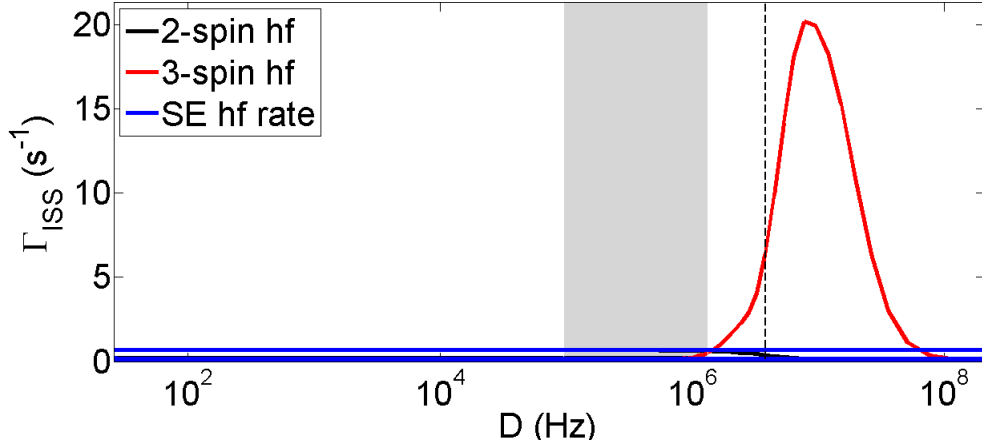


Figure 5.29: The effective three-spin interaction rate $\Gamma_k^{(ISS)}$ is plotted in red as a function of D , averaged over the 120 nuclear spins. The system is a cubic lattice with nearest neighbour separation of 6.8 \AA as previously. All other parameters are kept the same as in figure 5.27, with the exception of the decoherence time $T_2^{(S)} = 1 \mu\text{s}$. Reducing the decoherence time clearly shifts the peak with respect to figure 5.28.

With $T_2^{(S)}$ reduced to $1 \mu\text{s}$ the distribution showing the average effective rate value shifts from 3.8 MHz to $\sim 9 \text{ MHz}$. The dashed, vertical black line in figure 5.29 shows where the centre of the red curve was at $T_2^{(S)} = 10 \mu\text{s}$. In addition to the curve of the three-spin rate shifting to higher D values, the peak value increases by $\sim 15 \%$.

These results suggest that the rate $\Gamma_k^{(ISS)}$ depends on both D and $T_2^{(S)}$. These two parameters were then varied independently, and the rate $\Gamma_k^{(ISS)}$ recalculated each time. The results are shown in 2-D in figure 5.30.

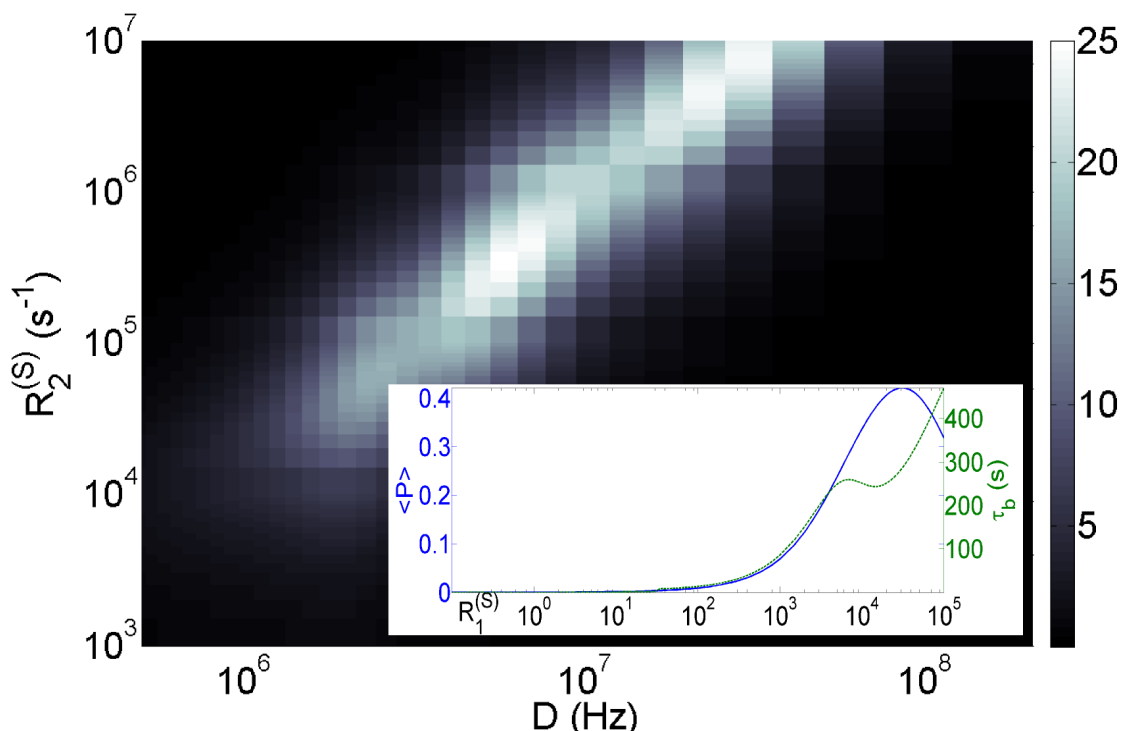


Figure 5.30: The effective three-spin interaction rate $\Gamma_k^{(ISS)}$ is mapped as a function of D , and $R_2^{(S)}$ averaged over the 120 nuclear spins. The grey-scale bar shows the magnitude of the rate $\Gamma_k^{(ISS)}$ for a particular set of D and $R_2^{(S)}$ values. The insert shows the steady-state polarization (blue) and build-up time (green) as a function of $R_1^{(S)}$ – the $T_1^{(S)}$ inverse. Due to the restriction of using a master equation, the system geometry in figure 5.15 was used for the insert calculation. A $T_2^{(S)}$ value of $10 \mu\text{s}$ was used for this calculation, $\omega_1 = 100 \text{ kHz}$, and $D = 3.8 \text{ MHz}$. The figure shows that for increasing D coupling strengths a shorter decoherence time is also required, and there exists an optimal $T_1^{(S)}$ for highest polarization.

A very clear dependence on both the transverse relaxation rate $R_2^{(S)}$ and the electronic dipolar coupling D is seen. For stronger dipolar coupling D there is a corresponding optimal $R_2^{(S)}$ value, that will maximise the value of the effective rate $\Gamma_k^{(ISS)}$. The insert also hints at the existence of an optimal $R_1^{(S)}$ value for which the steady-state polarization of the system will be greatest. Given the result of the comparison in figure 5.27 it can thus be expected that the efficiency of the CE-DNP mechanism, seen as an output in nuclear polarization, depends on the relaxation parameters of the electron spins, and the dipolar coupling between them.

AMUPol and TOTAPOL [65] are bi-radicals that perform quite well in MAS CE-DNP experiments, resulting in rapid build-up of polarization leading to large enhancements. The relaxation parameters measured for those bi-radicals in [73] (written out at the end of section 5.3.2) appear in agreement with the theoretical

prediction of figure 5.30. The $T_1^{(S)}$ time measured by the authors lies close to the peak of the insert in figure 5.30. The $T_2^{(S)}$ values measured by the authors, and the corresponding D values of those bi-radicals, which are accurately known, place these bi-radicals along the 'white' ridge of $\Gamma_k^{(ISS)}$ values of figure 5.30.

It is important to keep in mind that formalism we have developed is applicable to static samples, the studies of which are currently rather limited [69, 75, 76].

The output seen in figure 5.30 is likely to change with microwave field amplitude, however it is not expected the difference would be very significant. The trend with respect to D and $T_2^{(S)}$ is expected to be the same. The insert of figure 5.30 on the other hand is expected to be quite dependent on D , ω_1 , and $T_2^{(S)}$, but it is expected some optimum would exist for a chosen parameter set. The master equation in eq. (5.16) can be used for a set of desired parameters to determine the optimal $T_1^{(S)}$.

Microwave power

Regardless of the fact that the dependency of the efficiency of CE-DNP on the microwave field amplitude is less severe than that seen in SE-DNP [37], it is reasonable to expect that there may be some optimal level of microwave power. To investigate this, several simulations were ran for a cuboid system of 148 ^1H spins with a bi-radical embedded within the nuclear spin lattice. The separation between nearest-neighbour spins was set to 6.8 Å, D was set to 3.8 MHz (19 Å separation), $T_1^{(S)} = 100 \mu\text{s}$, $T_2^{(S)} = 10 \mu\text{s}$, $T_1^{(I)} = 10 \text{ mins}$, $T_2^{(I)} = 0.5 \text{ ms}$, $B_Z = 3.4 \text{ T}$, and a 3 % uniform randomization was applied to the position of the spins. Simulations were carried out for ω_1 values of 5 kHz, 20 kHz, 50 kHz, 100 kHz, 200 kHz, 400 kHz, 700 kHz, and 1000 kHz (the error for which has been verified to be below 5% at $D = 3.8 \text{ MHz}$). A comparison was then made between the mean nuclear polarization levels reached in each case, after an irradiation of 5 s. Error bars were established based on the error in the effective formalism, eq. (5.16) at the value of $D = 3.8 \text{ MHz}$. The result is shown in figure 5.31.

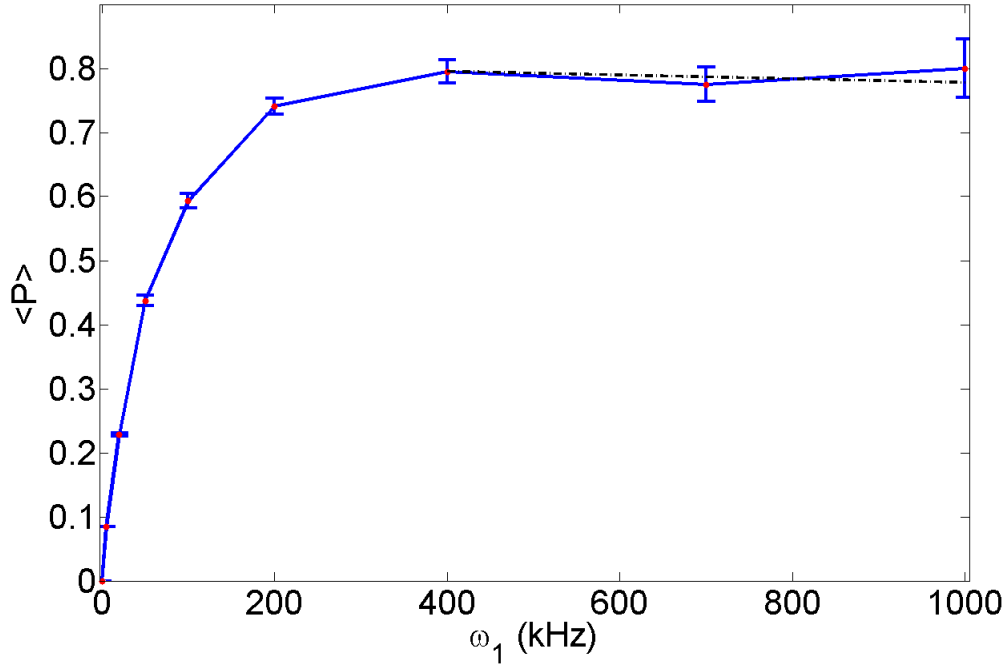


Figure 5.31: Mean sample polarization as a function of microwave field amplitude ω_1 , plotted with the estimated error bars. Each point corresponds to the mean nuclear polarization after 5 seconds of build-up, for a given microwave field amplitude. The black, dashed line shows a linear fit to the last three data points based on their scatter.

A line of best fit is also plotted for the last three points in order to take into account the larger magnitude of error that is seen for these points. The optimal point of microwave power appears to be around $\omega_1 = 400$ kHz, after that the polarization levels drop.

5.5.2 Simulations for bi-radicals with optimised parameters

Having determined a set of optimal parameters, a large spin simulation was implemented. The system of choice was the same cuboid ($5 \times 6 \times 5$) with 148 nuclear spins surrounding a pair of electronic spins. The separation between nearest-neighbour nuclear spins was 6.8 \AA , D was set to 3.8 MHz (19 \AA separation), $T_1^{(S)} = 100 \text{ } \mu\text{s}$, $T_2^{(S)} = 10 \text{ } \mu\text{s}$, $T_1^{(I)} = 10 \text{ mins}$, $T_2^{(I)} = 0.5 \text{ ms}$, $B_Z = 3.4 \text{ T}$, and a 3 % uniform randomization was applied to the position of the spins. The resonance offset terms λ_1 , λ_2 have been set to their optimal values, determined previously. The microwave field amplitude was, however, dropped to $\omega_1 = 100 \text{ kHz}$, as this reduced the computational time by a factor of ~ 16 . Figure 5.31 shows that a drop in ω_1 from 400 kHz to 100 kHz reduces the polarization level by 33 %, implying the build-up time has not been severely increased. The polarization build-up of

individual spins, in time is shown in figure 5.32.

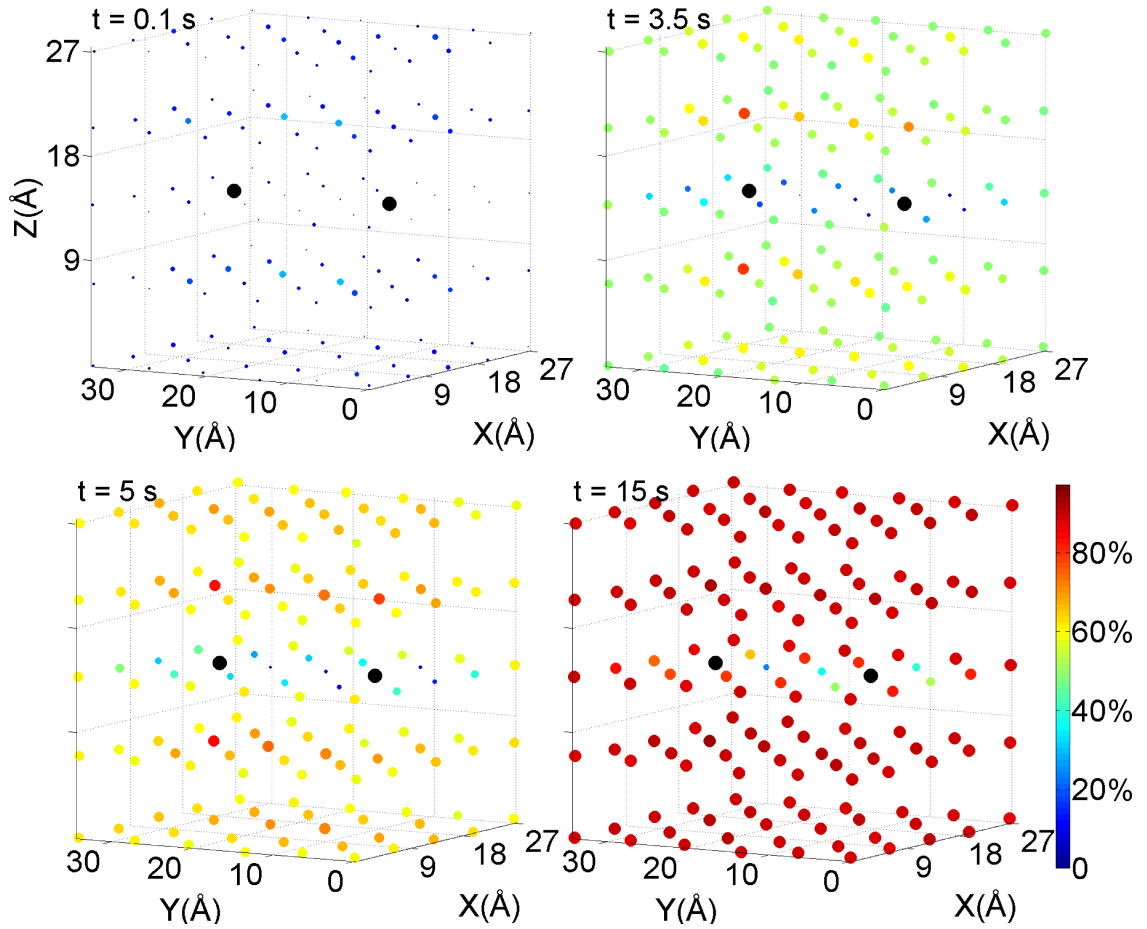


Figure 5.32: Time–shots showing the build–up of polarization in the cuboid system with optimised parameters. The diameter and colour of the spheres indicates the nuclear polarization value for each spin – the scale of which is shown on the colour bar. The black dots represent the electron spins. A very rapid build–up of polarization is seen. After 15 s the average nuclear polarization is 90 % and the spins are close to steady–state.

A rapid build–up of polarization is seen in the spin system, with most nuclei reaching $\sim 90\%$ polarization after 15 seconds of irradiation. Nuclei in–plane with the electron spin pair; i.e. the plane where the coordinate $Z \approx 0$, reach lower levels of polarization in comparison to the remainder of the system. Particularly the nuclei closest to either electron spin or those in–between the electron spins. These nuclei are shifted in frequency (an effect analogous to what has been described in section 4.3) due to the very strong secular coupling to the electronic spins, and thus the mechanism (corresponding to rates $\Gamma_k^{(ISS)}$, $\Gamma_k^{(IS)}$) of polarization transfer for these nuclei is less effective. The mechanism of CE–DNP was directly compared here to the mechanism of SE–DNP. The first electron spin was moved

far out of the system (figure 5.32) – the large spacing resulted in a D value of 1.7 kHz – which was previously determined to mean that the CE–DNP mechanism is quenched completely – and the simulation re–run with the same parameters. The comparison is shown in figure 5.33.

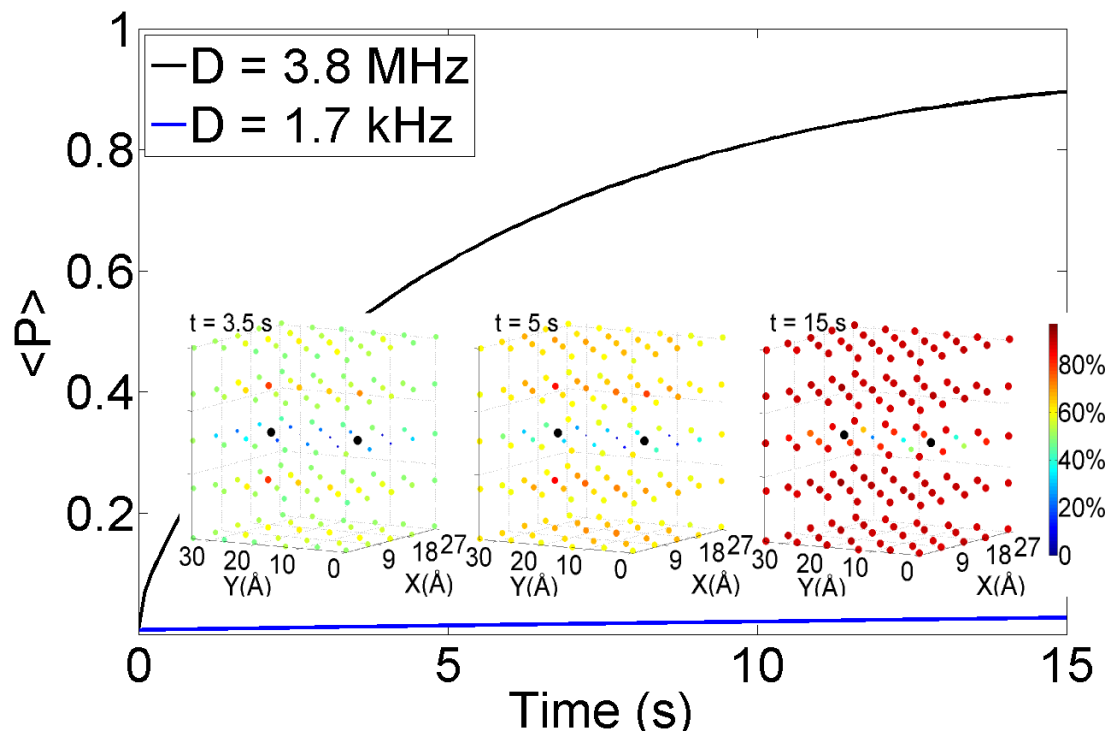


Figure 5.33: A direct comparison between a simulation where CE–DNP is the dominant polarization build–up mechanism (black line), for a carefully selected choice of parameters, to the case where CE–DNP is quenched and SE–DNP is the only active mechanism (blue line), as the first electron spin is placed 250 Å away from the second electron spin. In the case of CE–DNP a polarization level of 90 % is reached. For SE–DNP the level of polarization is at 2.7 %. The insert shows the time–shots at 3.5 s, 5 s, and 15 s from figure 5.32.

The nuclear spins in the system where CE–DNP is active reach a level 90 % mean polarization after 15 seconds. The build–up time constant has been estimated by a linear fit to be $\sim 5\text{s}$, and an extrapolation in time ($t \rightarrow \infty$) indicates that a level of 95 % polarization would be reached by this system. This is compared to the blue line (SE–DNP) where the level of polarization hardly changes. After 15 s of build–up, the system reaches a level of 2.7 % polarization. This shows the superiority of CE–DNP quite clearly. It is to be noted from previous work that the reflective boundary effects (3.3.1) experienced in the system due to its finite size exaggerate the polarization levels significantly, for both simulations.

5.5.3 CE–DNP at low temperature

It has been shown in this chapter that CE–DNP can be very efficient with the use of bi–radicals and high microwave power (generally leading to high ω_1), what is important there, as shown in figure 5.30 is that the $T_1^{(S)}$ time should be sufficiently short, so that the first electron is not completely saturated by the microwave radiation. Thus these experiments are often carried out at relatively high temperatures (typically 80–100 K) [24]. The longitudinal relaxation times T_1 are dependent on the temperature of the sample, and the magnetic field strength – in [69] for example the authors take measurements of $T_1^{(S)}$ for TOTAPOL at varying temperatures.

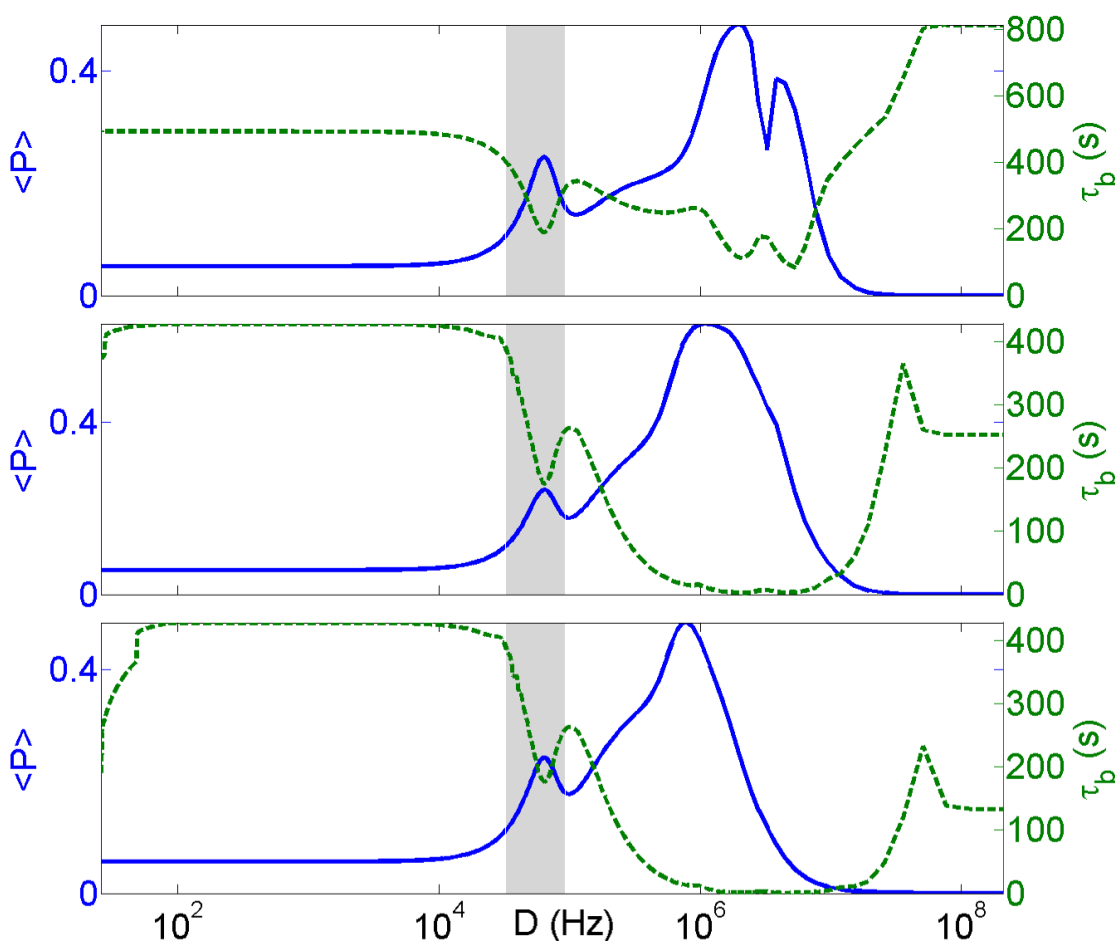


Figure 5.34: Steady–state polarization and build–up time calculated for the system geometry shown in figure 5.15. The parameters are as follows: $\omega_1 = 50$ kHz, $B_Z = 3.4$ T, $T_2^{(S)} = 10$ μ s, $T_1^{(I)} = 10$ mins., $T_2^{(I)} = 0.5$ ms. The $T_1^{(S)}$ has been varied from top to bottom as follows: top part – 100 μ s, middle part – 10 ms, bottom part – 100 ms. The shaded area shows the error regime for $\omega_1 = 50$ kHz. It can be seen that with longer $T_1^{(S)}$ times the peak of the polarization curve shifts to lower D values, implying that bi–radicals will probably not work well at very low temperatures.

At low temperatures the electronic T_1 time becomes significantly longer, and as seen in figure 5.30, with longer $T_1^{(S)}$, thus lower $R_1^{(S)}$ the efficiency of the CE–DNP mechanism would fall. The top part of figure 5.34 shows the simulation similar to that in figure 5.27 but with ω_1 reduced to 50 kHz. It can be seen that in comparison, the peak polarization value drops, and the peak of the curve (blue line) shifts to lower D values. The green curve on the same figure shows that the polarization build–up times increase significantly, even in the regime of optimal D values. The reduction in the microwave field amplitude reduces the region where the error is excessive – this is, as previously, shown by the grey shaded region of the plots.

For the middle part of figure 5.34 the $T_1^{(S)}$ time–constant has additionally been increased from 100 μs to 10 ms. Adjustment of the electronic relaxation time leads to an increase in steady–state polarization values in the regime of optimal D values, and a significant reduction in the build–up time – in comparison to the top part of the figure. The peak of the blue curve shifts again to lower D values. The bottom part of figure 5.34 shows the result for $T_1^{(S)}$ increased further, to 100 ms. Other than the peak of the blue curve further shifting to lower D values (sub–MHz) there is no significant difference.

The results included here indicate that for low temperature studies of CE–DNP, particularly where a gyrotron is not in use, and thus the microwave field amplitude ω_1 is much lower; bi–radicals with very strong coupling might not be very efficient. Instead bi–radicals with a greater spacing between the electron spins (leading to lower D) or mono–radicals at relatively high concentration might be beneficial, and prove more efficient for increasing nuclear polarization.

Large spin system simulations

As was the case with the SE–DNP effective formalism, the CE–DNP effective dynamics allow simulating large spin ensembles. Having established the parameter regions where the effective formalism is accurate, a cuboid spin system containing 808 ^{13}C nuclear spins, with a 10 Å spin–spin separation was simulated ($9\times 10\times 9$ dimension). This is the largest simulation we have implemented to date, for CE–DNP. A 5 % randomization in the position of spins was applied. The electron spins were placed at a separation of 30 Å. The time–shots showing the polarization of nuclear spins at various times are shown in figure 5.35. The magnetic field strength B_Z was set to 3.4 T, ω_1 was set to 50 kHz, and the relaxation parameters were set to: $T_1^{(S)} = 2$ ms, $T_2^{(S)} = 10$ μs , $T_1^{(I)} = 1$ h, $T_2^{(I)} = 100$ μs .

A rapid build–up of polarization is seen for nuclei with the highest $B_{k\pm}$ values, polarization is then transferred to the bulk nuclei via spin diffusion with the rate

of diffusion along the Z axis significantly (expected to be 2 times greater) faster than within the X–Y plane; as expected. After 1000 s the core nuclei of the system are approaching a steady–state, while the polarization of the edge nuclei is slightly lower. The final mean polarization level of the ensemble is 64 %.

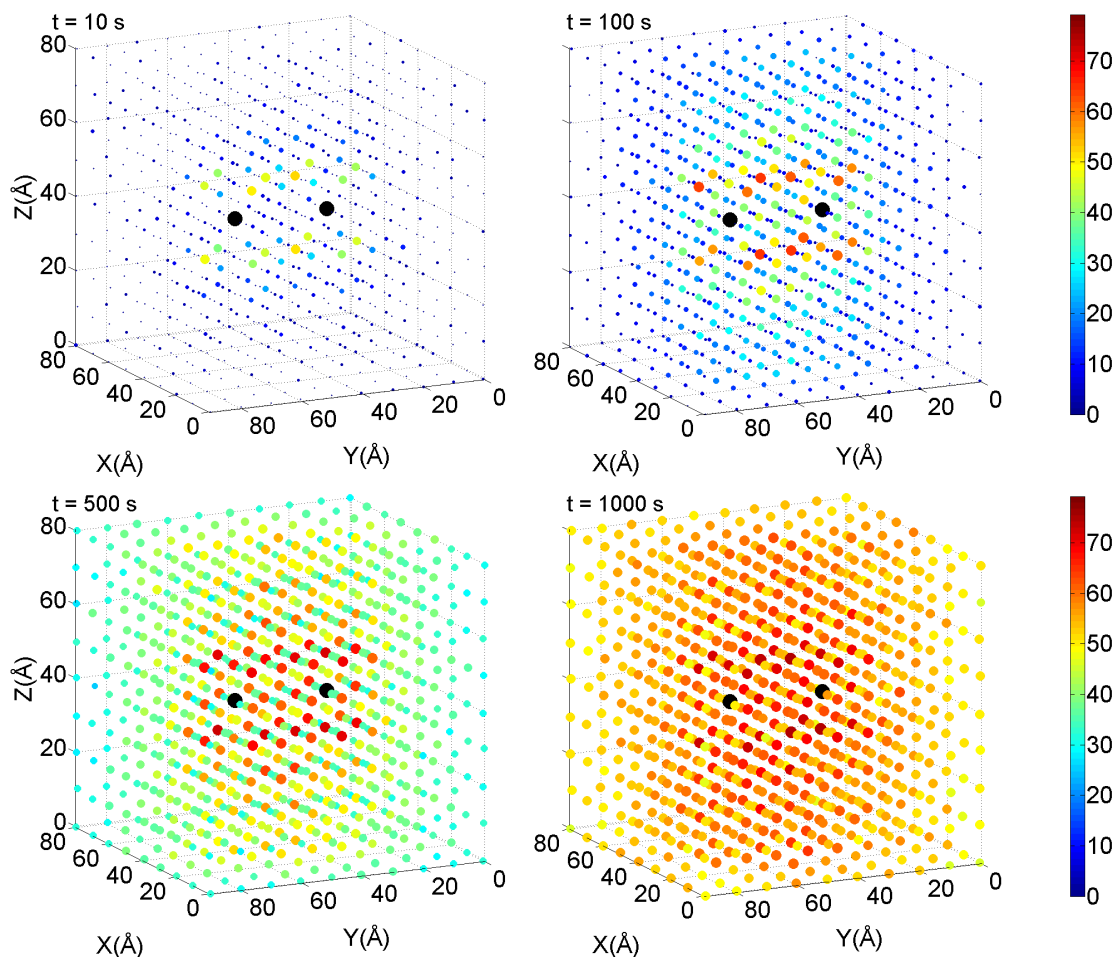


Figure 5.35: A cuboid lattice containing 808 ^{13}C spins, surrounding a bi-radical electron spin pair. The separation between the electron spins (black dots) is 30 Å, leading to D of ~ 0.5 MHz. The nearest-neighbour separation between spins is 10 Å, with a 5 % randomization in the position of each spin. The polarization levels of each nuclear spin are shown at times of 10 s, 100 s, 500 s, and 1000 s. Microwave irradiation was simulated for a time of 2000 s. The total simulation run-time was 36 days on a dual-processor Intel Xeon E5 2690 workstation.

Low temperature comparison between CE–DNP and SE–DNP

A similar system to that shown in figure 5.35 was used to make a comparison between the mechanisms of SE–DNP and CE–DNP at low temperatures for large spin ensembles. A symmetric cube was chosen ($9 \times 9 \times 9$ dimension) as this is preferred for SE–DNP simulations where the single electron spin is placed in the

centre of the system. To keep the symmetry for the equivalent CE–DNP system, the electron spins were placed at a separation of 40 Å, lowering D to 100 kHz. Such a system could correspond to a pair of mono–radical molecules whose electron spins are at the CE–DNP resonance condition ($\Delta_2 - \Delta_1 \approx \pm\omega_I$), due to a difference in their magnetic environment. The $T_1^{(S)}$ was increased to 11 ms. The microwave field amplitude was set to $\omega_1 = 100$ kHz for the system exhibiting SE–DNP (for higher efficiency), for the system with two electron spins it was left unchanged at $\omega_1 = 50$ kHz. In both systems, the nuclear–nuclear dipolar interaction was removed by setting the rates $\Gamma_{kk'}^{(II)}$ (eqs. (5.14), (3.25)) to 0. This was done to ignore spin–diffusion effects and directly compare the efficiency with which polarization is transferred directly from the electron spins to the surrounding nuclei.

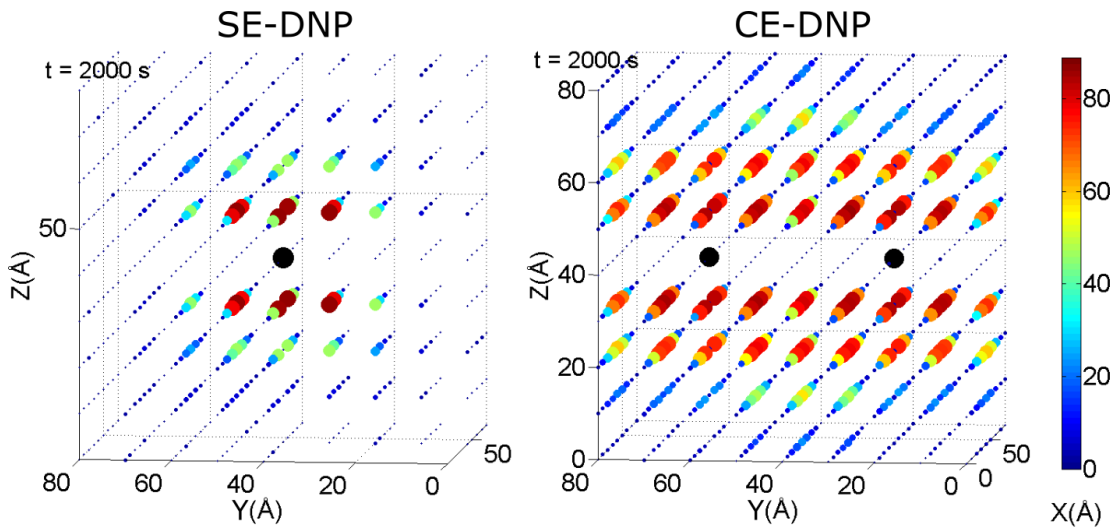


Figure 5.36: Comparison between SE–DNP and CE–DNP for the same system geometry. There are no nuclear interactions present in the system. The black dots denote electronic spins. The microwave field amplitude used in the SE–DNP simulation is twice as large as that in the case of CE–DNP, otherwise all parameters are identical. The colour bar shows the level of polarization each nucleus has at the end of the simulation. The same scale is used for both parts of the figure. With no polarization diffusion in the system, the figure illustrates that the effective range of interaction between the electrons and nuclei is significantly greater in CE–DNP.

The result is shown in figure 5.36. The figure shows a significant build–up of nuclear polarization for nuclei with relatively large $B_{k\pm}$ values. Other remaining nuclei show no polarization – as would be expected with no spin diffusion in the system. Selecting an arbitrary nuclear polarization level, and comparing the distance at which that level of polarization is found in each system; it was determined that the range of effective interaction between electrons and nuclei is greater for CE–DNP by at least a factor of $\sqrt{2}$.

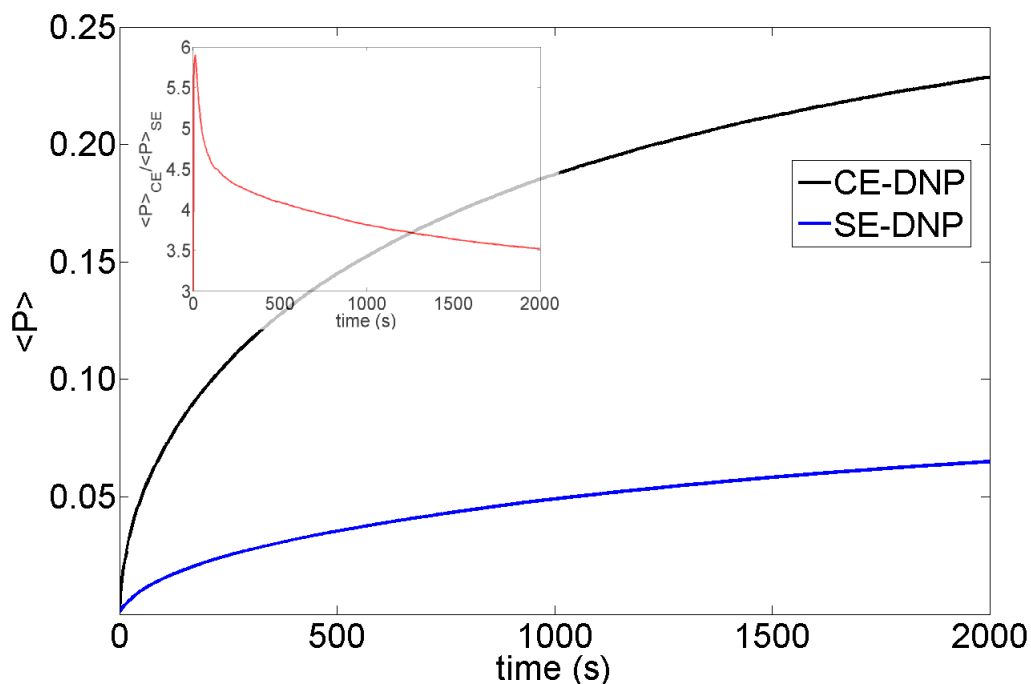


Figure 5.37: Comparison between the polarization build-up curves for SE-DNP and CE-DNP. This figure shows the mean nuclear polarization for the systems in figure 5.36. The insert shows the ratio between the polarization curves for CE-DNP (black line) to that of SE-DNP (blue line).

Figure 5.37 shows the polarization build-up curves averaged over the nuclear spin ensemble for CE-DNP (black line) and SE-DNP (blue line). The insert shows a ratio of the black curve to the blue as a function of time. It is clearly visible that the efficiency of CE-DNP is significantly higher, particularly at early times of the simulation, even though the D coupling strength here is much lower than that of bi-radicals. The relative polarization levels also show that the electron pair in CE-DNP is much more efficient at transferring polarization than two individual electrons at the SE-DNP resonance condition would be.

Chapter 6

Conclusion & Outlook

A new formalism was developed for SE-DNP and CE-DNP allowing large spin system simulations. This was carried out by projecting the dynamics of the Liouville von Neumann equation onto the diagonal of the density operator, with the use of adiabatic elimination and Nakajima-Zwanzig projection operators. The resulting, effective dynamics are incoherent and were written in the form of Lindbladian dissipators. This reduced the dimension of the dynamics from 4^n to 2^n for n spins. In addition the form of the effective dynamics allows the use of kinetic Monte Carlo algorithms, which avoid the exponential growth of the Liouville space with respect to an increasing number of spins. This permitted simulations of very large spin systems. The analytical form of the extracted effective rates provides a clear insight into the mechanism underlying SE-DNP and CE-DNP; a much clearer understanding than can be obtained from the full quantum-mechanical formalism.

A comprehensive error analysis was first carried out. We showed that our formalism is accurate for spin-spin separations down to 2 Å.

Although the formalism is accurate over a wide range of parameters, there are real systems where it is not suitable. One example of a system that cannot be modelled using the effective dynamics is a sample of silicon micro/nano-particles [74], [77]. Given the high concentration of electron radicals these samples may contain, it is questionable whether the SE-DNP mechanism is the dominant DNP mechanism, and whether the full Liouvillian in eq. (3.2) would be suitable to start with.

In our formalism the entire dynamics of SE-DNP are described using four rates, one of which is state-dependent. The rates described correspond to particular operations in the system e.g. single spin flips describing relaxation, and flip-flops describing polarization exchange between spins in the system. Simulating large linear spin systems we have found the mechanism of polarization transport to the bulk in DNP to be spin diffusion. We have simulated the polarization dynamics

in very large spin ensembles and demonstrated a possibility of fitting polarization curves of individual spins, in order to reduce the polarization error and the number of kMC trajectories executed in the simulation. We have shown the scaling of the random error associated with Monte Carlo algorithms, as well as the simulation run-time with respect to an increasing number of spins. In addition we have demonstrated how the projection onto the Zeeman subspace can be extended to heteronuclear systems, with nuclei close in Larmor frequency values. Finally for SE-DNP, we have found a formalism suitable for nuclei with lower γ values (e.g. ^{13}C) that relies on linear rates, avoiding kMC algorithms and quantum master equations, allowing one to simulate spin systems of tens of thousands of spins in a matter of minutes.

In chapter 4 the necessity and clear advantage of using large spin system simulations, when studying the mechanism of DNP, were shown. A study was conducted, analysing the effect of nuclei in immediate vicinity to the electron, on DNP performance – in terms of transport of polarization to the bulk. We studied the effect of the removal of core nuclei on polarization build-up rates of the remaining nuclei as well as their steady-state ensemble polarization values. A clear improvement in both can be seen when core nuclei – those in the immediate vicinity of the electron, are removed from the system. Build-up rates increase significantly, and the mean steady-state polarization level increases by more than a factor of 2. We have explained this using simulated DNP transition spectra, which illustrate the effect of linewidth narrowing with the removal of nuclei strongly coupled to the electron. The rate of spin-diffusion into the bulk is also significantly improved with the removal of core nuclei. Crucially, the improvement can be explained using the effective rates. The results presented here may give an insight or guidance in radical-design for optimised DNP experiments. The efficiency of designed radicals can be theoretically predicted and assessed.

Chapter 5 focuses on the effective dynamics of CE-DNP, obtained by adiabatic elimination. The entire dynamics of CE-DNP are described using seven rates, most of which are state dependent. As was the case with SE-DNP, the mechanism of polarization transport to the bulk was determined to be spin diffusion. A comprehensive error analysis was carried out and we have demonstrated that regions of excessive error can be predicted quite accurately. The formalism is suitable for simulating dynamics of systems containing bi-radicals or mono-radicals in close proximity – found at the CE-DNP resonance condition. The analytical form of the effective rates provides a clear insight into the mechanism underlying CE-DNP. A link is found between the magnitude of the three-spin rate, and the magnitude of the steady-state polarization and nuclear polarization

build-up time. The dependence of polarization on microwave power and electronic T_1 times is shown. A crucial dependence of the three-spin rate on the electronic dipolar coupling strength and decoherence times is also illustrated. The effective rates thus provide a means of predicting the efficiency of bi-radicals and give some optimisation capability; the effectiveness of a parameter choice can be studied from a theoretical point of view before synthesis. Large spin system simulations were then executed with an improved parameter choice, for bi-radicals, and this was seen to lead to a very rapid build-up of polarization.

The work presented here is one of many important steps taken to understand DNP, in order to maximise its effectiveness. We have provided a lot of new insight into the mechanisms of SE-DNP and CE-DNP for static solid-state samples, through a new formalism enabling simulations of large spin systems. The limitations of the formalism are that as it stands, it cannot be used to simulate frequency-sweep experiments nor MAS DNP. Future work will involve extensions of this formalism to the case of rotating solids.

It has been recently found that the dynamics of a system containing several electrons and one nuclear spin can be described by a master equation in the Lindblad form [78]. Work on TM-DNP and an effective formalism describing the dynamics there would be sought after. A formalism where any or all of the three solid-state DNP mechanisms are present would also be of interest. Especially since there are very few experiments published in the literature where SE-DNP seems to be the sole mechanism for generating non-thermal nuclear spin states.

Fundamental work by Vega and co-workers has demonstrated that a mixture of SE-DNP and CE-DNP is responsible for the build up of nuclear polarization at cryo-temperatures using the trityl radical [67, 79]. Even for such complex systems it appears to be feasible, based on our work involving the reduction of the required state space, to derive a set of equations that can describe the nuclear polarization dynamics.

Finally, it would be of interest to study the newly-discovered mechanisms of OE-DNP found in insulating solids during magic angle spinning, and the promising concept of pulsed DNP.

Appendix

A.1 Commutative form of Hamiltonian superoperators

As mentioned in the main text, the double-hat notation implies a commutation operation, i.e. for some arbitrary operator \hat{X} ; $\hat{\hat{X}} = [\hat{X}, \hat{\rho}]$. The form of superoperator \mathbf{M}_1 may be re-written as follows

$$\mathbf{M}_1 = -i [\hat{\hat{H}}_+, \hat{\hat{H}}_-]$$

$$\begin{aligned} [\hat{\hat{H}}_+, \hat{\hat{H}}_-] \hat{\rho} &= (\hat{\hat{H}}_+ \hat{\hat{H}}_- - \hat{\hat{H}}_- \hat{\hat{H}}_+) \hat{\rho} = \hat{\hat{H}}_+ (\hat{H}_- \hat{\rho} - \hat{\rho} \hat{H}_-) - \hat{\hat{H}}_- (\hat{H}_+ \hat{\rho} - \hat{\rho} \hat{H}_+) \dots \\ &= \hat{H}_+ \hat{H}_- \hat{\rho} - \hat{H}_+ \hat{\rho} \hat{H}_- - \hat{H}_- \hat{\rho} \hat{H}_+ + \hat{\rho} \hat{H}_- \hat{H}_+ \\ &\quad - \hat{H}_- \hat{H}_+ \hat{\rho} + \hat{H}_- \hat{\rho} \hat{H}_+ + \hat{H}_+ \hat{\rho} \hat{H}_- - \hat{\rho} \hat{H}_+ \hat{H}_- \dots \\ &= (\hat{H}_+ \hat{H}_- - \hat{H}_- \hat{H}_+) \hat{\rho} - \hat{\rho} (\hat{H}_+ \hat{H}_- - \hat{H}_- \hat{H}_+). \end{aligned}$$

Hence it is clear that

$$\mathbf{M}_1 = -i [\hat{\hat{H}}_+, \hat{\hat{H}}_-] \equiv -i \hat{\hat{H}}_1,$$

where

$$\hat{\hat{H}}_1 = (\hat{H}_+ \hat{H}_- - \hat{H}_- \hat{H}_+) = [\hat{H}_+, \hat{H}_-].$$

A.2 Explicit derivation of rate Γ^{IS} for a two-spin system

The two-spin SE-DNP, Zeeman-subspace Master equation is well approximated by

$$\dot{\hat{\rho}}_Z = (\Gamma' + \mathcal{P}_Z \mathbf{M}_2 \mathcal{P}_Z - \mathbf{L}_{0,01} \mathbf{L}_{11}^{-1} \mathbf{L}_{0,10}) \hat{\rho}_Z. \quad (6.1)$$

To find an explicit form of \mathbf{L}_{00}^{-1} , one is looking for an operator \hat{X} that satisfies

$$\mathbf{L}_{00}\hat{X}\hat{H}'_1\hat{\rho}_z = \hat{H}'_1\hat{\rho}_z.$$

Given $\hat{H}'_1 = -\frac{\omega_1}{4\omega_I} (B_+\hat{I}_+\hat{S}_- + B_-\hat{I}_-\hat{S}_+)$, we can define the operator $\hat{Y} = B_+\hat{I}_+\hat{S}_-$ for convenience. Its Hermitian conjugate is $\hat{Y}^\dagger = B_-\hat{I}_-\hat{S}_+$. With the lack of dipolar interactions in a system of one nucleus;

$$\mathbf{L}_{0,10} = \mathcal{Q}_C\hat{H}'_1\mathcal{P}_Z = \hat{H}'_1, \quad \mathbf{L}_{0,01} = \mathcal{P}_Z\hat{H}'_1\mathcal{Q}_C = \hat{H}'_1.$$

The right-hand side of eq. (6.1) is derived as follows

$$\begin{aligned} \mathbf{L}_{0,01}\mathbf{L}_{11}^{-1}\mathbf{L}_{0,10}\hat{\rho}_z &= \frac{\omega_1}{4\omega_I} (\hat{Y} + \hat{Y}^\dagger) \mathbf{L}_{00}^{-1} \frac{\omega_1}{4\omega_I} (\hat{Y} + \hat{Y}^\dagger) \hat{\rho}_z \dots \\ &= \frac{\omega_1^2}{16\omega_I^2} (\hat{Y} + \hat{Y}^\dagger) \mathbf{L}_{00}^{-1} (\hat{Y}\hat{\rho}_z + \hat{Y}^\dagger\hat{\rho}_z) \dots \\ &= \frac{\omega_A^2}{16\omega_I^2} (\hat{Y} + \hat{Y}^\dagger) \left((R_{12} + i\hat{D})^{-1} \hat{Y}\hat{\rho}_z + (R_{12} - i\hat{D})^{-1} \hat{Y}^\dagger\hat{\rho}_z \right). \end{aligned}$$

Here $R_{12} = (R_2^{(S)} + R_2^{(I)})$ and $\hat{D} = \lambda + \frac{\omega_1^2}{2\omega_I} - \frac{|B_\pm|^2}{8\omega_I}$. Both $(R_{12} \pm i\hat{D})^{-1}$ commute with \hat{Y} and \hat{Y}^\dagger , and $\hat{Y}\hat{Y}^\dagger\hat{\rho}_z = 0$ as well as $\hat{Y}^\dagger\hat{Y}\hat{\rho}_z = 0$. Thus,

$$\begin{aligned} \mathbf{L}_{z,00}\mathbf{L}_{00}^{-1}\mathbf{L}_{00,z}\hat{\rho}_z &= \frac{\omega_1^2}{16\omega_I^2} \left((R_{12} + i\hat{D})^{-1} \hat{Y}^\dagger\hat{Y}\hat{\rho}_z + (R_{12} - i\hat{D})^{-1} \hat{Y}\hat{Y}^\dagger\hat{\rho}_z \right) \dots \\ &= \frac{\omega_A^2}{16\omega_I^2} \left((R_{12} + i\hat{D})^{-1} (\hat{Y}^\dagger\hat{Y}\hat{\rho}_z - \hat{Y}^\dagger\hat{\rho}_z\hat{Y} - \hat{Y}\hat{\rho}_z\hat{Y}^\dagger + \hat{\rho}_z\hat{Y}\hat{Y}^\dagger) + \right. \\ &\quad \left. (R_{12} - i\hat{D})^{-1} (\hat{Y}\hat{Y}^\dagger\hat{\rho}_z - \hat{Y}\hat{\rho}_z\hat{Y}^\dagger - \hat{Y}^\dagger\hat{\rho}_z\hat{Y} + \hat{\rho}_z\hat{Y}^\dagger\hat{Y}) \hat{\rho}_z \right). \end{aligned}$$

Because $[\hat{\rho}_z, \hat{Y}\hat{Y}^\dagger] = 0$, $[\hat{\rho}_z, \hat{Y}^\dagger\hat{Y}] = 0$

$$\begin{aligned} \mathbf{L}_{z,00}\mathbf{L}_{00}^{-1}\mathbf{L}_{00,z}\hat{\rho}_z &= \dots \\ &- \frac{\omega_1^2}{16\omega_I^2} \left((R_{12} + i\hat{D})^{-1} + (R_{12} - i\hat{D})^{-1} \right) \left(\hat{Y}\hat{\rho}_z\hat{Y}^\dagger - \frac{1}{2} \{ \hat{\rho}_z, \hat{Y}^\dagger\hat{Y} \} \right) \dots \\ &- \frac{\omega_1^2}{16\omega_I^2} \left((R_{12} + i\hat{D})^{-1} + (R_{12} - i\hat{D})^{-1} \right) \left(\hat{Y}^\dagger\hat{\rho}_z\hat{Y} - \frac{1}{2} \{ \hat{\rho}_z, \hat{Y}\hat{Y}^\dagger \} \right). \end{aligned}$$

Since

$$\begin{aligned} \left(R_{12} + i\hat{D}\right)^{-1} + \left(R_{12} - i\hat{D}\right)^{-1} &= \frac{R_{12} - i\hat{D}}{R_{12}^2 + \hat{D}^2} + \frac{R_{12} + i\hat{D}}{R_{12}^2 + \hat{D}^2} = \frac{2R_{12}}{R_{12}^2 + \hat{D}^2}, \\ \mathbf{L}_{\mathbf{z},00}\mathbf{L}_{00}^{-1}\mathbf{L}_{00,\mathbf{z}}\rho_{\mathbf{z}} &= -\frac{\omega_1^2}{8\omega_I^2} \frac{R_{12}}{R_{12}^2 + \hat{D}^2} \left(\mathbf{D}[\hat{Y}] + \mathbf{D}[\hat{Y}^\dagger]\right) \rho_{\mathbf{z}}. \end{aligned}$$

The complex coefficients B_{\pm} can be factored out, by taking out the absolute value $|B_{\pm}|$, allowing the operator \hat{Y} to be re-written as $\hat{Y} = \hat{I}_+\hat{S}_-$, and hence the nuclear-electronic flip-flop dissipator becomes

$$\Gamma_1^{(IS)} = \frac{\omega_1^2 |B_{\pm}|^2}{8\omega_I^2} \frac{R_{12}}{R_{12}^2 + \hat{D}^2} \left(\mathbf{D}[\hat{Y}] + \mathbf{D}[\hat{Y}^\dagger]\right), \quad (6.2)$$

where as before $\hat{Y} = \hat{I}_+\hat{S}_-$, $R_{12} = R_2^{(S)} + R_2^{(I)}$, and $\hat{D} = \lambda + \frac{\omega_A^2}{2\omega_I} - \frac{|B_{\pm}|^2}{8\omega_I}$.

A.3 Computational form of operator-valued rates

For an arbitrary Hermitian operator \hat{S}_α , acting on an arbitrary density operator $\hat{\rho}$;

$$\hat{S}_\alpha = \begin{pmatrix} \alpha & \gamma \\ \gamma^* & \beta \end{pmatrix}; \quad \hat{\rho} = \begin{pmatrix} a & c \\ c^* & b \end{pmatrix}$$

where $\{a, b, c, \alpha, \beta, \gamma\} \in \mathbb{C}$; the column density matrix can be written in column-stacked form

$$\text{col } \hat{\rho} = \begin{pmatrix} a \\ c^* \\ c \\ b \end{pmatrix}. \quad (6.3)$$

The following is true in general:

$$\text{col} \left(\hat{S}_\alpha \hat{\rho} \right) = \begin{pmatrix} \alpha a + \gamma c^* \\ \gamma^* a + \beta c^* \\ \alpha c + \gamma b \\ \gamma^* c + \beta b \end{pmatrix} \neq \text{col} \left(\hat{\rho} \hat{S}_\alpha \right) = \begin{pmatrix} \alpha a + \gamma^* c \\ \alpha c^* + \gamma^* b \\ \gamma a + \beta c \\ \gamma c^* + \beta b \end{pmatrix}.$$

A superoperator form, which would give the same result when acting on the column-stacked density matrix i.e. $\text{col } \hat{\rho}$ in eq. (6.3) is sought after.

One such possibility is $(\hat{1} \otimes \hat{S}_\alpha)$ which acting on eq. (6.3) gives the following

result:

$$\hat{\mathbf{S}}_{\alpha} \text{col} \hat{\rho} = (\hat{\mathbf{1}} \otimes \hat{S}_{\alpha}) \text{col} \hat{\rho} = \begin{pmatrix} \alpha & \gamma & 0 & 0 \\ \gamma^* & \beta & 0 & 0 \\ 0 & 0 & \alpha & \gamma \\ 0 & 0 & \gamma^* & \beta \end{pmatrix} \text{col} \hat{\rho} = \begin{pmatrix} \alpha a + \gamma c^* \\ \gamma^* a + \beta c^* \\ \alpha c + \gamma b \\ \gamma^* c + \beta b \end{pmatrix}.$$

The other is $(\hat{S}_{\alpha}^* \otimes \hat{\mathbf{1}})$ - here the asterisk represents a matrix conjugate, not to be mistaken with a Hermitian conjugate.

$$\hat{\mathbf{S}}'_{\alpha} \text{col} \hat{\rho} = (\hat{S}_{\alpha}^* \otimes \hat{\mathbf{1}}) \text{col} \hat{\rho} = \begin{pmatrix} \alpha & 0 & \gamma^* & 0 \\ 0 & \alpha & 0 & \gamma^* \\ \gamma & 0 & \beta & 0 \\ 0 & \gamma & 0 & \beta \end{pmatrix} \text{col} \hat{\rho} = \begin{pmatrix} \alpha a + \gamma^* c \\ \alpha c^* + \gamma^* b \\ \gamma a + \beta c \\ \gamma c^* + \beta b \end{pmatrix}.$$

From this one can conclude that

$$\begin{aligned} \hat{S}_{\alpha} \rho &\equiv (\hat{\mathbf{1}} \otimes \hat{S}_{\alpha}) \text{col} \hat{\rho} \\ \rho \hat{S}_{\alpha} &\equiv (\hat{S}_{\alpha} \otimes \hat{\mathbf{1}}) \text{col} \hat{\rho}. \end{aligned}$$

This property is generally expected to be true for 2×2 matrix operators, and their Kronecker products - applicable to spin-1/2 systems.

If an arbitrary operator \hat{S}_{α} acts on a Lindbladian dissipator of the form

$$\dot{\hat{\rho}} = \hat{S}_{\alpha} \mathbf{D}[\hat{L}_k] \hat{\rho} = \hat{S}_{\alpha} \left(\hat{L}_k \hat{\rho} \hat{L}_k^{\dagger} - 1/2 \{ \hat{\rho}, \hat{L}_k^{\dagger} \hat{L}_k \} \right)$$

then if the Lindblad dissipator is re-written to act on a column density operator $\text{col} \hat{\rho}$, i.e.

$$\dot{\text{col} \hat{\rho}} = \mathbf{S}_{\alpha} \left(\hat{L}_k^* \otimes \hat{L}_k - \frac{1}{2} \hat{\mathbf{1}} \otimes \hat{L}_k^{\dagger} \hat{L}_k - \frac{1}{2} (\hat{L}_k^{\dagger} \hat{L}_k)^* \otimes \hat{\mathbf{1}} \right) \text{col} \hat{\rho},$$

then the superoperator \mathbf{S}_{α} has the form

$$\mathbf{S}_{\alpha} = (\hat{\mathbf{1}} \otimes \hat{S}_{\alpha}).$$

A.4 Overhauser Effect dynamics projected onto Zeeman subspace

Solid-state Overhauser Effect DNP (OE-DNP) is most prominent in samples where the electron radical is delocalised over a relatively large volume. An example of such systems exhibiting OE-DNP would be metal conductors, graphene and samples with free radicals. The mechanism relies on the stochastic interactions between an electron and nuclei, which lead to cross-relaxation flip-flop or flip-flip transitions of the electron and a nucleus, driven by saturation of the electronic spin transition. The stochasticity of the interaction between an electron and a nucleus arises due to rotations and/or vibrations in the lattice. The OE will be most efficient if in the spectral density spectrum of a sample, there is a large difference in density values between the frequencies corresponding to ZQ, and DQ transitions.

More recently OE-DNP has been shown to be present in insulating solids which are subject to MAS [24]. There the mechanism is advantageous as it appears that the DNP enhancement increases with an increase in the magnetic field strength.

The system Hamiltonian in the rotating frame of reference can be rewritten for convenience;

$$\begin{aligned}\hat{H}_Z &= \Delta \hat{S}_z + \sum_k \omega_I \hat{I}_{kz}, \\ \hat{H}_0 &= \lambda \hat{S}_z + \frac{\omega_1}{2} (\hat{S}_+ + \hat{S}_-) + \sum_k A_k \hat{S}_z \hat{I}_{kz} \\ &+ \sum_{kk'} d_{kk'} (2\hat{I}_{kz} \hat{I}_{k'z} - \frac{1}{2} \hat{I}_{k+} \hat{I}_{k'-} - \frac{1}{2} \hat{I}_{k-} \hat{I}_{k'+}), \\ \hat{H}_\pm &= \sum_k B_{k\pm} \hat{S}_z \hat{I}_{k\pm}.\end{aligned}$$

The system is also subject to longitudinal relaxation back to thermal equilibrium, decoherence, and double-quantum as well as zero-quantum cross-relaxation transitions

$$\begin{aligned}\Gamma &= \Gamma_+^{(S)} \mathbf{D}[\hat{S}_+] + \Gamma_-^{(S)} \mathbf{D}[\hat{S}_-] + \Gamma_z^{(S)} \mathbf{D}[\hat{S}_z] + \sum_k (\Gamma_{k+}^{(I)} \mathbf{D}[\hat{I}_{k+}] + \Gamma_{k-}^{(I)} \mathbf{D}[\hat{I}_{k-}] + \Gamma_{kz}^{(I)} \mathbf{D}[\hat{I}_{kz}]) \\ &+ \Gamma_{++}^{(SI)} \mathbf{D}[\hat{T}_+] + \Gamma_{--}^{(SI)} \mathbf{D}[\hat{T}_-] + \Gamma_{+-}^{(SI)} \mathbf{D}[\hat{U}_+] + \Gamma_{-+}^{(SI)} \mathbf{D}[\hat{U}_-],\end{aligned}$$

where the operators \hat{T}, \hat{U} are

$$\hat{T}_\pm = \hat{S}_\pm \hat{I}_{k\pm} \quad \hat{U}_\pm = \hat{S}_\pm \hat{I}_{k\mp}.$$

These are responsible for double-quantum and zero-quantum cross-relaxation transitions, respectively.

The OE resonance condition is $\Delta \approx 0$. At this condition, the Zeeman Hamiltonian becomes $\hat{H}_Z = \sum_k \omega_I \hat{I}_{kz}$.

As was the case with projections for SE-DNP and CE-DNP, the Liouville state space can be decomposed as

$$\mathcal{L} = \sum \mathcal{L}_q,$$

where \mathcal{L}_q is the subspace of q -quantum coherences,

$$\hat{H}_Z \hat{\rho} = q\omega_I \hat{\rho}, \quad \hat{\rho} \in \mathcal{L}_q, \quad q = 0, \pm 1, \dots, \pm(n+1). \quad (6.4)$$

Since

$$\omega_I \gg A_k, B_{k\pm}, d_{kk'}, \Gamma_z^{(S)}, \Gamma_{kz}^{(I)}, \Gamma_{\pm}^{(S)}, \Gamma_{k\pm}^{(I)}, \Gamma_{\pm\pm}^{(SI)}, \Gamma_{\pm\mp}^{(SI)},$$

dynamics in the subspace where $\hat{H}_Z \hat{\rho} = q\omega_I \hat{\rho}$, for $q \neq 0$ evolve on a time-scale much faster than the subspace where $\hat{H}_Z \hat{\rho} = 0$. It is thus possible to separate the dynamics between these subspaces. The Hilbert subspace that commutes with \hat{H}_Z is referred to from hereon as the zero-quantum subspace. It is in fact the zero-quantum subspace of the nuclear spins. This projection itself is analogous to projecting the dynamics onto the subspace of nuclear spins and the off-resonance electron in the CE-DNP case, as there the first (on-resonance) electron is also saturated by microwave radiation.

Under the conditions

$$(2R_2^{(I)})^2 \gg \frac{d_{kk'}^2}{4} \\ (R_2^{(S)})^2 \gg \left\{ \frac{\omega_1^2}{2}, R_1^{(S)}, R_1^{(I)}, \Gamma_{\pm\pm}^{(SI)}, \Gamma_{\pm\mp}^{(SI)} \right\} \quad (6.5)$$

using the adiabatic elimination procedure described in section 2.4 it is possible to project the OE-DNP dynamics onto the Zeeman subspace resulting in effective classical-like dynamics

$$\dot{\hat{\rho}} = \mathbf{L}_Z \hat{\rho}, \quad \mathbf{L}_Z = \mathbf{L}_{0,00} + \mathbf{M}', \quad \mathbf{M}' = -\mathbf{L}_{0,01} \mathbf{L}_{0,11}^{-1} \mathbf{L}_{0,10}. \quad (6.6)$$

Here

$$\mathbf{L}_{0,00} = \mathbf{\Gamma}' + \mathbf{\Gamma}'' ,$$

and the superoperator \mathbf{M}' is well approximated as

$$\mathbf{M}' = \sum_{k < k'} \Gamma_{kk'}^{(II)} \mathbf{D}[\hat{X}_{kk'}]. \quad (6.7)$$

where $\mathbf{\Gamma}'$ is

$$\begin{aligned} \mathbf{\Gamma}' = & \Gamma_+^{(S)} \mathbf{D}[\hat{S}_+] + \Gamma_-^{(S)} \mathbf{D}[\hat{S}_-] + \sum_k (\Gamma_{k+}^{(I)} \mathbf{D}[\hat{I}_{k+}] + \Gamma_{k-}^{(I)} \mathbf{D}[\hat{I}_{k-}]) \\ & + \Gamma_{++}^{(SI)} \mathbf{D}[\hat{T}_+] + \Gamma_{--}^{(SI)} \mathbf{D}[\hat{T}_-] + \Gamma_{+-}^{(SI)} \mathbf{D}[\hat{U}_+] + \Gamma_{-+}^{(SI)} \mathbf{D}[\hat{U}_-] \end{aligned}$$

and $\mathbf{\Gamma}''$ is

$$\mathbf{\Gamma}'' = \frac{\omega_1^2}{2} \frac{R_2^{(S)}}{(R_2^{(S)})^2 + \hat{\alpha}^2} \left(\mathbf{D}[\hat{S}_+] + \mathbf{D}[\hat{S}_-] \right) + \frac{|B_k|^2 R_2^{(I)}}{8\omega_I^2} \sum_k \left(\mathbf{D}[\hat{I}_{k+}] + \mathbf{D}[\hat{I}_{k-}] \right),$$

and

$$\begin{aligned} \Gamma_{kk'}^{(II)} &= \frac{d_{kk'}^2}{2} \frac{2R_2^{(I)}}{(2R_2^{(I)})^2 + \hat{\beta}_{kk'}^2}, \\ \hat{X}_{kk'} &= (\hat{I}_{k+} \hat{I}_{k'-} + \hat{I}_{k-} \hat{I}_{k'+}), \\ \hat{\alpha} &= \lambda \hat{1} + \sum_k A_k \hat{I}_{kz}, \\ \hat{\beta}_{kk'} &= (A_k - A_{k'}) \hat{S}_z + \frac{1}{8\omega_I} (|B_k|^2 - |B_{k'}|^2) \hat{1}. \end{aligned} \quad (6.8)$$

As was the case with SE-DNP and CE-DNP, the effective dynamics show a state-dependence - eq. (6.8). Kinetic Monte Carlo algorithms can be used to simulate large spin system ensembles.

Bibliography

- [1] I. Bertini, K.S. McGreevy, and G. Parigi. *NMR of Biomolecules*. Wiley–Blackwell, 2012.
- [2] K. Wütrich et al. Improved spectral resolution in cosy ^1H NMR spectra of proteins via double quantum filtering. *Biochem. Biophys. Res. Commun.*, 117(2):497–485, 1983.
- [3] S. B. Shuker, P. J. Hajduk, R. P. Meadows, and S. W. Fesik. Discovering high–affinity ligands for proteins: SAR by NMR. *Science*, 274(5292):1531–1534, 1996.
- [4] F. Chiti and C. M. Dobson. Protein misfolding, functional amyloid, and human disease. *Annu. Rev. Biochem.*, 75(1):333–366, 2006.
- [5] S. V. Dvinskikh, V. Castro, and D. Sandström. Heating caused by radiofrequency irradiation and sample rotation in ^{13}C magic angle spinning NMR studies of lipid membranes. *Magn. Reson. Chem.*, 42(10):875–881, 2004.
- [6] H. J. Jakobsen, A. R. Hove, R. G. Hazell, H. Bildsoe, and J. Skibsted. Solid–state ^{14}N MAS NMR of ammonium ions as a spy to structural insights for ammonium salts. *Magn. Reson. Chem.*, 44(3):348–356, 2006.
- [7] J.-L. Hodeau and R. Guinebretiere. Crystallography: past and present. *Appl. Phys. A*, 89(4):813–823, 2007.
- [8] F. W. Wehrli. On the 2003 nobel prize in medicine or physiology awarded to Paul C. Lauterbur and Sir Peter Mansfield. *Magn. Reson. Med.*, 51(1):1–3, 2004.
- [9] P.M. Matthews et al. Advances in functional and structural MR image analysis and implementation as FSL. *NeuroImage*, 23, Supplement 1:S208 – S219, 2004.
- [10] S. Ogawa, T.M. Lee, and D.W. Tank. Brain magnetic resonance imaging with contrast dependent on blood oxygenation. *Proc. Natl. Acad. Sci.*, 87(24):9868–9872, 1990.

- [11] E. J. Hall and D. J. Brenner. Cancer risks from diagnostic radiology. *Brit. J. Radiol.*, 81(965):362–378, 2008.
- [12] M. H. Levitt. *Spin Dynamics*. Wiley, 2008.
- [13] J. S. Natterer and J. Bargon. Parahydrogen induced polarization. *Prog. Nucl. Mag. Res. SP.*, 31(4):293 – 315, 1997.
- [14] P. Maletinsky et al. A robust scanning diamond sensor for nanoscale imaging with single nitrogen–vacancy centres. *Nature*, 7:320–324, 2012.
- [15] C. C. Vassiliou et al. Room–temperature in situ nuclear spin hyperpolarization from optically pumped nitrogen vacancy centres in diamond. *Nat. Commun.*, 6:8965, 2015.
- [16] T. G. Walker and W. Happer. Spin–exchange optical pumping of noble–gas nuclei. *Rev. Mod. Phys.*, 69:629–642, Apr 1997.
- [17] J. F. G. Vliegthart et al. Carbohydrate–protein interaction studies by laser photo CIDNP NMR methods. *Glycoconjugate J.*, 14(4):531–534, 1997.
- [18] D. C. Williamson et al. Reversible interactions with para–hydrogen enhance nmr sensitivity by polarization transfer. *Science*, 323(5922):1708–1711, 2009.
- [19] L. C. L. Hollenberg et al. The nitrogen–vacancy colour centre in diamond. *Phys. Rep.*, 528(1):1 – 45, 2013.
- [20] J. Wrachtrup et al. Dynamic polarization of single nuclear spins by optical pumping of nitrogen–vacancy color centers in diamond at room temperature. *Phys. Rev. Lett.*, 102:057403, Feb 2009.
- [21] H.R. Ward. Chemically induced dynamic nuclear polarization (CIDNP). I. Phenomenon, examples, and applications. *Acc. Chem. Res.*, 5(1):18–24, 1972.
- [22] S. H. Pine. Chemically induced dynamic nuclear polarization. *J. Chem. Educ.*, 49(10):664, 1972.
- [23] J. E. Harriman. *Theoretical Foundations of Electron Spin Resonance*, volume 37. Academic Press, 1978.
- [24] T.V. Can, Q.Z. Ni, and R.G. Griffin. Mechanisms of dynamic nuclear polarization in insulating solids. *J. Magn. Reson.*, 253:23 – 35, 2015.
- [25] R. G. Griffin and T. F. Prisner. High field dynamic nuclear polarization–the renaissance. *Phys. Chem. Chem. Phys.*, 12:5737–5740, 2010.

- [26] T. Maly et al. Dynamic nuclear polarization at high magnetic fields. *J. Chem. Phys.*, 128(5), 2008.
- [27] K. M. Brindle et al. Detecting tumor response to treatment using hyperpolarized ^{13}C magnetic resonance imaging and spectroscopy. *Nat. Med.*, 13:1382–1387, 2007.
- [28] J. A. Murray et al. Metabolic imaging of patients with prostate cancer using hyperpolarized $1\text{-}^{13}\text{C}$ pyruvate. *Science Trans. Med.*, 5:198ra108, 2013.
- [29] K. Golman et al. Increase in signal-to-noise ratio of $> 10,000$ times in liquid-state NMR. *Proc. Natl. Acad. Sci.*, 100(18):10158–10163, 2003.
- [30] C.-G. Joo, K.-N. Hu, J. A. Bryant, and R. G. Griffin. In situ temperature jump high-frequency dynamic nuclear polarization experiments: enhanced sensitivity in liquid-state NMR spectroscopy. *J. Am. Chem. Soc.*, 128(29):9428–9432, 2006.
- [31] A. W. Overhauser. Polarization of nuclei in metals. *Phys. Rev.*, 92:411–415, Oct 1953.
- [32] T. R. Carver and C. P. Slichter. Experimental verification of the overhauser nuclear polarization effect. *Phys. Rev.*, 102:975–980, May 1956.
- [33] A. K. Geim and K. S. Novoselov. The rise of graphene. *Nat. Mat.*, 6:183–191, 2007.
- [34] Y. Hovav, A. Feintuch, and S. Vega. Theoretical aspects of dynamic nuclear polarization in the solid state – spin temperature and thermal mixing. *Phys. Chem. Chem. Phys.*, 15:188–203, 2013.
- [35] E. C. Reynhardt and G. L. High. Dynamic nuclear polarization of diamond. I. solid state and thermal mixing effects. *J. Chem. Phys.*, 109(10):4090–4099, 1998.
- [36] D. Shimon, Y. Hovav, A. Feintuch, D. Goldfarb, and S. Vega. Dynamic nuclear polarization in the solid state: a transition between the cross effect and the solid effect. *Phys. Chem. Chem. Phys.*, 14:5729–5743, 2012.
- [37] Y. Hovav, A. Feintuch, and S. Vega. Theoretical aspects of dynamic nuclear polarization in the solid state – the solid effect. *J. Magn. Reson.*, 207(2):176 – 189, 2010.
- [38] Y. Hovav, A. Feintuch, and S. Vega. Dynamic nuclear polarization assisted spin diffusion for the solid effect case. *J. Chem. Phys.*, 134(7), 2011.

- [39] A. Karabanov, G. Kwiatkowski, and W. Köckenberger. Spin dynamic simulations of solid effect DNP: the role of the relaxation superoperator. *Mol. Phys.*, 112(14):1838–1854, 2014.
- [40] J. Preskill. Lecture notes for physics 229: Quantum information and computation. <https://docs.google.com/file/d/0B0xb4cr0vCgTdjgxcGxyM0k1azA/edit>, September 1998. California Institute of Tehnology.
- [41] A.J. Fisher et al. Graduate course notes on open quantum systems. University of Waterloo, 2004.
- [42] T.F. Havel. Robust procedures for converting among Lindblad, Kraus and matrix representations of quantum dynamical semigroups. *J. Math. Phys.*, 44(2):534–557, 2003.
- [43] C. Ates, B. Olmos, W. Li, and I. Lesanovsky. Dissipative binding of lattice bosons through distance–selective pair loss. *Phys. Rev. Lett.*, 109:233003, Dec 2012.
- [44] K. Dietz. Decoherence by Lindblad motion. *J. Phys. A-Math. Gen.*, 37(23):6143, 2004.
- [45] A. Isar, A. Sandulescu, H. Scutaru, E. Stefanescu, and W. Scheid. Open quantum systems. *Int. J. Mod. Phys. E*, 03(02):635–714, 1994.
- [46] A. Purkayastha, A. Dhar, and M. Kulkarni. Out–of–equilibrium open quantum systems: A comparison of approximate quantum master equation approaches with exact results. *Phys. Rev. A*, 93:062114, Jun 2016.
- [47] D. Stanek, C. Raas, and G. S. Uhrig. Dynamics and decoherence in the central spin model in the low–field limit. *Phys. Rev. B*, 88:155305, Oct 2013.
- [48] F. Mintert, M. Lapert, Y. Zhang, S. J. Glaser, and D. Sugny. Saturation of a spin-1/2 particle by generalized local control. *New J. of Phys.*, 13(7):073001, 2011.
- [49] V. V. Albert, G. D. Scholes, and P. Brumer. Symmetric rotating–wave approximation for the generalized single–mode spin–boson system. *Phys. Rev. A*, 84:042110, Oct 2011.
- [50] H. P. Breuer and F. Petruccione. *The theory of open quantum systems*. UOP Oxford, 2002.
- [51] C. D. Jeffries. *Dynamic Nuclear Orientation*. Interscience Publishers, 1963.

- [52] A. Karabanov, D. Wiśniewski, I. Lesanovsky, and W. Köckenberger. Dynamic nuclear polarization as kinetically constrained diffusion. *Phys. Rev. Lett.*, 115:020404, Jul 2015.
- [53] M. B. Plenio and P. L. Knight. The quantum-jump approach to dissipative dynamics in quantum optics. *Rev. Mod. Phys.*, 70:101–144, Jan 1998.
- [54] H.-P. Breuer, B. Kappler, and F. Petruccione. Stochastic wave-function method for non-markovian quantum master equations. *Phys. Rev. A*, 59:1633–1643, Feb 1999.
- [55] H. Carmichael. *An open systems approach to quantum optics*, volume 18. Springer Berlin Heidelberg, 1993.
- [56] F. Ritort and P. Sollich. Glassy dynamics of kinetically constrained models. *Adv. Phys.*, 52(4):219–342, 2003.
- [57] J. P. Garrahan and D. Chandler. Coarse-grained microscopic model of glass formers. *Proc. Natl. Acad. Sci.*, 100(17):9710–9714, 2003.
- [58] J. Crank. *The mathematics of diffusion*. Oxford University Press, 2nd edition, March 1980.
- [59] D. Wiśniewski, A. Karabanov, I. Lesanovsky, and W. Köckenberger. Solid effect DNP polarization dynamics in a system of many spins. *J. Magn. Reson.*, 264:30 – 38, 2016.
- [60] J.H. Ardenkjaer-Larsen, S. Macholl, and H. Johannesson. Dynamic nuclear polarization with trityls at 1.2 K. *Appl. Magn. Reson.*, 34:509 – 522, 2008.
- [61] V. Nagarajan, Y. Hovav, A. Feintuch, S. Vega, and D. Goldfarb. EPR detected polarization transfer between Gd 3+ and protons at low temperature and 3.3 T: The first step of dynamic nuclear polarization. *J. Chem. Phys.*, 132:214504, 2010.
- [62] K. Golman et al. EPR and DNP properties of certain novel single electron contrast agents intended for oximetric imaging. *J. Magn. Reson.*, 133:1 –12, 1998.
- [63] H. Johannesson, S. Macholl, and J.H. Ardenkjaer-Larsen. Dynamic nuclear polarization of [1-13C]pyruvic acid at 4.6 Tesla. *J. Magn. Reson.*, 197:167–175, 2009.
- [64] O. N. Martyanov et al. Hyperfine interactions of narrow-line trityl radical with solvent molecules. *J. Magn. Reson.*, 233:29–36, 2013.

- [65] K.-N. Hu, C. Song, H.-h. Yu, T. M. Swager, and R. G. Griffin. High-frequency dynamic nuclear polarization using biradicals: A multifrequency EPR line-shape analysis. *J. Chem. Phys.*, 128(5), 2008.
- [66] K.-N. Hu, H. h. Yu, T. M. Swager, and R. G. Griffin. Dynamic nuclear polarization with biradicals. *J. Am. Chem. Soc.*, 126(35):10844–10845, 2004.
- [67] S. Vega et al. The electron depolarization during dynamic nuclear polarization: measurements and simulations. *Phys. Chem. Chem. Phys.*, 17:226–244, 2015.
- [68] S. Vega et al. Effects of the electron polarization on dynamic nuclear polarization in solids. *Phys. Chem. Chem. Phys.*, 17:6053–6065, 2015.
- [69] D. Shimon, A. Feintuch, D. Goldfarb, and S. Vega. Static 1H dynamic nuclear polarization with the biradical TOTAPOL: a transition between the solid effect and the cross effect. *Phys. Chem. Chem. Phys.*, 16:6687–6699, 2014.
- [70] G. De Paepe et al. Nuclear depolarization and absolute sensitivity in magic-angle spinning cross effect dynamic nuclear polarization. *Phys. Chem. Chem. Phys.*, 17:21824–21836, 2015.
- [71] F. Mentink-Vigier, U. Akbey, H. Oschkinat, S. Vega, and A. Feintuch. Theoretical aspects of magic angle spinning – dynamic nuclear polarization. *J. Magn. Reson.*, 258:102 – 120, 2015.
- [72] R. Rizzato, I. Kaminker, S. Vega, and M. Bennati. Cross-polarisation edited ENDOR. *Mol. Phys.*, 111(18-19):2809–2823, 2013.
- [73] D. Mance, P. Gast, M. Huber, M. Baldus, and K. L. Ivanov. The magnetic field dependence of cross-effect dynamic nuclear polarization under magic angle spinning. *J. Chem. Phys.*, 142(23), 2015.
- [74] M. Lee, M. C. Cassidy, C. Ramanathan, and C. M. Marcus. Decay of nuclear hyperpolarization in silicon microparticles. *Phys. Rev. B*, 84:035304, Jul 2011.
- [75] K. R. Thurber, W.-M. Yau, and R. Tycko. Low-temperature dynamic nuclear polarization at 9.4 T with a 30 mW microwave source. *J. Magn. Reson.*, 204(2):303 – 313, 2010.
- [76] K. R. Thurber and R. Tycko. On mechanisms of dynamic nuclear polarization in solids. *Israel J. Chem.*, 54(1-2):39–46, 2014.
- [77] A. E. Dementyev, D. G. Cory, and C. Ramanathan. Dynamic nuclear polarization in silicon microparticles. *Phys. Rev. Lett.*, 100:127601, Mar 2008.

- [78] A. De Luca and A. Rosso. Dynamic nuclear polarization and the paradox of quantum thermalization. *Phys. Rev. Lett.*, 115:080401, 2015.
- [79] D. Banerjee, D. Shimon, A. Feintuch, S. Vega, and D. Goldfarb. The interplay between the solid effect and the cross effect mechanisms in solid state ^{13}C DNP at 95 GHz using trityl radicals. *J. Magn. Reson.*, 230:212–219, 2013.